UCSF
UC San Francisco Electronic Theses and Dissertations

Title
Quantitative imaging in small animals using SPECT-CT

Permalink
https://escholarship.org/uc/item/13d088hc

Author
Hwang, Andrew Bing

Publication Date
2006

Peer reviewed|Thesis/dissertation

eScholarship.org Powered by the California Digital Library
University of California

Quantitative Imaging in Small Animals Using SPECT-CT

by

Andrew Bing Hwang

DISSERTATION

Submitted in partial satisfaction of the requirements for the degree of

DOCTOR OF PHILOSOPHY

in

Bioengineering

in the

GRADUATE DIVISIONS

of the

UNIVERSITY OF CALIFORNIA, SAN FRANCISCO

AND

UNIVERSITY OF CALIFORNIA, BERKELEY

[redacted]

Date University Librarian

Degree Conferred: ______________________________

copyright 2006

by

Andrew Bing Hwang

Acknowledgements

Along the wandering road that has led me to and through graduate school, many people have helped me reach the milestone that is the completion of this dissertation. To them, I owe a great many thanks.

My dissertation advisor, Bruce Hasegawa, has been a wonderful mentor and a good friend. He has been extraordinarily generous with his time, particularly during the writing of this thesis. I have greatly enjoyed my time in his lab.

In addition to my advisor, I have been fortunate to have had many good mentors during my time in graduate school. Grant Gullberg has also been a great help and source of expertise. In addition, I am indebted to Ping Xia and John Kurhanewicz, who mentored me during research rotations. I also owe a special thanks to Dave Attwood and Nola Hylton for taking the time to read this dissertation.

The members of the Physics Research Lab have been good friends and colleagues. The postdocs, past and present, are a diverse group with whom I have enjoyed working. I owe special thanks to Philippe Després, Youngho Seo, and Kevin Teo for their help with Monte Carlo simulations and for sharing their computing resources. My fellow students, Carmen Taylor and Mingshan Sun, and Cathy Devine, our peerless administrative assistant, always manage to brighten my day.

I have also had the pleasure of working with some extraordinary colleagues. Dongwei Gao, Danzo Pan, and Benjamin Franc have been very generous to share the animal data that is presented in this thesis, and Ying Lu was kind enough to help me with the statistical analysis.

Outside the lab, I have had the friendship and support of many wonderful people. My parents, grandparents, and the whole of my extended family have truly been a blessing to me since the day that I was born. Their love and help have been unconditional. My wife, Anne, has been a great help and encouragement, particularly during the most stressful times of graduate school. I eagerly anticipate journeying down the road of life together with her. Finally, thanks and praise to God, the giver of every good and perfect gift.

Abstract

Quantitative Imaging in Small Animals Using SPECT-CT

by Andrew Bing Hwang

The use of noninvasive imaging to assess animal models of disease has the potential to revolutionize the fields of biological research and drug development by allowing *in vivo* assessments of physiological function. Radionuclide imaging using single photon emission computed tomography (SPECT) because it can extract physiological, metabolic, and molecular information from intact animals using radiolabeled tracers and probes. By combining SPECT with CT, the functional information of radionuclide imaging can be fused with the high resolution anatomical information of x-ray CT imaging to increase the utility of the resulting data. However, to maximize the acceptance and usefulness of imaging as an alternative to traditional invasive techniques, such as tissue harvesting, it is necessary to assess and optimize the quantitative accuracy of small animal SPECT.

The term "radionuclide quantification" has a number of different meanings in the medical imaging literature. Within the scope of this thesis, radionuclide quantification is used to mean absolute physical quantification, or the measurement of the absolute concentration of radiotracer within a volume of interest.

To achieve this goal of improved radionuclide quantification, we have incorporated models of photon attenuation, scatter, and the depth-dependent spatial resolution of the pinhole collimator into an iterative reconstruction algorithm. These algorithms were tested used to reconstruct experimentally acquired data, and were found to improve the quality of reconstructed SPECT images (*e.g.*, improved spatial resolution, contrast). We then used Monte Carlo simulations and experimental measurements to assess the effect of photon attenuation, partial volume errors, and photon scatter on the quantitative accuracy of the SPECT images. The simulated data was also used to demonstrate that the improved reconstruction algorithms also result in improved quantitative accuracy. We also tested the combined methods and techniques described in this thesis on phantom data, and found that including models for photon attenuation and collimator response resulted in improved quantitative accuracy. Finally, the techniques were applied to an animal study performed to characterize the behavior of a new imaging agent for prostate cancer.

Bruce Hasegawa

Bruce H. Hasegawa, PhD
dissertation chair

Table of Contents

List of Tables viii

List of Figures ix

Chapter 1: Introduction **1**
- 1.1. Statement of thesis 1
- 1.2. Background 2
- 1.3. Project goal 11

Chapter 2: X-SPECT System Description **14**
- 2.1. Overview 14
- 2.2. System description 14
- 2.3. Data acquisition and reconstruction 22
- 2.4. Image co-registration 32
- 2.5. Prediction and assessment of system performance 40
- 2.6. Description of second X-SPECT system 56
- 2.7. Conclusion 57

Chapter 3: Calibration of SPECT Imaging Geometry **60**
- 3.1. Overview 60
- 3.2. Simulations 67
- 3.3. Experimental measurements 76
- 3.4. Conclusion 86

Chapter 4: Improved SPECT Reconstruction **87**
- 4.1. Overview 87
- 4.2. Photon attenuation 90
- 4.3. Collimator response 107
- 4.4. Depth of interaction 124
- 4.5. Scatter correction 129
- 4.6. Conclusion 146

Chapter 5: Error Sources in Quantitative SPECT Imaging **150**
- 5.1. Introduction 150
- 5.2. Monte Carlo simulations 155
- 5.3. Experimental measurements 172
- 5.4. Conclusion 190

Chapter 6: Application of Quantitative Imaging **193**
- 6.1. Background 193
- 6.2. Monte Carlo simulations 195
- 6.3. Calibration measurements 207
- 6.4. Phantom study 217
- 6.5. Animal studies 221
- 6.6. Conclusions 230

Chapter 7: Conclusions 233

Appendix 1: Geometric Calibration Programs 239

Appendix 2: Ray-driven Projector Program 245

Appendix 3: Iterative Reconstruction Algorithm with Collimator Response and Attenuation Correction 251

List of Tables

1.1	Selected radionuclide tracers and applications	10
2.1	Common isotopes used in SPECT imaging	17
2.2	Estimated spatial resolution in tomographic images	49
2.3	Comparison of the two UCSF X-SPECT systems	57
3.1	Constraints on geometric parameter values	66
3.2	Parameters used in simulations to test geometric calibration	69
3.3	Correlation between parameters values used in simulation with calibration results	73
3.4	Results of X-SPECT geometric calibration	81
4.1	Materials used in the solid CT calibration phantom	96
4.2	CT image values of calibration materials	99
4.3	Parameter values for linear fit of CT calibration results	100
4.4	Pinhole aperture dimensions for simulations	115
4.5	Reconstruction time needed for various algorithms	124
4.6	Components of the linear attenuation coefficient for water	144
5.1	Energy resolution and energy windows in Monte Carlo simulations	155
5.2	Photon energies used in Monte Carlo simulations	159
5.3	Change in VOI values due to scatter	163
5.4	Dimensions of microspheres	173
5.5	X-ray CT acquisition parameters for microsphere experiments	175
5.6	SPECT imaging parameters for microsphere experiments	176
5.7	Linear fitting results for VOI values *vs.* (activity × time)	181
5.8	Linear fitting results for VOI values *vs.* (activity × time)	181
6.1	Parameters for Monte Carlo simulations	197
6.2	SPECT acquisition and reconstruction parameters	208
6.3	CT acquisition and reconstruction parameters	208
6.4	Coregistration parameters for new X-SPECT scanner	214
6.5	Correlation between measured and true radioactivity concentration in the phantom	220
6.6	Variability in the definition of the volume of interest	230

List of Figures

1.1 Number of references to “molecular imaging” in literature 3

2.1 Photograph of the X-SPECT scanner 15
2.2 Photograph of the X-SPECT scanner pinhole collimators 18
2.3 Drawings of knife edge and keel edge pinhole apertures 19
2.4 Photograph of the animal bed in the X-SPECT scanner 22
2.5 Drawing of the X-SPECT configured for SPECT imaging 23
2.6 Drawing of the X-SPECT configured for CT imaging 24
2.7 Photograph of the uniform flood phantom 25
2.8 Formation of projection images in x-ray CT 29
2.9 Image of phantom used to obtain coregistration parameters 37
2.10 Magnification factor for coregistration of CT and SPECT 38
2.11 Calculation of the field of view for SPECT imaging 42
2.12 Plot of the expected field of view *vs*. radius of rotation 43
2.13 Pinhole imaging geometry parameters 45
2.14 Measured and calculated SPECT spatial resolution 47
2.15 Photographs of phantoms used to assess SPECT spatial resolution 48
2.16 Reconstructed SPECT images of hot rod phantom 48
2.17 Measured and calculated SPECT detection efficiency 51
2.18 Measured and calculated detection efficiency of SPECT, without flat field correction 52
2.19 Geometry of x-ray imaging system 54

3.1 Example of an artifact caused by misalignment of the gamma camera 60
3.2 Illustration of geometric parameters in SPECT imaging 62
3.3 Illustration of geometric parameters in SPECT imaging 63
3.4 Illustration of geometric parameters in SPECT imaging 63
3.5 Illustration of the depth of interaction effect 71
3.6 Comparison of measured *vs*. estimated projection locations in simulated data 72
3.7 Plot of estimated *vs*. simulation focal length 73
3.8 Tomograms of point sources showing artifacts due to geometrical errors 74
3.9 Effect of mechanical shift on spatial resolution 75
3.10 Phantom used for geometrical calibration 78
3.11 Plot of distance measured in detector pixels *vs*. physical distance 80
3.12 Plot of measured *vs*. nominal magnification 82
3.13 Comparison of measured *vs*. estimated projection locations in experimental data 84
3.14 Effect of calibration on length measurements in images 85

4.1	Overview of the iterative reconstruction process	88
4.2	Drawing of the CT calibration phantom for liquid materials	95
4.3	Photograph of the CT calibration phantom with solid materials	95
4.4	Plot of photon attenuation at 140 keV *vs.* CT image values	100
4.5	Plot of photon attenuation at 27.5 keV *vs.* CT image values	100
4.6	Effect of x-ray tube potential on CT image values	101
4.7	Effect of x-ray tube current on CT iamge values	102
4.8	SPECT image demonstrating cupping artifact due to photon attenuation	103
4.9	SPECT imaging demonstrating that attenuation correction eliminates the cupping artifact	103
4.10	CT image demonstrating effect of beam hardening	106
4.11	Comparison of ideal *vs.* real pinhole collimator	108
4.12	Collimator response modeling using multiple rays	109
4.13	Coordinate system used in reconstruction algorithm	112
4.14	Flowchart describing collimator response modeling using multiple rays	113
4.15	Geometry used for Monte Carlo simulations	115
4.16	Sensitivity *vs.* distance for multi-ray projector	119
4.17	Sensitivity *vs.* angle for multi-ray projector	119
4.18	Point spread function for multi-ray projector (2 mm pinhole)	120
4.19	Point spread function for multi-ray projector (1 mm pinhole)	120
4.20	Images of hot rod phantom reconstructed with different number of iterations with and without collimator response	122
4.21	Images of hot rod phantom acquired with different pinholes and reconstructed with and without collimator response	122
4.22	Noise *vs.* spatial resolution trade-off	123
4.23	Illustration of the depth of interaction modeling	126
4.24	Point spread function with and without depth of interaction	128
4.25	Image of hot rod phantom reconstructed with DOI modeling	129
4.26	Geometry used in scatter correction algorithm	133
4.27	Simulation geometry used to determine angular distribution of photon scatter	134
4.28	Scatter-to-primary ratio for a source inside a cylinder of water	137
4.29	Energy spectrum of I-125 photons with and without scatter	138
4.30	Angular distribution of scattered I-125 photons	139
4.31	Scatter source estimate from scatter correction algorithm	141
4.32	Reconstructed image of data used to evaluate scatter correction	141
4.33	Line profile through data used to evaluate scatter correction	142
4.34	Projection data of I-125 filled sphere showing effect of scatter	143
4.35	Reconstructed image of an I-125 filled sphere showing effect of scatter correction	144
4.36	Angular distribution of Rayleigh and Compton scatter	145
4.37	Number of scatter interactions prior to detection	146

5.1 Photon transmission through water for four isotopes used in SPECT 153
5.2 Illustration of partial volume error due to "spill-out" 154
5.3 Illustration of partial volume error due to "spill-in" 154
5.4 Scatter to primary ratio for I-125 and Tc-99m 160
5.5 Effect of photon attenuation on VOI values for I-125 imaging 161
5.6 Effect of photon scatter on VOI values for I-125 imaging 162
5.7 Quantitative effect of scatter and scatter correction for I-125 imaging 162
5.8 Quantitative effect of photon attenuation on Tc-99m imaging 164
5.9 Quantitative effect of photon scatter on Tc-99m imaging 164
5.10 Effect of partial volume errors on quantitative accuracy 165
5.11 Effect of background radioactivity on quantitative accuracy 167
5.12 Effect of background radioactivity on quantitative accuracy 167
5.13 Effect of background radioactivity on the convergence of reconstruction algorithms 168
5.14 Demonstration of non-linearity of the reconstruction process 171
5.15 Effect of detector pixel size on partial volume errors 172
5.16 Images of microsphere phantoms 174
5.17 SPECT image of microsphere phantom 177
5.18 Plot of voxel values *vs*. product of radioactivity concentration and imaging time 177
5.19 Plot showing the effect of photon attenuation on measured radioactivity 178
5.20 Plot demonstrating the quantitative effect of photon attenuation correction 179
5.21 Plot showing quantitative effect of microsphere size 180
5.22 Plot showing quantitative effect of microsphere size 180
5.23 Comparison of experimental and simulated results for partial volume effect 183
5.24 Effect of mechanical shift on partial volume errors 185
5.25 Plot of measured count rate *vs*. amount of radioactivity 187
5.26 Comparison of experimental and simulated results for partial volume effect after correction for count rate non-linearity 188

6.1 Effective attenuation coefficient for lutetium-177 *vs*. path length in water 201
6.2 Average voxel value in the volume of interest as a function of source size 203
6.3 Voxel values for a simulated source in a cylinder of water as a function of the cylinder radius 204
6.4 Effect of scatter on the measured radioactivity 204
6.5 Scatter-to-primary ratio for lutetium-177 205
6.6 Effect of the radius of rotation on voxel values 206
6.7 CT image calibration results for the new X-SPECT scanner 212

6.8	Plot of the measured *vs* the nominal magnification	213
6.9	Reconstructed image of a lutetium-177 filled microsphere	215
6.10	Image showing lutetium-177 adsorbed on phantom surfaces	216
6.11	Plot of SPECT image values *vs.* the radioactivity concentration in phantom	217
6.12	Plot of the radioactivity concentration in a phantom measured by imaging *vs.* the known concentration	219
6.13	Tumor volume measured with CT *vs.* tumor mass	225
6.14	Total radioactivity in tumor measured with SPECT *vs.* measured with dose calibrator	226
6.15	Error in radioactivity measurement as a function of the time between injection and imaging	228
6.16	SPECT-CT images of mice injected with Lu-177 labeled immunoconjugate	229

Chapter 1: Introduction

1.1. Statement of thesis

The use of noninvasive imaging to assess animal models of disease has the potential to revolutionize the fields of biological research and drug development by allowing *in vivo* assessments of physiological function. Radionuclide imaging using single photon emission computed tomography (SPECT) and positron emission tomography (PET) are important imaging modalities in these fields because they can extract physiological and in some cases, metabolic and molecular information from the intact animal using radiolabeled tracers and probes.

SPECT images are usually interpreted in a qualitative manner in clinical practice. However, to maximize the value of SPECT as a scientific tool, quantitative results are needed. For example, when SPECT is used to study the distribution of a radiolabeled drug or tracer in an animal, it is advantageous, and sometimes essential, to know in absolute terms the amount of uptake in a particular organ or tissue. Although this is simple in theory, it is difficult in practice due to a number of factors, including physical perturbations such as photon attenuation, spatial resolution limitations in SPECT, and lack of anatomical landmarks. Many of these limitations can be addressed with the use of structural information obtained from x-ray computed tomography (CT) images that are coregistered with the SPECT image data.

The purpose of this research project is first to assess the effect of various physical perturbations on the quantitative accuracy of small animal SPECT-CT imaging, and then to demonstrate that SPECT-CT can be a quantitative imaging modality for *in vivo* assessments of mammalian biology and human disease using small animals.

1.2. Background

Nuclear medicine encompasses the use of radioactive materials for therapeutic and diagnostic purposes, and dates back to the discovery of radium at the end of the 19th century by Marie Curie. At that time, radium was used as an alternative to x-ray tubes in the production of transmission images, but x-rays eventually became the method of choice for diagnostic transmission imaging. In addition, the use of radium as a photon source for transmission imaging does not involve the tracer principle, which is a hallmark of modern diagnostic nuclear medicine.

The tracer principle is one of the foundations of modern nuclear medicine, and it was first developed and applied by Georg de Hevesy. Simply stated, the tracer principle postulates that radioisotopes and radiolabeled chemicals ("radiopharmaceuticals") can be used as tracers to mimic the behavior of naturally occurring molecules *in vivo*, and that the small amount of radioisotopes and radiopharmaceuticals used does not perturb the system being studied. One example is the landmark study of Blumgart and Weiss in 1927, who measured the transit time of blood from the venous to arterial sides of the circulatory system by injecting radon intravenously into one arm vein and measuring the time for radioactivity to appear in the circulatory system in other arm [1]. A short list of modern radionuclide tracers and applications is shown in Table 1.1. In fact, there currently are over 40 radiopharmaceuticals approved for medical use and hundreds have been and are being investigated in research settings for both animal and human imaging.

Most radioisotopes used in nuclear medicine are not naturally occurring, and must be produced using one of several methods. Many isotopes, particularly those used in PET imaging, are manufactured using cyclotrons, which was invented by Ernest Lawrence in the 1930's [2]. This was followed by the development of nuclear reactors in the mid- to late-1940's which allowed production of radionuclides in larger quantities. Nuclear reactors, as well as cyclotrons and other accelerators, remain the source of most SPECT tracers.

Table 1.1: Selected radionuclide tracers and applications

Tracer Name	Application	Modality
^{99m}Tc-sestamibi	Cardiac perfusion	SPECT
^{18}F-fluorodeoxyglucose	Tumor metabolism	PET
Xenon-133	Pulmonary ventilation	SPECT
^{99m}Tc-methylene diphosphonate	Bone turn-over	SPECT

Although cyclotrons and nuclear reactors are capable of producing a wide variety of radionuclides, they are large and expensive, and thus the number of installations is limited. This creates logistical problems, particularly with shorter lived isotopes such as technetium-99m ($T_{1/2}$ = 6 hrs). The development of the radionuclide generator, therefore, was a key factor in the growth of nuclear medicine. In a generator system, a desired isotope (*e.g.*, technetium-99m) is first produced by decay from a longer lived isotope and is then removed from the generator for use. The most common example, technetium-99m, is produced from the decay of molybdenum-99 adsorbed onto an alumina column that can be eluted to extract the daughter radionuclide, technetium-99m. Molybdenum-99 has a half-life of 66 hours, so the generator has a productive life of approximately 1 week. This makes it possible to transport generators to imaging centers not located close to a source of radioisotopes. Over the course of a week, technetium-99m can be eluted from the column at various intervals and used to label various radiopharmaceuticals.

The availability of radionuclides and the recognition that radionuclides could be used to diagnose and treat disease led to the development of instruments designed specifically for imaging or recording the *in vivo* distribution of radiopharmaceuticals. In the 1950's, development of the rectilinear scanner (1951) allowed *in vivo* imaging of radionuclide distributions. The rectilinear scanner used one or two radiation detectors, each consisting of a single photomultiplier tube coupled to a scintillator and a focused collimator. This detector was scanned over a patient in a raster pattern in order to generate a planar image of the radionuclide distribution [3]. However, the rectilinear scanner had relatively poor spatial resolution (>1 cm) and required an hour or more to image large regions of the patient's body, as is needed to identify the extent of cancer.

The Anger camera (1957), also known as the gamma camera, greatly improved the speed and resolution of radionuclide imaging [4], and its basic design is still used in modern systems. The camera consists of multiple photomultiplier tubes coupled to a single, large area scintillator, and a parallel hole collimator to obtain planar images of patients. While planar images can be very useful, they can be difficult to interpret due to the superposition of 3-dimensional structures in the body on a 2-dimensional image. Similarly, it can be difficult to determine the true 3-dimensional distribution of the tracer within the body. These limitations can be addressed through the use of tomographic imaging techniques, in which 2-dimensional data are acquired at multiple angles around the patient. This data can then be reconstructed with various algorithms in order to determine the 3-dimensional radionuclide distribution within patients. Although the mathematical basis for this operation had been established almost a century ago by Radon

[5], image reconstruction techniques for tomography were first applied to clinical nuclear medicine in the 1970's, and are continuing to advance to this day.

Although the Anger camera was a major development in the imaging of radionuclides, it was designed for imaging gamma-rays having energies below 367 keV (*i.e.*, primarily technetium-99m at 140 keV, up to that of iodine-131), and therefore is not an ideal instrument for imaging isotopes that decay by positron emission. Positrons emitted by these isotopes quickly annihilate within the body, with each annihilation resulting in the emission of two 511 keV photons, traveling in opposite directions. The penetration of these high energy photons through lead makes absorptive collimation ineffective, reducing the effectiveness of the gamma camera. However, the development of the positron emission tomography (PET) scanner in 1973 took advantage of the fact that the two photons are emitted simultaneously and in opposite directions to eliminate the need for absorptive collimation [6]. This was a major development that increased both the detection efficiency and spatial resolution when imaging positron emitting radioisotopes.

Through the years, many imaging modalities (*e.g.*, planar radiography, x-ray fluoroscopy, computed tomography, diagnostic ultrasound, magnetic resonance imaging) have been developed and applied to clinical use, but nuclear medicine has remained clinically valuable for many reasons. The primary advantage of nuclear medicine is that both SPECT and PET have the capability to image physiological function, as opposed to displaying only anatomical features and changes. For example, the most commonly performed SPECT clinical procedure is myocardial perfusion imaging, in which blood flow to the cardiac muscle is assessed. This allows physicians to determine the presence of ischemia, which can not be detected using only anatomical information. In addition, nuclear medicine tracers have no natural background, allowing the imaging study to be performed after administration of very small amounts of tracers. The concentration of the tracer in the human body is usually in the picomolar to nanomolar range, so that the tracer has no pharmacologic effect. This sensitivity also allows the detection of specific biological molecules, which are almost always present in low concentrations, without perturbing the function of the biological system. In addition, because SPECT imaging systems can distinguish photons of different energies, multiple tracers labeled with different radioisotopes can be imaged simultaneously, enabling the study of multiple processes.

The variety of different imaging modalities also emphasizes that each imaging technique has its own unique capabilities. For example, x-ray CT images have very good spatial resolution and anatomical detail but provide limited information about biological function. Conversely, SPECT images provide functional information but generally lack the spatial resolution needed to provide detail about anatomical structure or localization. Therefore, overlaying a SPECT image onto a CT image can aid the interpretation of the SPECT imaging, increasing its diagnostic value. This can be performed by acquiring the SPECT and CT images independently, and then relying on image fusion software so that the radionuclide data can be displayed in color and overlaid on the anatomically-correlated grayscale CT images. However, a number of obstacles hinder the accurate coregistration of one set of image data onto another. One difficulty is that patients generally are not positioned identically between scans. Between two imaging procedures, the patient can lie with his or her head, arms, and legs in different positions on tables with different surface shapes. Additionally, internal organs can vary in shape and size over the course of just several hours. For example, the bladder can empty or fill, affecting the position of nearby organs; various locations of the gastrointestinal system can contain different contents, including air, in various amounts. Another difficulty is that the patient can be imaged at different points of the respiratory cycle, which results in changes in the size and position of the lungs. Because of these and other factors, accurately fusing two data sets from different imaging systems is a non-trivial problem, especially when the images are taken at different times of the day, or even on different days.

The challenge of accurately registering data from two imaging systems was one strong motivation that led to the development of dedicated dual modality systems. Dual modality imaging systems have been available commercially since 1999, starting with the GE Hawkeye® SPECT-CT system. This system consists of a gamma camera and x-ray CT system configured with a common patient bed, so that the patient can have an x-ray CT scan and a SPECT scan performed while remaining in a single position during a single study. By acquiring both scans within the same study, changes in the position of internal organs can be minimized. In addition, because the patient does not have to move between scans, problems with changes in patient position can be reduced. Therefore, using a dedicated dual modality system simplifies the process of combining images from different modalities.

In addition to providing anatomical details to improve the qualitative interpretation of the image, the CT data can also be used to improve the quantitative accuracy of the radionuclide data. For example, photon attenuation due to the interaction of gamma photons with matter can lead to image artifacts, such as a reduction in apparent activity structures deep inside the body. These can be corrected by using image reconstruction algorithms that model the effect of photon attenuation. One way to generate this model for photon attenuation is to use x-ray CT data. In fact, the data reconstructed from CT actually is expressed in terms of the linear attenuation coefficient at each location in the imaged volume. CT images can also provide information about the size, shape, and composition of structures within the body. As explained later in this thesis, this information can be used to compensate for partial volume and other errors in the radionuclide data, and leading to a more accurate determination of the radionuclide distribution. For these reasons, combined SPECT-CT and PET-CT dual modality imaging systems have started to supplant conventional scanners that offer SPECT or PET alone.

At the same time that radionuclide imaging techniques were being developed in the 1950's, the structure of DNA was being elucidated (1953), leading to a significant change in our understanding of the genetic and molecular underpinnings of biology and pathology. The discovery of the double helix structure of DNA led to the so-called "central dogma" of modern biology, which essentially states that genetic information stored in DNA is transcribed to RNA, which in turn undergoes translation to form proteins. The proteins comprise the majority of the functional machinery of the cell. Thus, the effect of genetic changes can be understood at the molecular level. Additionally, cellular function can be manipulated by modifying DNA or directly targeting the proteins.

These discoveries have had a profound impact on the study of disease and the development of new therapies. For example, drug discovery was once a random search for new compounds with pharmaceutical effects. Now, molecules can be designed in a rational manner to target specific proteins in order to achieve a desired effect. For example, the pharmaceutical Herceptin® (trastuzumab, Genentech, Inc.) is a monoclonal antibody targeted to the HER2/*neu* (human epidermal growth factor receptor) protein over-expressed in certain forms of breast cancer. These new molecularly targeted agents potentially will be more efficacious than traditional chemotherapeutics. In addition, the genetic basis of disease has become better understood, as the functions of various genes have been elucidated. One key development is the ability to manipulate the genomes of animals such as mice. This has led to the development of animal models for many diseases providing researchers with a better understanding of both the pathology as well as potential treatments.

Although biologists have developed a number of techniques to study animals at the molecular level, *in vivo*, non-invasive imaging techniques have only been recently applied to the field of molecular biology. This has resulted in the formation of a new field, molecular imaging, which can be defined as the field focused on "noninvasive, quantitative, and repetitive imaging of targeted macromolecules and biological processes in living organisms" [7]. This can be contrasted with conventional imaging, which is focused on imaging anatomic structure and macroscopic function within the body. For the molecular biologist, imaging tools provide new ways to visualize the effect of molecular and cellular changes within a living organism. On the other hand, discoveries in molecular biology will lead to the development of improved tracers for use in imaging.

The growth in this field over the last several five to ten years has been dramatic. A search for the phrase "molecular imaging" shows that the number of citation has increased rapidly over the last five years (Fig. 1.1) in the biomedical literature. This growth is also evidenced by the recent founding of two societies dedicated to molecular imaging, the Society for Molecular Imaging (Kerrville, TX) and the Academy of Molecular Imaging (Los Angeles, CA). In addition, a number of manufacturers are offering dedicated small animal imaging systems, including major manufacturers of clinical imaging equipment.

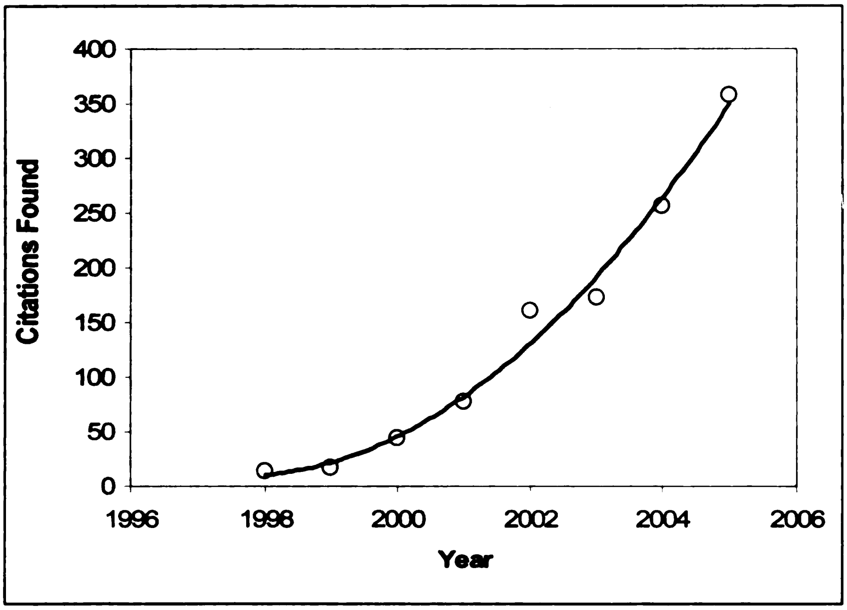

Fig. 1.1: A search was performed using PubMed, with the phrase "molecular imaging". The number of citations found increased each year from 1998 to 2005, demonstrating the growth of molecular imaging as a distinct area of study.

Application of both molecular and conventional imaging techniques to small animals (*i.e.*, mice and rats) is an active and vital field of research. Mice and rats have long been used in biological research for multiple reasons, including their biological similarity to humans, ease of care, and rapid reproduction [8]. For these and other reasons, a large number of well characterized disease models, ranging from Alzheimer's disease to obesity [9, 10], using mice and rats are available, and research using these species is increasing correspondingly.

Non-invasive, *in vivo* imaging offers many advantages in the study of these animal models. First, imaging can be performed in live animals, which allows the measurement of functional parameters while the animal is still alive. Secondly, imaging allows each animal to be studied repeatedly, enabling longitudinal studies where each animal serves as its own control, decreasing the variability in the study and increasing the statistical power. In addition, many traditional techniques used in animal studies such as histology and autoradiography are labor intensive. The application of imaging techniques can reduce the amount of labor required, and thus reduce the cost of studies. In recent years, a number of imaging modalities have been used in small animals, including most of the modalities represented in human imaging. Dedicated small animal systems using MRI, CT, SPECT, PET, ultrasound, and optical imaging have become available [11-15].

Although dual-modality imaging is well accepted for use in clinical applications, it is not yet commonly used in small animal research applications. However, we anticipate that small animal dual-modality imaging will have the same advantages as dual modality imaging performed on human subjects and seek to demonstrate some of these advantages in this thesis project.

1.3. Project goal

In this thesis project, we use a combined SPECT-CT system for imaging studies involving small animals. The studies pursued in this project involve a commercial small animal SPECT-CT system, the X-SPECT® scanner (Gamma Medica-Ideas, Inc., Northridge, CA), which is installed and available in our laboratory at University of

California, San Francisco. The system can be used to perform dual-modality imaging studies of small animals using SPECT-CT. Our aim in this project focuses on developing the quantitative capabilities of small animal SPECT-CT, and specifically on assessing the magnitude of physical effects such as photon attenuation and partial volume errors that affect the image quality and the quantitative accuracy of small animal radionuclide imaging, and developing compensation methods for these effects. Our overall goal is to use these compensation methods to allow small animal imaging systems to be used for scientific studies in which it is important to be able to quantitatively measure the uptake of radiotracers in specific tissues to measure the underlying biological processes under study.

References

[1] H. L. Blumgart and S. Weiss, "Studies on the velocity of blood flow. II. The velocity of blood flow in normal resting individuals, and a critique of the methods used," *Journal of Clinical Investigations*, vol. 4, pp. 15-31, 1927.

[2] E. O. Lawrence and D. Cooksey, "On the apparatus for multiple acceleration of light ions to high speeds," *Physical Review*, vol. 50, pp. 1131-1140, 1936.

[3] G. L. Brownell, S. Aronow, and G. G. Hine, "Radioisotope Scanning," in *Instrumentation in Nuclear Medicine*, vol. I, G. G. Hine, Ed. New York, NY: Academic Press, Inc., 1967, pp. 381-428.

[4] H. O. Anger, "Scintillation camera," *Review of Scientific Instruments*, vol. 29, pp. 27-33, 1958.

[5] J. Radon, "On the determination of functions from their integrals along certain manifolds," *Berichte Sächsiche Akademie der Wissenschaft*, vol. 69, pp. 262-77, 1917.

[6] M. E. Phelps, E. J. Hoffman, N. A. Mullani, and M. M. Ter-Pogossian, "Application of annihilation coincidence detection to transaxial reconstruction tomography," *Journal of Nuclear Medicine*, vol. 16, pp. 210-224, 1975.

[7] H. R. Herschman, "Molecular Imaging: Looking at Problems, Seeing Solutions," *Science*, vol. 302, pp. 605-608, 2003.

[8] K. Paigen, "A miracle enough: the power of mice," *Nature Medicine*, vol. 1, pp. 215-220, 1995.

[9] L. Carroll, J. Voisey, and A. van Daal, "Mouse models of obesity," *Clinical Dermatology*, vol. 22, pp. 345-349, 2004.

[10] G. A. Higgins and H. Jacobsen, "Transgenic mouse models of Alzheimer's disease: phenotype and application," *Behavioural pharmacology*, vol. 14, pp. 419-438, 2003.

[11] J. S. Lewis, S. Achilefu, J. R. Garbow, R. Laforest, and M. J. Welch, "Small animal imaging: current technology and perspectives for oncological imaging," *European Journal of Cancer*, vol. 38, pp. 2173-2188, 2002.

[12] S. R. Cherry, Y. Shao, R. W. Silverman, K. Meadors, S. Siegel, A. Chatziioannou, J. W. Young, W. Jones, J. C. Moyers, D. Newport, A. Boutefnouchet, T. H. Farquhar, M. Andreaco, M. J. Paulus, D. M. Binkley, R. Nutt, and M. E. Phelps, " MicroPET: a high resolution PET scanner for imaging small animals," *IEEE Transactions on Nuclear Science*, vol. 44, pp. 1161-1166, 1997.

[13] M. J. Paulus, S. S. Gleason, S. J. Kennel, P. R. Hunsicker, and D. K. Johnson, "High resolution x-ray computed tomography: an emerging tool for small animal research," *Neoplasia*, vol. 2, pp. 62-70, 2000.

[14] M. J. Paulus, S. S. Gleason, M. E. Easterly, and C. J. Foltz, "A review of high-resolution X-ray computed tomography and other imaging modalities for small animal research," *Lab Animal*, vol. 30, pp. 36-45, 2001.

[15] R. W. Coatney, "Ultrasound imaging: principles and applications in rodent research," *Interational Laboratory Animal Research*, vol. 42, pp. 233-247, 2001.

Chapter 2: X-SPECT System Description

2.1. Overview

This thesis project involved experimental studies with small animal SPECT-CT, and specifically used the "X-SPECT®", developed, manufactured, and sold by Gamma Medica-Ideas, Inc. (Northridge, CA). According to the manufacturer, the X-SPECT system is designed to perform SPECT-CT imaging of animals ranging in size from mice to rhesus monkeys. Two systems of this type (of approximately 40 available worldwide) are available at the UCSF Center for Molecular and Functional imaging, and were used to perform the experimental work described in this thesis. This chapter will describe the imaging system, the data acquisition process, and the image reconstruction process that form the basis of much of this thesis. The X-SPECT was the first system of its type, and the only commercial system of its type available when this thesis project was started. Since that time, several other small animal SPECT-CT systems have been introduced for experimental studies and the results in developed and presented in this thesis project generally are applicable to all of these systems.

2.2. System description

2.2.1. Overview

The X-SPECT scanner is a small animal SPECT-CT imaging system was developed, and now is sold by Gamma Medica-Ideas, Inc. (Northridge, CA) [1]. It was the first commercially available dual-modality system designed specifically for imaging small animals. It was predated by the A-SPECT™ imaging system, also developed by Gamma Medica-Ideas, which included up to two compact scintillation cameras for *in vivo* radionuclide imaging of small animals, but did not include x-ray imaging capabilities. In addition, the A-SPECT rotated the animal in an upright vertical position unlike the X-

SPECT (Fig. 2.1) which is built with a gantry that allows SPECT and CT imaging components to rotate around the animal, which is positioned horizontally, thus maintaining the animal in a more natural position.

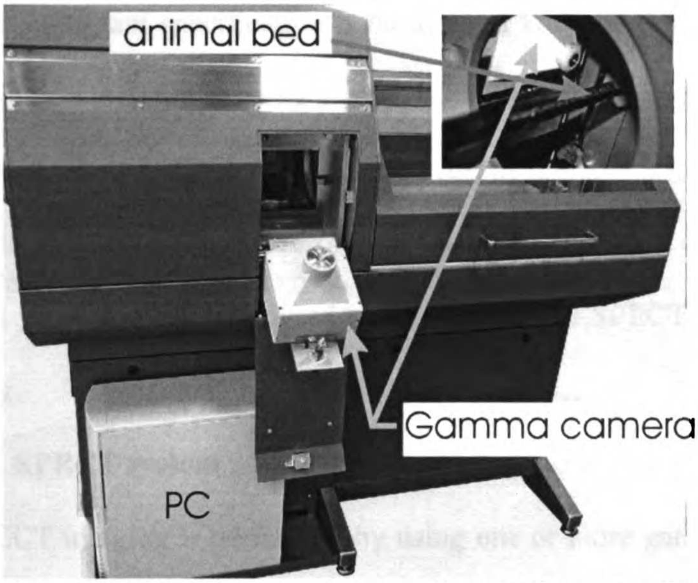

Fig. 2.1: The X-SPECT small animal SPECT-CT system. The gamma camera can be swung out from its normal imaging position to facilitate collimator changes. The inset photo on the left shows the gamma camera in its imaging position, as well as the mouse holder.

In designing a small animal imaging system, a number of objectives must be considered, including spatial resolution, radiation dose, and imaging time. Specifically, because animals such as mice are much smaller than humans, the imaging system must have sufficient spatial resolution to visualize key structures. For example, a typical adult mouse weighs approximately 25-30 g, compared to approximately 80 kg for the average American adult male. Correspondingly, the linear dimensions in the mouse are approximately 10 times smaller than in a human. For example, the thickness of the myocardial wall in a mouse is 1.0-1.5 mm [2], which is approximately one tenth the thickness of the myocardium in the human heart [3]. Because clinical SPECT scanners have a spatial resolution of approximately 1 cm, a SPECT scanner for mouse imaging needs a spatial resolution of approximately 1 mm, an order of magnitude improvement, to achieve similar performance. Likewise, a CT scanner for mice should have a spatial resolution of approximately 100 μm or better, to match the 1 mm spatial resolution used for clinical CT imaging. Another important specification is the field of view (FOV), which must be large enough to encompass the animal being studied. For a mouse, a field of view with a diameter of 3 cm is probably sufficient, whereas for a rhesus monkey a field of view of 10-20 cm may be needed. Both the spatial resolution and size of the field of view are important characteristics that must be considered in the design of a SPECT/CT system for small animal imaging.

2.2.2. SPECT system

SPECT imaging is performed by using one or more gamma camera to acquire multiple "views" of an object that has been injected with a radionuclide tracer. The set of multiple views, or set of "projection data", then is fed to an image reconstruction algorithm to reconstruct the data into a three-dimensional data set consisting of cross-sectional planes perpendicular to the axis of rotation. Therefore, in most SPECT imaging systems, tomography requires either rotating the object being imaged, or rotating the detector around the object.

The radionuclide imaging process begins by injecting (or otherwise administering) the subject (animal or human) with a radiopharmaceutical that distributes within the body according to its biochemical properties. For example, sestamibi or "MIBI" (hexakis-2-methoxyisobutyl isonitrile) is an agent that is labeled with technetium-99m and that distributes in proportion to blood flow in the myocardium and other tissues. In comparison, antibodies can be labeled with iodine-123 or indium-111, and used to target proteins such as those that are specific to particular types of tumors. After the radiopharmaceutical has accumulated according to its biological properties, the labeled tissues emit radiation (*i.e.*, γ-rays and x-rays) in proportion to the radiopharmaceutical concentration.

The distribution of the radiopharmaceutical in the body then is recorded using an imaging detector, such as the gamma camera. The gamma camera records both the interaction position (on the detector face) and the energy of photons emitted from radionuclide tracers such as iodine-125, technetium-99m, and lutetium-177 (Table 2.1). A typical gamma camera for small animal imaging, such as the one found in the X-SPECT, uses a segmented NaI(Tl) scintillator and position sensitive photomultiplier tubes (PS-PMT's). The scintillator is used to convert the incident photons into visible light, which are then converted by the PS-PMT's into electrical signals. The electrical signals are then processed by read-out electronics, digitized, and stored in the data acquisition computer. The signals provide information about the energy of the detected photon, and about the position of the interaction of the incident photon on the detector surface (*i.e.*, in the scintillator). Both X-SPECT scanners in our laboratory are equipped with one of these gamma cameras, although each X-SPECT scanner can accommodate up to two gamma cameras for increased detection efficiency at extra cost.

Table 2.1: Common isotopes used in SPECT imaging

Isotope	Half-life	Photon Energy	Decay Mode
Iodine-123	13.2 hours	159 keV	Electron capture
Iodine-125	59.5 days	27-32 keV	Electron capture
Indium-111	2.8 days	171, 245 keV	Electron capture
Lutetium-177	6.6 days	113, 210 keV	β- decay
Technetium-99m	6.0 hours	140.5 keV	Isomeric transition
Thallium-201	72.9 hours	69-83 keV	Electron capture

In addition to detecting the emitted photons, the radionuclide imaging system also must provide information about the trajectory of the photon prior to its interaction with the scintillator. In gamma-ray imaging, including SPECT, this is almost always done by using absorptive collimation. A variety of collimator configurations are available, including pinholes, parallel hole, and converging hole collimators. The X-SPECT can be equipped with either parallel hole collimators or pinhole collimators, and the choice of collimator is determined by the desired trade-offs between spatial resolution, detection sensitivity, and field of view. The parallel hole collimator has good detection sensitivity and a large field of view, but relatively poor spatial resolution of 2 mm or higher. The pinhole collimator has superior performance for imaging smaller objects in terms of its spatial resolution and detection efficiency, but generally offers a more restricted field of view. The X-SPECT comes with two different pinhole collimators, the low energy and the medium energy pinhole collimator (Fig. 2.2). The primary difference between the two collimators is that the medium energy pinhole collimator has thicker shielding in order to minimize the penetration of higher energy photons.

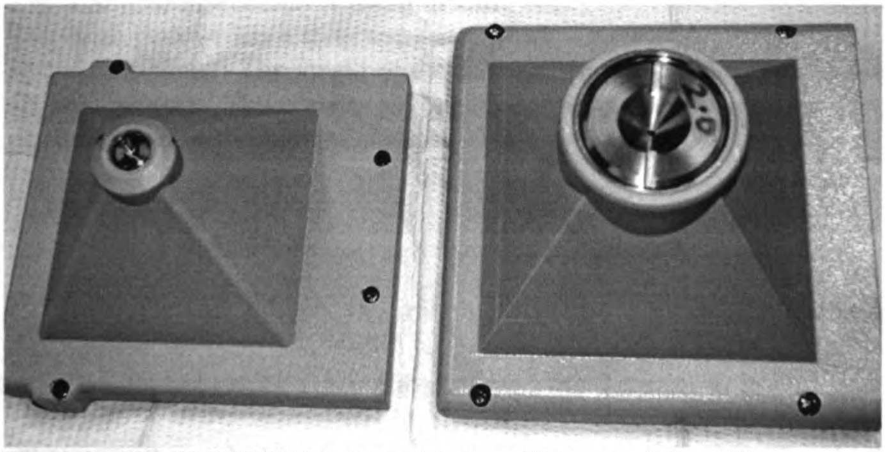

Fig. 2.2: The X-SPECT has two pinhole collimators. The collimator on the left is used for lower energy isotopes such as I-125 (27.5 keV) and Tc-99m (140 keV). The collimator on the right has increased shielding, and is used for imaging higher energy isotopes such as indium-111 (171 keV, 245 keV). The pinhole inserts are removable, and can be switched to optimize the compromise between spatial resolution and detection efficiency.

Each collimator comes with interchangeable pinhole inserts, with diameters of 0.5 mm, 1 mm, or 2 mm that can be used to achieve the desired balance between spatial resolution and detection sensitivity. Based on information from the manufacturer, we know that the pinhole apertures are keel edge pinholes (also known as channel pinhole) with a 90° cone angle made of machinable tungsten. The keel edge pinhole is a modification of the traditional knife edge pinhole that flattens the edge of the aperture (Fig. 2.3), in order to decrease septal penetration and improve spatial resolution at the expense of decreased detection efficiency. The cone angle limits the field of view of the pinhole, and is chosen to match the field of view of the detector. All the work done for this thesis focused on imaging with pinhole collimators.

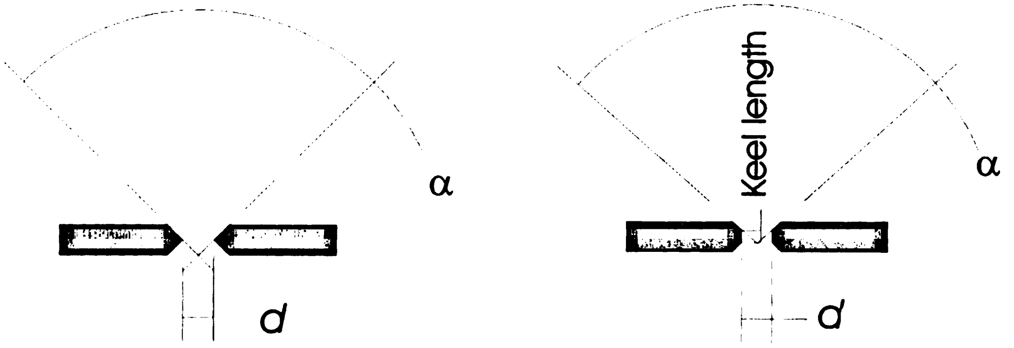

Fig. 2.3: Cross-sectional drawing of knife edge (left) and keel edge (right) pinholes. The keel edge pinhole has a flattened edge, which decreases septal penetration and improves spatial resolution. The length of the flattened edge is the keel length (also known as the channel height). The cone angle (α) of the pinhole aperture limits the angles at which photons can pass through the pinhole.

2.2.3. X-ray CT system

CT scanners, like other x-ray imaging systems, consist of a radiation source and a detector. The source emits x-ray photons, and the detector is positioned to record the photons that pass through the object being imaged, thus recording the shadow cast by the object. The resulting image is a two-dimensional representation of the object, where the image intensity corresponds to the product of the linear attenuation coefficient and thickness of the object. To obtain three-dimensional information about the object, it is necessary to either rotate the object being imaged, or to rotate the x-ray source and detector(s) around the object.

The CT subsystem in the X-SPECT, like all x-ray CT scanners, uses an x-ray tube as a source of photons for imaging. X-ray tubes generate x-rays by accelerating an electron beam from a cathode into a target (the anode). The accelerated electrons create photons through *bremsstrahlung* interactions of the electrons with the anode material. The resulting *bremmsstrahlung* photons are not monoenergetic, but instead have a broad spectrum which is determined by the accelerating potential and the anode material. In addition, the x-ray tube also produces characteristic x-rays having discrete photon energies produced when upper shell electrons fill vacancies in lower electron shells created by electron interactions with inner shell electrons. The rate of x-ray production is governed by the cathode current, the electron potential used to accelerate the electron beam, as well as the type of target material (*e.g.*, molybdenum *vs.* tungsten). The X-SPECT scanner is equipped with a microfocus x-ray tube having a fixed tungsten anode that produces a maximum tube current of 1 mA at 50 kVp, and with a nominal focal spot size of 100 μm. These values are fairly typical for x-ray sources used in small animal x-ray computed tomography.

A variety of detectors types and configurations have been used for x-ray CT imaging in order to convert the incoming radiation into an electrical signal. Detectors used in human CT scanners include xenon filled ionization chambers, and scintillators coupled to photodiodes [4]. CT scanners for small animal and specimen imaging commonly use scintillators coupled to a solid-state CMOS (complementary metal oxide semiconductor) or CCD (charge coupled device) detector that records the light emitted by the scintillator and converts it to an electronic signal that can be digitized and stored, or displayed, by a computer. In general, CCD detectors have the advantage in image quality (better uniformity, lower noise, higher dynamic range), but have a relatively small active area (*e.g.*, 1 cm^2). As a result to achieve an imaging area of sufficient size (*i.e.*, 5×5 cm2, the scintillator must be coupled to the CCD chip using a fiber optic taper which reduces its quantum efficiency. In comparison, CMOS detectors have the advantage in terms of higher readout speed, resulting in faster data acquisition, and reduced power consumption, which is advantageous in consumer applications (*i.e.*, digital cameras), but unlike CCDs have a sufficiently large active area so that it can be coupled to the scintillator without a fiber optic taper. In the case of the X-SPECT scanner, the x-ray detector is a CMOS based detector with 2368×2240 pixels with 50 μm pixel pitch. The detector has a nominal frame rate of 2-9 frames per second, depending on the amount of binning in the detector. Developments in both CCD and CMOS technologies have narrowed the gap between the two types of detectors, and both continue to be used in small animal CT systems.

2.2.4. Ancillary systems

In addition to the imaging components, small animal imaging systems must also include provisions for positioning and supporting the animal during the imaging process. The animal holder must support the animal in the field of view, while not interfering with the imaging process. As a result, it must be made of a material that does not significantly attenuate x-rays and gamma rays, such as metal. Carbon fiber, as used on the X-SPECT, is strong, light, and not excessively attenuating. The X-SPECT scanner has interchangeable animal holders, appropriately sized for animals of different sizes (Fig. 2.4). The holders are mounted to a translation stage, which allows the animal to be correctly positioned within the field of view.

For most *in vivo* studies, it is also necessary to anesthetize the animal to minimize movement. Therefore, the X-SPECT system in our laboratory has tubing installed to allow the use of gaseous anesthesia (isofluorane) while the animal is in the scanner. Finally, while small animals such as mice are anesthetized, it is necessary to provide heating to maintain the body temperature. Various solutions such as heated animal beds, heat lamps, and forced air heating are used to maintain animal body temperature in small animal imaging systems.

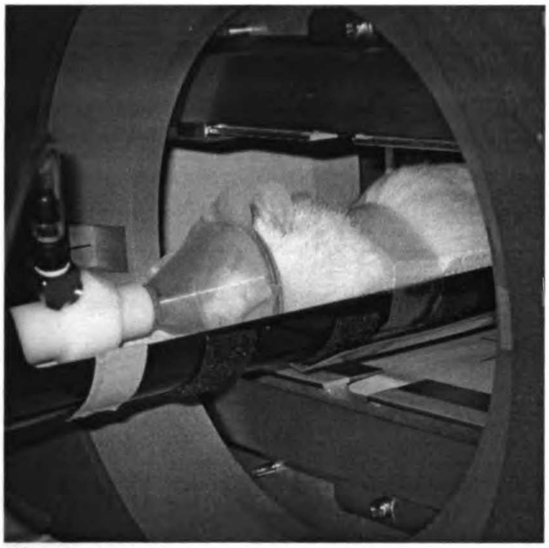

Fig. 2.4: A close up view of the larger (rat sized) animal bed. This photograph shows a rat positioned for imaging with the anesthesia nose cone installed. Image courtesy of Carmen Taylor.

2.3. Data acquisition and reconstruction

2.3.1. SPECT acquisition

While the concept of radionuclide imaging is relatively simple in concept, several steps must be followed in a practical system to perform a SPECT study. First, the detectors must be positioned so that they are aligned with the object being imaged. The X-

SPECT system, for example is designed so that SPECT detectors can be moved on linear translation stages both toward the rotational axis (isocenter) for imaging, or away from the isocenter so that they don't interfere with x-ray beam during acquisition of a CT image. Similarly, for acquisition of SPECT data, it first is necessary to move the x-ray tube and x-ray camera to their outermost positions so that the gamma camera can be positioned as close as possible to the object being imaged. The geometrical configuration of the radionuclide detectors and the x-ray source and detector for both x-ray imaging and radionuclide imaging are shown in Fig. 2.5 and Fig. 2.6. The animal holder can also be translated parallel with the axis of rotation in order to correctly position the animal within the field of view.

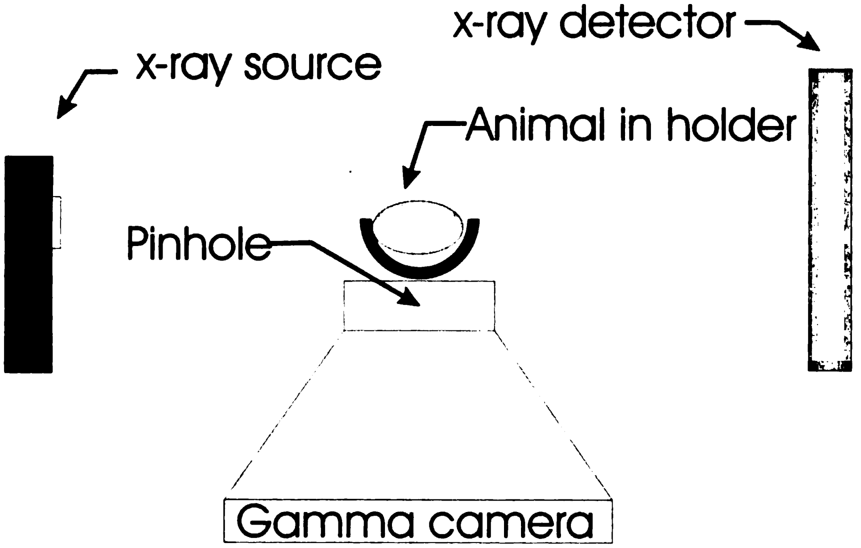

Fig. 2.5: Axial representation of the X-SPECT system configured for SPECT imaging. The gamma camera is positioned close to the animal in order to optimize spatial resolution and sensitivity. The x-ray CT imaging components are retracted. The imaging components rotate about a common axis perpendicular to the plane of the page.

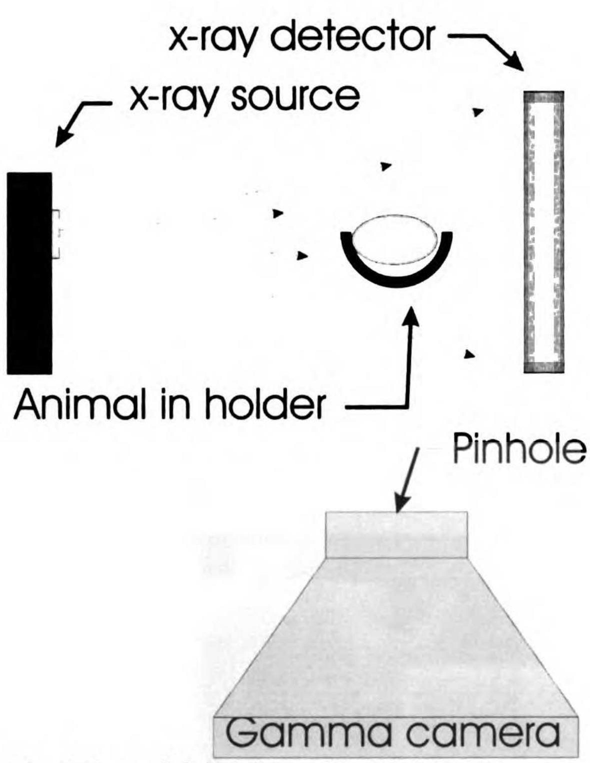

Fig. 2.6: Axial drawing of the X-SPECT system configured for x-ray CT imaging. The gamma camera is withdrawn, so as to avoid interfering with the x-ray imaging. The x-ray tube and camera are positioned so that the field of view covers the animal being imaged. The imaging components rotate about a common axis perpendicular to the plane of the page.

In addition, quality control and calibration data must be acquired to maximize the quality of the recorded image. For this reason, before experimental data are acquired, it is useful to acquire uniformity data to calibrate the system and check system performance. Typically, the uniformity data are acquired at the beginning of each day by imaging a uniform flood phantom (Fig. 2.7) filled with an aqueous solution of the desired radionuclide. The gamma camera can record the data either without a collimator (*i.e.*, an "intrinsic" measurement), or more commonly with the X-SPECT, with the appropriate collimator (*i.e.*, either pinhole or parallel hole) for an "extrinsic" uniformity measurement; the manufacturer suggests that 5×10^6 events should be acquired to insure adequate statistical quality for a uniformity measurement of this type. The radionuclide distribution within the flood phantom is assumed to be uniform, so that the resulting information can be used by the data acquisition software to perform uniformity correction on subsequent projection images due to spatial variations in detector response or imperfections in the collimator. Additionally, this correction compensates for the angular dependence of the detection efficiency (flat field correction) of the pinhole collimator. After the uniformity correction data are acquired, another image is acquired with the flood phantom to verify that the uniformity correction is correct as a final quality control check.

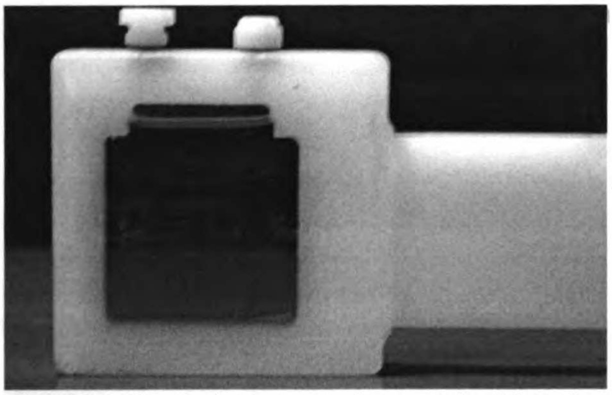

Fig. 2.7: Flood phantom used to acquired data for uniformity correction. The phantom is filled through two holes on the top, which are then plugged with plastic screws.

When acquiring experimental data, it is necessary to first position the animal or phantom so that it lies within the field of view of the imaging system. This can be done injecting the object or animal with the radiopharmaceutical, positioning it in front of the gamma camera, and then simply viewing the gamma camera output displayed on a computer monitor. It is also possible to use planar x-ray imaging to help accurately position the subject. When a pinhole collimator is used, the pinhole should be positioned as close to the object as possible, to maximize spatial resolution and detection efficiency, but sufficiently far away so that the object being imaged is encompassed in the field of view of the SPECT detector. Tomographic imaging with the X-SPECT scanner generally requires that data are acquired over 180° or 360° at 64 or 128 projection angles. In both planar and tomographic imaging, the object can centered within the imaging field by moving the animal bed from side-to-side. On the other hand, if the field of view is too small to encompass the object, the field of view can be enlarged by moving the pinhole collimator away from the object. The overall goal of this process is to ensure that the entire object can be viewed within the field of view at all projection angles at which data are acquired.

2.3.2. X-ray CT data acquisition

The CT data usually are acquired after SPECT imaging is complete. Although the CT scan could be acquired first, SPECT imaging usually is performed first because the SPECT field of view with a pinhole collimator is smaller than the CT field of view. Therefore, if the region of interest falls within the SPECT field of view, then the CT field of view will encompass the region of interest as well. When acquiring CT data, it is necessary to first move the gamma camera (or cameras) to its outermost position so that it does not obscure the x-ray beam as it passes from the x-ray source to the x-ray detector (Fig. 2.6). If the gamma cameras are fitted with parallel hole collimators, the gamma camera shutters must be closed to prevent damage due to scatter radiation produced in the object by the x-ray beam. The x-ray tube output is adjusted, and then projection data are acquired over 360° at 128, 256, or 512 projection angles, a decision that is governed by the desired trade-off between spatial resolution, and imaging time. The raw projection data are stored on the data acquisition computer for reconstruction.

The choice of x-ray CT acquisition parameters is primarily a balance between image quality and radiation dose. Radiation dose is minimized by reducing the number of photons passing through the body, and minimizing the number of photons interacting absorbed in the body. The number of photons (or flux) can be reduced by proper design of the system (beam collimator and shutter), as well as by minimizing the exposure time, number of projections, and tube output. The number of photons being absorbed in the body can be reduced by increasing the energy of the emitted photons, which is controlled by the tube voltage. The image quality is maximized by increasing the signal to noise ratio by increasing the photon flux and contrast. The flux is controlled by the tube current and total exposure time, while the contrast is controlled by the tube voltage.

2.3.3. Image reconstruction

The objective of tomographic imaging is to measure the three-dimensional spatial distribution of a physical parameter, *e.g.*, the photon attenuation coefficient in x-ray CT or the concentration of a radiopharmaceutical in SPECT. In SPECT and CT, the measured data consist of a set of two dimensional projection views acquired at multiple angles, which are reconstructed into a set of cross-sectional views of the object being imaged. This section will briefly give a general description of the image reconstruction process, and then review two common algorithms used for image reconstruction. Finally, we will describe the methods used to reconstruct the data acquired on the X-SPECT system.

As stated above, the measured data in SPECT and CT imaging consist of two dimensional projection views acquired at different angles. In CT imaging, (Fig. 2.8), the detected image intensity on each point on a CT projection can be defined by the following equation:

$$P_\theta(u,v) = I_0(u,v)\exp(-\int_L \mu(x,y,z)ds) \qquad (2.1)$$

where θ is the projection angle, I_0 is the intensity recorded on the detector in the absence of attenuation, $\mu(x,y,z)$ describes the linear attenuation coefficient, and L is the line from the point (u,v) on the detector surface to the x-ray source. By dividing the measured projection data, and taking the natural logarithm, we obtain a function where each point is expressed as a line integral:

$$F_\theta(u,v) = -\ln(\frac{P_\theta(u,v)}{I_0(u,v)}) = \int_L \mu(x,y,z)ds \qquad (2.2)$$

In SPECT imaging, each point on a projection is defined by the number of photons from the radionuclide-containing object detected at that point on the detector. In an ideal system, each point on the detector is illuminated by a "pencil beam" of radiation passing through an ideal (*i.e.*, infinitesimally small) collimator opening. Thus, the number of photons detected at a particular point of a detector is proportional to the line integral of the activity concentration through the object as defined by the collimator geometry for a specific point on the detector:

$$P_\theta(u,v) = k\int_L A(x,y,z)ds \qquad (2.3)$$

where k is a proportionality constant that converts the projected radionuclide concentration to units of photons per second per unit area recorded by the detector. In addition, $A(x,y,z)$ describes the spatial distribution of the radiopharmaceutical concentration, L is a line in space defined by the position of the collimator opening and (u,v), and consists of the points from where emitted photons can be detected at the location (u,v) on the detector.

After acquisition, the data must be reconstructed in order to create a three-dimensional image data set, where each voxel (volume element) represents the value of the physical property (*e.g.*, photon attenuation coefficient) that is being measured. Because Eq. 2.2 and Eq. 2.3 have the same mathematical form, the same image reconstruction algorithms can be applied for SPECT and CT.

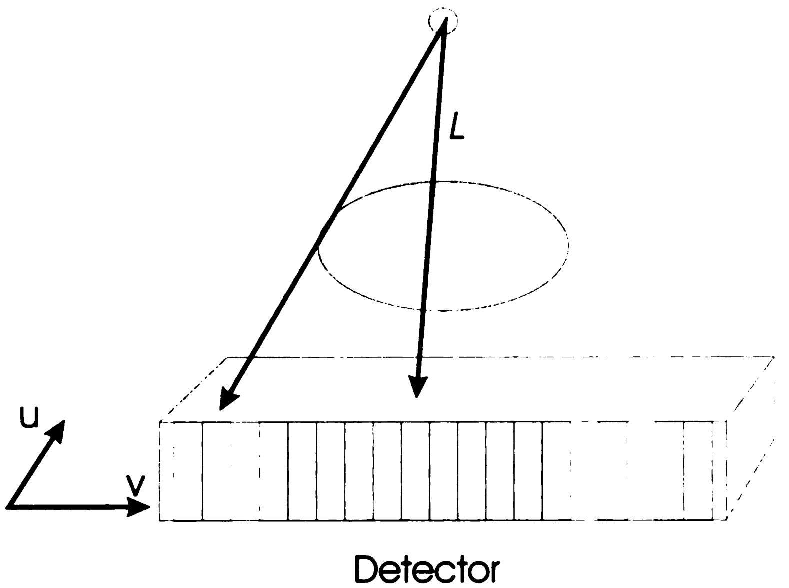

Fig. 2.8: In this example, each point on a CT projection can be defined by a line integral through the object of interest:

$$P(u,v) = \exp(-\int_L \mu(x,y,z)ds)$$

where $P(u,v)$ is the measured data, $\mu(x,y,z)$ is the spatial distribution of the linear attenuation coefficient, and L is the path from the source to the point (u,v) on the detector.

Algorithms used for tomographic reconstruction are can generally be classified as either analytical or iterative algorithms. Analytical solutions apply a single transform to the projection data in order to estimate the 3-dimensional image. One such algorithm, filtered backprojection, is one of the earliest algorithms, and dates back to Johan Radon's derivation in 1917 of what now is known as the "Radon Transform" [5]. In this algorithm, the projection data are first filtered using a high pass filter, then "backprojected", which is the process of smearing the values of each pixel in the filtered projection image evenly along the line that contributed to the value recorded in that pixel. Iterative algorithms, as their name implies, use multiple iterations and a model of the imaging process in order to produce the image. Although they are more computationally intensive than analytical algorithms, iterative algorithms can yield results with better spatial resolution and improved noise properties, compared to analytical algorithms [6]. As a result, iterative methods are increasingly popular, particularly for radionuclide image reconstruction.

2.3.3.1. Feldkamp algorithm

A commonly used variation of the filtered backprojection algorithm for reconstructing pinhole SPECT and cone beam x-ray CT data was derived by Feldkamp, *et al* [7]. This algorithm is an approximation of the exact solution to the inversion of the Radon transform, and was originally derived for microCT, although it is also applicable to microSPECT, which uses the same cone beam geometry. The algorithm is analogous to the filtered backprojection algorithm for the fan beam imaging geometry, with the addition of a weighting step which is applied to the projection prior to filtering to account for the specific properties of the cone beam geometry. In addition, the backprojection step also has an extra weighting term, also to account for the cone-beam geometry. This algorithm is described in more detail by Kak, *et al* [5, 8].

2.3.3.2. ML-EM algorithm

A popular iterative reconstruction algorithm for reconstruction of radionuclide imaging data is the maximum likelihood-expectation maximization (ML-EM) algorithm, originally derived by Shepp and Vardi [9], and by Lange and Carson [10]. This algorithm estimates the radionuclide tracer distribution which maximizes the Poisson probability of observing the measured data. The algorithm assumes that each detector measurement is independent, and that the data behave statistically according to a Poisson distribution (as is true for counting statistics). The logarithm of the likelihood function is maximized using an iterative expectation maximization process.

A drawback of the ML-EM (and other iterative) algorithm is the computational time required. One way to accelerate this process by an order of magnitude is to use ordered subsets, which divides the projection data into subsets, or blocks, and updates the image estimate using the subset of the projection data [11]. This approach can be used for ML-EM and other iterative algorithms; when applied to ML-EM, the resulting algorithm is known as the ordered subsets-expectation maximization, or OS-EM.

2.3.3.3. SPECT image reconstruction

In SPECT imaging, the reconstruction algorithm has a major effect on the quality of the reconstructed image. Although the software that is shipped with the X-SPECT scanner includes both filtered backprojection and iterative reconstruction (OSEM) for pinhole SPECT data, we have implemented an improved version of the ordered subset-expectation maximization (OSEM) algorithm. This improved algorithm includes models for effects such as photon attenuation, and distance dependent collimator behavior. This work constitutes a major part of this thesis, and will be described in detail in Chapter 4.

2.3.3.4. CT image reconstruction

CT images are generally reconstructed using analytical algorithms, although iterative algorithms also can be used for this purpose. However, in comparison to iterative techniques, analytical algorithms generally are preferred for CT because they are less computationally expensive then iterative techniques; a major advantage in the reconstruction of the large data sets encountered in x-ray CT. In addition, most CT data have relatively low noise, so there is less benefit to using an iterative algorithm. Cone beam CT reconstruction is especially challenging because of the large matrix sizes involved, which can require a long time to reconstruct. For example, Kole *et al*, reported reconstruction times of up to several days to reconstruct a 1024×1024×200 dataset into a 512×512×128 matrix (without acceleration) [12]. However, a number of companies and researchers have managed to address this problem using various approaches, including both hardware and software acceleration [13-15]. In our case, the CT projection data were reconstructed using the software (supplied by Exxim Computing Corporation) that was shipped with the X-SPECT. This software enables rapid reconstruction using ordinary PC hardware. The data are output in 512 individual slices, each with a 512×512 matrix format. For the sake of simplicity, the reconstructed data were usually rebinned into a single file with a matrix format of $(256)^3$ prior to analysis.

2.4. Image co-registration

Accurate co-registration is necessary for correct image interpretation, as well as for accurate attenuation correction [16]. Because the X-SPECT system is designed such that the animal is anesthetized and is not moved between scans, the registration problem is relatively simple. However, due to differences in image matrix sizes, field of view, and spatial alignment between the SPECT and CT subsystems, it is necessary to take steps to ensure that the data sets are accurately aligned.

A variety of transforms are available for use in image registration to match the two different reconstructed images. These include rigid, affine, projective, and curved transforms [17]. The rigid transform only includes rotations and translations. An affine transform will map parallel lines onto parallel lines, and combines the operations of a rigid transform with the addition of scaling operations (magnification or minification) that may vary by direction. A projective transform maps lines onto lines, without any constraints for maintaining parallelism, and a curved transform is one maps lines onto curves. The choice of transform depends on the complexity of the coregistration problem. For example, a rigid transformation is usually sufficient for registering images of the skull, which is rigid and does not deform, but a curved transform may be needed to register images of the heart acquired at different points of the cardiac cycle.

In this section, we describe the methods we used to coregister the SPECT and CT images, including the image transform, a method to estimate the image transformation matrix, and an evaluation of the image registration accuracy.

2.4.1. Materials and methods

We performed image registration by finding values for the transformation matrix that mapped the points in CT image onto the corresponding points in the SPECT image. The previous section summarized several image registration approaches, and here we will describe the transformation that we chose and the method used to experimentally obtain the values for the transform parameters.

A general affine transform to relate the CT and SPECT coordinates can be described by the following set of equations:

$$\begin{aligned} x_{CT} &= A_{11}x_{SPECT} + A_{12}y_{SPECT} + A_{13}z_{SPECT} + t_1 \\ y_{CT} &= A_{21}x_{SPECT} + A_{22}y_{SPECT} + A_{23}z_{SPECT} + t_2 \\ z_{CT} &= A_{31}x_{SPECT} + A_{32}y_{SPECT} + A_{33}z_{SPECT} + t_3 \end{aligned} \tag{2.4}$$

where x_{SPECT}, y_{SPECT}, and z_{SPECT} are the coordinates of a point in the SPECT image, x_{CT}, y_{CT}, and z_{CT} are the coordinates of the point in the CT image, and the remaining variables are constants. This transform has 12 unknown parameters represented by the 9 matrix values $\{a_{ij}\}$ and the 3 coordinates of the translation vector $\{t_k\}$. However, because the geometry of the scanner fixes the geometrical relationships between the CT and SPECT data, we can assume that the only parameters needed are a scaling factor, rotation about the z-axis, and shifts along each of the axes. Thus, the transformation (Eq. 2.4) can be simplified to the following equations:

$$\begin{aligned} x_{CT} &= (m\cdot\cos\theta)x_{SPECT} + (m\cdot\sin\theta)y_{SPECT} + t_1 \\ y_{CT} &= (-m\cdot\sin\theta)x_{SPECT} + (m\cdot\cos\theta)y_{SPECT} + t_2 \\ z_{CT} &= m\cdot z_{SPECT} + t_3 \end{aligned} \tag{2.5}$$

where m is the scaling (or magnification) factor, θ is the rotation angle, and t_1, t_2, and t_3 are shifts along the x-, y-, and z-axes, respectively between the CT and SPECT coordinate frames. We can express this in matrix notation using the equation:

$$\begin{bmatrix} x_{CT} \\ y_{CT} \\ z_{CT} \end{bmatrix} = \begin{bmatrix} m\cdot\cos\theta & m\cdot\sin\theta & 0 \\ -m\cdot\sin\theta & m\cdot\cos\theta & 0 \\ 0 & 0 & m \end{bmatrix} \begin{bmatrix} x_{SPECT} \\ y_{SPECT} \\ z_{SPECT} \end{bmatrix} + \begin{bmatrix} t_1 \\ t_2 \\ t_3 \end{bmatrix} \tag{2.6}$$

or equivalently,

$$\mathbf{x}_{\mathbf{CT}} = \mathbf{A}\mathbf{x}_{\mathbf{SPECT}} + \mathbf{t} \tag{2.7}$$

In order to determine the parameter values, it is necessary to define points in the CT image, and to find the coordinates of the corresponding points in the SPECT image, or *vice versa*. Given this data, we seek to find the parameter values that minimize the distance between the positions of the points in the CT image and the position of the points in the transformed SPECT image. In mathematical terms, we seek to minimize the value in Eq. 2.8:

$$\sum_{i=1}^{N} \left|\mathbf{x}_{CT} - (\mathbf{A}\mathbf{x}_{SPECT} + \mathbf{t})\right|^2 \tag{2.8}$$

In order to find the coordinates needed to perform the minimization, it is necessary to be able to define points in the CT image, and to define the corresponding points in the

SPECT image. This was done by imaging fiducial markers, which are objects designed to be visible and well defined in both SPECT and CT. In this project, fiducial markers were created using anion exchange resin beads (A-520E, Purolite, Inc.), soaked in an aqueous solution of approximately 200 MBq ^{99m}Tc-NaTcO$_4$ (sodium pertechnetate) to form "point sources" with a diameter of approximately 0.6-0.9 mm. The pertechnetate ion is adsorbed from the solution onto the beads, making the beads visible with SPECT, which are also visible with CT because of their physical density (~1.1 mg/mL). With only five co-registration parameters (*i.e.*, m, θ, t_1, t_2, and t_3) that need to be determined, two points (*i.e.*, 6 coordinate values) are theoretically sufficient to determine the image registration parameters. However, we usually used four or more points in order to obtain a better fit.

In practice, these sources were glued to a plastic centrifuge tube that could be attached to the animal bed and imaged to obtain data to derive the co-registration matrix. The sources were placed at random locations near the end of the tube, although care was taken to space the points appropriately, so that the points would all be within the field of view of the gamma camera, and to avoid obvious symmetry, such as positioning the points in a co-linear manner. The tube was then attached to the animal bed for data acquisition. SPECT data were acquired at 64 projections over 360°, followed by CT data acquisition.

The SPECT data were reconstructed using an iterative reconstruction algorithm, and the CT data were reconstructed using the Feldkamp image reconstruction software included with the scanner. The CT data were re-binned to a $(256)^3$ matrix format following reconstruction. The coordinate values for each point source were defined manually in both the SPECT and CT images using an image display program, which gave the "matrix" position of the point.

The coordinates of the point source in the SPECT and CT images were fed to a computer program, which derived the coregistration parameters expressed in Eq. 2.5. This program finds these parameter values by minimizing the cost function in Eq. 2.8 using Powell's algorithm, a direction-set method to find minima [18]. This algorithm seeks the find the minima in a function of *n* variables by searching along lines in different directions in *n* dimensional space. The set of directions can be defined by a set of unit vectors. The algorithm first finds the minimum along a line defined by the initial estimate and the first vector, and then proceeds down the next direction until it reaches a minimum. The values of the *n* variables which are being minimized are then updated to be equal to this new point in *n* dimensional space. From this point, the algorithm searches for a minimum along the line defined by the next vector and changes the values of the variables accordingly. The process is repeated for all *n* unit vectors, and then the set of directions is updated based on the previous results. The process is repeated until the algorithm converges on a minimum.

After the values for the coregistration parameters have been determined, it is possible to apply the image transform to the CT image to match it to the SPECT data, which was done using another software program that we implemented. This program loops through the image matrix in the SPECT coordinate space, and calculates the coordinates of each SPECT voxel in the coordinates of the CT image using Eq. 2.5. The program then determines the voxel values of the output image using trilinear interpolation of the CT image at the coordinates determined in the previous step. The end result is that the CT image has been resampled to match the SPECT image.

2.4.2. Results

The first step of the image registration process consisted of imaging the calibration phantom described above, then identifying the fiducial markers on both the CT and SPECT images. The ion exchange resin beads worked well as point sources for fiducial markers in that they were easily visible in SPECT images, and also could be seen in CT (Fig. 2.9). Although there was little image contrast between the beads and the plastic tube on which they were attached, in the CT image, the outline of the beads was always obvious because they protruded beyond the surface of the tube. In addition, in the SPECT image, the bead was radioactive and could be readily identified and differentiated form the plastic tube which was not radioactive. These characteristics allowed us to identify the fiducial markers on both the CT and SPECT images, with their coordinates extracted so that the parameters in Eq. 2.5 could be identified.

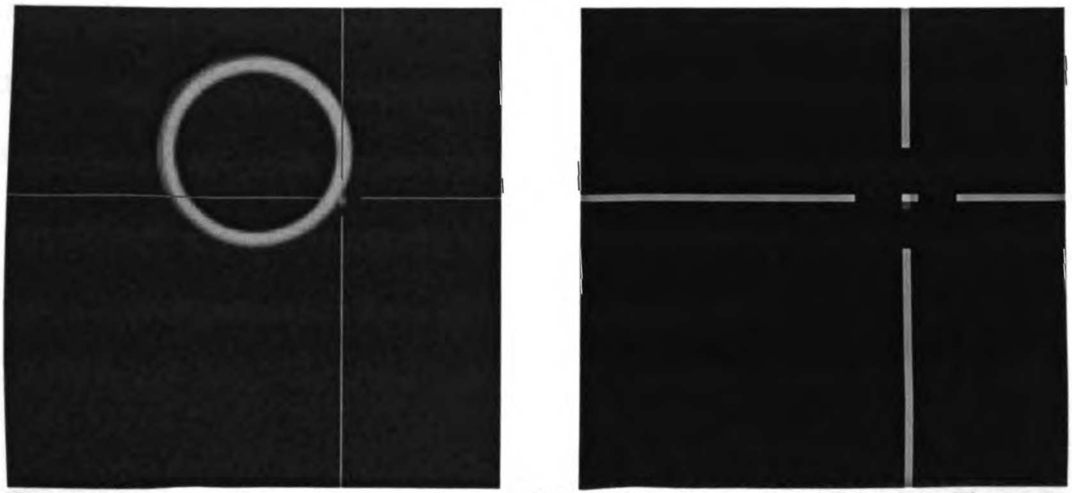

Fig. 2.9: Image of coregistration phantom from CT (left) and SPECT (right). The cross hairs are aligned with the ion exchange resin bead that served as a fiducial marker.

In this process, it is important to recognize that the values obtained for the image co-registration matrix **A** (Eq. 2.7) depend on the parameters used for reconstruction of the SPECT and CT images. In particular, the magnification value is dependent on the SPECT radius of rotation, and the field of view of the SPECT image. Given accurate knowledge of the voxel dimensions in the reconstructed images, the magnification can be calculated by the following equation:

$$m = \frac{VoxSize_{SPECT} \times N_{SPECT}}{VoxSize_{CT} \times N_{CT}} \tag{2.9}$$

where VoxSize is the length of the voxel in the specified image, N_{CT} is the size of the CT image space in voxels, *and* N_{SPECT} is the length of the SPECT image space in voxels.

The magnification value was determined for experimental data acquired using various values for the radius of rotation, and was plotted as a function of the radius of rotation. As expected, the magnification was dependent on the radius of rotation (Fig. 2.10), because the image reconstruction algorithm changes the voxel size based upon the radius of rotation. In addition, Fig. 2.10 also shows that the experimental results agreed with the expected values for magnification calculated from Eq. 2.9, which provides confidence that the image dimensions in the SPECT and CT images are correct.

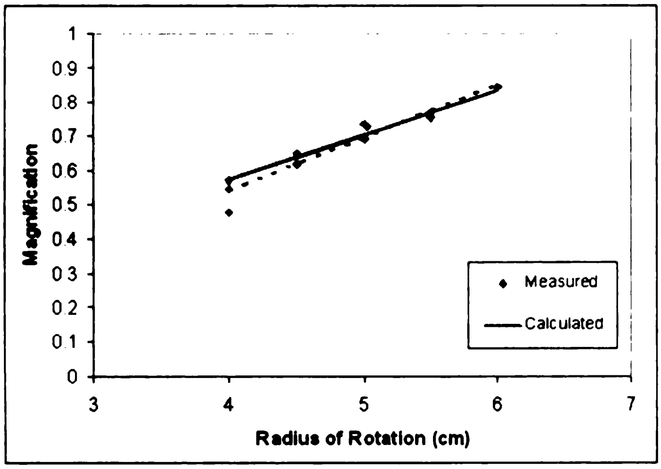

Fig. 2.10: Magnification factor needed to correlate the SPECT and CT data. The measured data agrees well with the predicted values.

In addition to the magnification *m*, it also is necessary to determine θ, the angle of rotation about the z-axis, as well as the translations t_1, t_2, and t_3 between the SPECT and CT coordinate systems. In this example, the rotation angle was measured to be $\theta = 0.6° \pm 1.9°$. The shifts (t_1, t_2) in the x and y directions are both very small (0.18±0.13, and 0.24±0.17), and not statistically significant. The z-shift t_3 is larger, and was measured to be 2.3 ±0.8 mm (range of -1.5 mm to -3 mm). Nevertheless, these differences between the SPECT and CT data can be corrected easily by applying Eq. 2.6 to transform the CT data into the SPECT coordinate system, as described above.

We then evaluated the effectiveness of the coregistration transform by checking the accuracy of the registration between the SPECT and CT images with a scan of a second set of point sources. This second set of sources was created in the same manner as the first set of markers, but the point sources were located in different positions. The second SPECT-CT scan was performed using the same data acquisition parameters as the first scan, and the data were reconstructed with the same algorithms and parameters as the previous data. The coregistration parameters derived from the first set of data are used to register the reconstructed SPECT and CT images from the second scan, and the position difference is calculated for each point:

$$r_{CT} = \sqrt{(x'_{CT} - x_{CT})^2 + (y'_{CT} - y_{CT})^2 + (z'_{CT} - z_{CT})^2} \qquad (2.10)$$

where x_{SPECT}, y_{SPECT}, and z_{SPECT} are the coordinates of the point in the SPECT image, and x_{CT}, y_{CT}, and z_{CT} are the coordinates of the corresponding point in the coregistered CT image. The mean position difference was found to range from 0.2 to 0.4 mm, which is less than the spatial resolution of the SPECT images. This allows us to conclude that the coregistration algorithm has aligns the SPECT and CT with accuracy better than the spatial resolution of the SPECT system, and indicates that a more complicated approach likely is unnecessary.

The approach described above was used to coregister data for all the work presented in this thesis, and is sufficient for registering the SPECT and CT image coordinate systems. However, in biological systems, the coregistration problem could be complicated by motion, such as that due to respiration and cardiac function, as well as by the possibility of animal movement during or between the SPECT and CT studies. Such errors would require more complicated registration scheme, possibly involving anatomical landmarks in the animal, or the use of fiducial markers attached to the surface. These approaches are specific to the design of particular imaging studies, and are outside the scope of this thesis.

2.5. Prediction and assessment of system performance

The performance of the X-SPECT scanner was characterized for both x-ray CT and SPECT. The system was characterized with experimental measurements that were compared with calculated values. The results will help to predict the limits of quantitative accuracy that can be achieved, determine the optimal imaging parameters for a study, and determine the usefulness of the X-SPECT for particular applications.

2.5.1. SPECT

The SPECT performance of the X-SPECT scanner was characterized by evaluating the field of view, spatial resolution, and detection efficiency. These three characteristics are important in determining the suitability of the imaging system for many applications. The size of the field of view is important in tomographic imaging because structures that fall outside the field of view at certain projection angles can result in artifacts in reconstructed images. In addition, the field of view must also encompass all the structures of interest, in order for a study to be useful. The spatial resolution is important in allowing structures to be resolved in imaging, and having high detection efficiency is critical for minimizing the amount of imaging time and the dose of radiopharmaceutical used in a study. Therefore, optimizing the trade-offs between these three parameters is an important part of performing a SPECT imaging study.

2.5.1.1. Field of view

The size of the field of view has a strong influence on the utility of an imaging system for a particular application. If the data acquired fall partially out of the field of view in some or all of the projection views, the reconstructed image will have artifacts. For SPECT imaging with a pinhole collimator, the field of view is determined by the detector size, cone angle of the pinhole aperture, and the radius of rotation. We calculated the size of the field of view as a function of the radius of rotation for SPECT imaging with the X-SPECT scanner based on the following geometrical argument. We start by looking at the center cross-sectional plane of the image (Fig. 2.11). The field of view is the region which can be imaged by the detector at all projection angles. By symmetry, we deduce that this region must be a circle centered at the axis of rotation. In most situations, the angle 2*a*, defined by the lines drawn from the edges of the detector to the pinhole, is smaller than the pinhole cone angle, and the field of view is limited by the size of the detector. The field of view is the circle bordered by the lines drawn from the pinhole and the edges of the detector (Fig. 2.11). The radius R_{FOV} of the field of view therefore is defined by the line segment drawn from the axis of rotation (isocenter) to the tangent line drawn through the pinhole to the edge of the detector, and which has a value equal to:

$$R_{FOV} = b \cdot \sin\left[\tan^{-1}\left(\frac{0.5 \cdot DetWidth}{F}\right)\right] \tag{2.11}$$

where b is the radius of rotation of the pinhole around the isocenter, *DetWidth* is the width of the detector, and F is the focal length of the collimator.

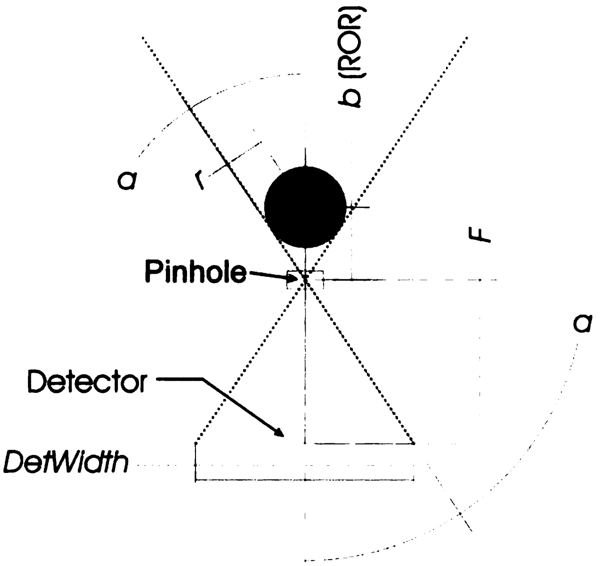

Fig. 2.11: Illustration of the geometry used to calculate the field of view. The dotted lines are drawn from the ends of the detector through the pinhole. Angle *a* is the maximum angle from the perpendicular at which a photon can pass through the pinhole and hit the detector and is calculated using the arctangent of half the detector width divided by the collimator focal length, *F*. As long as 2*a* is less than the pinhole acceptance angle (α), then the field of view is the centered at the axis of rotation that is tangent to the (dotted) lines drawn from the edge of the detector through the pinhole aperture.

The theoretically derived diameter of the field of view (Eq. 2.11) is plotted as a function of the radius of rotation in Fig. 2.12. The calculation was based on the nominal dimensions of the detector (12×12 cm^2). The pinhole acceptance angle is large enough that it should not limit the field of view. The result shows that the field of view with the pinhole collimator can be varied by changing the radius of rotation (*i.e.*, moving the gamma camera toward or away from isocenter) to accommodate animals of different sizes (*e.g.*, mice *vs*. rats), although the larger field of view is obtained with an associated loss of spatial resolution and detection sensitivity.

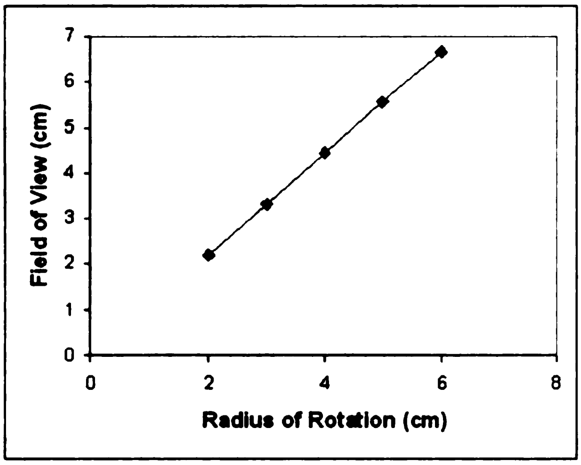

Fig. 2.12: Plot of the expected SPECT field of view for the X-SPECT with pinhole collimation as a function of the radius of rotation.

2.5.1.2. Spatial resolution

Another key characteristic of imaging systems is spatial resolution, which has a strong effect on the ability of a system to detect and distinguish various features within the field of view. Spatial resolution of SPECT and planar radionuclide imaging is determined by adding the intrinsic resolution of the detector and the collimator spatial resolution in quadrature. The intrinsic resolution is the spatial resolution of the detector without a collimator, or in other words, the width of the response of the detector to an infinitesimally thin pencil beam of radiation. The collimator resolution is the width of the projection of a point source onto the detector. For a pinhole collimator, the system resolution (R_s) in the image plane is related to the intrinsic resolution (R_i) and the collimator resolution (R_c) by the follwing equation:

$$R_s = \frac{1}{M}\sqrt{R_c^2 + R_i^2} \tag{2.12}$$

where M is the magnification of the image from the image plane onto the detector, which for a pinhole collimator is equal to the focal length (F) divided by the radius of rotation (b). As stated above, the system resolution is determined by adding the contributions of the intrinsic resolution and collimator resolution in quadrature, and then correcting for the magnification of the image onto the detector face by multiplying by $1/M$, so that the system resolution represents the spatial resolution in the plane of the object.

For pinhole collimation, the spatial resolution of the collimator is described by the following equation [19]:

$$R_c \approx d_{eff}\frac{(F + b)}{F} \tag{2.13}$$

where d_{eff} is the effective pinhole diameter, and F and b are the perpendicular distances between the pinhole and detector, and between the pinhole and the plane of the object, respectively (Fig. 2.13). This expression is derived by calculating the width of the pinhole aperture when projected onto the detector face from a point source located at the center of rotation.

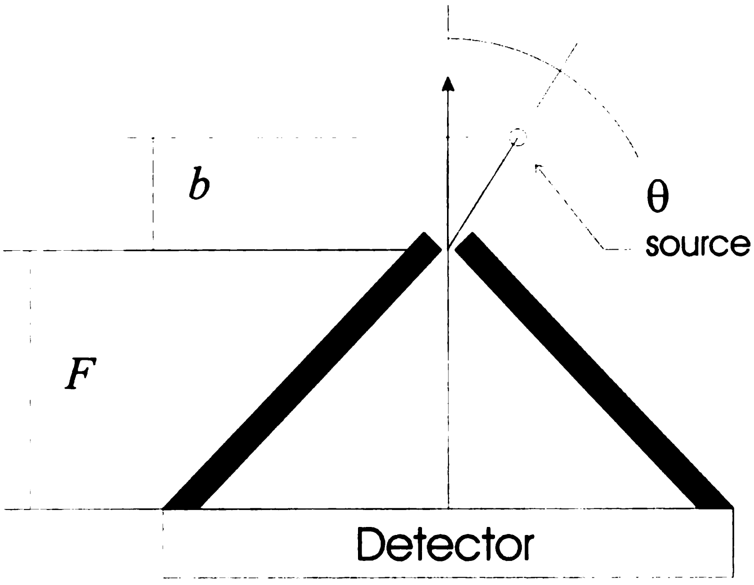

Fig. 2.13: Pinhole imaging geometry. This figure shows the parameters *F*, *b*, and *θ*. The parameter *F* is the focal length of the collimator, and is the distance from the detector to the pinhole center. The parameter *b* is the radius of rotation, and the angle *θ* is the angle of the source with respect to the normal axis of the pinhole collimator.

The previous equation (Eq. 2.13) shows that the collimator spatial resolution is proportional to the effective pinhole diameter, d_{eff}. The effective pinhole diameter accounts for photon penetration through the edges of the pinhole aperture, and is related to the pinhole geometry, material, and photon energy by the following equation:

$$d_{eff} = \sqrt{d\left(d + \frac{2}{\mu}\tan(\frac{\alpha}{2})\right)} \tag{2.14}$$

where μ is the photon attenuation coefficient for the pinhole and α is the cone angle of the knife edge pinhole. Accorsi and Metzler have also investigated the calculation of an effective pinhole diameter for use in spatial resolution calculations [20], and obtained a more general result. In either case, the effective diameter of the pinhole is essentially equal to the physical diameter when imaging low and medium energy gamma photons (*e.g.*, iodine-125 and technetium-99m), and increases when imaging radioisotopes that emit higher energy photons, due to increased penetration of photons through the edges of the pinhole.

The system spatial resolution of the gamma camera also was experimentally measured by imaging a capillary line source having an inner diameter of 250 μm and filled with ^{99m}Tc-NaTcO$_4$. The source was placed in front of the pinhole aperture and imaged with the gamma camera. This was repeated using both the 1 mm and 2 mm pinhole apertures with the source at distances of 3-5 cm from the pinhole. The full-width half-maximum (FWHM) of the line response function, was calculated by linear interpolation of the pixel values in the projection image. The spatial resolution in the image plane was then determined by scaling the spatial resolution at the detector by (b/F) where b is the distance of the source to the pinhole, and F is the distance from the pinhole to the detector, in order to correct for the magnification of the image onto the detector. The results are shown in Fig. 2.14 along with the values predicted using Equations 2.12-2.14. The predicted values were calculated using the value of d_{eff} calculated using the equations for a knife edge pinhole, the nominal collimator focal length of 9 cm, and the nominal pixel pitch (2.2 mm) for the intrinsic resolution of the detector. The data from the 1 mm pinhole were slightly lower than the predicted values, and the experimental results with the 2 mm pinhole gave smaller than expected values for the FWHM. The actual spatial resolution may be lower than the theoretical spatial resolution because of the segmentation of the detector crystal, which leads to a non-Gaussian point spread function. The differences between the two pinholes may be related to the geometry of the pinhole, specifically the longer keel length (1.8 mm) which will reduce the width of the collimator point spread function.

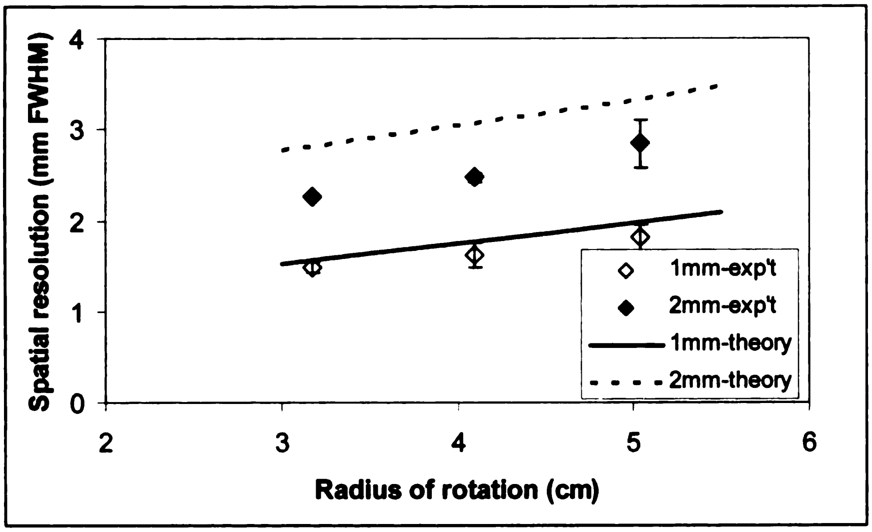

Fig. 2.14: Spatial resolution in planar images obtained using the X-SPECT scanner, determined by using a line source. The result is reported in terms of the full width half maximum in the image plane.

In addition to measuring the planar spatial resolution, we measured the spatial resolution of reconstructed tomographic data. The tomographic resolution differs from the planar imaging data, due to the influence of the reconstruction algorithm on spatial resolution. In addition, various parts of the field of view are closer or farther from the pinhole, depending on the projection angle. Although the planar spatial resolution is a test of the gamma camera, the tomographic spatial resolution also needs to be measured to assess the performance of the integrated imaging system.

Data were obtained using a high resolution test pattern (Fig. 2.15) filled with approximately 140 MBq aqueous ^{99m}Tc-NaTcO$_4$. Data were acquired at 128 projections over 360° using various combinations of pinhole sizes (0.5, 1, and 2 mm diameters) and radius of rotation values (3.5, 4.0, and 4.5 cm). The data were reconstructed using 5 iterations of the X-SPECT manufacturer's OSEM software, and the results were upsampled by a factor of 2 using cubic B-spline interpolation to reduce the effect of pixelation on the image. Results are shown in Fig. 2.16 for data collected with a radius of rotation of 4.0 cm, and illustrate the effect of pinhole aperture size on spatial resolution.

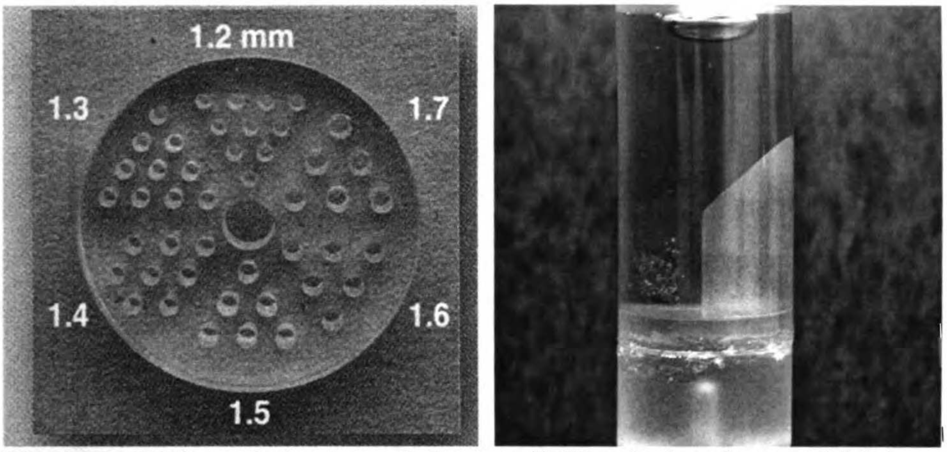

Fig. 2.15: High resolution hot rod phantom (left) and edge phantom (right) used to assess spatial resolution of SPECT images.

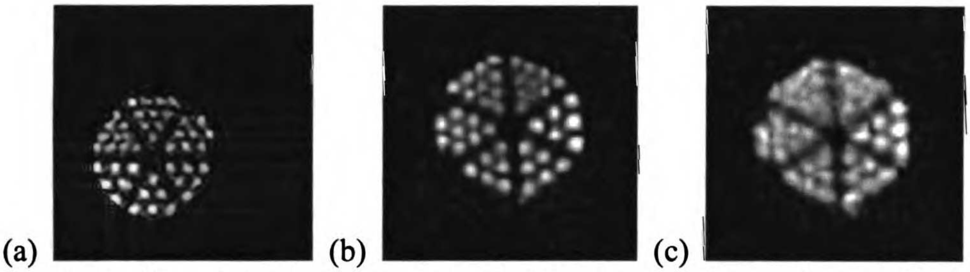

Fig. 2.16: Slices from the center plane of SPECT images of the high resolution hot rod phantom acquired using various collimator inserts with pinhole diameters of : (a) 0.5 mm, (b) 1 mm, and (c) 2 mm. Radius of rotation was 4.0 cm for all data sets, and data were reconstructed using the OSEM algorithm shipped with the X-SPECT scanner. The phantom contains rods with diameters of 1.2, 1.3, 1.4, 1.5, and 1.6 mm.

Another independent measurement of spatial resolution in reconstructed images was obtained by imaging a technetium-99m filled phantom containing an edge (Fig. 2.15 (right)). The phantom was filled with approximately 300 MBq of aqueous ^{99m}Tc-$NaTcO_4$, and data were acquired over 360° at 64 angles and 40 seconds per projection. The radius of rotation was either 4 or 5 cm, and data were acquired with both the 1 mm and 2 mm pinhole inserts. After data acquisition of the phantom, the projection data were reconstructed using 5 iterations an OSEM algorithm (8 subsets). The line profile drawn across the edge in the reconstructed image can be fit with an equation of the form [21]:

$$A+\frac{B}{1+(\exp((x-x_0)/\sigma)} \tag{2.15}$$

where the parameters A, B, x_0, and σ are unknowns, and the full-width-half-maximum of the system point spread function is equal to 3.525σ. Least-squares fitting was performed using the "solver" tool in Microsoft Excel for data from ten locations near the center of each reconstructed image. For each fit, two slices were averaged in order to reduce noise. The results are summarized in Table 2.2, and are consistent with the results obtained with the resolution test pattern. The spatial resolution estimates for the X-SPECT scanner predict that the scanner will be able to resolve structures separated by approximately 1 or 2 mm, depending on the collimator and radius of rotation.

Table 2.2: Estimated spatial resolution in tomographic images

Radius of rotation (cm)	Pinhole Size	Spatial Resolution (mm FWHM)
4.0	1 mm	1.1±0.2
5.0	1 mm	1.2±0.3
4.0	2 mm	1.4±0.2
5.0	2 mm	1.6±0.2

2.5.1.3. Detection efficiency

Detection efficiency or sensitivity is defined as the ratio between detected photons and photons emitted, and has an important role in determining the imaging time, injected dose, and the resulting signal to noise ratio. In general, system performance is improved by increasing the detection efficiency as long as other characteristics, especially spatial resolution, are not sacrificed. The detection efficiency of the system is a multiplicative function of the geometric efficiency of the collimator and the detection efficiency of the detector. As is the case with spatial resolution, the dominant factor in determining the detection efficiency is the collimator. The theoretical geometrical sensitivity of the pinhole collimator is described by the following equation:

$$g = \frac{d_{eff}^2 \cos^3 \theta}{16b^2} \tag{2.16}$$

where the effective pinhole diameter (d_{eff}) accounts for penetration of photons through the edges of a pinhole (Eq. 2.14), and the parameters b and θ are the perpendicular distance from the pinhole to the source and the angle between a line drawn from the pinhole to the source and a line perpendicular to the detector, respectively (Fig. 2.13). This equation predicts that the sensitivity can be increased by using a larger pinhole aperture, decreasing the radius of rotation, and positioning the object in the center of the field of view.

The detection efficiency was also measured, to compare the predicted values with experimentally obtained results. The measurement was performed using a 63 μL Micro Hollow Sphere phantom (Data Spectrum, Inc.) filled with 30 MBq ^{99m}Tc-NaTcO$_4$. The activity was measured using a dose calibrator (Atomlab 100, Biodex Medical Systems), and the phantom imaged with the X-SPECT scanner. Data were acquired at 64 projections over 360°, using radius of rotation values from 3-5 cm. Data were acquired using both the 1 mm and 2 mm pinholes. The sensitivity was calculated by dividing the measured counts by the theoretical number of photons emitted, which was calculated based on the imaging time and the measured activity. A plot of the theoretical pinhole geometric efficiency as a function of distance is shown in Fig. 2.17, along with the measured detection efficiency.

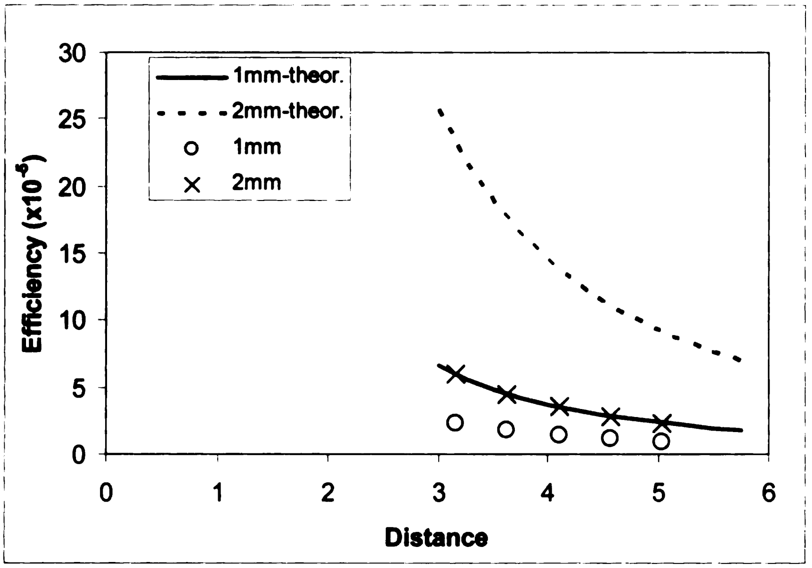

Fig. 2.17: The detection efficiency as a function of distance. The theoretical pinhole geometric efficiency is given by the lines, and the symbols represent the measured efficiency.

The measured efficiency is lower than the theoretical geometric efficiency for several reasons. First, the detection efficiency of the gamma camera is approximately 80% because 20% of the 140 keV photons striking the scintillator crystal will pass through without interaction (Transmission=exp(-μL)=1-exp(-0.6 cm·2.57 cm^{-1})=0.21). Additionally, the segmented scintillator crystal is not active over its entire area; the area between the pixels does not contain scintillation material. The detector uses square 2 mm pixels separated by 0.2 mm of reflective material [1], which leads to an approximately 20% loss in detection efficiency because only 83% ($2^2/2.2^2$) of the detector surface area is scintillator material. Finally, the data acquisition software applies a flat field correction, which reduces the apparent sensitivity at the center of the field of view in order to correct for the angular dependence of detection sensitivity.

We measured the effect of removing the flat field correction on sensitivity by manipulating the data acquisition software so that the flat field correction was not applied.

The experimental measurement for detection sensitivity was repeated, and it was found that the detection efficiency increased by 42% for the 1 mm pinhole, and by 86% for the 2 mm pinholes. In other words, the flat field correction leads to a reduction in apparent detection sensitivity by approximately 30% for the 1 mm pinhole and 50% for the 2 mm pinhole. The effect of the flat field correction was more pronounced for the 2 mm pinhole, and accounted for the relatively small (2.5-fold) efficiency advantage of the 2 mm pinhole compared to the 1 mm pinhole. The experimental data acquired without flat-field correction were compared with the theoretical detection efficiency in Fig. 2.18. In this figure, the theoretical detection efficiency has been corrected for the detector stopping power and the presence of reflective material between the pixels. The 1 mm pinhole measurement agrees reasonably well with the theoretical measurement, but the 2 mm pinhole has noticeably lower than expected sensitivity. This reduction in sensitivity is probably due to the longer (1.8 mm) keel length of the 2 mm pinhole, which improves spatial resolution at the expense of geometric efficiency.

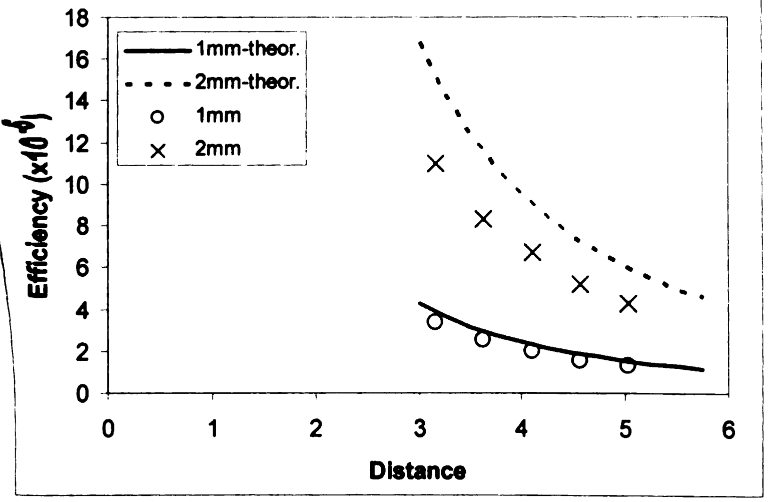

Fig. 2.18: Plot of detection efficiency measured from experimental data without flat field correction. Also plotted is the theoretical detection efficiency, which is accounts for the geometric sensitivity of the pinhole, the stopping power of the detector, and the active area of the detector crystal.

In summary, to maximize the detection efficiency of the X-SPECT system when imaging with a pinhole, it would be best to obtain the data without flat field correction, and to apply a correction to the data that does not reduce the total number of counts. Unfortunately, the flat-field correction is built into the data acquisition software of the X-SPECT scanner, and circumventing the flat field correction while correcting for non-uniformities in the detector is not a straightforward process.

2.5.2 CT system performance

Spatial resolution is a key parameter describing the performance of a small animal CT system, and limits the smallest features that can be seen in the reconstructed image. This section describes the method of calculating the theoretical spatial resolution of an x-ray CT system. The spatial resolution of the CT component of the X-SPECT system is predicted, and then the calculated value compared against experimental measurements.

The expected spatial resolution of projection data can be calculated using the method outlined by Paulus [22], where the total system resolution (σ_{Total}) is expressed as the sum of detector (σ_d) and x-ray focal spot (σ_x) blurring. These two effects are assumed to be Gaussian, and thus they add in quadrature:

$$\sigma_{Total} = \sqrt{\sigma_x^2 + \sigma_d^2} \tag{2.17}$$

The detector blurring is defined by the following equation:

$$\sigma_d = \left(\frac{d_{xs}}{d_{xs} + d_{sd}} \right) \frac{x_d}{2} \tag{2.18}$$

where x_d is the pixel spacing on the detector, and d_{xs} and d_{sd} are the distance from the object to the x-ray source, and the distance from the object to the detector, respectively (Fig. 2.19). This equation assumes that the detector resolution is limited by the pixel size, and calculates the effect of the detector resolution in the image plane. The x-ray focal spot blurring is described by the following equation:

$$\sigma_x = \left(\frac{d_{xs} + d_{sd}}{d_{xs}} \right) \frac{x_{fwhm}}{2.35} \tag{2.19}$$

where x_{fwhm} is the full width half maximum of the x-ray tube focal spot. The term in parentheses is the product of multiplying the blurring by $(\frac{d_{sd}}{d_{xs}})$ and $\left(\frac{d_{xs} + d_{sd}}{d_{xs}} \right)$, where the first term accounts for the scaling introduced by projecting the focal spot blurring onto the detector, and the second term results from backprojecting the blurring from the detector plane into the image plane. The factor of 2.35 converts the full-width half-maximum to the standard deviation for a Gaussian distribution.

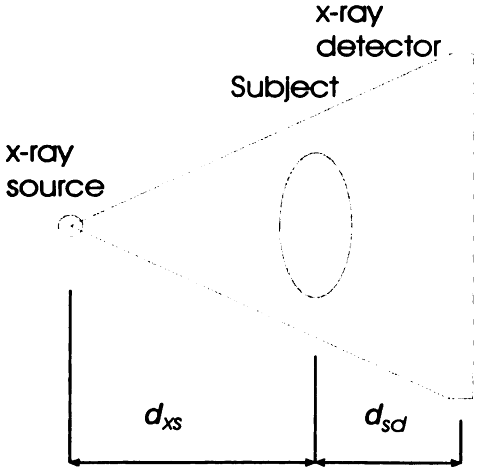

Fig. 2.19: Geometry of an x-ray imaging system. The dimension d_{xs} is the x-ray source to subject distance, and d_{sd} is the source to detector distance.

This equation can be used to calculate the planar spatial resolution of the CT component. Using the standard imaging geometry of the X-SPECT, the values of d_{xs} and d_{sd} are 22 cm and 7 cm, respectively. The detector pixel pitch is 50 μm, but data are usually binned in a 2×2 manner, so the effective pixel pitch is 100 μm. The focal spot size (x_{fwhm}) was estimated to be 100 μm, based on information presented about the A-SPECT [23], the imaging system which predated the X-SPECT. Based on these values, the spatial resolution is estimated to be 160 μm FWHM). This value can also be used as an estimate for the limit of the spatial resolution of the reconstructed tomographic images obtained with this system.

The CT spatial resolution was also evaluated experimentally by scanning a gold wire (nominal diameter approximately 25 μm), which can be used to calculate the point spread function in the transaxial plane. The wire was positioned in the center of the field of view by stretching in a cardboard frame, which was positioned on the animal holder. The wire was imaged using 256 projections over 360°, with the x-ray tube operated at 50 kVp and 0.6 mA. The data were reconstructed, and the in-plane spatial resolution was determined by performing a least-squares fit to the data with a two dimensional Gaussian of the form:

$$f(x) = B + A\exp[-(((x-x_0)^2 + (y-y_0)^2)/(2\sigma^2)] \qquad (2.20)$$

having parameters A, B, x_0, y_0, and σ [21]. The spatial resolution described in terms of its full-width half maximum is equal to 2.35σ, and was estimated to be 340 μm.

Additionally, the spatial resolution was measured by imaging a block of acrylic to obtain the edge response. Data were acquired at 256 projections using the CT imaging parameters described above. The data were fit with a curve of the form described by Eq. 2.14, and the spatial resolution was estimated to be 340 μm FWHM. This result, like the result obtained using the wire, is worse than expected.

After these spatial resolution measurements were completed, calibration measurements were made of the imaging geometry by personnel from the system manufacturer (Gamma Medica-Ideas, Inc.). The results of the calibration measurements were used with a revised reconstruction algorithm which corrected for non-idealities in the imaging geometry. The calibration measurements were repeated, and the spatial resolution improved to 260 μm FWHM, which is still worse than the predicted value. The source of this discrepancy is unknown, but there a several possible sources. One possible cause of is the reconstruction algorithm, which could include a smoothing filter to reduce noise at the expense of reducing image resolution. Another possible source of decreased spatial resolution is misalignments in the imaging geometry. As mentioned above, calibration of the imaging geometry by a service engineer reduced spatial resolution from 340 μm to 260 μm, but there may be residual errors in the imaging geometry. Finally, the focal spot dimension as quoted by the manufacturer may be inaccurate, as accurate measurements of the focal spot size are difficult to perform.

The x-ray CT spatial resolution is not as good as expected, it is still at least three- or four—fold better than the SPECT spatial resolution. Therefore, the CT will be adequate for providing anatomical landmarks for image fusion, and for photon attenuation correction.

2.6. Description of second X-SPECT system

In 2005, another X-SPECT scanner was added to the laboratory, and was used to acquire some of the data presented later this thesis. The second scanner outwardly is very similar to the first scanner, but has a few differences. The CT system has been upgraded with a more powerful x-ray tube, which enables faster CT acquisitions. The higher voltage (kVp) of the x-ray tube should also reduce the radiation dose delivered to the animal during CT acquisition. The gamma camera has been changed such that the scintillator crystal now has 82×82 pixels, which should potentially improve the intrinsic spatial resolution of the gamma camera by reducing the nominal pixel pitch from 2.2 mm (in the first scanner) to 1.5 mm (in the second scanner). The differences between the scanners are summarized in Table 2.3, but the basic design of the system has not changed, and the two scanners are expected to have similar characteristics.

Table 2.3: Differences between the two scanners

Parameter	**First (Older) Scanner**	**Second (Newer) Scanner**
Maximum x-ray tube output	50 kVp, 1 mA	80 kVp, 0.6 mA
X-ray imaging modes	step-and-shoot	step and shoot or continuous
Gamma camera pixel pitch	2.2 mm	1.5 mm

2.7. Conclusions

The X-SPECT is a small animal SPECT-CT imaging system that combines SPECT and CT imaging modalities on a single gantry. In this chapter, we described this system, and evaluated its basic performance characteristics for both radionuclide and x-ray CT imaging. The resolution of the SPECT system was measured to be on the order of 1-2 mm FWHM, which when corrected for the size of mice and rats, is similar to the performance of clinical system for imaging humans. The detection sensitivity ranged from 2-10 $\times 10^{-5}$, depending on the radius of rotation and the choice of pinhole aperture size. Detection sensitivity could also be improved by the installation of a second detector head. The CT spatial resolution was measured to be 260 μm FHWM.

The performance measurements indicate that the X-SPECT system is not a state of the art system in terms of either SPECT or CT. For example, the U-SPECT has superior sensitivity and spatial resolution [24], and Seguin, *et al* reported microCT spatial resolution of approximately 50 μm [25]. However, it is the first commercially available integrated SPECT-CT scanner, and offers the advantage of dual-modality imaging in an integrated system.

References

[1] L. R. MacDonald, B. E. Patt, J. S. Iwanczyk, B. M. W. Tsui, Y. Wang, D. E. Wessell, P. D. Acton, and H. F. Kung, "Pinhole SPECT of Mice Using the LumaGEM Gamma Camera," *IEEE Transactions on Nuclear Science*, vol. 48, pp. 830-836, 2001.

[2] P. A. Doevendans, M. J. Daemen, E. D. de Muinck, and J. F. Smits, "Cardiovascular phenotyping in mice," *Cardiovasc Res*, vol. 39, pp. 34-49, 1998.

[3] M. C. Wu, "Development and Application of a High-Resolution Nuclear Medicine Imaging System," Ph.D. dissertation, University of California San Francisco and University of California Berkeley, San Francisco, CA, 2001.

[4] W. A. Kalender, *Computed Tomography*. Munich: Publicis MCD Verlag, 2000.

[5] A. C. Kak and M. Slaney, *Principles of Computerized Tomographic Imaging*. New York: IEEE Press, 1988.

[6] J. A. Fessler and W. L. Rogers, "Spatial resolution properties of penalized-likelihood image reconstruction: space-invariant tomographs," *IEEE Transactions on Image Processing*, vol. 5, pp. 1346-1358, 1996.

[7] L. Feldkamp, L. Davis, and J. Kress, "Practical cone-beam algorithm," *J. Opt. Soc. Am.*, vol. 1, pp. 612-618, 1984.

[8] A. C. Kak and B. Roberts, "Image reconstruction from projections," in *Handbook of Pattern Recognition and Image Processing*, T. Y. Young and K. S. Fu, Eds. New York, NY: Academic Press, 1986.

[9] L. A. Shepp and Y. Vardi, "Maximum Likelihood Reconstruction for Emission Tomography," *IEEE Transactions on Medical Imaging*, vol. M1-1, pp. 113-122, 1982.

[10] K. Lange and R. Carson, "EM reconstruction algorithms for emission and transmission tomography," *Journal of Computer Assisted Tomography*, vol. 8, pp. 306-316, 1984.

[11] H. M. Hudson and R. S. Larkin, "Accelerated image reconstruction using ordered subsets of projection data," *IEEE Transactions on Medical Imaging*, vol. 13, pp. 601-609, 1994.

[12] J. S. Kole, M. A. Viergever, and F. J. Beekman, "Evaluation of accelerated iterative x-ray CT reconstruction using floating point graphics hardware," presented at Nuclear Science Symposium, Rome, Italy, 2004.

[13] K. Mueller, R. Yagel, and J. J. Wheller, "Fast implementations of algebraic methods for three-dimensional reconstruction from cone-beam data," *IEEE Transactions on Medical Imaging*, vol. 18, pp. 538-548, 1999.

[14] J. S. Kole and F. J. Beekman, "Evaluation of accelerated iterative x-ray CT image reconstruction using floating point graphics hardware," *Physics in Medicine and Biology*, vol. 51, pp. 875-889, 2006.

[15] S. Schaller, T. Flohr, and P. Steffen, "An efficient Fourier method for 3-D Radon inversion in exact cone-beam CT reconstruction," *IEEE Transactions on Medical Imaging*, vol. 17, pp. 244-250, 1998.

[16] H. Fricke, E. Fricke, R. Weise, A. Kammeier, O. Lindner, and W. Burchert, "A method to remove artifacts in attenuation-corrected myocardial perfusion SPECT introduced by misalignment between emission scan and CT-derived attenuation maps," *Journal of Nuclear Medicine*, vol. 45, pp. 1619-1625, 2004.

[17] J. B. A. Maintz and M. A. Viergever, "A survey of medical image registration," *Medical Image Analysis*, vol. 2, pp. 1-36, 1998.

[18] W. H. Press, B. P. Flannery, S. A. Teukolsky, and W. T. Vetterling, *Numerical Recipes in C*. Cambridge: Cambridge University Press, 1988.

[19] S. R. Cherry, J. A. Sorenson, and M. E. Phelps, *Physics in Nuclear Medicine*, 3rd ed. Philadelphia: Elsevier Science, 2003.

[20] R. Accorsi and S. D. Metzler, "Analytic Determination of the Resolution-Equivalent Diameter of a Pinhole Collimator," *IEEE Transactions on Medical Imaging*, vol. 23, pp. 750-763, 2004.

[21] P. A. Assimakopoulos, D. P. Boyd, W. Jaschke, and M. J. Lipton, "Spatial Resolution of Computed Tomographic Images," *Investigative Radiology*, vol. 21, pp. 260-271, 1986.

[22] M. J. Paulus, S. S. Gleason, S. J. Kennel, P. R. Hunsicker, and D. K. Johnson, "High resolution x-ray computed tomography: an emerging tool for small animal research," *Neoplasia*, vol. 2, pp. 62-70, 2000.

[23] K. Iwata, L. R. MacDonald, J. Li, S. P. Williams, A. B. Hwang, A. E. Sakdinawat, M. C. Wu, B. E. Patt, J. S. Iwanczyk, and B. H. Hasegawa, "Dual isotope imaging with dedicated small animal SPECT-CT system," presented at Academy of Molecular Imaging Annual Conference, 2002, 2002.

[24] F. J. Beekman, F. van der Have, B. Vastenhouw, A. J. A. van der Linden, P. P. van Rijk, J. P. H. Burbach, and M. P. Smidt, "U-SPECT-I: A novel system for submillimeter-resolution tomography with radiolabeled molecules in mice," *Journal of Nuclear Medicine*, vol. 46, pp. 1194-1200, 2005.

[25] F. H. Seguin, P. Burstein, P. J. Bjorkholm, F. Homburger, and R. A. Adams, "X-ray computed tomography with 50-µm resolution," *Applied Optics*, vol. 24, pp. 4117-4123, 1985.

Chapter 3: Calibration of SPECT Imaging Geometry

3.1. Overview

In tomographic imaging, full knowledge of the imaging geometry is crucial for accurate image reconstruction. Due to the high spatial resolution of small animal imaging systems, small errors in geometric parameters can lead to errors and artifacts in the reconstructed image. For example, the tomographic reconstruction algorithm assumes that the detector rotates around a specific point in space, typically called the "center of rotation". If the algorithm assumes that the center of rotation is different than the actual (*i.e.*, physical) center of rotation, then this misalignment of the gamma camera with the axis of rotation can lead to artifacts. This is illustrated in Fig. 3.1, which shows images reconstructed from a small point source with different amounts of misalignment between the mathematical center of rotation and the physical center of rotation. If the physical and mathematical centers of rotation coincide, then the reconstruction algorithm accurately produces the small point source (Fig. 3.1(left)). However, any discrepancy in the mathematical and physical center of rotation will cause point objects to appear as small circles in the tomographically reconstructed images.

UCSF LIBRARY

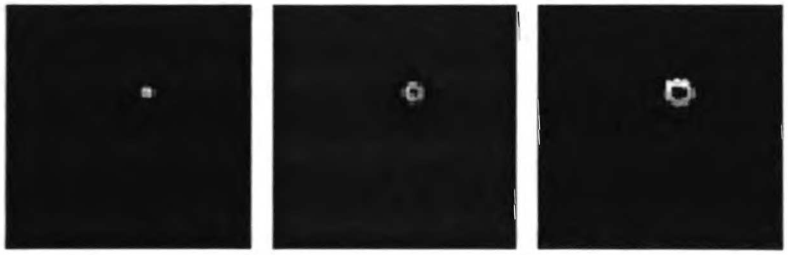

Fig. 3.1: These images were reconstructed from simulated data to demonstrate the artifact in which point objects are reconstructed as small circles. These artifacts are created by an uncorrected mechanical shift, as in the case of a misalignment of the gamma camera. From left to right, data were reconstructed from data with mechanical shifts of 0, 2, and 3 mm.

Although it is difficult to align or measure the imaging geometry to the desired degree of accuracy, it is possible to calculate the geometry of the pinhole camera from experimentally obtained data. After these parameters are calculated, they then can be included in the geometrical description of the imaging system that is part of the image reconstruction algorithm. This provides a means of adjusting or calibrating the reconstruction algorithm for the specific characteristics of the imaging system to remove these artifacts from the reconstructed images. A number of methods to solving this problem have been proposed [1-3]. In this chapter, we implement the method described Beque *et. al.,* which uses measured projection data, obtained using point sources in order to estimate the value of seven parameters needed to define the imaging geometry. The method generates calculated projection data, and fits the calculated projection data to the measured projection data by varying the geometric parameters. This method was used to characterize the SPECT imaging geometry of the X-SPECT scanner in our laboratory.

3.1.1. Definition of geometric parameters

Beque, *et al.*, defines the imaging geometry for a system with a single gamma camera with a pinhole collimator by specifying seven different parameters denoted symbolically as F, e_u, e_v, b, m, ϕ, and ψ. The parameter F is the distance from the center of the detector surface to the pinhole aperture. The deviation of the origin of the detector coordinate system from the center of the detector is described by the electrical shifts, e_u and e_v. The focal length, F, along with e_u and e_v, form a complete description of the gamma camera. The remaining parameters (b, m, ϕ, and ψ) describe the positioning of the gamma camera in relationship to the image matrix. The radius of rotation, b, is the distance from the pinhole to the axis of rotation, measured parallel to the y' axis, which is defined by rotating the standard coordinates about the z-axis by the projection angle θ. The x'', y'', z'' coordinate system is defined by rotation about the x'-axis by the detector tilt angle ϕ. The lateral shift of the detector is m, and is defined as the distance of the pinhole from the axis of rotation along the x''-axis. The twist is represented by ψ, and is the angle difference between the u,v coordinate axes on the detector and the x'' and z'' axes in the rotated image space. These geometrical parameters are illustrated in Fig. 3.2 to Fig. **3.4**, and are sufficient to completely describe the pinhole SPECT imaging geometry.

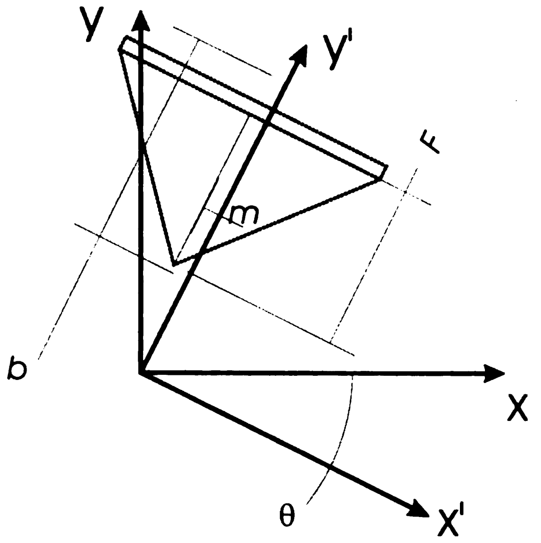

Fig. 3.2: Illustration of the geometric parameters F (focal length), b (radius of rotation), m (mechanical shift), and θ (projection angle). In this image, the axis of rotation (z-axis) is perpendicular to the page. The x', y', and z' axes are defined by rotation about the z-axis by the projection angle, θ.

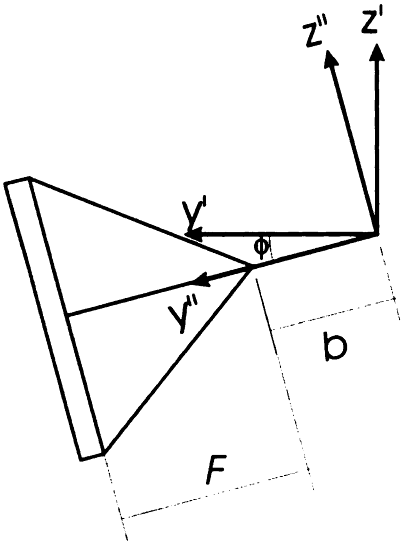

Fig. 3.3: Illustration of the detector tilt (ϕ), focal length (F), and radius of rotation (b). The detector is viewed from the side, and rotates about the z' axis. The x', y', and z' axes are defined by rotating the gamma camera around the z-axis by θ, the projection angle. The x'', y'', and z'' axes are the result of rotating the x', y', and z' axes around the x-axis by ϕ.

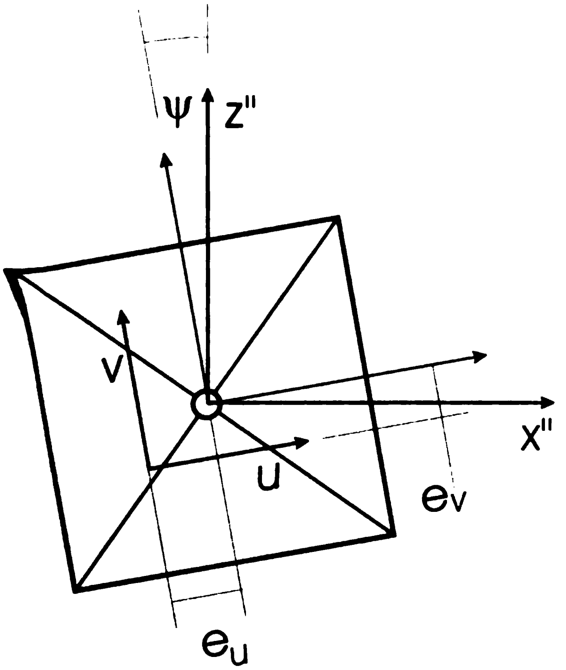

Fig. 3.4: Illustration of detector twist (ψ), and electrical shifts (e_u and e_v). In this drawing, the detector is viewed along the y'' axis, which was defined by rotating the image space coordinate axes about the projection angle (θ) and the tilt angle (ϕ). The electrical shifts define the shift of the origin of the detector coordinate system center of the detector.

3.1.2. Fitting method

As mentioned previously, it is possible to estimate the values of the geometrical parameters from projection data obtained with point sources. The problem can be formulated as a minimization problem, where we minimize the difference between the measured point source projection locations and the expected point source projection locations by varying the values of the different geometrical parameters. In each projection view, the centroid of the projection of each point source on the detector can be calculated as a position in the detector coordinate system, and expressed as a pair of coordinates, $\left(u_{ij}^{img}, v_{ij}^{img}\right)$, where the subscripts i and j represent the point number and projection number, respectively. A corresponding position can be calculated using estimated values for the point source locations and geometrical parameters. The objective function that is being minimized is the distance between the estimated and measured point source projection locations, and can be described mathematically using the cost function (Eq. 3.1) below:

$$\text{Error} = \sum_i \sum_j (u_{i,j}^{img} - u_{i,j}^{est})^2 + (v_{i,j}^{img} - v_{i,j}^{est})^2 \qquad (3.1)$$

where u_{ij} and v_{ij} are the coordinates of the projection of point i in projection j, and the superscripts *img* and *est* refer to measured and estimated positions, respectively.

If the position of a point source is known, then the expected point source projection location (u_{ij}^{est} and v_{ij}^{est}) can be calculated analytically by using simple geometric methods described below. However, because of the difficulty in defining the origin of the coordinate system and accurately positioning point sources, it is easier to include the position of the point sources among the parameters to be estimated. Beque, *et al.*, demonstrate that three point sources are sufficient, so that the total number of parameters is increased from 7 to 16 because the position of each of the three point sources is described by three parameters. However, the three distances between the point sources can be easily fixed by the phantom design or physically measured, reducing by three the number of parameters required to specify the point source locations. The six parameters used to specify the location of the point sources consist of rotations about each of the three axes, and translations along each of the three axes. Thus, the total number of unknown parameters becomes thirteen; seven parameters for the imaging geometry, and six parameters to specify the location of the point sources.

We minimized the error described by Eq. 3.1 by varying the geometric parameters and point source locations, using an implementation of Powell's method [4], a "direction-set" method for finding the minimum of a multi-dimensional function, which is described in Chapter 2. This algorithm was implemented with a computer program written in the C programming language (see Appendix 1). In this program, u_{ij} and v_{ij} were determined analytically using the following method. Given the point source location in the image coordinate system, the point source locations in the x', y', z' frame was calculated by rotating around the z-axis by θ. The coordinates were then transformed into the x'', y'', z'' coordinates by rotating around the x' axis by the tilt angle ϕ. Finally, the point source location was transformed into the x''', y''', z''' coordinate system by rotation about the y'' axis by the twist angle ψ. The projection location is calculated by using similar triangles, and then shifting the results by e_u and e_v for the u and v results, respectively, in order to account for the shift in the origin of the u, v coordinates due to the electrical shift. The resulting equations are:

$$u_{ij}^{est} = -f \cdot \frac{(x'''-m_s \cdot \cos(\psi))}{b+y'''} + m_s \cdot \cos(\psi) + e_u \qquad (3.2)$$

$$v_{ij}^{est} = -f \cdot \frac{(z'''-m_s \cdot \sin(\psi))}{b+y'''} + m_s \cdot \sin(\psi) + e_v \qquad (3.3)$$

where the geometric parameters are as defined in Figures 3.2-3.4. The positions x''', y''', and z''' are the coordinates of the point source after rotation of the coordinate system for projection angle, detector tilt, and detector twist. Constraints were added to limit the range of the variables, such that if any variable was outside the limits, a penalty proportional to the square of the deviation from the limit was added to the cost function described in Eq. 3.1. The constraints are shown in Table 3.1 below.

Table 3.1: Constraints on geometric parameter estimates

Parameter	Minimum Value	Maximum Value
Focal Length, F	85% initial estimate	115% initial estimate
Radius of Rotation, b	80% initial estimate	120% initial estimate
Mechanical shift, m	-10 mm	10 mm
Electrical shift, e_u	-10 mm	10 mm
Electrical shift, e_v	-10 mm	10 mm
Tilt, ϕ	-15°	15°
Twist, ψ	-15°	15°
Rotation about x-axis	-180°	180°
Rotation about y-axis	-180°	180°
Rotation about z-axis	-180°	180°
Translations	-10 cm	10 cm

A second version of the program was implemented to perform a more limited fitting where the values of e_v, ψ, and ϕ were constrained to 0, in an effort to simplify the algorithm and to improve the accuracy and repeatability of the results. The value of e_u was constrained to be equal to m, so that the origin of the detector coordinate system would be positioned underneath the pinhole, or equivalently, such that the detector and pinhole are shifted parallel to the x'-axis as a single unit. This will be referred to as "limited fitting", in contrast to the "full fitting" algorithm which estimated the value of 7 geometric parameters.

3.2. Simulations

In this section, we describe studies involving simulated projection data, which were used to achieve three different objectives. The first goal was to validate the geometric calibration algorithm by varying the geometric parameters used to generate simulated calibration data. This simulation and calibration process allowed us to test the calibration method using data having known attributes, and gave us confidence in applying the calibration data to experimental data obtained from the X-SPECT system. In addition, simulated data were also used to assess the qualitative effects of geometric errors on reconstructed SPECT images, by reconstructing simulated projection data without correcting for variations in the geometric parameters. Finally, the effect of geometric errors were assessed quantitatively by generating simulated projection data using a numerical edge phantom, and reconstructing the data without correcting for the variation in the geometric parameters.

3.2.1. Methods

Simulated projection data were generated using a ray-based projector (Appendix 2) modeling an ideal pinhole, *i.e.*, a pinhole with an infinitesimally small aperture. This method to generate the projection data is independent of the equations used in the calibration algorithm, and therefore "decouples" the simulation process from the calibration process, so that the calibration process can be tested and validated without bias. The imaging geometry was based on the X-SPECT system, with a 12 cm×12 cm detector and a pinhole collimator with a 9 cm focal length. The numerical phantoms used for the simulation contained three points of equal intensity represented in an (80×80×80) matrix. The three points were positioned so that they did not fall on a single line, with approximately 1-2 cm separating the sources. The points were positioned according to the criteria described by Beque, *et al.* [2], such that at least one point was on either side of the central plane, none of the points was on the axis of rotation, and none of the points was in the central plane coincident with the axis of rotation. For each simulation, 64 projection views were generated over 360°.

In order to use the simulated data for testing the geometric calibration algorithm, it was necessary to extract the centroid of each of the points in each projection view. This was done using a semiautomated process, using a Matlab® (The Mathworks, Inc.) script that calculated the centroid of each source from the pixels within a small region in each projection view. The limits of the region for centroid calculation were defined by the user for the first projection, and updated automatically for each subsequent view based on the previously calculated centroid position. This was repeated for each point, and the results were written to a text file containing the centroid locations, which served as one of the input files to the geometric calibration algorithm (see Appendix 2 for more details). The geometric calibration program was then run to estimate the geometric parameters. The initial estimates for the geometric parameters were also varied, in order to test the stability of the geometric calibration. The estimated parameter values were then plotted as a function of the parameters input to the projector program.

In order to study the effect of geometric errors on reconstructed SPECT images, simulated projection data were generated using numerical phantoms consisting of three point sources like the ones described above. The simulated projection data were reconstructed using an implementation of the Feldkamp filtered backprojection reconstruction algorithm created by Wu [5, 6]. Multiple sets of projection data were generated using various values for the geometrical parameters that deviated from the standard imaging geometry (Table 3.2). The projection data were then reconstructed with the Feldkamp algorithm using standard values of the imaging geometry. The reconstructed point source data were used to qualitatively demonstrate the effect of errors in the geometric calibration parameters.

Another set of simulated projection data were generated using a numerical edge phantom consisting of a uniform cube at the center of the field of view, and the ray-driven projector described above. These data were generated with deviations in the geometric parameters, and were then reconstructed using the Feldkamp algorithm without correcting for the changes in the imaging geometry. The reconstructed data were used to estimate the spatial resolution, by fitting the data to the curve described in Eq. 2.14. The degradation in spatial resolution was then correlated to the magnitude and type of geometric calibration errors.

Table 3.2: Imaging parameter values and ranges

Parameter Name	Standard Value	Tested Range
Focal Length	90 mm	80-100 mm
Radius of rotation	45 mm	40-50 mm
Mechanical shift	0 mm	0-3 mm
Electrical shift, u	0 mm	0-6 mm
Electrical shift, v	0 mm	0-6 mm
Detector twist	0 deg	0-15 deg
Detector tilt	0 deg	0-15 deg

Finally, simulated projection data were generated using a model of the collimator behavior, in order to assess the effect of the point spread function on the characterization of the imaging geometry. The data were generated using the ray-driven projector described earlier, but with multiple rays which were positioned and weighted to model the depth-dependent spatial resolution and sensitivity of the pinhole, including septal penetration. The data were simulated to model the imaging of three technetium-99m point sources using a 1 mm keel edge pinhole aperture of the type used in the X-SPECT scanner. The numerical phantom was configured as described previously. The centroid positions were calculated for the projection data and input to the geometric calibration program. The results were compared to the results obtained using projection data generated with a model of the ideal collimator.

Data generated using the realistic collimator model were also combined with a model for the depth of interaction (DOI) of the photon. The depth of interaction (DOI) effect, or parallax is a consequence of detecting photons that strike the detector at an oblique angle. The photons interact at a finite, varying depth within the scintillator, which affects the lateral position of interaction recorded by the detector (Fig. 3.5).

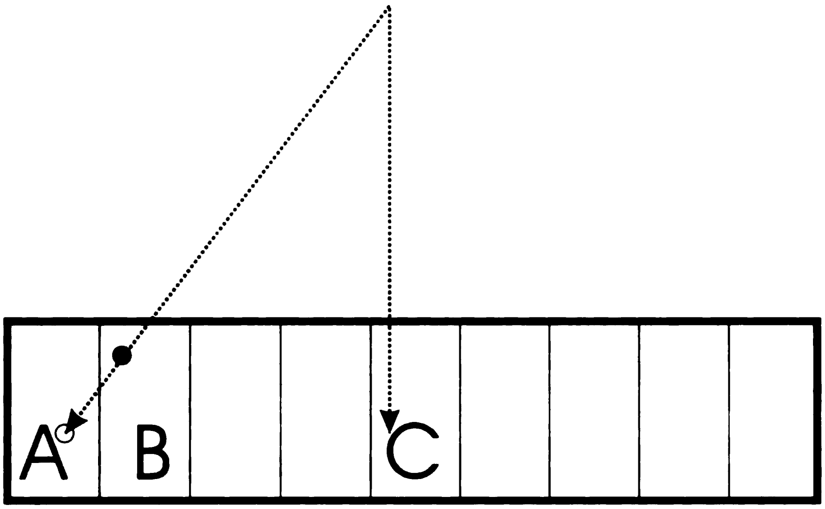

Fig. 3.5: A photon that strikes the detector at an angle can interact in either Pixel A or Pixel B, leading to uncertainty in the trajectory of the detected photon. A photon that strikes the center of the detector (Pixel C) can only interact with one pixel, eliminating the uncertainty.

The magnitude of the effect is dependent on the angle of incidence of the incoming photons, the energy of the photons, detector pixel size, and the photon attenuation properties of the detector. A computer program was written to model this effect on projection data. This program was applied to the projection data generated above, to yield sets of projection data that included modeling for both the collimator behavior and the depth of interaction effect. The projection data were processed, and the geometric calibration program was then used to estimate the values of the geometric parameters.

3.2.2. Results

3.2.2.1. Testing of calibration algorithm

The first step in evaluating the calibration algorithm was to verify that the algorithm converged to a minimum. This was demonstrating by creating a plot of the centroid locations from simulated data is shown in Fig. 3.6, overlaid with the centroid locations predicted by the geometric calibration program (u_{ij}^{est} and v_{ij}^{est} from Eq. 3.1). The average deviation in position estimated between the estimated and measured centroid locations was 0.1 mm. The strong correlation between the two sets of data provides confidence that the algorithm performs the minimization correctly.

After establishing that the algorithm converges to a reasonable solution, the next step is to demonstrate that the solution is correct. This was done by changing the geometry used to generate the projection data, and then calculating the geometrical parameters from the resulting projection data. Because the projection data were generated using a method independent of the calibration algorithm, a correlation between the calibration result and the parameter values used in the simulation will demonstrate that the algorithm is indeed working correctly. The estimated focal length plotted as a function of the simulated focal length is shown in Fig. 3.7, and the results show an excellent correlation between the estimated value and the expected value, with a slope of 0.97 and intercept of 2.4, demonstrating that the calibration algorithm consistently gives the correct result for focal length. Similar plots drawn for the other geometrical parameters also show good results (Table 3.3). These results combine to demonstrate that the fitting algorithm converges to the correct solution in the case of simulated, ideal data.

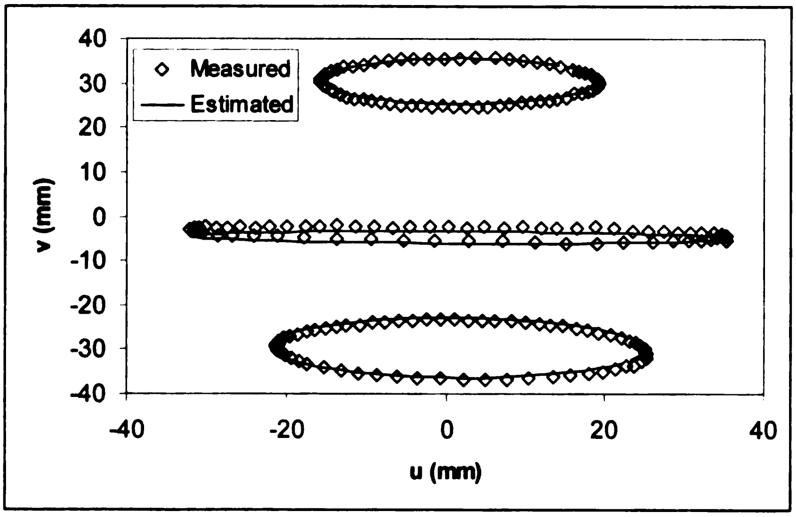

Fig. 3.6: The projection positions of three point sources (over 64 angles) are plotted (diamonds), along with the projection positions calculated by the fitting program (lines).

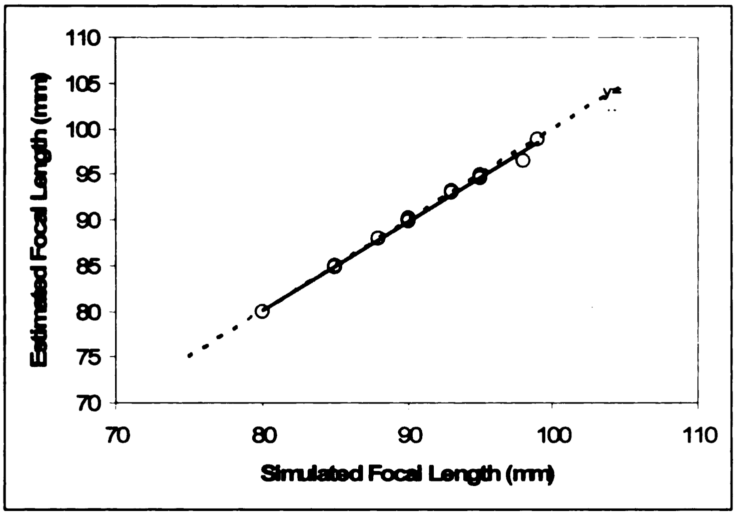

Fig. 3.7: Plot of the estimated focal length as a function of the simulated focal length. A linear fit of the results lies almost exactly on top of the line $y=x$ ($y=0.97x+2.4$). These results demonstrate the accuracy of the geometric calibration algorithm, and also confirm that the projector is behaving as expected.

Table 3.3: Correlation between parameters values used in simulation with calibration results

Parameter	Slope	Intercept	r^2
Focal length, *f* (mm)	0.97±0.02	2.4±1.5	0.996
Radius of rotation, *d* (mm)	0.97±0.01	1.2±0.4	0.999
Mechanical shift (mm)	1.00±0.01	0.04±0.02	0.998
Electrical shift, u (mm)	0.89±0.05	0.26±0.08	0.96
Electrical shift, v (mm)	1.05±0.04	-0.48±0.07	0.98
Tilt (deg)	1.02±0.03	0.00±0.05	0.99
Twist (deg)	1.01±0.01	0.01±0.02	0.999

3.2.2.2. Effect of geometrical errors

Figure 3.8 shows images reconstructed from simulated projection data that have been reconstructed with errors in the various geometric parameters. Multiple sets of projection data were created using the numerical phantom and ray-driven projector, using different values for the geometric parameters. The top row shows different slices from the data reconstructed without any errors in the parameter values. The second row shows slices in images reconstructed from data with deviations in the different geometrical parameters, and demonstrates some of the artifacts that result from reconstructing data with errors in the imaging geometry.

It was found that the mechanical shift (*m*) and electrical shift in the direction of rotation (e_u) had the strongest effect on spatial resolution. As shown in Fig. 3.9, the full width-half maximum spatial resolution increases almost proportionally to the mechanical shift. These errors are equivalent to an error in the center of rotation. As a result, the backprojections from different angles are misaligned, resulting in blurring, or in extreme cases, a circular artifact reconstructed when, in fact, the object was a small point source.

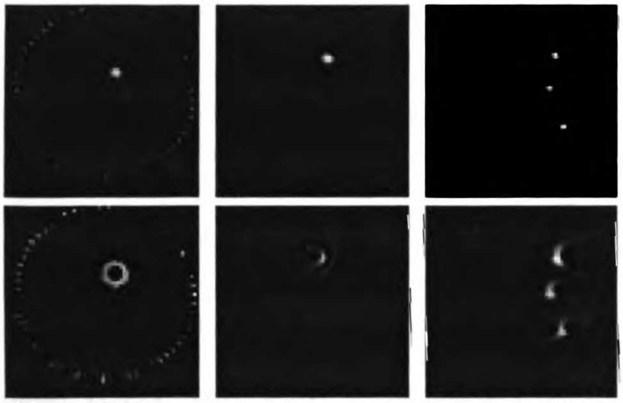

Fig. 3.8: Reconstructed tomograms of three simulated point sources. The top row shows images reconstructed using ideal parameters without any geometric errors. The second row shows corresponding images reconstructed with various geometric errors. The left images show an axial slice 4 mm from the central plane, and show the effect of a 2 mm error in the electrical shift (e_u) in the direction of the tomographic rotation. The center images show an axial slice through another point located 10 mm from the central plane, and demonstrate the effect of a 10 degree error in the twist angle. The right images show a sagittal slice coplanar with all three simulated point sources, and illustrate the effect of a 10 degree error in the tilt angle.

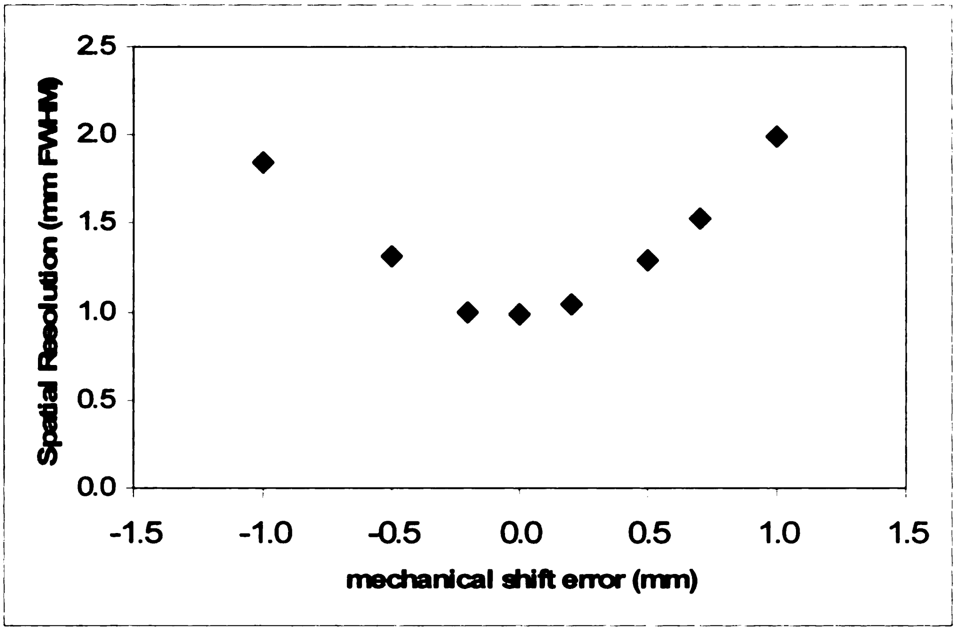

Fig. 3.9: Effect of mechanical shift (*m*) on spatial resolution in reconstructed image. The electrical shift in the direction perpendicular to the axis of rotation (*u*) had a similar effect on spatial resolution.

Errors in the focal length and radius of rotation affected the apparent size of the reconstructed phantom, but had relatively small effects on spatial resolution. For example, errors in the focal length value from -10 to +10 mm resulted in insignificant (less than 0.1 mm FWHM) changes in the spatial resolution. These errors affect the magnification of the object onto the detector, and therefore the reconstructed images are magnified or minified.

The tilt and twist had also relatively small effects, which were found to be position dependent. The tilt effectively causes a position dependent change in focal length, and the twist results in a position dependent error in mechanical shift. However, at small angles the resulting errors are not large enough to cause significant changes in the reconstructed data.

3.2.2.3. Effect of realistic collimator behavior

The use of realistic collimator response to generate projection data did not significantly affect the calibration results for focal length, radius of rotation, mechanical shift, or magnification. The addition of the depth of interaction effect did increase the effective focal length by 1.8±0.7 mm, which agrees with the mean depth of interaction calculated to be approximately 2.2 mm. The depth of interaction effect had no influence on the other geometric parameters. Therefore, we expect that the geometric calibration algorithm will also yield good results with experimental data.

3.3. Experimental measurements

3.3.1. Methods

Experimental measurements were performed to characterize and calibrate the imaging geometry of the X-SPECT, in order to optimize the quality of the reconstructed images. In addition to removing artifacts in the image, the geometric calibration also ensures that the linear dimensions (*e.g.*, apparent size of reconstructed objects) in the reconstructed are correct. The calibration was performed using the method and algorithm from Beque, *et al.*, as described above.

3.3.1.1. Measurement of pixel size

In order to perform the geometric calibration, it is necessary to either measure or assume a detector pixel size, so that the projection positions on the detector face can be converted from pixel locations to absolute u,v coordinates. We chose to measure the detector pixel size by fitting the gamma camera with a parallel hole collimator because it does not magnify or minify the recorded data. We then placed point sources on the camera head separated by known distances. The point sources were placed on a template printed with a grid, marking the desired locations of the point sources so that the distances between the point sources were measured and well defined. After acquiring the projection data, the centroid locations of the point sources were calculated from the projection data, and the distances between the points were calculated in terms of the number of pixels between the points. By plotting the distance between the points in the projection images as a function of the known physical distance between the point sources, it is possible to determine the mean pixel pitch of the detector in physical units of mm/pixel.

3.3.1.2. X-SPECT geometric calibration

After determining the pixel pitch, we applied the methods described in Sections 3.1 and 3.2 to calibrate the geometrical configuration of the system. This is necessary since the reconstruction algorithm requires parameters that describe the actual geometrical relationships of the scanner, and failure to perform this calibration can produce image artifacts as illustrated in Fig. 3.1 and Fig. 3.8. As in the case of the simulations (Section 3.2), this experimental calibration was performed by imaging three point sources using the X-SPECT system. The point sources were prepared by soaking beads of ion exchange resin in a ^{99m}Tc-NaTcO$_4$ solution, as described in Chapter 2. Because the calibration method requires that we know the distances between the calibration points, we printed a template on which we positioned three point sources at known locations (Fig. 3.10). The phantom was attached to a 5 cm × 5 cm, 0.3 cm thick acrylic sheet for rigidity and placed on the mouse bed in the X-SPECT scanner. The gamma camera output was then checked to ensure that none of the point sources was lying on the rotational axis, and or in the plane of the rotational orbit. The SPECT projection data were acquired over 360° at 64 projection angles with a nominal radius of rotation of 4.5 cm, representing the acquisition parameters used for small animal imaging studies in our laboratory. The acquisition was repeated with the radius of rotation values from 4 to 6 cm, in order to characterize the relation between the nominal and actual values for the radius of rotation. These measurements were acquired using various point source configurations over a period of several months in order to determine the stability of the imaging geometry and the repeatability of the measurements.

After imaging, the centroids of each of the projected point sources were calculated with the semiautomated approach using Matlab scripts described above. The measured centroids then were used to determine the geometric parameters by applying the algorithm described previously in Section 3.1 of this chapter.

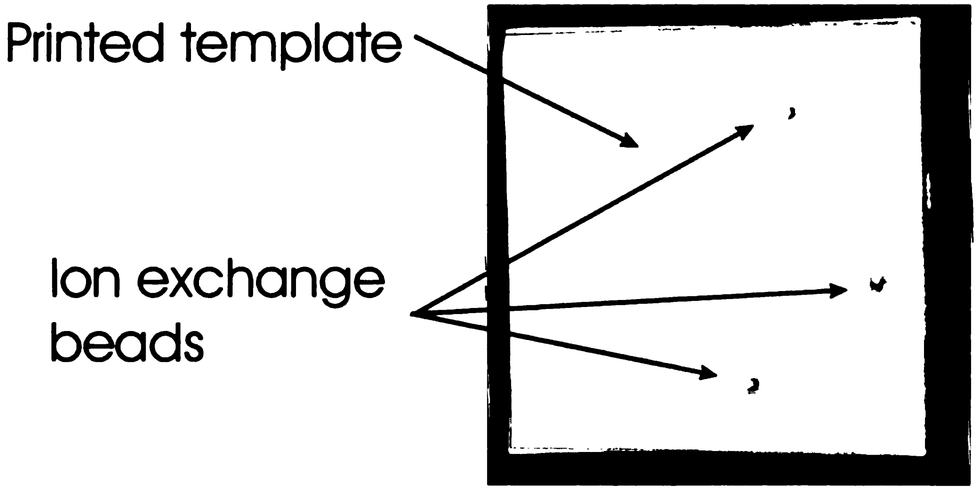

Fig. 3.10: Phantom used for geometric calibration of the X-SPECT. It consists of three point sources made of ion exchange beads soaked in ^{99m}Tc-sodium pertechnetate. The three point sources are glued to a printed paper template that is attached to a piece of acrylic (approximately 5 cm × 5 cm) for stiffness.

We also used these data to verify that the calibration results obtained for image reconstruction gave the correct linear dimensions in the reconstructed images; this was performed using the geometric parameter values obtained in a second calibration study to reconstruct the projection data. The data obtained in the second study were generated using the same imaging parameters, but a different set of point sources. The distances between the points in the first phantom were calculated using the reconstructed image, and compared with the known point spacing. This was done for three sets of data to confirm the reliability of the calibration method.

3.3.2. Results

3.3.2.1. Detector pixel size estimation

As noted earlier, the physical size of the pixel (in dimension of millimeters) is an important unit needed to characterize the geometry of the imaging system accurately. In this study, the pixel size was calculated by imaging several point sources with the parallel hole collimator, then relating their known physical distance to their distance measured in pixel values as extracted from the image (Fig 3.11). As expected, the relationship between the physical distance and the distance measured in pixels was linear for both the horizontal and vertical directions in the image. These values were fit to a linear regression line, with the slope representing the pixel pitch which was measured to be 2.23 mm, which is in agreement with the nominal pitch of 2.2 mm (Chapter 2). As noted earlier, this value was used to convert the location of the point source projection on the detector from units of pixels to coordinates in physical units (mm).

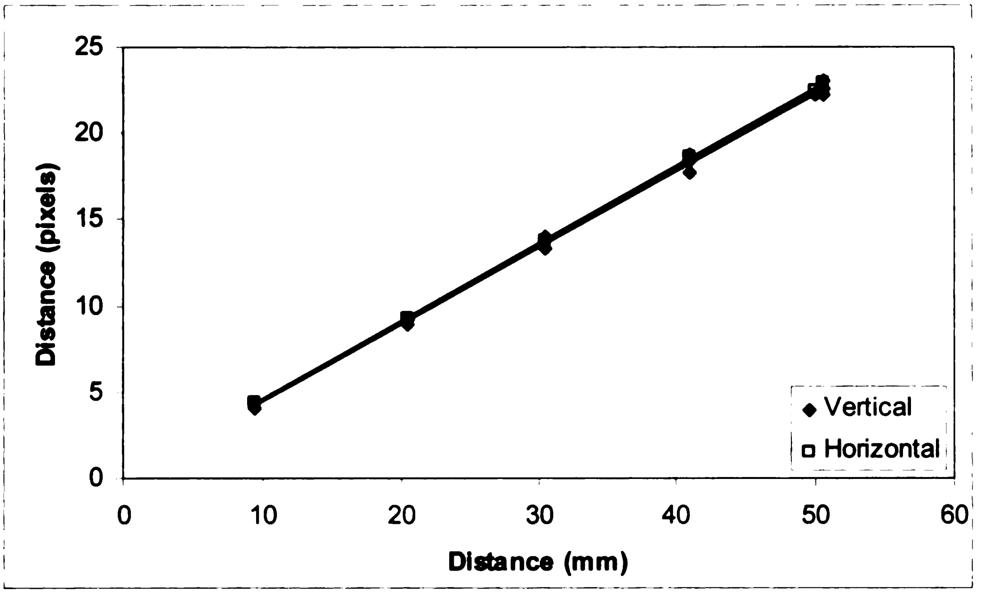

Fig 3.11: Plot of the distance between point sources placed on the detector face, with the distance measured in the image on the y-axis. The difference between the two lines is not statistically significant, and the combined results estimate the pixel pitch on the gamma camera to be 2.23 mm in both the horizontal and vertical directions.

3.3.2.2. X-SPECT geometry calibration

The calibration method described in this chapter was used to extract the values of the geometrical parameters for the scanner, which in turn were incorporated into the reconstruction algorithm to improve the accuracy of its model of the imaging system and improve the overall quality and accuracy of the reconstructed images. These results (Table 3.4) show that some of the parameters, notably the electrical shifts and the mechanical shift (e_u, e_v, and m), were not estimated reproducibly. The radius of rotation was excluded from this table because the nominal value for this parameter was varied between experimental acquisitions. Although the measured values for the focal length (*F)* and the radius of rotation (*d)* varied from experiment to experiment, one key result showed that the actual magnification factor (*F*/*d*) was consistently higher than the value given by the nominal geometry (Fig. 3.12). This error in magnification affected the measurement of size in the reconstructed images, such that objects appeared larger in the reconstructed images than the actually were. This error may be in part due to the depth of interaction which could increase the effective focal length by up to 6 mm (the thickness of the crystal), accounting for approximately half of the difference between the measured and nominal magnification factor.

The calibration process also found that the measured values (Table 3.4) of the twist (ϕ)and tilt (ψ) are not significantly different than zero. In addition, the measured values of the twist and tilt introduced small displacements in the pixel locations of 0.1 mm and 0.05 mm at the edges of the detector, which are significantly smaller than a pixel width. We therefore do not anticipate that the measured values of the twist and tilt obtained from the scanner would affect image quality to any appreciable degree.

Table 3.4: Results of X-SPECT geometric calibration

Parameter	Full Fitting	Limited Fitting	Expected Value
Focal Length, F (mm)	94.1±5.0	94.9±5.0	90
Mechanical shift, m (mm)	0.8±1.6	0.55 ±0.10	0
Electrical shift, e_u (mm)	-1.8±5.5	0.55 ±0.10	0
Electrical shift, e_v (mm)	0.1±7.6	-	0
Tilt, ϕ (degrees)	-0.05±0.30	-	0
Twist, ψ (degrees)	-0.1±4.0	-	0

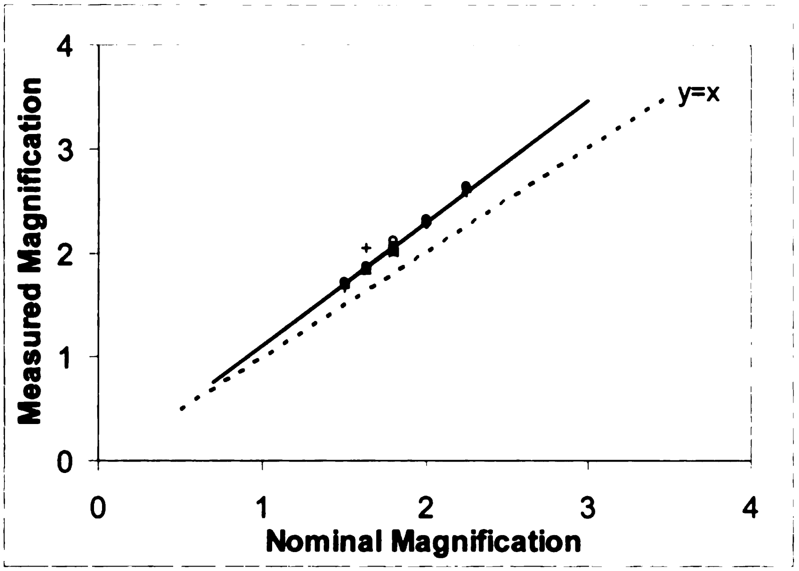

Fig. 3.12: Plot of measured magnification (*F*/*b*) versus the nominal value. The results show that the actual magnification is consistently larger than the nominal magnification. The measured magnification is related to the nominal magnification by the equation $y = 1.18x - 0.07$.

We found that the electrical shifts and the mechanical shift were difficult to estimate reproducibly using the full fitting algorithm. According to Beque, *et al.*, there is a strong correlation between e_u and m, which would explain the difficulty in reliably fitting these values [2]. In other words, a change in the u-axis electrical shift (e_u) affects the measured data in a manner very similar to a change in the mechanical shift (m), making it difficult to separate the contribution of these two parameters to the measured data. Additionally, the values of e_v seem to be closely linked to the position estimates of the source. This also results in high variability in the estimates for the z position of the point source locations and in the value for e_v. As was the case with the mechanical shift and the u-axis electrical shift, changes in the z-position of the point source affect the measured data in a manner very similar to changes in the v-axis electrical shift.

As mentioned earlier, the measured values of the tilt ϕ and twist ψ were not significantly different from 0, and that the value of the electrical shift e_u is closely correlated with the mechanical shift m. We therefore applied a limited fitting algorithm which, as described above, assumed that the tilt and twist were negligible (*i.e.*, $\phi = \psi = 0$), and that the electrical shift equaled the mechanical shift (*i.e.*, $e_u = m$). As mentioned previously, setting the electrical shift (e_u) equal to the mechanical shift represents a lateral displacement of the center of the gamma camera from the axis of rotation. The twist and tilt were ignored to reflect the small magnitude of these parameters obtained from the results of the prior measurements.

With the full fitting algorithm, the average deviation between the estimated and measured point source location in the projection images was 1.75 mm. Using the limited fitting algorithm, this error only increased to 1.94 mm, which still is less than the width of a single pixel. Therefore, we can conclude that the limited fit gives results that are, for all practical purposes, equivalent to the results from full fitting (Fig. 3.13). Thus, it is possible to obtain high quality reconstructed images from the X-SPECT data by using 3, rather than 6, parameters to calculate the imaging geometry. This allows the use of the limited-fit algorithm for geometric calibration, which gives more repeatable results, and also reduces the number of parameters needed to model the imaging geometry in the reconstruction algorithm.

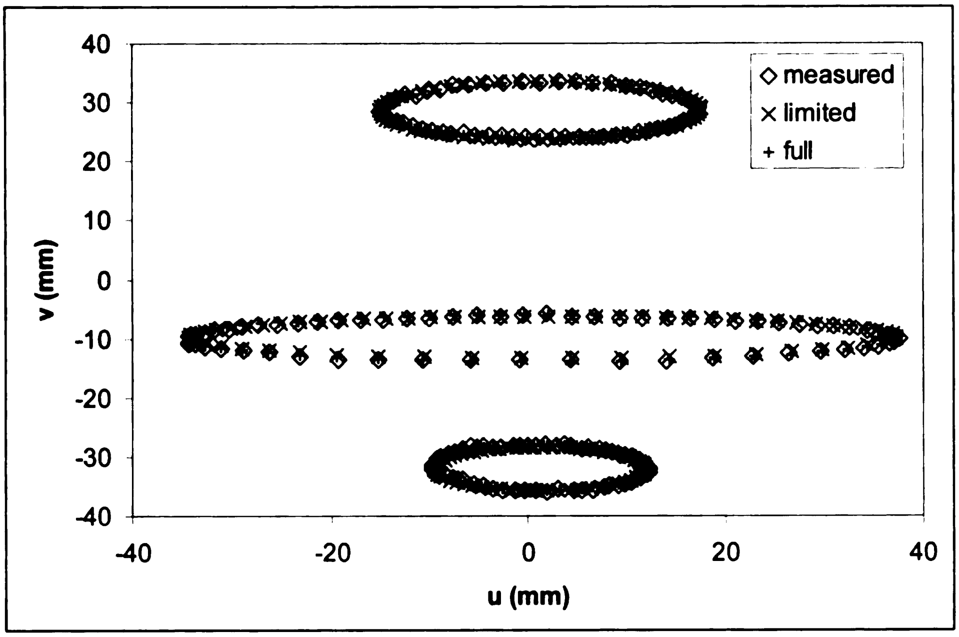

Fig. 3.13: Plot of the measured and estimated projection location for three point sources over 64 projection angles. This figure demonstrates that the limited fitting provides an excellent fit for the projection data.

3.3.2.3. Effect of geometric calibration on image scaling

Having full knowledge of the imaging geometry is necessary to accurately reconstruct SPECT data. In the previous section, we found that the measured magnification (focal length divided by radius of rotation) was consistently larger than the nominal value. Although this error did not cause obvious artifacts in the reconstructed images, it did result in reconstructed images that consistently appeared to be larger than their actual values. The deviation in the magnification value described above appears to result from a combination of a radius of rotation value (*d*) that is less than the nominal value reported from the scanner and an effective focal length that is longer than the nominal detector focal length. Part of this error may be accounted for by the depth of interaction effect, and the remaining error is most likely a systematic error in the design or calibration of the system.

In order to verify that the measured magnification was correct, we used the geometric parameters obtained using one set of point sources to reconstruct the projection data obtained during a second geometric calibration scan. We also reconstructed the projection data obtained during the second scan using the nominal values for the scanner geometry. Using the nominal scanner geometry, we found that the distances between points were overestimated. Linear least-squares fitting was performed on the data, and yielded the relationship $y = 1.14x - 0.4$ for uncorrected data, where y is the measured distance between two points in the reconstructed image in mm, and x is actual distance between the points (also in mm). By changing the radius of rotation to obtain the correct magnification according to the results shown in Fig. 3.12, the correct distances were measured in the reconstructed SPECT images, as shown in Figure 3.14 below. A linear least-squares fit for the corrected data yields the relationship $y = 1.01x - 0.3$, demonstrating that the distances in the reconstructed image are correct.

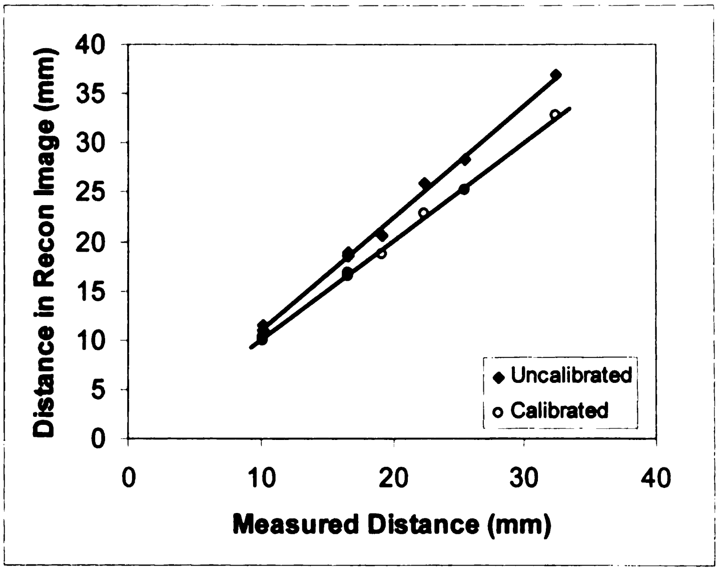

Fig. 3.14: Plot of distance between points measured in the reconstructed image vs. the measured distance.

3.4. Conclusion

Accurate knowledge of the geometric parameters of the imaging system is a prerequisite for properly reconstructed images. Because of the high spatial resolution required for small animal imaging, it is necessary to know these parameters to a high degree of accuracy. A method to determine these parameters from projection data was implemented, tested with simulated data, and then applied to the X-SPECT scanner. This allowed us to obtain accurate estimates of the geometric parameters needed to accurately reconstruct SPECT data.

References

[1] G. T. Gullberg, B. M. W. Tsui, C. R. Crawford, J. G. Ballard, and J. T. Hagius, "Estimation of Geometrical Parameters and Collimator Evaluation for Cone Beam Tomography," *Medical Physics*, vol. 17, pp. 264-272, 1990.

[2] D. Beque, J. Nuyts, G. Bormans, P. Suetens, and P. Dupont, "Characterization of Pinhole SPECT Acquisition Geometry," *IEEE Transactions on Medical Imaging*, vol. 22, pp. 599-612, 2003.

[3] J. Li, R. Jaszczak, H. Wang, K. Greer, and R. Coleman, "Determination of both mechanical and electronic shifts in cone beam SPECT," *Physics in Medicine and Biology*, vol. 38, pp. 743-754, 1993.

[4] W. H. Press, B. P. Flannery, S. A. Teukolsky, and W. T. Vetterling, *Numerical Recipes in C.* Cambridge: Cambridge University Press, 1988.

[5] L. Feldkamp, L. Davis, and J. Kress, "Practical cone-beam algorithm," *J. Opt. Soc. Am.*, vol. 1, pp. 612-618, 1984.

[6] M. C. Wu, "Development and Application of a High-Resolution Nuclear Medicine Imaging System," Ph.D. dissertation, University of California San Francisco and University of California Berkeley, San Francisco, CA, 2001.

Chapter 4: Improved SPECT Reconstruction

4.1. Overview

The design of the algorithm used to reconstruct tomographic data obviously affects the quality of the resulting image. Historically, tomographic images from x-ray CT, SPECT, and PET have been reconstructed using analytic methods such as filtered backprojection. Over the past decade, statistically based iterative reconstruction algorithms such as maximum likelihood expectation maximization (ML-EM) and ordered subsets – expectation maximization (OS-EM) increasingly have been used to reconstruct radionuclide tomographic data from both SPECT and PET in clinical settings, and represent a major improvement over analytical reconstruction algorithms. Unlike analytic methods, ML-EM and OS-EM reconstruction algorithms inherently account for the Poisson statistics of the radionuclide data, and also can be designed to compensate the reconstructed data for physical effects such as photon attenuation and scattered radiation. The iterative reconstruction algorithm begins with an initial estimate of the radionuclide distribution (typically assumed to be uniform), from which the algorithm models the imaging process to estimate the projection data. The estimated projection data then are compared with the experimentally measured projection data to derive a correction term, which is used to update and derive a new estimate of the radionuclide distribution (Fig. 4.1), which then can be used to calculate a new estimate of the projection data. This process is repeated iteratively until the algorithm reaches a predetermined criteria (*e.g.*, number of iterations, mean-squared error between the estimated and measured projection data) to obtain the final result, which is a tomographic image representing the radionuclide distribution within the object being imaged.

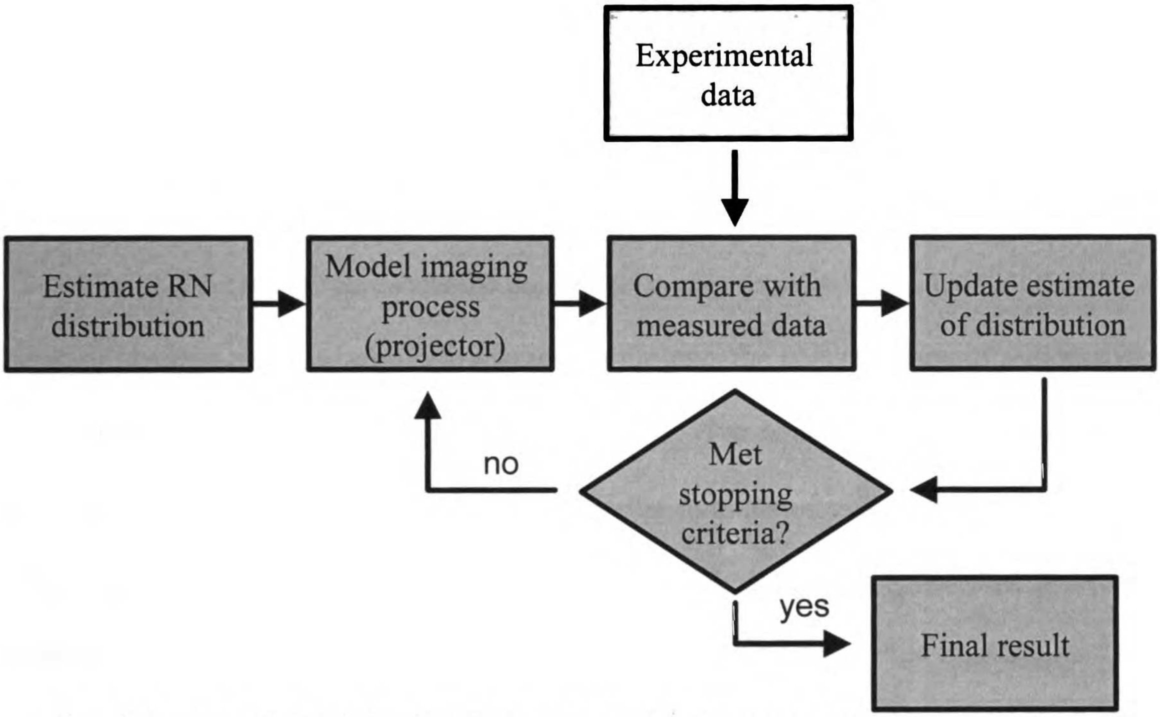
Experimental data
Estimate RN distribution
Model imaging process (projector)
Compare with measured data
Update estimate of distribution
Met stopping criteria?
no
yes
Final result

Fig. 4.1: Overview of the iterative reconstruction process. The general scheme in iterative reconstruction involves a model of the imaging process, and a comparison between the estimated projection data with the measured projection data. The results of the comparison are used to update the estimate of the radionuclide (RN) distribution, and the process is repeated until the stopping criterion (*e.g.*, number of iterations) has been satisfied.

The quality and accuracy of the reconstructed image depends on the how accurately the reconstruction algorithm models the physics of the imaging process, as well as other factors such as the angular and spatial sampling of the object during the acquisition process. For example, a common artifact in SPECT imaging results from the attenuation of emitted photons in the object, since simple algorithms assume that the photons emerge without any absorption or scatter. This causes decreased image intensity at the center of the object relative to the periphery. However, by modeling the physical process of photon attenuation in the reconstruction algorithm, this artifact can be reduced or eliminated in the reconstructed image.

As mentioned previously, accurately modeling the physics of the imaging process is an important component of the ML-EM and OS-EM algorithms. This mathematical model is performed in the forward projector, or simply the projector (see Fig. 4.1), and is mathematically expressed using the following equation:

$$y(d) = \sum_{b=1}^{N} p(b,d)\lambda(b) \tag{4.1}$$

The value $y(d)$ formally represents the number of events recorded (*e.g.*, units of counts) at detector position d. Similarly, $\lambda(b)$ formally represents the concentration of radioactivity (*e.g.*, units of MBq/cm^3) at image voxel location b. (For simplicity, we simply will call $\lambda(b)$ the "activity" at voxel b.) Finally, N is the number of voxels in the image, and $p(b,d)$ represents the probability that a photon emitted from voxel b is detected at detector position d. The backprojection operation is used in revising the image estimate, and can be thought of as a smearing of each measured detector value $y(d)$ back into the voxels which contributed to the measurement in that detector location. It is expressed using the equation:

$$\lambda(b) = \sum_{d=1}^{N_d} p(b,d)y(d) \tag{4.2}$$

where $\lambda(b)$ is the value of voxel b, $y(d)$ is the value to be backprojected from detector position d, N_d is the number of detector positions, and $p(b,d)$ is the same as in Eq. 4.1. As before, the detector values $y(d)$ formally are expressed in units of counts, where the voxel values $\lambda(b)$ formally are expressed in units of MBq/cm^3. (However, in practice both $y(d)$ and $\lambda(b)$ are unitless and simply represent variables that are proportional to the physical units described above.) In the ML-EM and OS-EM reconstruction algorithms described by Fig. 4.1, the backprojected quantity is the ratio of the measured counts to the expected number counts calculated using the forward project. The resulting value is then used to update the image estimate.

The projection and backprojection processes are usually implemented in one of two manners that can be described as being either "voxel-driven" or "ray-driven". In voxel-driven methods, the algorithm loops sequentially through the voxels in the radionuclide distribution (*i.e.*, the image), and adds the contribution of each voxel to the estimated projection data recorded by the detector elements. In the ray-driven technique, the algorithm performs a projection or backprojection through the image matrix along rays that simulate the "view" of that detector element. In the projection process, the algorithm samples the image matrix along each ray, and changes the output value of the detector element accordingly. In the backprojection process, the algorithm adjusts the image voxels along each ray according to the value of the detector element. We have implemented a version of the ordered-subset expectation-maximization (OS-EM) reconstruction algorithm using the C programming language. Our specific implementation uses a ray-driven projector/backprojector [1, 2]. In this project, we implemented the reconstruction algorithm using a projector/backprojector pair that made it relatively straightforward to include attenuation correction and collimator response. In this chapter, we describe our implementation of a reconstruction algorithm that includes models for several physical effects that degrade SPECT images: photon attenuation, depth dependent collimator response, and photon scatter.

4.2. Photon attenuation

Ideally, radionuclide measurements with biomedical imaging would produce tomograms that accurately represent the radionuclide distribution within the body of the animal or patient being imaged. However, in reality, the source generally is distributed within the body and surrounded by tissues of different chemical composition (*e.g.*, fat *vs.* bone *vs.* lean soft tissue) and different physical densities (*e.g.*, bone *vs.* muscle *vs.* lung).

As a result, the photons emerging from the radioactivity distribution are absorbed by the surrounding tissue. As photons pass through matter, they can interact with the atoms in several different ways, which for the photon energies encountered in SPECT are dominated by absorption through photoelectric interactions, or scattering through Compton interactions [3]. Rayleigh scattering also can be significant at lower photon energies, whereas pair production becomes increasingly important for photon energies above 1.02 MeV. As a result, both the number and the spatial distribution of photons detected by the gamma camera are dependent on the radioactivity distribution as well as the distribution and type of tissue, which decreases and modulates the voxel values in the reconstructed images.

Because the amount of attenuation depends on the type and thickness of the material that the photons traverse prior to detection, one might expect photon attenuation to be negligible at the smaller length scales encountered in small animal imaging, especially in comparison to human imaging. However, photon attenuation nevertheless can be important for small animal imaging in several ways. First, small animal imaging can be performed with iodine-125 which is a useful radiolabel due to its low cost, long half-life, ready availability, and versatility due to the relative ease of labeling organic compounds with iodine [4]. It also serves as a useful, low-cost substitute for iodine-123 for preliminary studies of new imaging agents in mice and rats [5, 6]. However, iodine-125 emits low energy photons (~27.5 keV) that are unsuitable for imaging humans, and that will be more strongly attenuated than photons from radionuclides such as technetium-99m (140 keV) and iodine-123 (159 keV) commonly used for human imaging. Additionally, small animal imaging is usually performed as part of a scientific study, in contrast to the clinical applications of nuclear medicine in humans. Thus, there is a greater emphasis on quantitative accuracy in small animal imaging, and less reliance on qualitative or visual interpretation. Finally, small animal images often are interpreted by biologists, who may not be as familiar with image artifacts caused by photon attenuation. For all of these reasons, it is desirable to correct for the effects of photon attenuation in small animal radionuclide imaging.

The methods proposed for attenuation correction for SPECT can be divided into two classes. The first class of algorithms consists of those that do not use an external source of information about the attenuation distribution. These algorithms generally assume uniform attenuation, such as the commonly used Chang technique [7], or simultaneously estimate the attenuation and radionuclide distributions based on the radionuclide emission data [8]. However, these intrinsic methods either can produce inaccurate results, or are difficult to implement. For this reason, we will focus on the second class of attenuation correction algorithms that derive spatially-dependent attenuation information about the object from some form of anatomical imaging, such as transmission scans using an external radionuclide source, magnetic resonance imaging, or x-ray CT scans of the object [9-12].

4.2.1. Materials and methods

Extrinsic correction methods for photon attenuation require that the attenuation properties be determined and then incorporated into an iterative tomographic algorithm to compensate for the effects of photon attenuation on reconstructed images. The most direct way to obtain this photon attenuation information is to perform tomographic measurements of the object with an external radionuclide or x-ray source. The resulting transmission projection data then can be reconstructed to produce tomograms, or “attenuation maps”, where the image values represent the linear attenuation coefficients at each point within the object. The first implementation of attenuation correction algorithms used attenuation maps that were produced with radionuclide transmission sources. However, the advent of dual-modality imaging in SPECT and PET, including the SPECT-CT system used in this project, provides a ready method for generating object specific attenuation maps using x-ray CT. While the x-ray CT image is a measure of the attenuation properties of the object being imaged, the values in the reconstructed image are not necessarily equal to the actual linear attenuation coefficients within the object, primarily because the x-ray CT data usually are recorded with a polyenergetic spectrum with photon energies that are not equivalent to the energy of the monoenergetic photon recorded in the radionuclide emission data. In addition, CT images generally are recorded in "Hounsfield units" (HU), which scale the resulting image values from a value of -1000 HU for air to 0 HU for water. On this scale, bone produces values generally in the range of 1000-2000 HU, depending on its physical density. As a result, the x-ray CT images must be calibrated so that they can be used as an attenuation map for the photon energies of the radionuclide being imaged with SPECT. As demonstrated in human imaging [10], this calibration can be performed by deriving a calibration curve to rescale the CT image so that the voxel values in the CT image are equal to the linear attenuation coefficient values for the photon emitted by the radionuclide.

We therefore developed a technique, similar to the one used in clinical imaging, which generates this calibration curve by acquiring microCT scans of a calibration phantom containing materials of known composition. The voxel values in the CT image of the calibration phantom then were correlated with the linear attenuation coefficient of the corresponding materials at the radionuclide photon energy. The resulting correlation curve then could then be used to rescale CT images on a voxel-by-voxel basis to represent linear attenuation coefficient values, which were incorporated into the iterative SPECT reconstruction algorithm and used for attenuation correction of the SPECT data.

4.2.1.1. CT calibration phantoms

For the purpose of calibrating the CT data to obtain quantitatively accurate attenuation maps, two different phantoms were designed and fabricated. The first phantom used liquid calibration materials, and the second phantom was designed to use solid calibration materials. The liquid phantom is advantageous in that it can be used with a variety of easily available materials, whereas the solid phantom has the advantage of being easier to fabricate and being chemically and mechanically more stable.

The first (liquid) phantom was designed and fabricated in the form of an outer cylindrical tube (diameter = 3.2 cm) containing three smaller tubes (inner diameter = 0.6 cm) filled with various calibration fluids (Fig. 4.2). The outer cylinder was filled with water in order to simulate beam hardening caused by the animal torso. In this project, the size and shape of the phantom were chosen to approximate the torso of an adult rat, but also could be designed to represent the geometry of the mouse torso. The calibration materials included water, air, and potassium phosphate dibasic (K_2HPO_4) solutions. K_2HPO_4 is used to simulate bone, and is commonly used in imaging studies of bone mineral density [13]. In our experiments, the concentration of K_2HPO_4 solutions varied over physiological-relevant levels from 50 mg/mL to 200 mg/mL. Additionally, 1-octanol and ethanol were used to simulate fat because they, like fat, contain primarily carbon and hydrogen, and are less dense and have a lower oxygen concentration (*i.e.*, lower effective atomic number) than water.

The second CT calibration phantom was constructed entirely of solid plastic materials (Fig. 4.3). It consists of a polystyrene cylinder (diameter = 3.8 cm) containing 5 smaller rods (diameter = 0.6 cm) of various proprietary materials supplied by Mindways Software Inc. (San Francisco, CA), a company that specializes in bone densitometry and body-composition measurements using x-ray CT [14]. The attenuation characteristics of each material are expressed in terms of equivalent amounts of water and K_2HPO_4 (Table 4.1). The phantom was also imaged with rods removed in order to measure the CT image values for air, to provide another data point for the calibration.

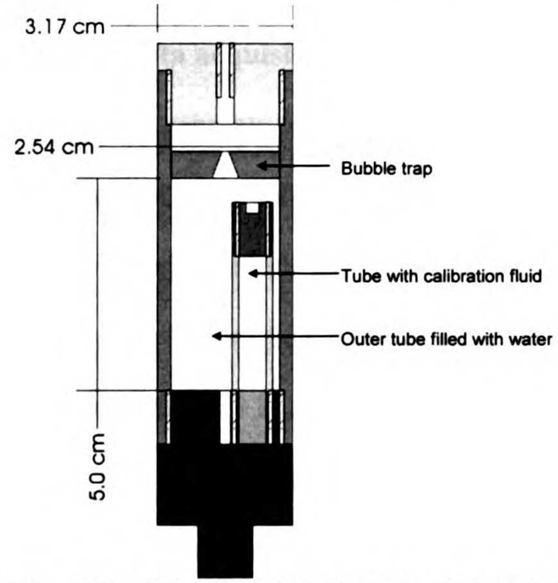

Fig. 4.2: CT calibration phantom designed for use with liquid materials. The phantom was designed with an outer cylinder that holds three smaller tubes that can be filled with liquid calibration materials.

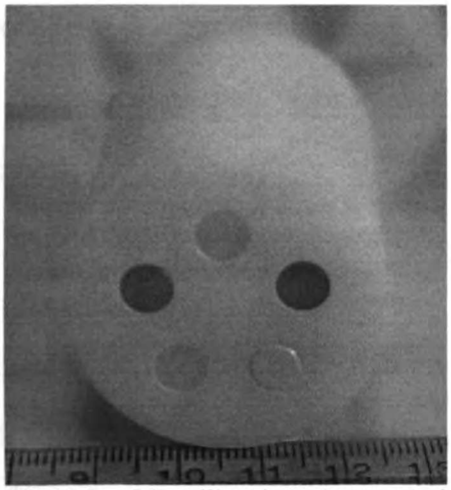

Fig. 4.3: CT calibration phantom with solid calibration materials. The outer cylinder is a polystyrene rod 3.8 cm in diameter. The inner rods have diameter of 0.6 cm.

Table 4.1: Attenuation characteristics of the materials used in the solid CT calibration phantom expressed in terms of equivalent density of water and K_2HPO_4

Material	H_2O equivalent density (mg/cm^3)[a]	K_2HPO_4 equivalent density (mg/cm^3)
A	1012±2	-51.8±0.1
B	1056±2	-53.4±0.1
C	1104±2	58.9±0.1
D	1120±2	157.1±0.3
E	923±2	375.8±0.9

4.2.1.2. CT data acquisition and analysis

In order to generate tomograms of the CT calibration phantoms, they were scanned at 256 projections over 360 degrees, using a technique of 50 kVp and 0.6 mA. When the solid calibration phantom was used, a plastic bottle containing water (diameter = 3.8 cm) was placed on animal bed directly adjacent to the phantom during the scan in order to provide an additional calibration measurement. The projection data were reconstructed using the software supplied with the X-SPECT scanner, as described in Chapter 2, and then were rebinned to a $(256)^3$ format. The first step of the calibration process was to extract CT image values from manually defined volumes of interest (VOIs) in each image corresponding to the location of the individual calibration materials. In addition, a VOI was defined in a region containing water to obtain the average voxel value for water. The CT image values then were converted to Hounsfield units (HU) using the following equation:

$$HU = 1000 \times \left(\frac{I}{I_{water}} - 1\right) \qquad (4.3)$$

where I is the image intensity of a given voxel, and I_{water} is the image intensity associated with water. The data were then fit to a piece-wise linear curve of the form described in Eq. 4.4 using a least squares fit:

$$\begin{aligned} \mu &= m_1 \cdot HU + b, HU < 0 \\ \mu &= m_2 \cdot HU + b, HU \geq 0 \end{aligned} \tag{4.4}$$

where *HU* is the CT image value in Hounsfield units, and μ is the predicted linear attenuation coefficient as a function of photon energy. The piece-wise linear fit was selected because the materials less dense than water (*i.e.*, voxels with intensity less than 0 HU) are assumed to be composed of a mixture of soft tissue and air which contain materials with low atomic number (carbon, hydrogen, oxygen, nitrogen), and materials denser than water (*i.e.*, voxels with intensity greater than 0 HU) are assumed to be a mixture of soft tissue and bone, which contain materials with higher atomic number (*Z*), specifically calcium(*Z*=20) and phosphorous (*Z*=15). Because the linear attenuation coefficient is a function of atomic number, two different parameters (m_1 and m_2) are needed to derive the calibration curve [15]. However, the value of the intercept *b* were forced to be identical in the two equations (Eq. 4.4), so that the curves matched for water (*i.e.*, when HU = 0).

Theoretically, the calibration curves should depend on the energy of the x-ray beam, and therefore the x-ray tube potential, used to collect the calibration data, but should be relatively independent of the x-ray tube current. These effects were measured by acquiring data using the solid phantom with different x-ray tube settings. The calibration curve for each x-ray setting then was generated using the procedure described above. The calibration curves then were compared to assess the effect of tube potential and current in generating the calibration curve.

4.2.1.3. Procedure for generating attenuation map

The process to produce an attenuation map required that the voxel values in the CT image first be converted to values of the linear attenuation coefficient at the radionuclide photon energy. The resulting attenuation map then was registered geometrically with the coordinates of the SPECT image space, and finally was reformatted to match the matrix dimensions of the SPECT image. This was done using a simple procedure that involved several steps. CT data were first reconstructed, and then rebinned to a $(256)^3$ matrix format to reduce noise and to reduce the amount of digital data that needed to be processed. The voxel values were rescaled to Hounsfield units on a voxel-by-voxel basis, and converted to values of linear attenuation coefficient using the calibration curve described above. The resulting attenuation map then was coregistered with the SPECT image space as discussed in the previous chapter. The attenuation map was low-pass filtered in order to prevent aliasing during the downsampling process using two applications of the following 3×3×3 kernel:

$$\frac{1}{64}\begin{bmatrix} 1 & 2 & 1 \\ 2 & 4 & 2 \\ 1 & 2 & 1 \end{bmatrix} \quad \frac{1}{32}\begin{bmatrix} 1 & 2 & 1 \\ 2 & 4 & 2 \\ 1 & 2 & 1 \end{bmatrix} \quad \frac{1}{64}\begin{bmatrix} 1 & 2 & 1 \\ 2 & 4 & 2 \\ 1 & 2 & 1 \end{bmatrix} \tag{4.5}$$

where each submatrix listed above represents one plane of the kernel. The smoothed image then was downsampled in order to match the SPECT matrix format, yielding the final attenuation map used in the attenuation correction algorithm.

4.2.1.4. SPECT measurement

In order to demonstrate the effect of attenuation correction on reconstructed SPECT images, SPECT data were acquired of a cylindrical phantom (diameter = 3.8 cm) filled with water containing approximately 25 MBq of ^{125}I-NaI. The phantom was placed in the SPECT-CT system, and SPECT data acquired with a total of 64 projections over 360° for 60 seconds/projection using the 2 mm pinhole collimator. Following SPECT acquisition, an x-ray CT scan was performed, and the resulting CT data were reconstructed and processed as described above to create an attenuation map. The SPECT data were reconstructed using an OS-EM algorithm both with and without attenuation correction. A line profile was drawn through the reconstructed image, in order to determine if attenuation correction compensated for the decreased intensity at the center of the image caused by photon attenuation.

4.2.2. Results

4.2.2.1. CT image calibration results

The results for the CT image calibration are summarized in Table 4.2 and Table 4.3, and in Figures 4.4 through 4.7. The CT imaging values (in Hounsfield units) for the various calibration materials are shown in Table 4.2, and the CT calibration curves are shown in Fig. 4.4 and Fig. 4.5 for technetium-99m and iodine-125, respectively. The results of the least squares fitting are summarized in Table 4.3. These results show the relationship between the CT image values and the linear attenuation coefficient for SPECT (technetium-99m and iodine-125) photons, and show good correspondence with the piece-wise linear model used to approximate the energy-dependence of the linear attenuation coefficients of the calibration materials used in this study. In addition, the calibration curves obtained from the liquid and solid phantoms are in good agreement with one another.

Table 4.2: CT image values for various calibration materials

Material	CT image value (HU)
Solid A	-310±6
Solid B	-256±13
Solid C	376±11
Solid D	899±30
Solid E	1710±36
Air	-908±24
50 mg/mL K_2HPO_4	182±46
100 mg/mL K_2HPO_4	403±24
200 mg/mL K_2HPO_4	836±31
60% ethanol	-206±36

Table 4.3: Calibration results

	Slope (HU<0)	Intercept	Slope (HU>0)
Tc-99m, liquid phantom	1.62×10^{-4}	0.154	2.87×10^{-5}
Tc-99m, solid phantom	1.16×10^{-4}	0.154	3.34×10^{-5}
I-125, liquid phantom	4.85×10^{-4}	0.43	5.84×10^{-4}
I-125, solid phantom	4.45×10^{-4}	0.43	5.22×10^{-4}

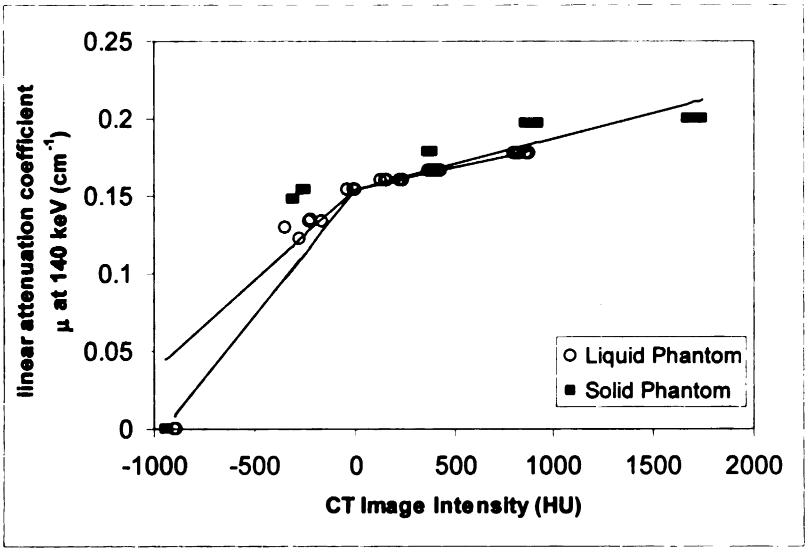

Fig. 4.4: Plot of the linear attenuation coefficient at 140 keV as a function of image intensity for both the liquid and solid phantoms.

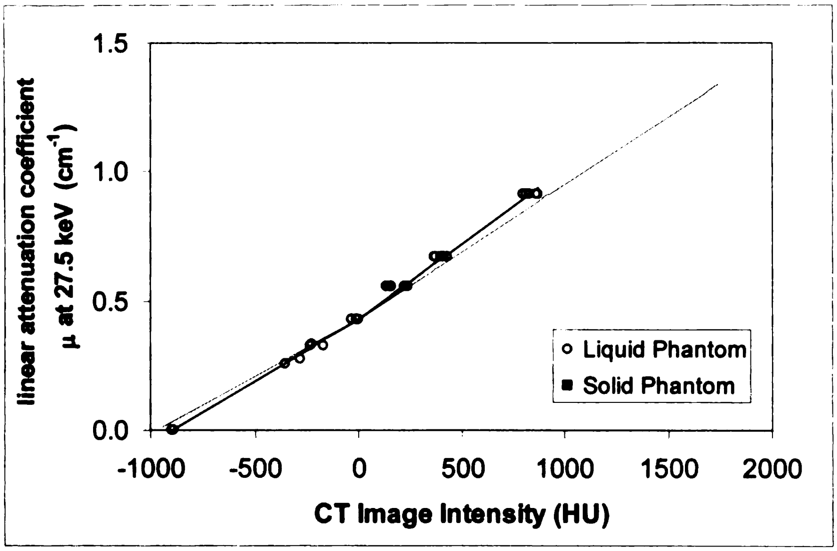

Fig. 4.5: Plot of the linear attenuation coefficient at 27.5 keV vs. HU for the liquid and solid phantoms.

The effect of changing the tube voltage on the reconstructed CT image values is shown in Fig. 4.6. In this figure, the CT image intensity (HU) is the dependent variable and is plotted as a function of the linear attenuation of the various calibration materials at 27.5 keV. The results show that changing the voltage will change the relationship between the measured CT values (HU) and the linear attenuation coefficient (μ) of the material, although the change is slight when changing the tube potential from 40 kVp to 50kVp. Moreover, as expected, the slope of the curve decreases with increasing x-ray potential, corresponding to the lower radiographic contrast obtained at higher photon energies. Finally, as expected, changing the x-ray tube current has no measurable effect on the slope and intercept of the calibration curve, as shown in Fig. 4.7, which plots the image intensity in units of Hounsfield units for different values of tube current as a function of the different calibration materials, as represented by their linear attenuation coefficients at 27.5 keV.

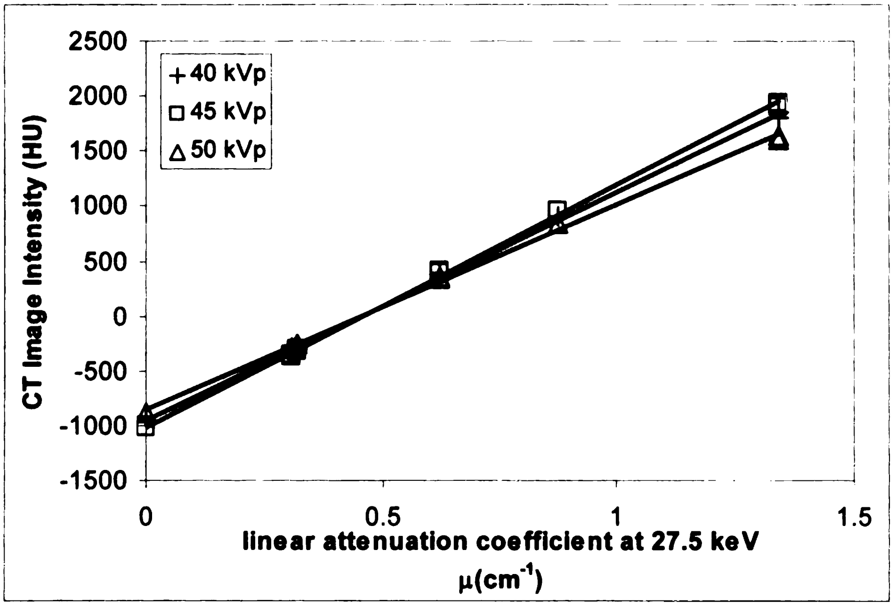

Fig. 4.6: Plot of image intensity as a function of the material linear attenuation coefficient. Data were obtained by imaging the solid calibration phantom at various x-ray tube voltages. The x-ray tube current was held constant at 0.7 mA.

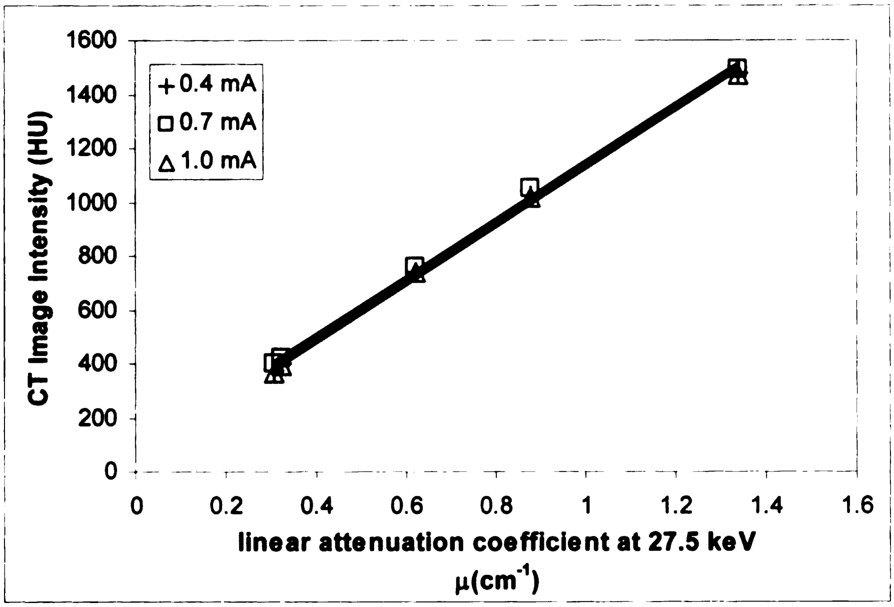

Fig. 4.7: Plot of the image intensity as a function of the material linear attenuation coefficient. Data were acquired using the solid calibration phantom and various values for the x-ray tube current. The tube voltage was held constant at 50 kVp.

4.2.2.2. SPECT measurements

The SPECT data from a uniform phantom were reconstructed first with no attenuation correction, and then with attenuation correction. As expected, the SPECT images obtained without attenuation correction are reconstructed with a characteristic "cupping artifact" in the center of the image (Fig. 4.8). In comparison, the SPECT data reconstructed with attenuation correction demonstrates that attenuation correction effectively compensates for the cupping artifact resulting from photon attenuation. This is shown by Fig. 4.9 below, where the SPECT image reconstructed with attenuation correction does not have decreased image intensity in the center, and more accurately represents the known uniform radionuclide concentration in the cylindrical phantom. This result gives us confidence that the algorithm is correcting for the effect of photon attenuation.

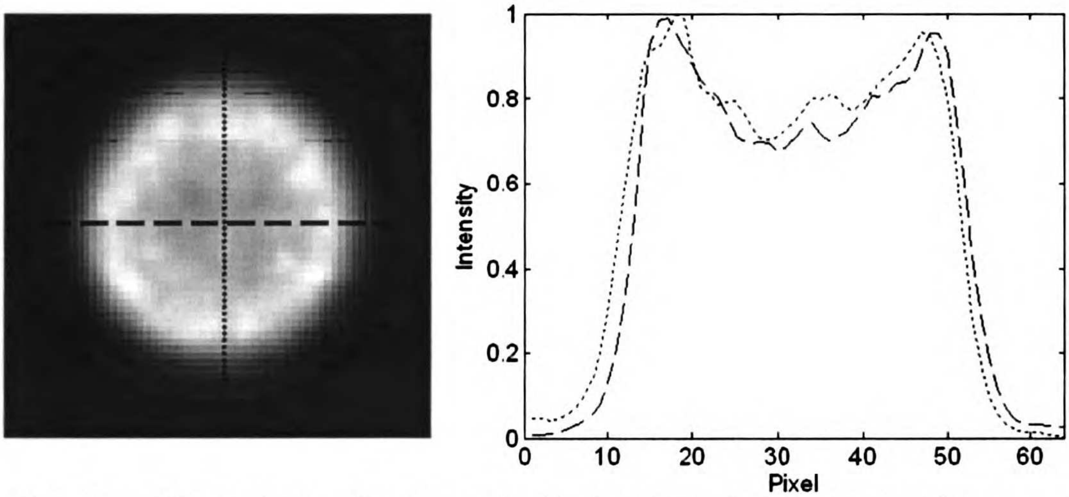

Fig. 4.8: This axial slice through a cylindrical uniform phantom filled with water and ^{125}I-NaI illustrates the cupping artifact associated with photon attenuation.

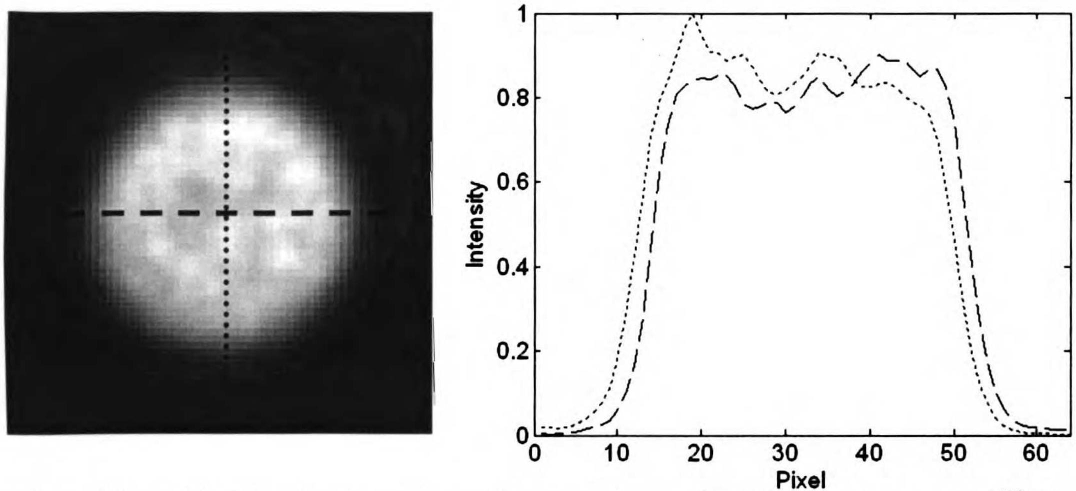

Fig. 4.9: SPECT images of a uniform cylinder filled with water and ^{125}I-NaI reconstructed with attenuation correction. A line profile drawn through the center of the image shows that there is no decrease in image intensity in the center of the image (*i.e.*, the cupping artifact due to photon attenuation has been removed). This demonstrates that photon attenuation correction corrects for the cupping artifact caused by photon attenuation shown in Fig. 4.8.

4.2.3. Discussion

4.2.3.1. CT calibration results

As shown in Fig. 4.7, the CT calibration results were found to be a function of the x-ray tube voltage setting. Therefore, a particular CT calibration is valid for a specific x-ray tube voltage setting, and will not be valid if the voltage is changed, or if the beam filtration is modified. In addition, the calibration should be repeated routinely as an x-ray tube ages, since tungsten from the anode can vaporize and plate onto the output port of the tube, thereby increasing the intrinsic filtration and hardening the beam. Also, as expected, the CT calibration was found to be independent of the x-ray tube current (Fig. 4.6) because this parameter does not affect the output spectrum of the x-ray tube. Therefore, the x-ray tube current can be varied to either increase image quality or decrease radiation dose without any effect on the calibration of the attenuation map.

The CT calibration curve (Fig. 4.5) for iodine-125 shows a linear, rather than a piece-wise linear calibration curve for the linear attenuation coefficient (μ) as a function of calibration material (represented by its CT image value in *HU*). This indicates that the effective photon energy of the x-ray tube when operated at 50 kVp is almost identical to that of the average photon energy of iodine-125.

4.2.3.2. Comparison of phantoms

The solid and liquid phantoms produced similar calibration curves (Fig. 4.5) for radionuclide imaging of iodine-125. However, there is some deviation between calibration curves produced from the phantoms for higher energy radionuclides such as technetium-99m (Fig. 4.4), particularly for calibration materials less dense than water. This difference is due to the fact that all the solid materials, including those less attenuating than water, were described using water and K_2HPO_4 as basis materials, because the materials were originally intended for calibrating measurements of bone density. Conversely, the liquid calibration materials less dense than water only contained low Z materials (*e.g.*, carbon, hydrogen, oxygen). In creating the attenuation map, we assume that materials less dense than water (*i.e.*, density less than 0 HU) are composed of mixtures of fat, soft tissue, and air. Therefore, calibration curve generated using the solid phantom should be applied only to areas with density greater than water.

4.2.3.3. Beam hardening

The generation of the attenuation map depends on consistent CT reconstructions of the calibration phantom, as well as of the object being imaged. For this reason, care must be taken so that the CT images produced with the SPECT-CT system are relatively free of artifacts and errors. In this process, x-ray beam hardening is an important and well known phenomenon in which the x-ray spectrum changes as the x-ray beam passes through an object. The lower energy photons are preferentially absorbed, such that the average photon energy increases. For objects imaged with CT, beam hardening can cause a decrease in the observed attenuation values in the center of the CT image (Fig. 4.10). The effect of beam hardening can also be seen in this study in the CT image value of air when it is measured from a VOI within the phantom, which is about -900 HU (Fig. 4.5), instead of the value of -1000 HU, which is the image value measured for air outside the phantom.

Beam hardening has two effects on the attenuation map. The first effect is that the linear attenuation coefficient near the center of the object being imaged will be underestimated relative to the values at the edge. In the image of a water filled cylinder (diameter = 5 cm), the decrease in image intensity in the center of the image is approximately 10% (Fig. 4.10), which will lead to a corresponding error in the estimation of the linear attenuation coefficient. The second effect of beam hardening is a size dependent shift in the calibration curve, leading to a decrease in the apparent linear attenuation coefficient for larger objects relative to values obtained for small objects.

Therefore, the amount of beam hardening in the object being imaged should be similar to the amount of beam hardening in the calibration phantom.

Although we did not correct for beam hardening, the SPECT images produced with correction by the x-ray derived attenuation maps were relatively uniform and certainly were improved by the attenuation correction process. However, it would still be desirable to apply a beam hardening correction [16-18] so that the reconstructed CT images and attenuation coefficient calibrations will be independent of the variations that result from changes in object size and associated in beam hardening of the x-ray CT data.

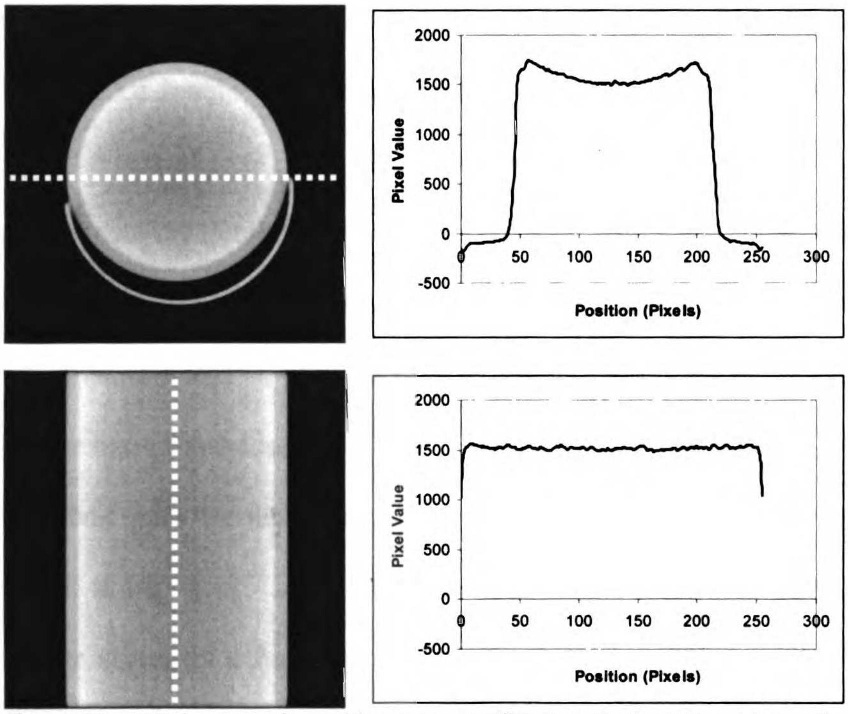
2000
1500
1000
500
0
-500
Pixel Value
0
50
100
150
200
250
300
Position (Pixels)
2000
1500
1000
500
0
-500
Pixel Value
0
50
100
150
200
250
300
Position (Pixels)

Fig. 4.10: CT image of a uniform, water filled cylinder (diameter = 5 cm). An axial slice is shown on the left, a coronal image is shown on the right. These images demonstrate that there is little systematic variation in CT image intensity across the field of view except for a slight decrease in image intensity in the center of the cylinder due to beam hardening.

4.3. Collimator response

The performance of SPECT imaging systems is strongly influenced by the characteristics of the collimator, the design of which is a trade-off between the competing demands of spatial resolution and detection efficiency. A pinhole with a small aperture will have good spatial resolution, but have poor detection efficiency, resulting in data having poor photon statistics, requiring long scan times, requiring increased levels of injected radioactivity, or having some combination of these attributes. Conversely, a pinhole with a large opening will have high detection sensitivity, reducing statistical noise in the image and shortening the acquisition time, but the resulting projection data will be blurred leading to the degradation in the spatial resolution of the reconstructed image. The loss of spatial resolution can make it difficult to separate small features in the images, reduce the detectability of abnormalities, and lead to quantitative errors.

In reconstruction algorithms, the pinhole collimator is often modeled as an ideal pinhole, meaning that all photons pass through an infinitely small aperture. However, the collimator has an aperture with finite diameter, leading to nonideal behavior. In addition, photons can pass through the surrounding collimator material (septal penetration) as illustrated in Fig. 4.11. In addition, the spatial resolution and detection efficiency of the collimator varies as a function of distance from the pinhole. This nonideal collimator behavior leads to a loss in spatial resolution, for which various analytical compensation methods have been proposed [19, 20]. Alternatively, this effect can also be compensated by incorporating a realistic model of the collimator in an iterative reconstruction algorithm [21]. This technique also is known as resolution recovery or geometrical response compensation.

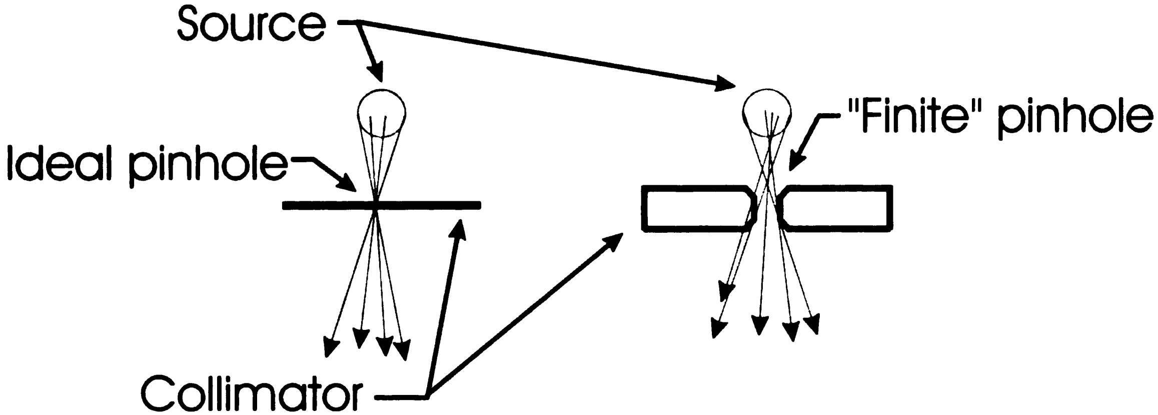

Fig. 4.11: Ideal (left) and realistic (right) collimator response. The ideal collimator response treats the pinhole as an infinitely small hole in an infinitely thin material, with no photons passing through the surrounding material. The realistic pinhole models the finite size of the pinhole opening, as well as photon penetration through the surrounding material.

4.3.1. Methods and Materials

4.3.1.1. Modeling collimator response

As described earlier, the reconstruction algorithm models the behavior of the imaging system in reconstructing the tomographic data. Formally, the mathematical model of the imaging system is performed when the algorithm estimates the expected projection data from a prior estimate of the radionuclide distribution, also called the "forward projection" step. This is in essence a mathematical model of the radionuclide imaging process that can include physical effects such as photon attenuation, scatter radiation, as well as the geometrical response of the collimator. Our reconstruction algorithm includes a ray-driven "projection" process in which the collimator response was modeled by defining multiple rays (rather than a single ray) from each detector pixel directed through the object (*i.e.*, image space), and in which the orientation and weighting of the rays are selected so as to accurately model the geometrical effect of the collimator on the imaging process. Each ray was defined by two points, a starting point on the detector, and one of n^2 possible intermediate point selected from a $n \times n$ grid surrounding the pinhole aperture (Fig. 4.12(left)), where the maximum value of n was determined by a number of different factors, including the amount of computer memory available, and the minimum value was determined by the sampling requirement that the rays not miss any voxels. In practice, we used values of *n* from 12 to 16. The extent of the grid was determined by the pinhole aperture geometry, the photon energy, and the photon attenuation characteristics of the pinhole. Specifically, the maximum lateral extent of the grid is limited to the point where the transmission of photons through the collimator along a line parallel to the pinhole axis is 1%. In this configuration, some of the rays pass directly through the aperture and are not attenuated while other rays pass through and penetrate the material surrounding the aperture and must be weighted to account for attenuation introduced by the collimator material.

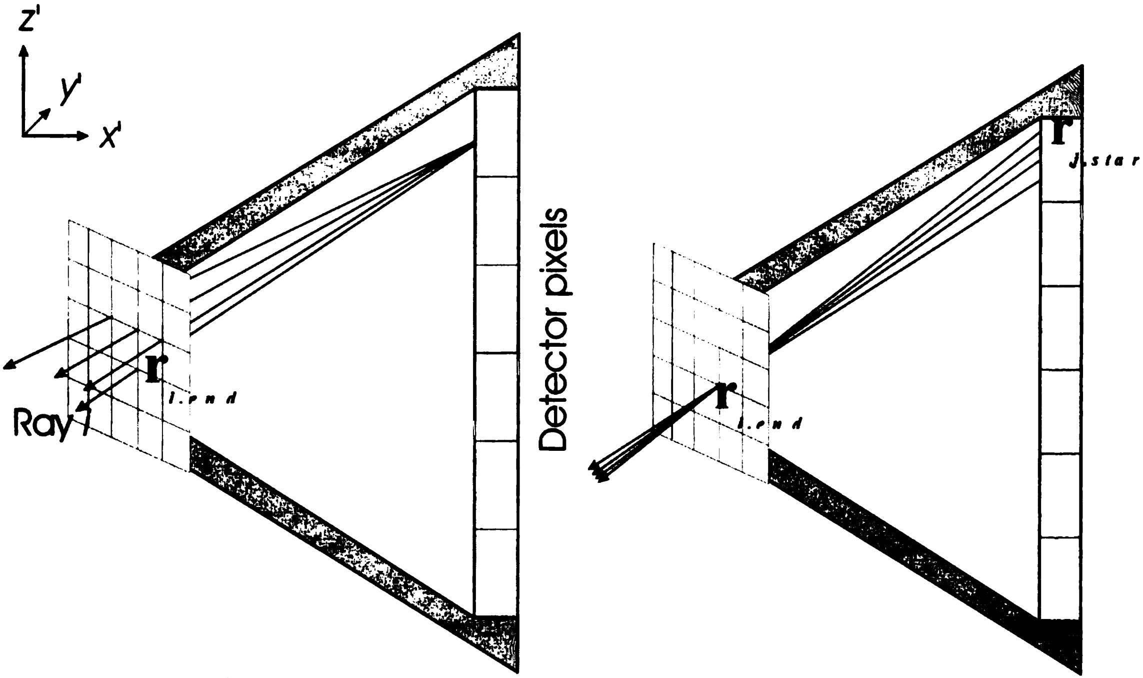

Fig. 4.12: (left): Multiple rays are drawn for each detector pixel, with each ray starting on the detector surface and passing through an intermediate point ($\mathbf{r}_{i,end}$) selected from a grid surrounding the pinhole aperture. (right): The starting point in the pixel and weighting factor for each ray are calculated by sampling multiple starting positions ($\mathbf{r}_{j,start}$) covering the area of the detector pixel. These values are averaged to yield one ray per pixel for each ray intermediate point.

We applied a weight to each ray shown in Fig. 4.12(left) that accounted for shading and partial attenuation the pinhole collimator. This weighting factor was determined first by defining a grid on the detector pixel of origin, to account for the finite size of that pixel, then by defining a set of multiple "raylets" from each point on the grid to a specific point on the grid around the pinhole as shown in Fig. 4.12 (right). The weighting factor for the ray was calculated by averaging the transmission of the raylets through the pinhole and surrounding material. We can define τ_i as the transmission of the i^{th} raylet through the pinhole aperture (*i.e.*, $\tau_i = 1$ if the raylet passes unattenuated through the pinhole, and $0<\tau_i<1$ if the "raylet" partially or fully intercepts the material surrounding the aperture). The weighting factor $W(\mathbf{r}_{i,start}$ to $\mathbf{r}_{i,end})$ for a specific ray from $\mathbf{r}_{i,start}$ to $\mathbf{r}_{i,end}$ shown in Fig. 4.12(right) was then calculated as:

$$W(\mathbf{r}_{i,start}, \mathbf{r}_{i,end}) = \frac{a_o^2}{M} \sum_{j=1}^{M} \frac{\tau_j \cos\gamma_j}{a_j^2} \tag{4.6}$$

where the index j accounts for the raylets, and M represents the total number of raylets for each ray. Finally, γ_j is the angle between the j^{th} raylet and the pixel surface, and a_o represents the distance between the center of the detector and the center of the pixel shown in Fig. 4.12(left), while a_i represents the distance between the pixel and the grid for the j^{th} raylet. The term a_0^2 / a_j^2 adjusts the ray weighting for detector pixels away from the center of the detector, to compensate for the longer pixel to pinhole distance which effectively reduced the solid angle subtended by each ray. The term $\cos\gamma_j$ accounts for the angle with which the ray leaves the pixel surface. The starting location of the i^{th} ray $(x'_{s,i}, y'_{s,i}, z'_{s,i})$ from the pixel was calculated by taking the weighted average of the possible starting locations in the y' and z' directions (Fig. 4.13), where the prime symbol indicates that the positions have been rotated about the z-axis to account for the projection angle. The value of $y'_{s,i}$ is given by the following equation:

$$y'_{s,i} = \frac{\sum_{j=1}^{m} W(\mathbf{r}_{j,start}, \mathbf{r}_{i,end}) y'_{j,start}}{\sum_{j=1}^{m} W(\mathbf{r}_{j,start}, \mathbf{r}_{i,end})} \qquad (4.7)$$

where the index j loops over the possible starting locations in the detector pixel with W used to calculate ray weight given two points on the ray as shown in Fig. 4.12(left). As shown in Fig. 4.12(right), $\mathbf{r}_{j,start}$ is the j^{th} starting position of the ray sampled in the pixel, $\mathbf{r}_{i,end}$ is the pre-selected end location of the ray, and $y'_{j,start}$ is the y' component of $\mathbf{r}_{j,start}$. The x' position of $\mathbf{r}_{\text{j,start}}$ is assumed to be on the detector face, and the x' position of $\mathbf{r}_{\text{i,end}}$ is at the center of the pinhole. The value of $z'_{s,j}$ is calculated in the same way:

$$z'_{s,i} = \frac{\sum_{j=1}^{m} W(\mathbf{r}_{j,start}, \mathbf{r}_{i,end}) z'_{j,start}}{\sum_{j=1}^{m} W(\mathbf{r}_{j,start}, \mathbf{r}_{i,end})} \qquad (4.8)$$

The calculations in Eq. 4.6 through Eq. 4.8 effectively integrate the raylet weights over the surface of each detector pixel to account for the effect of finite pixel size, and then bas the ray starting position on the weighted average of the result.

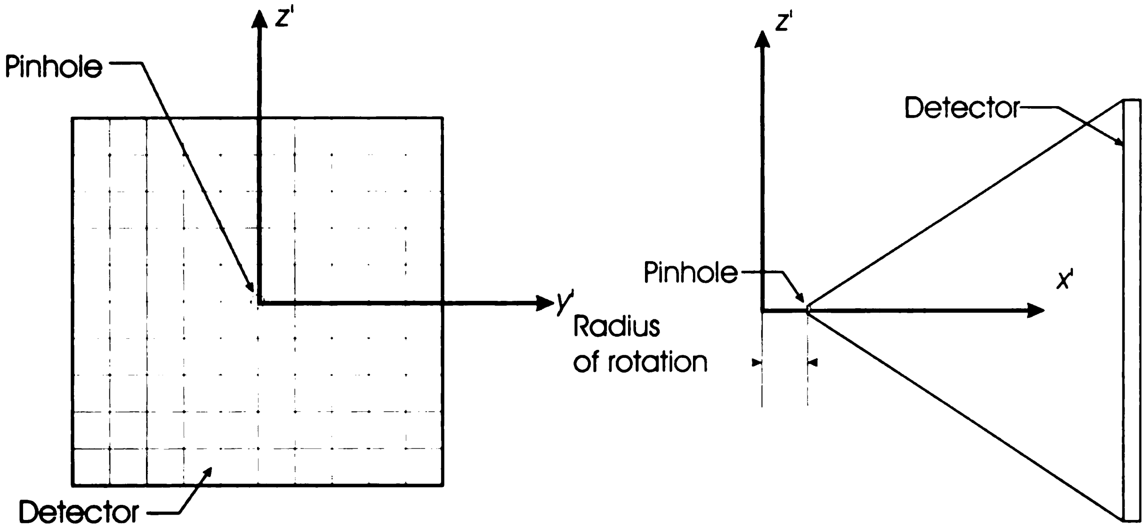

Fig. 4.13: The definition of the coordinate system used in the reconstruction algorithm is shown in this figure. The (x', y', z') coordinates are defined by rotation about the z-axis by the projection angle. In the left figure, the x'-axis extends into the page, and is orthogonal to the plane of the detector. In the drawing on the right, the y'-axis extends into the page.

Once the starting point of the ray was determined, the ray was then propagated through the image matrix (*i.e.*, the object) to mimic the image acquisition process, with information about the ray path through the image matrix stored in computer memory for later use. The process repeated for the other rays and detector pixels, as shown in the flow chart in Fig. 4.14. After the ray paths and weights have been determined, the projection images can be determined by following the rays through the image matrix to numerically calculate the line integral along each ray. The same rays can also be used for backprojection. Details about the projection and backprojection processes can be found in Appendices 2 and 3.

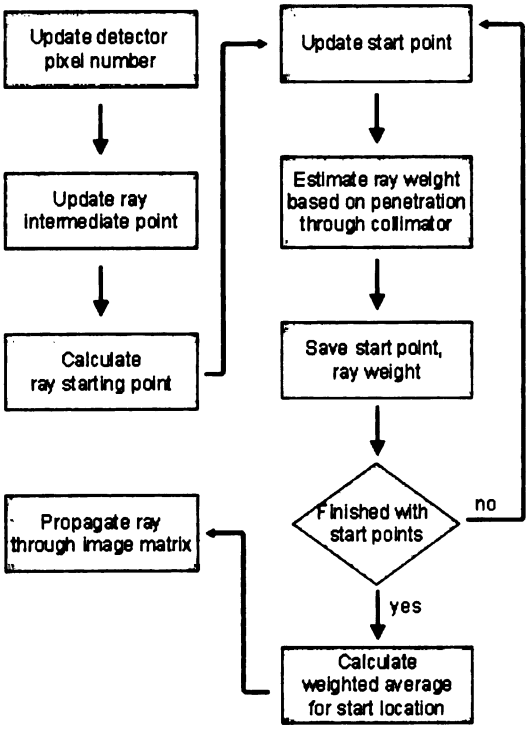
Update detector pixel number
Update ray intermediate point
Calculate ray starting point
Propagate ray through image matrix
Update start point
Estimate ray weight based on penetration through collimator
Save start point, ray weight
Finished with start points
no
yes
Calculate weighted average for start location

Fig. 4.14: Flow chart describing the process for determining the two points which define the path of a ray.

4.3.1.2. Monte Carlo simulations

In order to test and evaluate the reconstruction algorithm described in the previous section, we generated radionuclide projection data using Monte Carlo simulation. In particular, Monte Carlo simulations are useful because they can be used to model stochastic processes such as photon absorption and scatter in the object, collimator, and detector, and allow precise and repeatable control of source geometry and location, which is otherwise difficult given the small length scales encountered in small animal imaging. In addition, simulations can model useful ideal cases, such as a point source, which can not be physically created. The Monte Carlo simulations in this thesis were performed using the GATE software package(Geant4 Application for Tomographic Emission) [22, 23]. This package was created by the OpenGATE collaboration, and is an application developed for PET and SPECT based on the Geant4 libraries, which are general purpose

Monte Carlo simulation codes used in a wide variety of physics applications such as high energy, space and radiation, and nuclear physics. The simulations in this section were performed to study the collimator response and to verify the accuracy of the ray-tracing model used in the projector/backprojector.

The Monte Carlo simulation performed with GATE followed photons emitted by the radionuclide in the object as they passed through the pinhole and are captured by the detector. Both primary and scattered photons reaching the detector were recorded in terms of their (x,y) locations on the detector as well as their individual energies. The simulations used a simplified model of the X-SPECT imaging geometry (Fig. 4.15). The pinhole aperture was accurately modeled in terms of the dimensions and angles used to construct the "keel-edge" pinhole aperture (Fig. 4.15); however, the collimator "cone" used to support the pinhole in front of the detector was replaced with a tungsten disk positioned in space in front of the detector to simplify the simulation geometry. The distance from the front surface of the detector to the center of the pinhole was 9 cm to mimic the pinhole-detector distance on the X-SPECT system. The detector was modeled as a single, rectangular crystal of NaI(Tl), with dimensions of 12.5×12.5 cm and a thickness of 6 mm, surrounded on the sides by a rectangular lead shield. The "energy blurring module" in GATE was used to add realistic energy resolution to the data, and the simulated projection data were recorded in a 54×54 matrix that modeled the pixelation of the detector in the X-SPECT system. The energy resolution of the simulated system was based on the value of 11.3±1.4 %FWHM at 140 keV published by the manufacturer [24]. The energy resolution was adjusted appropriately for the different isotopes by scaling the energy resolution at 140 keV by $\sqrt{\frac{140\,\text{keV}}{E}}$, where E is the photon energy in keV. This correction assumes that the energy resolution is proportion to the standard deviation of the Poisson-distributed number of scintillation photons produced by each gamma ray captured by the detector, that in turn is proportion to the energy E of the captured gamma ray. .

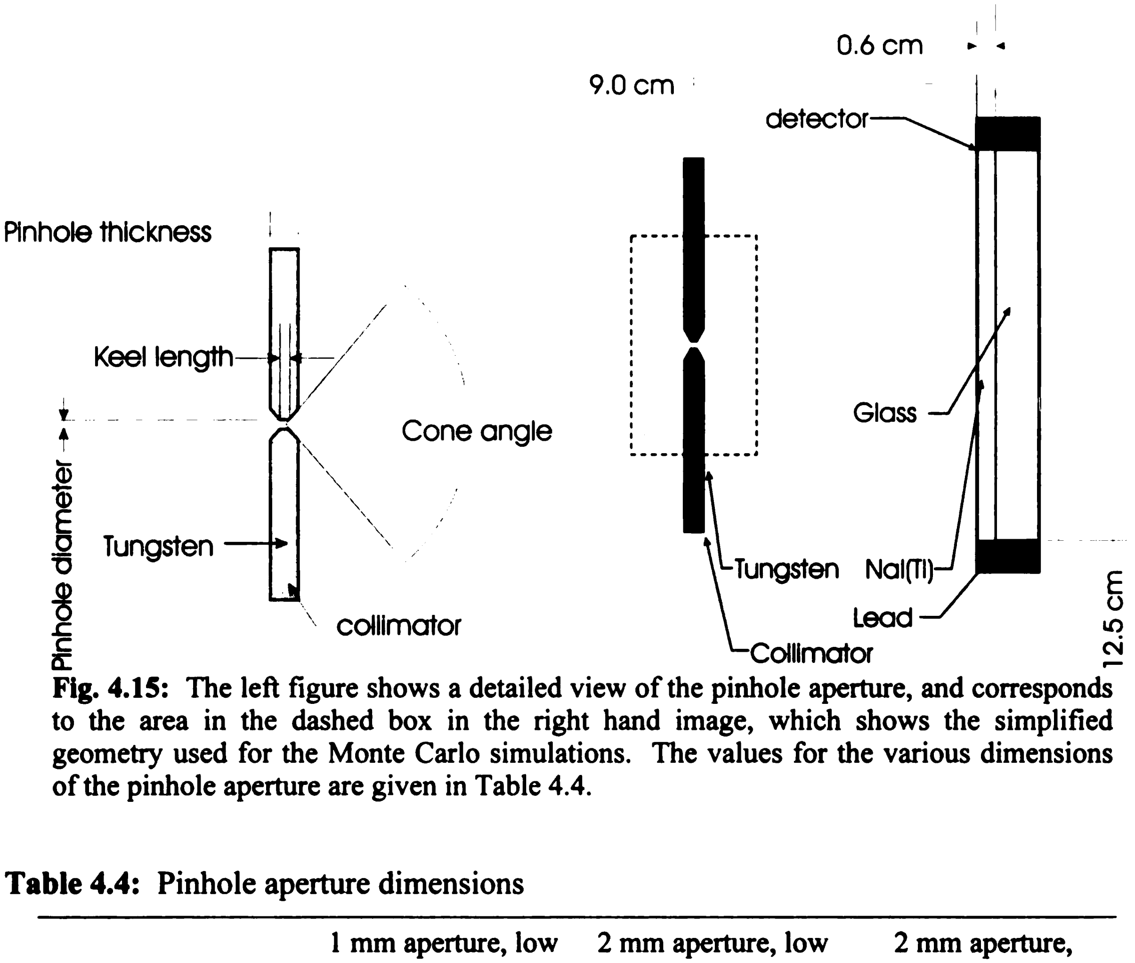
Pinhole thickness
Keel length
Pinhole diameter
Tungsten
collimator
Cone angle
9.0 cm
0.6 cm
detector
Glass
Tungsten
NaI(Tl)
Lead
Collimator
12.5 cm

Fig. 4.15: The left figure shows a detailed view of the pinhole aperture, and corresponds to the area in the dashed box in the right hand image, which shows the simplified geometry used for the Monte Carlo simulations. The values for the various dimensions of the pinhole aperture are given in Table 4.4.

Table 4.4: Pinhole aperture dimensions

	1 mm aperture, low energy	2 mm aperture, low energy	2 mm aperture, medium energy
Pinhole thickness	6.4 mm	6.4 mm	23 mm
Pinhole diameter	1 mm	2 mm	2 mm
Keel length	0.8 mm	1.8 mm	1.8 mm
Cone angle	90°	90°	90°

4.3.1.3. Testing of the projector

The behavior of the projector was characterized using numerical phantoms consisting of a source placed in different locations. A "point" source was modeled as a small cube, with dimensions of $0.7\times0.7\times0.7$ mm^3 ($2\times2\times2$ voxels). The first step was to measure the sensitivity as a function of distance from 3-6 cm between the point source and the pinhole aperture. The second test measured the relative sensitivity of the collimator, expressed in terms of the relative intensity in the projection image as a function of angle, for a simulated point source placed at difference lateral positions across the field of view. Finally, the point spread functions for sources at different locations and calculated using the ray-driven projector (Section 4.3.2.1) were compared with results generated with Monte Carlo simulations.

4.3.1.4. SPECT measurements

Phantom studies were performed experimentally, and the data were reconstructed to determine how modeling the collimator response in the reconstruction algorithm affected the spatial resolution in the resulting tomograms. The spatial resolution measurements were performed using both a hot rod phantom with rods 1.2-1.6 mm in diameter and an edge phantom (Chapter 2, Fig. 2.15). The hot rod phantom was filled with ^{99m}Tc-NaTcO$_4$, and then imaged with the X-SPECT scanner using the radionuclide detector fitted with a pinhole collimator having a 2 mm diameter aperture. Projection data were acquired at 64 angles over 360°, with approximately 200,000 counts per angular view. The acquisition was repeated using the 1 mm pinhole aperture using the same parameters, with only 90,000 counts per angular view, due to the reduced detection efficiency of the smaller pinhole opening. Data were also acquired using an edge phantom to provide an independent measure of spatial resolution. The edge phantom was filled with approximately 300 MBq of ^{99m}Tc-NaTcO$_4$, and then scanned with both 1 mm and 2 mm pinholes using a nominal radius of rotation of 4.0 cm. A total of 64 projections over 360° (40 s/projection) were acquired using each pinhole. Data from both phantoms were reconstructed using an OS-EM algorithm with corrections for collimator response as described in Section 4.3.2.1. For comparison, data were also reconstructed using an OS-EM algorithm that modeled the collimator as an ideal pinhole, and the resulting images were visually inspected to evaluate the effect of collimator response on the quality of reconstructed images.

For the edge phantom, spatial resolution was calculated using the procedure described in Chapter 2. In addition, the image noise was estimated by calculating the standard deviation of the image voxel values within a 5×5×3 voxel volume of interest in a uniform region within the image of the edge phantom, and then dividing the standard deviation by the mean voxel value to yield the relative standard deviation. Results were calculated for data reconstructed with and without collimator response, and measured for the 1 and 2 mm pinholes.

4.3.2. Results

This section first presents simulation results demonstrating that the projector is correctly modeling the behavior of the pinhole aperture, and then uses experimental results to demonstrate the improved image quality obtained when the collimator behavior is correctly modeled in the reconstruction algorithm.

4.3.2.1. Test of the projector model

From Chapter 2, we know that the geometric sensitivity g of the pinhole collimator is proportional to $1/b^2$, where b is the distance between the source and the pinhole (Fig. 2.13). In addition, the geometric sensitivity g is proportional to the square of the effective diameter (d_{eff}) of the pinhole aperture (Eq. 2.14), and as expressed in Eq. 2.16, varies in proportion to $cos^3\theta$, where θ is the angle between the line normal to the plane of the pinhole and the ray passing through the point of interest, *i.e.*,

$$g = \frac{d_{eff}^2 \cos^3\theta}{16b^2} \tag{2.16}$$

We therefore simulated projection data obtained using numerical phantoms and the forward projector described in Section 4.3.2.1, and compared the characteristics of the resulting simulations against the theoretical characteristics expressed in Eq. 2.16. We first calculated the detection sensitivity of the projector model as a function of object-pinhole distance (b), and fit the data to a function of the form $1/b^n$ (Fig. 4.16), for which we obtained a value n=2.003, which agrees with the theoretical value of the exponent, n=2 (Eq. 2.15). This demonstrates the expected inverse square dependence of the collimator sensitivity as a function of object-pinhole distance. We also plotted the collimator sensitivity as a function of object angle θ (Fig. 4.17) obtained from both the Monte Carlo simulations and the projector model (Section 4.3.2.1) as well as from the Monte Carlo simulations (Section 4.3.2.2). In addition, we plotted a curve proportion to $\cos^3\theta$, as predicted theoretically by Eq. 2.15. The results of the both the Monte Carlo simulation and the projector model decrease in sensitivity with angle faster than that of an ideal knife edge pinhole (Eq. 2.15). This is the consistent with the expected result for a keel edge pinhole, which is designed to minimize septal penetration, and thus optimize spatial resolution, at the cost of decreased acceptance angle and detection efficiency in regions lying off the central axis of the pinhole [25, 26].

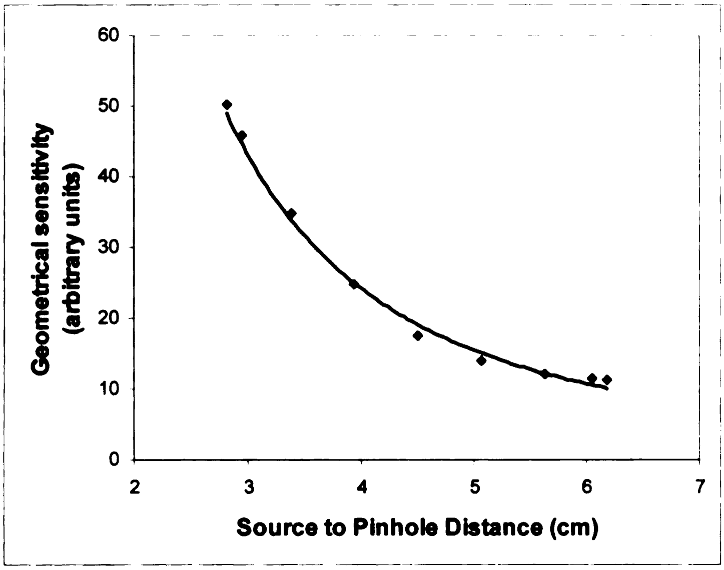

Fig. 4.16: Test of sensitivity as a function of distance for the multi-ray projector. A line fit to the points has the equation of 388 $r^{-2.003}$, which demonstrates the expected relation between the source to pinhole distance r and the geometric sensitivity.

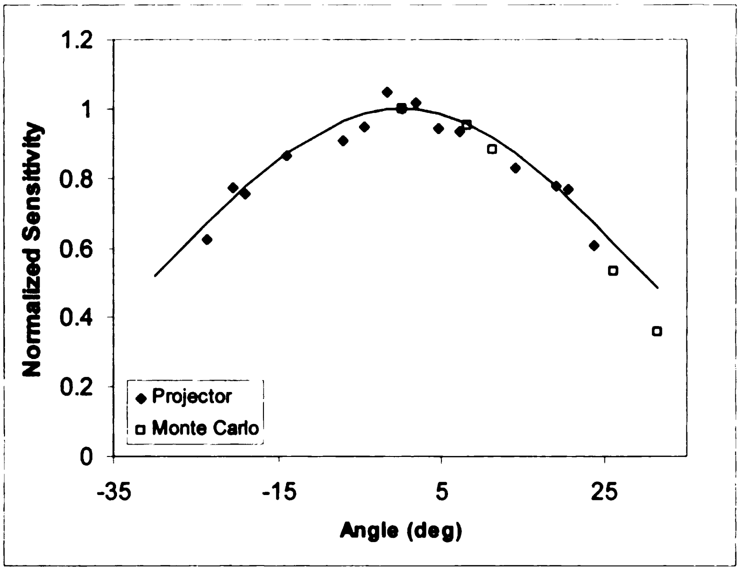

Fig. 4.17: Projection values as a function of angle. The angular sensitivity falls off faster than $\cos^3\phi$ (line), which is the expected result for a keel edged pinhole aperture. The Monte Carlo simulation results are shown as for comparison.

The simulated point spread functions at various locations are shown below in Fig. 4.18 and Fig. 4.19, and the results show that the projector accurately models the width and the location of the point spread function. However, the projector does not perfectly model the edges of the point spread function. Later, this was found to be due to the depth of interaction (DOI) effect, also known as parallax error, which was described in Chapter 3, and which will be discussed in more detail in Section 4.3.4.1 below.

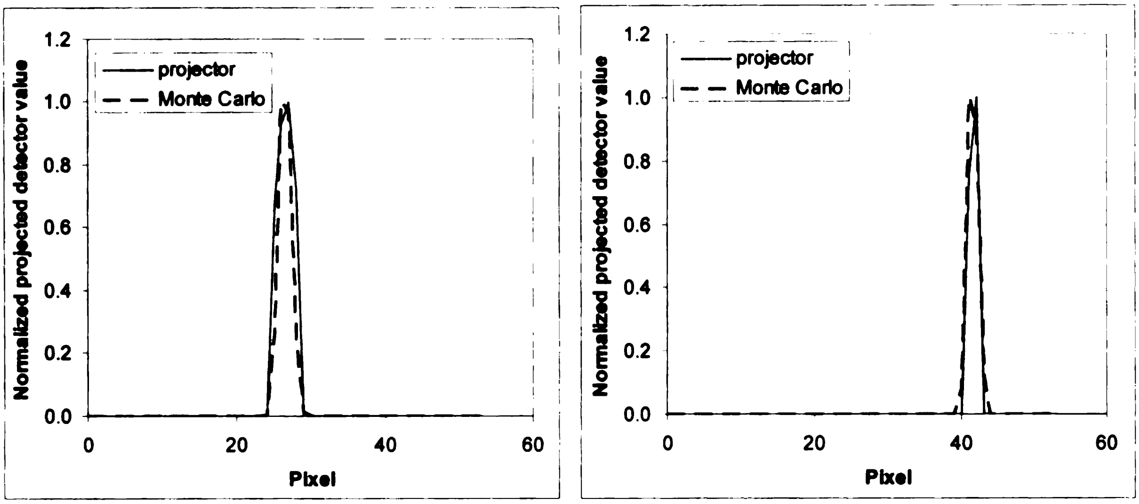

Fig. 4.18: Line profiles through the point spread function for the 2 mm pinhole collimator generated using Monte Carlo simulation compared with PSF created from numerical simulations. The data shown here represent a point at the center of the field of view (left), and one towards the edge of the field of view (right). The full widths at half maximum of the point spread functions in the left image are 7.9 mm and 11.7 mm for the projector and Monte Carlo results, respectively. In the right image, the FWHM values are 4.0 mm and 4.5 mm for the projector and Monte Carol results, respectively.

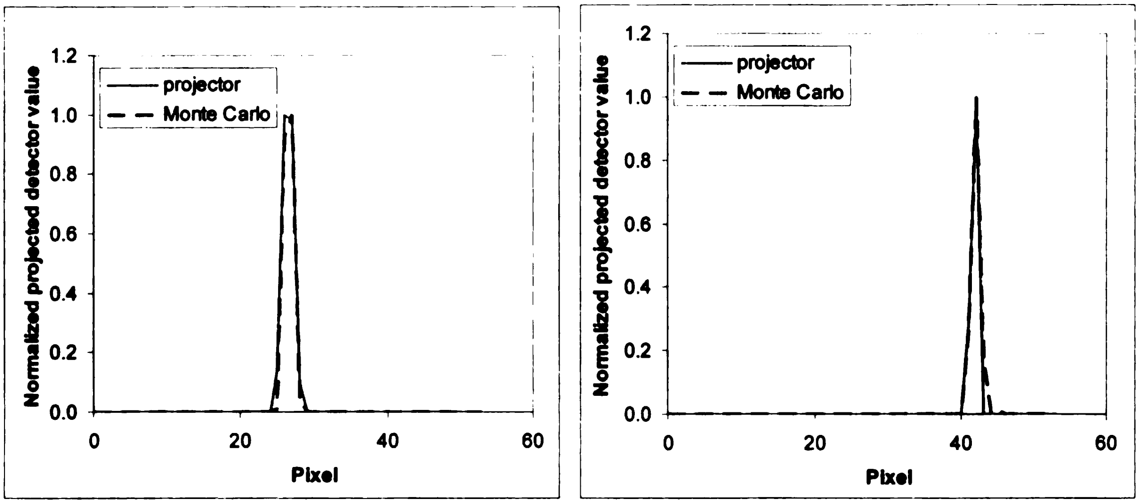

Fig. 4.19: Line profiles through the point spread function (PSF) for the 1 mm pinhole collimator generated using Monte Carlo simulations compared with PSF created from numerical simulations. The data shown here represent a point at the center of the field of view on the left, and one towards the edge of the field of view on the right. The FWHM of the PSF in the left image is 4.7 mm for the projector and 4.3 mm for the Monte Carlo. The FWHM values in the right image are 2.6 mm and 2.8 mm for the projector and Monte Carlo simulation results, respectively.

4.3.2.2. SPECT measurements

The image quality (*e.g.*, spatial resolution and noise) of SPECT images depends on several factors, including the detector performance, collimator design, acquisition protocol, and the algorithm used to reconstruct the data. The following results show the effect of modeling the collimator response in the reconstruction algorithm on SPECT images obtained from experimentally measured data. The results in Fig. 4.20 show images of the hot rod phantom reconstructed using OS-EM with collimator response. These images demonstrate improved spatial resolution at the cost of needing more iterations (*i.e.*, more computational time) by the reconstruction algorithm, which is a known property of reconstruction algorithms which model the collimator response [27]. In comparison, data reconstructed without collimator response for many subsets do not show improved spatial resolution after 5 iterations. The improvement in spatial resolution is particularly improved with the larger pinhole apertures (Fig. 4.21), because the larger pinholes deviate more from ideal, and thus accurately modeling their behavior will have a larger impact on the reconstructed image.

The edge phantom data gave results for the full-width-half-maximum that were consistently slightly lower better the results that are obtained by visually interpreting the test pattern. The noise is plotted as a function of spatial resolution in Fig. 4.22 for various combinations of reconstruction algorithms and pinhole sizes. The noise and spatial resolution were varied by modifying the number of iterations. These results demonstrate that the trade-off between noise and spatial resolution can be adjusted by changing the number of iterations in the reconstruction algorithm. The results also show that modeling the collimator response in the algorithm will improve both spatial resolution and noise.

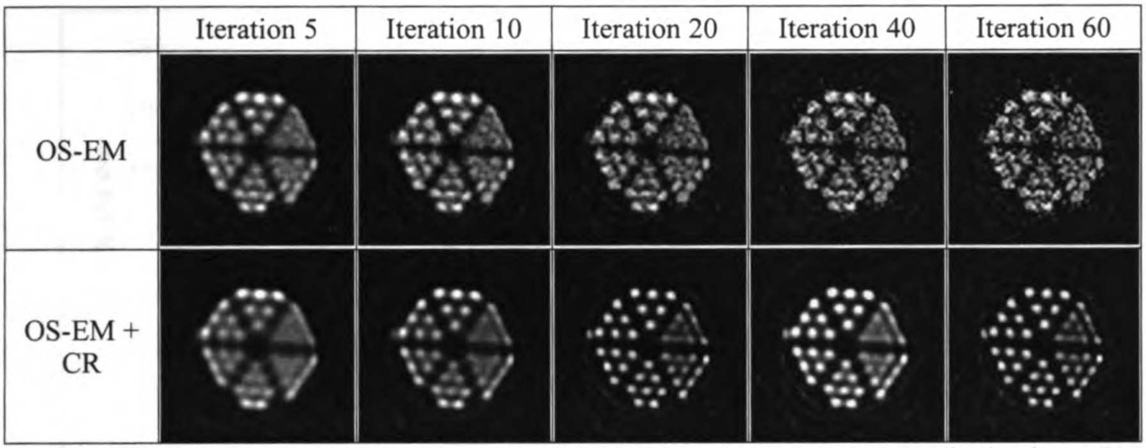
Iteration 5
Iteration 10
Iteration 20
Iteration 40
Iteration 60
OS-EM
OS-EM + CR

Fig. 4.20: Image resolution versus iteration (8 subsets). Data were acquired using a 2 mm pinhole with a radius of rotation of 3.5 cm and the test pattern shown in Fig. 2.15. Data were reconstructed using OS-EM with 8 subsets, and iteration 5, 10, 20, 40, 60 are shown. The top row shows results reconstructed without collimator response, and the bottom row shows results reconstructed with collimator response. Note that images with collimator response require more iterations to converge.

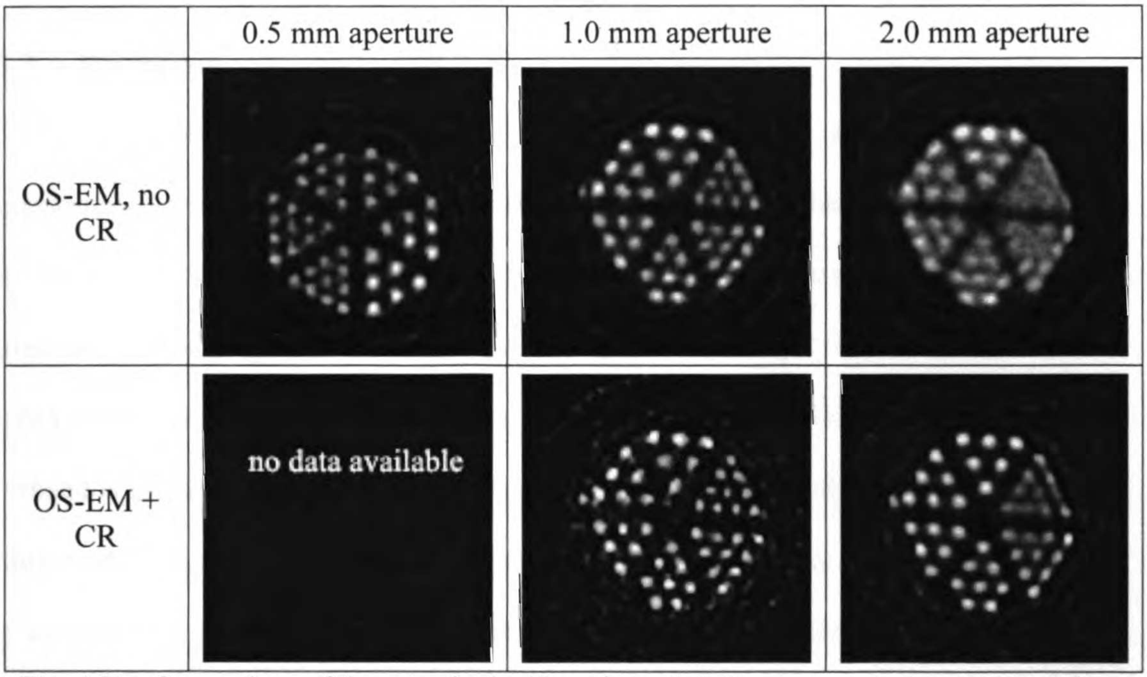
0.5 mm aperture
1.0 mm aperture
2.0 mm aperture
OS-EM, no CR
OS-EM + CR
no data available

Fig. 4.21: Comparison of data acquired with various pinhole apertures and reconstructed with different algorithms. Data acquired at ROR = 3.5 cm and the test pattern shown in Fig. 2.15. Note that the image acquired with the 0.5 mm aperture is oriented differently than the other data because of the placement of the phantom in the scanner was different. Data without collimator response were reconstructed using 5 iterations (8 subsets) and data with collimator response were reconstructed using 50 iterations (8 subsets).

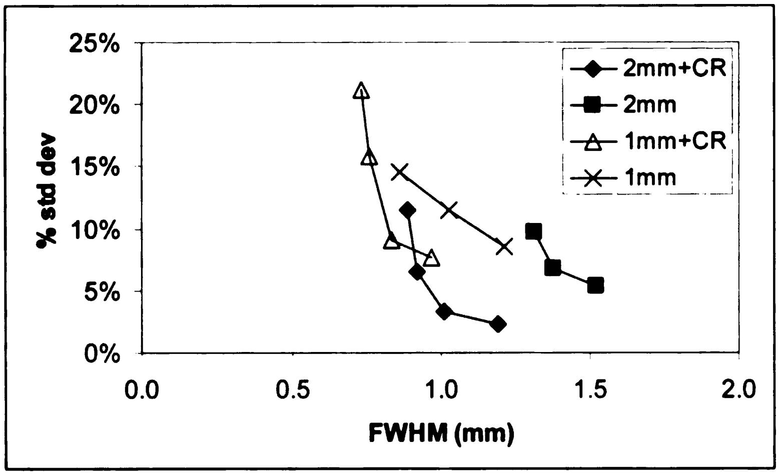

Fig. 4.22: Plot of the noise as a function spatial resolution for data acquired using 1 mm and 2 mm pinholes, and reconstructed using OSEM with and without collimator response. The trade-off between spatial resolution and noise was accomplished by varying the number of iterations used in reconstructing the image. Iterations 3, 5, 10, and 20 were plotted for data reconstructed with collimator response. Iterations 2, 3, and 5 were plotted for data reconstructed without collimator response.

4.3.3. Discussion

One cost of modeling the depth dependent collimator response is increased reconstruction time. This is due to the increased number of iterations needed to realize improved spatial resolution, as well as the increased computation complexity required to realistically modeling the behavior of the pinhole. The reconstruction time is approximately proportional to the number of iterations (approximately 5 to 10 minutes overhead is required to pre-calculate ray paths and estimate the normalization matrix). In addition, the reconstruction time is also a function of the number of rays used to model the collimator. Depending on the specific details (*i.e.*, number of projection angles, number of iterations, image matrix size), reconstruction time can be increased from approximately 20 minutes (no collimator response, 5 iterations) to approximately 2 hours (collimator response, 20 iterations) on a 1.8 GHz Pentium 4, using a matrix size of $(64)^3$. The time needed to reconstruct a test case (54×54×64 projection matrix size, $(64)^3$ output size) using different algorithms on a 1.8 GHz personal computer are shown in Table 4.5.

Given the decreasing cost of computer memory and the increasing availability of multi-processor computers, the increased computational complexity should not prevent the use of a reconstruction algorithm that models the collimator response.

Table 4.5: Reconstruction time for a $(64)^3$ image using a personal computer

Algorithm	Rays / pixel	Iterations (subsets)	Reconstruction time (minutes)
OSEM, no CR	49	5 (8)	11
OSEM, with CR	100	5 (8)	21
OSEM, with CR	100	20 (8)	74
OSEM, with CR	256	20 (8)	134

4.4. Depth of interaction

In pinhole imaging, photons can reach the detector with a trajectory that is not normal to the detector surface. This can result in blurring of the recorded image through the depth of interaction (DOI) effect (also known as parallax) because the photons interact at a finite depth within the scintillator crystal, rather than at the scintillator surface,, which affects the position of interaction recorded by the detector. The magnitude of this effect increases when the energy of the incoming photon is increased or the photons enter the detector at a more oblique angle.

The depth of interaction effect results photons interacting at varying depths within the scintillator crystal. When the photons strike the detector at an oblique angle, the interaction of the photons with the scintillator may be recorded in multiple detector pixels. This effect is not a significant factor in clinical SPECT imaging which is normally performed with parallel hole collimation where the photons are received normal to the detector surface. However, because small animal data are acquired using pinhole collimation and require high resolution images, the loss of image quality from the depth of interaction effect may become significant.

4.4.1. Methods

We first describe a method that models the depth of interaction effect in the reconstruction algorithm by modifying the result given by the ray-driven projector described earlier in this chapter. We then demonstrate the effect of DOI on the point spread function, and finally use the experimentally acquired SPECT data of a hot rod phantom to demonstrate the effect of modeling depth of interaction on reconstructed images.

4.4.1.1. Modeling depth of interaction effect

We modeled the depth of interaction effect using an algorithm applied to projection data estimated using a forward projector such as the one described in Section 4.3.2.1. The algorithm used simple physical model of the process, in which the scintillator was divided into 50 slices (Fig. 4.23). A line passing through the center of the pinhole is drawn through the center of a detector pixel. The algorithm starts at the top surface of the detector, and steps through stacked "slices" of the scintillator. At each slice, we can calculate the number Δn of photons deposited in thickness Δx of the scintillator slice as:

$$\frac{\Delta n}{n} = -\mu \Delta x \qquad (4.9)$$

where n is the number of photons entering the scintillator slice, and μ is the linear attenuation coefficient of the scintillator. The value of n for the first slice is obtained from the results of the ray-driven projector. The number of deposited photons is added to the detector bin corresponding to the center of the line segment traversing the slice, and then subtracted from the incident number of photons to calculate the number of photons entering the following slice. The process is repeated until either all photons have been absorbed (*i.e.*, n = 0), or the ray has traversed all the slices forming the scintillator. The algorithm performs this process for all the detector elements, with the final result being a projection image that accounts for the effect of depth of interaction on the data.

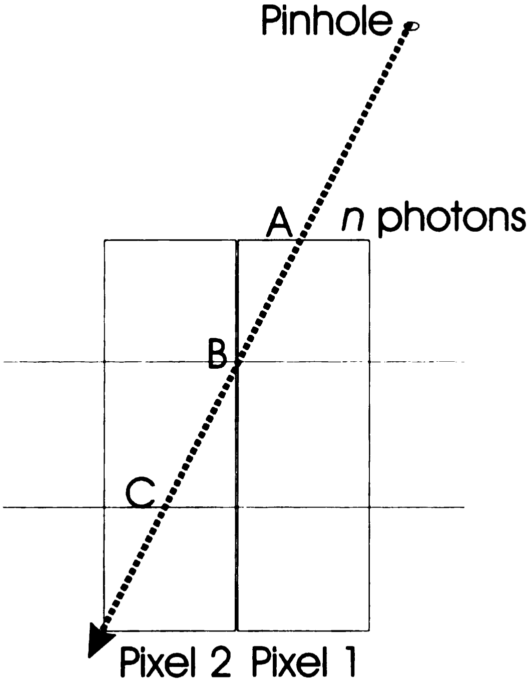

Fig. 4.23: Schematic diagram of the method used to add blurring due to the depth of interaction (DOI) effect to simulated projection data. The scintillator crystal is divided into thin slices, and a line is drawn from the pinhole to the center of a pixel (point A). The number of incident photons *n* is taken from the original result (without DOI). The number of photons deposited in the first slice (and thus in pixel 1) is proportional to *n*, the distance between points *A* and *B*, and the linear attenuation coefficient of the scintillator material. The number of photons is updated, and the process is repeated for the scintillator volume between points *B* and *C*.

4.4.1.2. Testing of DOI model

The DOI model was tested by comparing the analytically derived results with the results of the Monte Carlo simulations. A point spread function was estimated using the ray-driven forward projector with a numerical phantom as described in Section 4.3.2.3. The estimated projection data obtained with the ray-driven projector was modified by blurring the image with the depth of interaction model,and the final point spread function was compared with the result obtained using Monte Carlo simulation described in Section 4.3.2.2.

4.4.1.3. Application to experimental data

The effect of depth of interaction modeling on reconstructed data was experimentally assessed using SPECT projection data acquired using the hot rod phantom and the 2 mm pinhole aperture, as described in Section 4.3.3.2. The data were reconstructed using 50 iterations (8 subsets) of the OS-EM with collimator response, with and without depth of interaction modeling.

4.4.2. Results

4.4.2.1. Comparison with simulation results

We previously found that the point spread function generated by the ray-driven projector did not exactly match the point spread function obtained using Monte Carlo simulations, particularly for point sources located away from the center axis of the gamma camera. After the projector program was modified to include the depth of interaction effect, the resulting point spread function is a much closer match to the result predicted by the Monte Carlo simulation (Fig. 4.24). The inclusion of the DOI effect shifts the location of the maximum by 1 pixel (2.2 mm), and changes the shape of the peak.

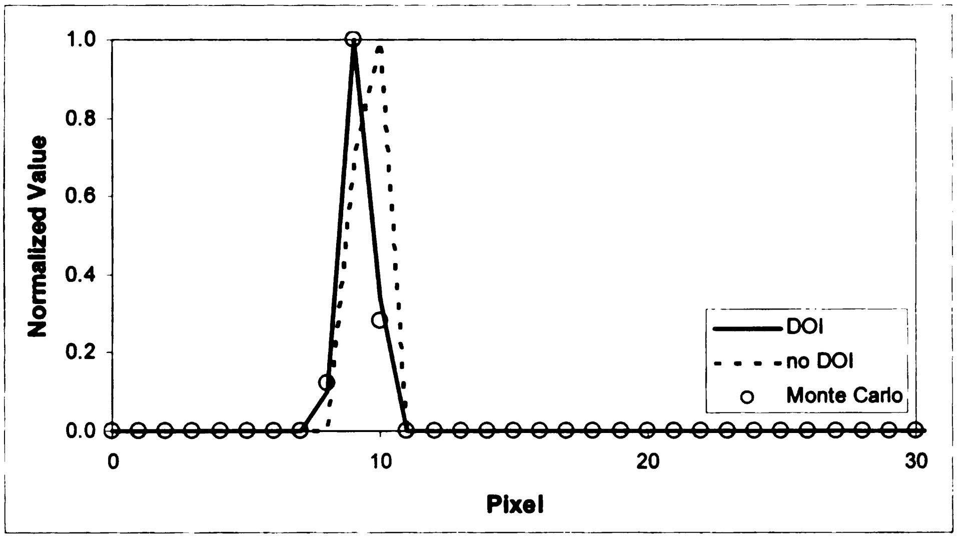

Fig. 4.24: Line profiles through the point spread function, where the source is located 22 degrees off the central axis. The point spread functions were generated using the ray-driven projector both with and without the depth of interaction effect, simulating the projection of a technetium-99m point source located 23° off of the normal axis through a 1 mm pinhole. The results including the DOI effect better matched the results obtained with Monte Carlo simulations.

4.4.2.2. Experimental results

We found that when imaging technetium-99m using the pinhole collimator with the X-SPECT scanner, the depth of interaction effect degrades the images slightly, particularly near the edge of the field of view, and can be compensated by modeling the effect in the reconstruction algorithm (Fig. 4.25). With technetium-99m the effect was observed to be very subtle, but the DOI effect is expected to be larger when imaging higher energy isotopes such as indium-111. In addition, the detector pixel size was fairly large (2.2 mm), which would also reduce the effect of this error on image quality. Other factors which are expected to increase the effect of DOI errors include larger angles of incidence of the incoming photons, and scintillator (or detector) materials with lower linear attenuation coefficient.

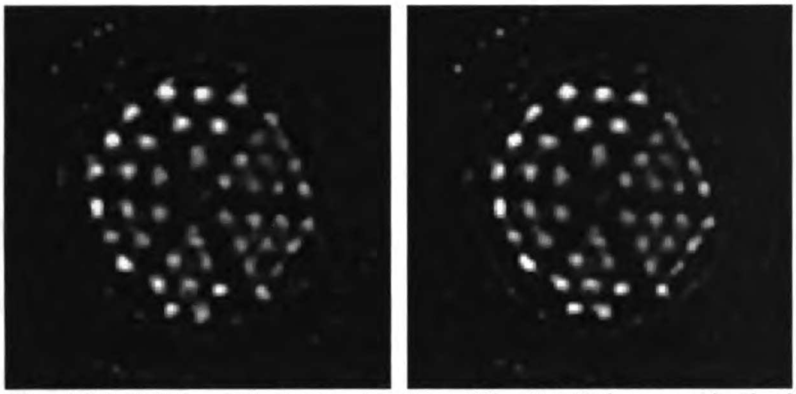

Fig. 4.25: High resolution test pattern (Fig. 2.15) data acquired with a 2 mm pinhole, and reconstructed using OSEM with collimator response. The "hot rods" range in size from 1.2 – 1.7 mm in diameter. The image on the right was reconstructed using OSEM with both collimator response and a model for the depth of interaction effect, and exhibits slightly sharper images of the rods near the edge of the field of view. Both images were reconstructed using 120 iterations (8 subsets).

4.5. Scatter correction

As mentioned previously, photons emitted by the radionuclide tracer within the body can interact with surrounding tissues in various ways. If the photon interacts through a photoelectric interaction, it is absorbed and as a result does not emerge from the body and is not detected. However, if a photon interacts with matter through Rayleigh or Compton scatter, it is still possible for it to reach the gamma camera and be detected. If the photon has lost energy through its interaction with matter, it is then possible for the gamma camera to distinguish the scattered photon from a "primary", or unscattered, photon, and the scattered photon can be rejected electronically so that it does not contribute to the final image. However, it is also possible for the scattered photon to have an energy that lies within the acceptance window of the gamma camera, in which case the scattered photon can not be distinguished from a primary photon. This leads to an error in the formation of the image, because the trajectory of the scattered photon has been altered by the scattering event.

In clinical imaging, scatter radiation degrades the quality of the reconstructed images. This primarily results in a reduction of contrast in the recorded images, arising from the distribution of events in areas outside of the actual distribution of radioactivity in the body. As with photon attenuation, the magnitude of the effect depends on the composition and distribution of tissue, and thus scatter is expected to be less important in small animal imaging than in human imaging.

Scatter correction algorithms can be divided into four broad categories [28]. The first category attempts to compensate for scatter by applying deconvolution to the reconstructed image [29]. The second and third categories remove scatter from the projection data prior to reconstruction, using either data from transmission measurement data or obtained from the energy spectrum of the detected photons [29, 30]. The last category of algorithms attempts to model photon scatter in the reconstruction algorithm [31-33]. The first method (deconvolution of reconstructed images) has limitations because the blurring due to scatter is not invariant throughout the image. Methods using analysis of the energy spectra to remove scatter from projections have been shown to be quite accurate, but may not be applicable to imaging iodine-125, where the photons have relatively low energy resulting in poor energy resolution performance with most gamma camera designs. Because we have anatomical information from coregistered CT images, the last approach (iterative reconstruction with scatter modeling) was selected as the best candidate for the measurements pursued in this dissertation project.

4.5.1. Methods

4.5.1.1. Determination of scatter-to-primary ratio

Scatter, like photon absorption, is a function of the size, shape, chemical composition, and physical density of the object, as well as the energy of the incident photon. In human imaging with technetium-99m, the scatter-to-primary ratio (the number of scattered photons detected divided by the number of unscattered photons detected) is estimated to be approximately 45% (simulation results obtained using a 20% energy window and energy resolution of 10% FWHM) [34]. However, the photon scatter in small animal imaging has not been extensively studied. Therefore, we first performed a Monte Carlo simulation using GATE in order to estimate the scatter-to-primary ratio in small animal imaging for both technetium-99m and iodine-125, to estimate the magnitude of scatter in small animal imaging. These two isotopes were selected because their photon energies bracket the lower range of photon energies commonly encountered in SPECT imaging. In the simulation, a spherical source (2 mm radius, 50000 Bq) was placed at the center of a cylinder of water. The water cylinder had a height of 3 cm, with its radius varied between 0 and 2.5 cm to assess the effect of the cylinder dimensions on the amount of scatter. The simulated imaging geometry was defined as described in the previous section (see Fig. 4.15). The detector energy resolution was 26% FWHM and 12% FWHM for iodine-125 and technetium-99m, respectively, based on published values for the X-SPECT detector energy resolution for technetium-99m [24]. The energy windows were defined from 10-50 keV for iodine-125, and 126-161 keV for technetium-99m, which are the windows used for performing experimental measurements with the X-SPECT scanner. A total of 64 projections (30 s/proj) were generated for each simulation. The simulations were used to model the SPECT imaging process in generating projection data. The results were used to estimate the amount of scatter in small animal SPECT projection data.

4.5.1.2. Model of scatter

In order to correct for the effects of photon scatter, an analytical model of the scatter was incorporated into the OS-EM reconstruction algorithm that also modeled photon attenuation and collimator response. Photon scatter is modeled in the reconstruction algorithm by using the estimated radionuclide distribution in combination with results from Monte Carlo simulations and information provided by the attenuation map, in a manner analogous to that described by Welch, *et al* [35]. The first step in this process is to create a virtual "scatter source". The scatter source is an image where each voxel's intensity represents the number of photons scattered towards the pinhole from that location for a given distribution of radionuclide tracers and material characteristics expressed by the three dimensional distribution of linear attenuation coefficients in the object. This scatter source is then used as an input to the forward projector of the reconstruction algorithm. The projector produces the scatter projection, which represents the contribution of scatter photons to the expected projection image.

To create the scatter source, the algorithm loops over all image voxels, and treats each in turn as a potential scatter site. Each other voxel then represents a source of photons that can be scattered at the voxel of interest. The scatter angle, ϕ, required for a photon emitted at the source to scatter into to the pinhole from the scatter site is calculated, and the contribution of the source voxel to the scatter voxel is then calculated using the following equation:

$$x_{ij} = \frac{kF(\phi)}{d^2}\mu_j \exp(-\int \mu dx) \tag{4.10}$$

where k is a proportionality constant determined empirically using Monte Carlo simulations, x_{ij} is the contribution from the voxel i to voxel j in the scatter image and has the same units as the reconstructed image (*i.e.*, activity/volume), $F(\phi)$ is the angular distribution of scatter photons detected within the energy window (as determined by Monte Carlo simulation), $1/d^2$ accounts for the geometric probability of a photon interacting at the scatter site, and the exponential term accounts for photon attenuation between the source and scatter voxels (Fig. 4.26). This model assumes that the majority of scattered photons that are detected are only scattered once, and that the probability of scattering is proportional to the linear attenuation coefficient. The scatter image is then used as an input to the forward projector along with the attenuation map to generate the scatter projection, which represents the expected contribution of photon scatter to the estimated projection data.

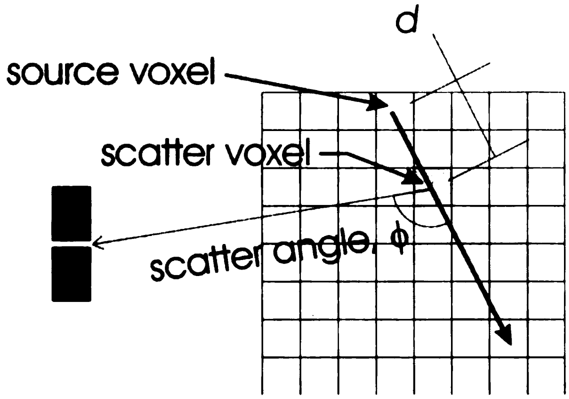

Fig. 4.26: Geometry used for estimating scatter. The algorithm loops over the image space and treats each voxel as a potential scatter site, and then calculates the contribution from all the other voxels to the scatter at the scatter voxel. The scatter voxel has linear attenuation coefficient μ_j.

A Monte Carlo simulation was performed in order to determine the angular dependence of photon scatter, to estimate $F(\phi)$ in Eq. 4.10. As shown in Fig. 4.27, to model scattering of photons from iodine-125, a simulated photon source emitted a beam of 27.5 keV photons directed at a small cube of water. The photons were then detected using a simulated spherical detector. Unscattered photons and photons that had a measured energy outside the 10-50 keV energy window were rejected. The scatter angle then was calculated for each of the 25000 remaining photons to calculate values of $F(\phi)$.

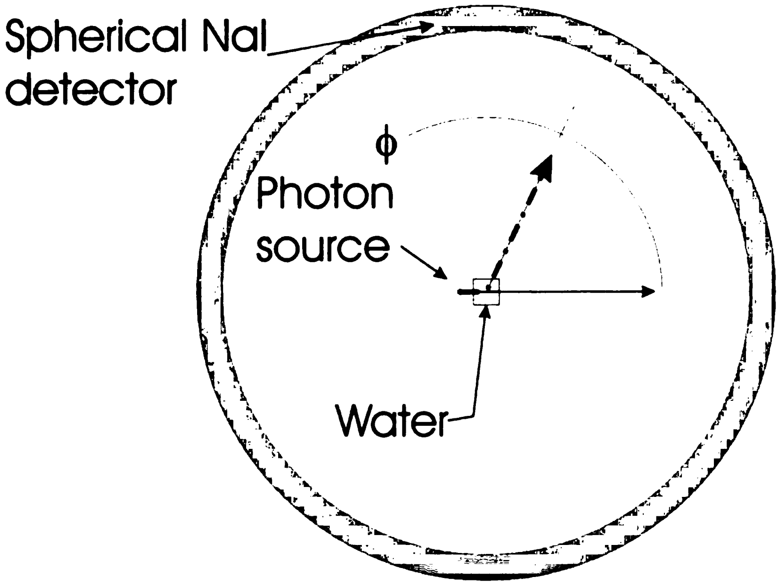

Fig. 4.27: Simulation geometry used to determine the amount of scatter as a function of scatter angle. The simulated NaI(Tl) detector is actually spherical, so this drawing represents a slice through the simulation geometry.

4.5.1.3. Acceleration methods for scatter correction

Although this scatter model is physically intuitive, it also is computationally intensive because the calculation is of order n^6, where n is the voxel dimension of the reconstructed image matrix, where n^3 source voxels need to be considered for each of the n^3 voxels. Thus, in order for scatter correction to be feasible, several approximations based on the work of Kadrmas, *et al.* [36] were introduced in the calculation of the scatter image.

The first approximation is to down-sample the matrix by a factor of 2 in all dimensions (*e.g.*, 64×64×64 to 32×32×32) when calculating the scatter source. Because the number of computations required is approximately proportional to n^6, where n is the matrix size, a reduction in the matrix size by a factor of two leads to approximately a thirty-fold reduction in computation time. This approximation takes advantage of the fact that the scatter projection generally is smooth spatially, and thus little information is lost by down-sampling. The second approximation is to limit the number of updates to the scatter estimate. This approximation is based on the fact that the scatter estimate does not change much after the first several iterations of the algorithm. This is reasonable, given that the scatter estimate is dependent on the estimated radioactivity distribution, which only requires a few iterations to reach an approximation of its final form. The third approximation is to only include scatter in the forward projector. This concept is known as the mismatched projector / backprojector, and has been shown to be a valid approach for iterative reconstruction by Zeng, *et al.* [37].

The net result of these approximations is a significant reduction in the time needed to reconstruct data with scatter correction. Without down-sampling, a 1.8 GHz Pentium 4 personal computer would require approximately 15 hours to generate 64 scatter projections for a $(64)^3$ voxel scatter matrix size. If 64 scatter projections are generated for each iteration, then reconstructing the data could take several days. With all the approximations used to accelerate the reconstruction, the total time to reconstruct the data is reduced to approximately 6 hours.

4.5.1.4. Simulation for testing

Monte Carlo simulations were used to generate projection data for testing the scatter correction algorithm. The first simulation had a spherical source of iodine-125 (2 mm radius) at the center of a cylinder of water (radius=2 cm). The source emitted 27.5 keV photons that were imaged using the detector geometry described above, and a 2 mm pinhole. A second simulation used an annular source, with radial thickness 0.4 cm, an outer radius of 1 cm, and an inner radius of 0.5 cm. Inside the annulus was a cylinder of water, with a radius of 0.5 cm and height of 0.4 cm. The geometry of this simulated phantom was designed to demonstrate qualitatively the effects of scatter, by placing a scattering medium close to the source, and with minimal attenuation outside the source.

One advantage of using Monte Carlo simulations is that the unscattered and scattered photons can be distinguished. Therefore, the simulation results were organized to generate two projection data sets for each simulation. The first set of projection data for each simulation included all detected photons within the energy window, while the second set of projection data set was generated using only primary photons. By creating these two data sets, we are able to reconstruct the data without any scatter, allowing us to directly assess the effect of scatter on the reconstructed images.

4.5.1.5. Experimental measurement

A phantom containing iodine-125 was imaged in order to assess the effects of scatter on experimental data and to evaluate the scatter correction algorithm. A micro hollow sphere phantom (0.25 mL volume, 7.8 mm diameter, Data Spectrum Corporation) filled with approximately 0.5 MBq ^{125}I-NaI was placed at the center of a water filled acrylic cylinder having an outer diameter of 3.2 cm. SPECT projection data were acquired with the 2 mm pinhole collimator at 64 projection angles over 360°, using an energy window of 10-50 keV. The SPECT acquisition was followed by acquisition of CT data, which were used to create an attenuation map. The data were reconstructed using the OS-EM algorithm with and without attenuation correction, and also were reconstructed with the OS-EM algorithm that included the scatter correction model in addition to attenuation correction. The reconstructed images were evaluated by defining volumes of interest corresponding to the source and the surrounding cylinder. The total radioactivity in these volumes was measured, and the ratio of radioactivity in the target VOI to the radioactivity in the surrounding VOI was calculated.

4.5.2. Results

4.5.2.1. Scatter-to-primary ratio

The scatter-to-primary ratio is plotted for technetium-99m and iodine-125 as a function of the radius of the surrounding water cylinder in Fig. 4.28. The results lead us to believe that scatter will not significantly degrade data acquired with technetium-99m. The result for iodine-125 shows much more scatter than the result for technetium-99m, but the scatter-to-primary ratio is still lower than the scatter-to-primary ratio of approximately 50% observed in human imaging with technetium-99m. Energy spectra obtained from Monte Carlo simulations of iodine-125 imaging are shown in Fig. 4.29 for a simulated sphere in air and for a simulated sphere in the center of a cylinder of water with 2 cm radius. The results show that the spectrum is not significantly changed by the presence of water, thus making the use of energy spectrum based scatter correction infeasible.

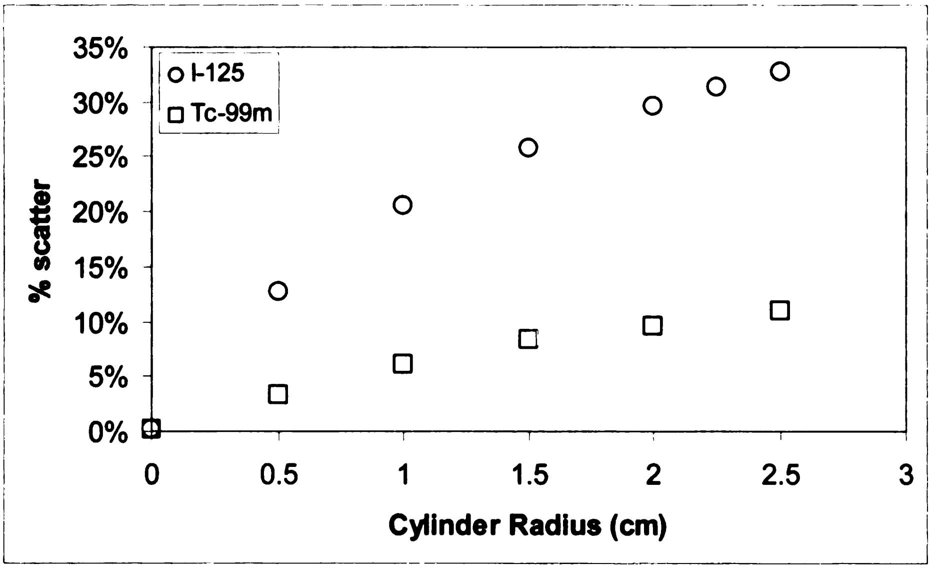

Fig. 4.28: Scatter-to-primary ratio detected from a source at the center of a cylinder of water. The scatter-to-primary ratio is defined as the number of scattered photons detected within the energy window divided by the number of primary photons detected in the window.

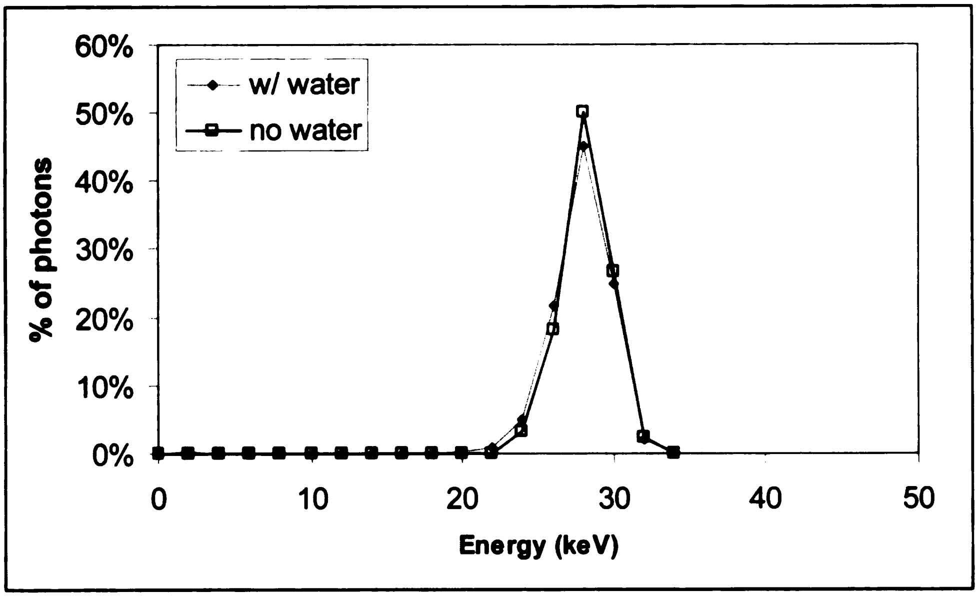

Fig. 4.29: Energy spectrum obtained by simulating the imaging of an iodine-125 source with and without a cylinder of water of 2 cm radius surrounding the source. A detector energy resolution of 25% full-width at half-maximum is modeled in the simulation. The spectrum is not changed significantly by the presence of water.

4.5.2.2. Simulations for scatter angle

A graph of the probability of scatter as a function of angle is shown in Fig. 4.30, in which 0° represents the direction of the incident photon. A second order polynomial was fit to the data to create a simple model for $F(\phi)$ (for $0° \leq \phi \leq 180°$) in Eq. 4.10, for use in the scatter model. The results show that a large number of photons which scatter at angles between 5 and 15 degrees from the forward direction, with a smaller number being backscattered (*i.e.* scattered at 180°).

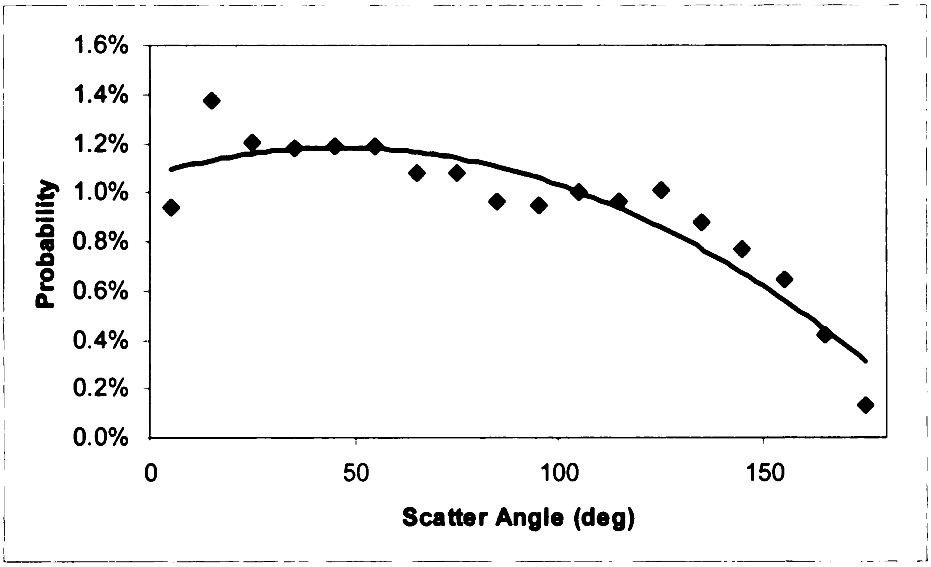

Fig. 4.30: Histogram of scatter angle. A second order polynomial was fit to the data, in order to provide a simple model for scatter as a function of angle.

4.5.2.3. Monte Carlo simulations

Projection data generated using Monte Carlo simulations were reconstructed in order to verify that the reconstruction algorithm correctly compensated for photon scatter. A key step in this process is to verify that the algorithm correctly models scatter in the imaging process. An image of the scatter source estimate generated by the reconstruction of the Monte Carlo simulation data is shown in Fig. 4.31, along with the corresponding projection data. As expected, the scatter source is asymmetric, with more "forward" scatter compared to back scatter, and the resulting scatter projection looking similar to the result predicted by the Monte Carlo simulation, albeit without any noise. A line profile through the scatter contribution to the projection data estimated by the reconstruction algorithm is compared to the result predicted by Monte Carlo simulation, and shows reasonable agreement between the analytical scatter estimate and the Monte Carlo simulation, with the main difference in regions close to the source. This difference is likely due to an underestimation of small angle scatter due to the polynomial fit used to model the angular distribution of scatter. Nevertheless, the results indicate that the algorithm gives a reasonable estimate for the detected scatter.

The image reconstructed from the projection data generated with the simulated annular source is shown in Fig. 4.32. A line profile through the image (Fig. 4.33) shows that scatter causes the spurious appearance of radioactivity in the center of the annulus. When the data were reconstructed using only primary photons, the apparent radioactivity in the center is reduced, but not eliminated, and arises from blurring caused by the finite spatial resolution of the system. In order to quantitatively analyze the effect of scatter, the area under the curve in the line profile can be divided into two areas. The first area contains the two peaks and corresponds to the annulus. The second area consists of the region between the peaks (*i.e.*, the valley), which contains water and no radioactivity. In the ideal case, the peak to valley ratio is infinite. In the three reconstructed images, the ratio was 15:1 when the image was reconstructed with only attenuation correction, 34:1 with the addition of scatter correction, and 29:1 using attenuation correction with scatter free data. This demonstrates that scatter correction effectively compensates for the contrast lost due to photon scatter.

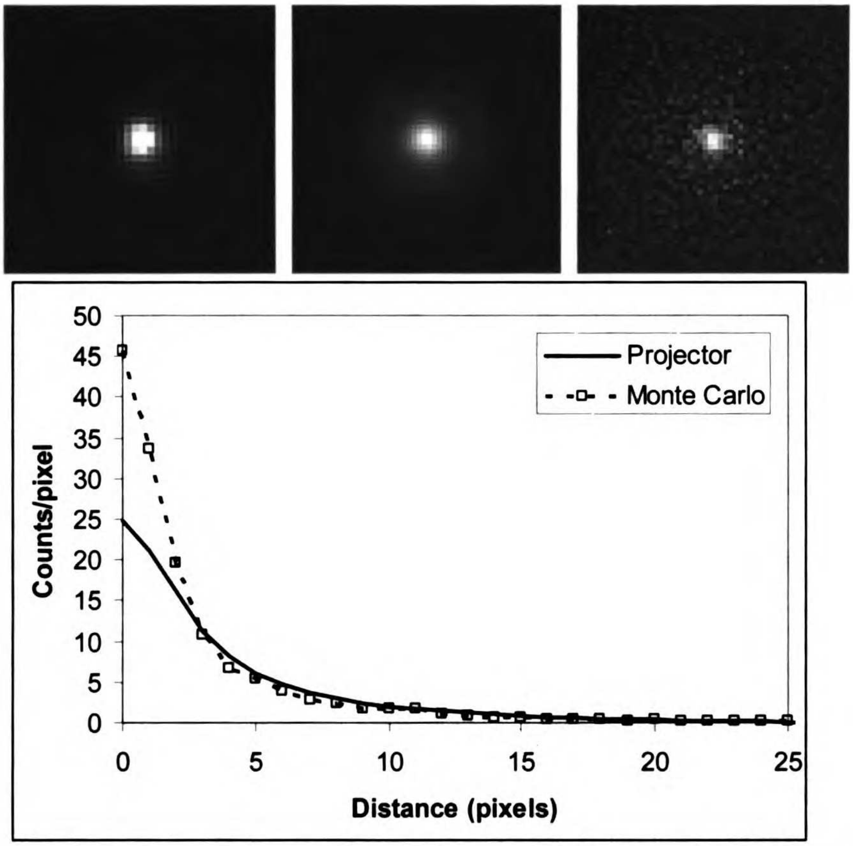

Fig. 4.31: Scatter source estimate used in reconstruction of the data (top left). The intensity of each voxel represents the probability that a photon scattered in that voxel will be detected. The image oriented such that the pinhole is positioned to the right, along the x-axis. This scatter source is used as an input to the forward projector to calculate the scatter contribution to the projection data (top middle). The scatter in the projection as predicted by the Monte Carlo simulation is shown on the top right. On the bottom is shown a line profile through the scatter projection estimated by the reconstruction algorithm and the corresponding Monte Carlo result.

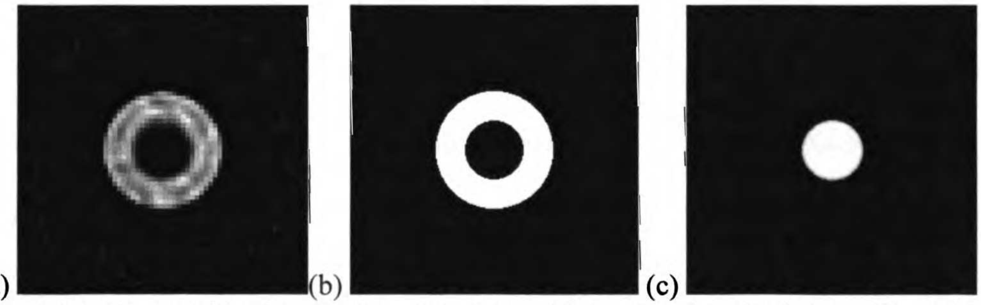

Fig. 4.32: Center slice from image reconstructed from the simulated projection data.
(a) The data reconstructed using OSEM with collimator response, attenuation correction, and scatter correction. (b) The source distribution used to generate projection data. (c) The attenuation distribution is a uniform cylinder of water at the center of the annulus.

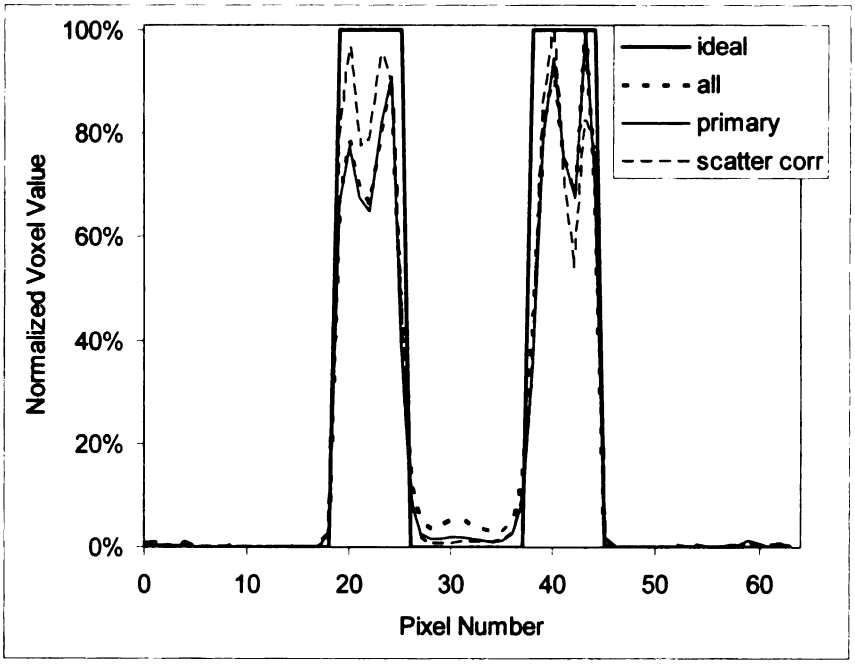

Fig. 4.33: Line profiles through the image reconstructed from Monte Carlo simulation generated projection data of an annular source (solid line) around a cylinder of water. The data were reconstructed with attenuation correction using either all photons (dotted line), only primary photons (solid line), and all photons with scatter correction (dashed line). The results demonstrate that scatter correction reduces the apparent radioactivity introduced by scatter.

4.5.2.4. Experimental measurement

A single projection image of an iodine-125 filled sphere in a cylinder of water is shown in Fig. 4.34. The corresponding projection, imaged without surrounding water, is also shown for comparison. The contrast has been adjusted in the images in order to accentuate the scatter contribution to the projection images. As can be seen, the sphere surrounded by water has more scatter in the projection data, as demonstrated by the line profile in Fig. 4.34.

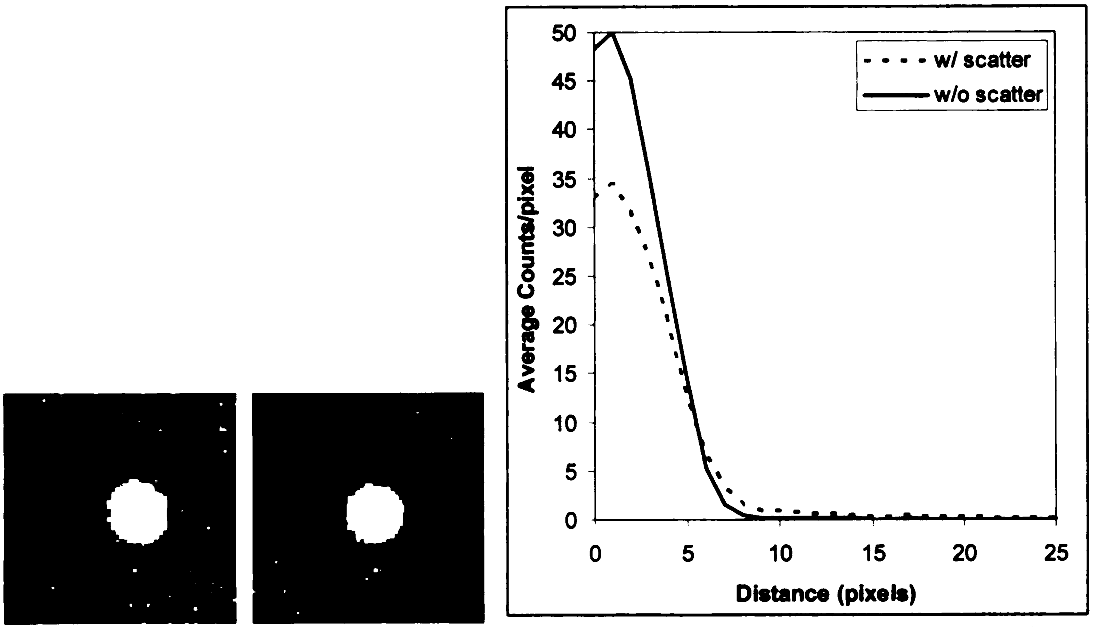

Fig. 4.34: Projection views of a microsphere surrounded by water (left). A projection view of the same sphere without surrounding water is shown in the center. In both images, scatter from the plastic rod supporting the sphere is visible below each sphere. The contrast in the images has been adjusted to accentuate the scatter. A plot of the radial count density (counts/pixel) also shows how scatter reduces the contrast by increasing the number of accounts in pixels surrounding the image of the sphere.

A slice through the reconstructed image of the microsphere imaged in water is shown in Fig 4.35 in order to demonstrate the effect of scatter correction. Although the scatter correction does not appear to make a difference initially, when the image contrast is adjusted, it can be seen that the scatter is decreased in the image with scatter correction. In addition, the result can be analyzed quantitatively by calculating the ratio of apparent radioactivity in the target volume to the apparent radioactivity in the surrounding volume. This value increased from 1.5:1 to 2.7:1 with the addition of scatter correction, demonstrating that scatter correction reduced the effect of scatter on the reconstructed image.

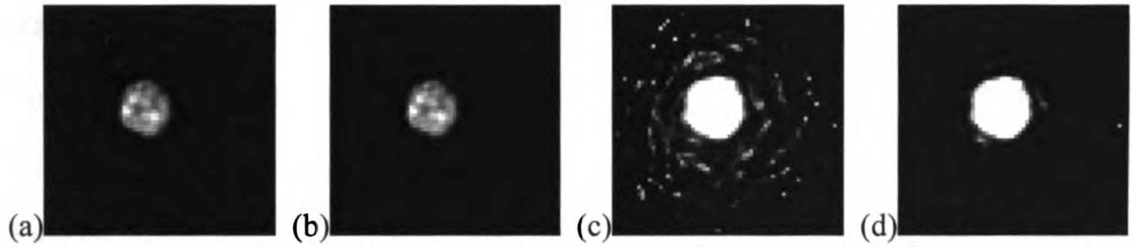

Fig 4.35: A slice from the reconstructed image of an iodine-125 filled microsphere imaged in a water filled cylinder. Image (a) and (c) were reconstructed with attenuation correction and collimator response. Images (b) and (d) were reconstructed using the same algorithm with the addition of scatter correction. Images (a) and (b) are displayed using normal contrast, and appear very similar. However, increasing the contrast in the images reveals that scatter correction reduces the noise caused by scattered photons (Images (c) and (d)).

4.5.3. Discussion

As shown in Fig. 4.28, the scatter-to-primary ratio in mouse or rat imaging with iodine-125 can reach 30% or more, which is an unexpectedly high value, though still lower than the scatter-to-primary ratio typically encountered in human imaging with technetium-99m. However, this result can be explained by examining the contribution of various mechanisms to the linear attenuation coefficient of water. As shown in Table 4.6, the Compton component of the linear attenuation coefficient is higher at 27.5 keV than it is at 140 keV. Additionally, Rayleigh (coherent) scatter becomes significant at these low energies. These factors, combined with the decrease in primary photons due to attenuation, explain the unexpectedly high scatter-to-primary ratio.

Table 4.6: Linear attenuation coefficient for water

Photon energy (keV)	Rayleigh Scattering (cm^{-1})	Compton scattering (cm^{-1})	Photoelectric absorption (cm^{-1})	Total attenuation (cm^{-1})
27.5	0.0541	0.182	0.194	0.430
140	0.0028	0.150	0.0009	0.154

The histogram of scatter angle also gave an unexpected result (Fig. 4.27). Although the results look similar to the predictions of the Klein-Nishina equation for Compton scatter, there is an extra peak at low angle (5 degrees) in our simulation data which arises from the low angle Rayleigh (coherent) scatter. By comparing the contributions of the different components to the linear attenuation coefficient of water, it can be seen that the coherent scatter accounts for about 20-25% of the scatter interactions, which is consistent with the result of the Monte Carlo simulation which showed that approximately 24% of the detected scatter photons underwent coherent scatter. Rayleigh scatter should not degrade image quality as much as Compton scatter, because the scattering angles resulting from coherent scatter are relatively small, thereby leading to smaller errors in the photon trajectory. Therefore, despite the relatively high scatter-to-primary ratio observed when imaging with iodine-125, scatter correction in small animal imaging with iodine-125 will not be as important as scatter correction in human imaging with technetium-99m and other radionuclides commonly used for diagnostic imaging in the nuclear medicine clinic.

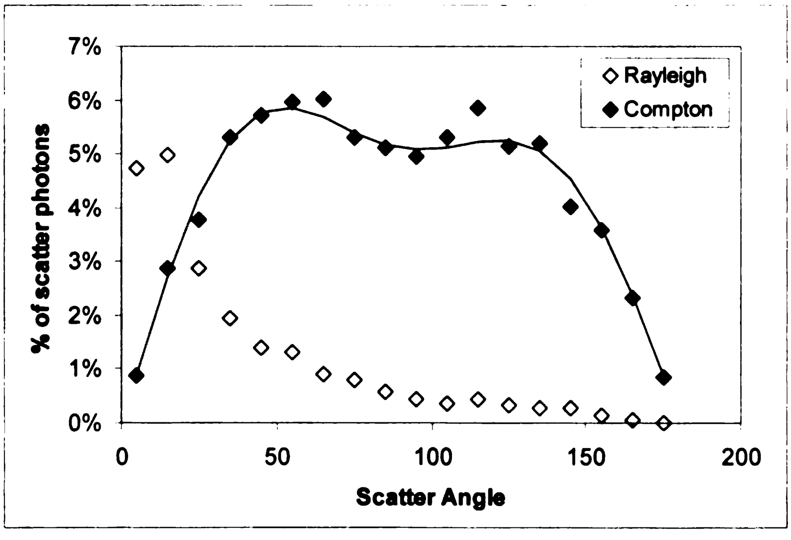

Fig. 4.36: The angular distribution of photon scatter from an iodine-125 source, determined by simulating a beam of photons directed at water. The Rayleigh scatter accounts for the low angle scatter. The angular distribution of the Compton scatter agrees with the result predicted from the Klein-Nishina equation, which is shown by the line.

The scatter model used in the reconstruction algorithm assumes that photons are only scattered once in the object prior to detection. This assumption is validated by the results of the Monte Carlo simulations, which show that the majority of detected scatter photons are only scattered once in the phantom (Fig. 4.37).

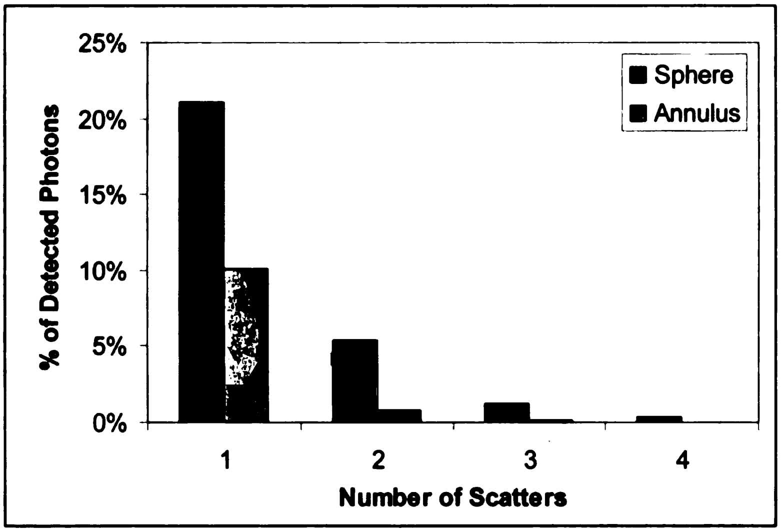

Fig. 4.37: Number of photons as a function of the number of scatter events in the phantom for photons detected within the energy window in the Monte Carlo simulations. Data are from simulations of a spherical source and of an annular source within a cylinder of water.

4.6. Conclusion

This chapter described improvements to the SPECT image reconstruction algorithm that result in improvements to image quality. These improved algorithms create a more accurate model of the imaging process by including realistic models for the collimator response, photon attenuation, and photon scatter.

Adding collimator response can greatly improve the spatial resolution of the reconstructed images, particularly with larger apertures or with higher energy isotopes where septal penetration is significant. However, a large number of iterations is necessary to fully realize the improved spatial resolution. Alternatively, a smaller number of iterations can be performed to produce images with reduced noise.

Attenuation and photon scatter correction are important mainly for low energy isotopes such as iodine-125, and is less important for higher energy isotopes. In this chapter, we have described a method to calibrate and rescale x-ray CT data to create attenuation maps, which were used as input to the reconstruction algorithm. We then demonstrated that CT data can be used to correct for photon attenuation and scatter to reduce artifacts in images reconstructed from data acquired with iodine-125. Data acquired with technetium-99m are not significantly degraded by photon scatter, due to the short path lengths encountered in small animal imaging; the scatter to primary ratio was estimated to be less than 15% for small animals such as mice and rats.

References

[1] G. T. Gullberg, R. H. Huesman, J. A. Malko, J. P. Norbert, and T. F. Budinger, "An attenuated projector-backprojector for iterative SPECT reconstruction," *Physics in Medicine and Biology*, vol. 30, pp. 799-816, 1985.

[2] G. L. Zeng and G. T. Gullberg, "A Study of Reconstruction Artifacts in Cone Beam Tomography Using Filtered Backprojection and Iterative EM Algorithms," *IEEE Transactions on Nuclear Science*, vol. 37, pp. 759-767, 1990.

[3] S. R. Cherry, J. A. Sorenson, and M. E. Phelps, *Physics in Nuclear Medicine*, 3rd ed. Philadelphia: Elsevier Science, 2003.

[4] A. G. Weisenberger, R. Wojcik, E. L. Bradley, P. Brewer, S. Majewski, J. Qian, A. Ranck, M. S. Saha, K. Smith, M. F. Smith, and R. E. Welsh, "SPECT-CT System for Small Animal imaging," *IEEE Transactions on Nuclear Science*, vol. 50, pp. 74-79, 2003.

[5] J. L. Musachio, U. Scheffel, P. A. Finley, Y. Zhan, T. Mochizuki, H. N. Wagner, and R. F. Dannals, "5-[I-125/123]Iodo-3(2(S)-azetidinylmethoxy)pyridine, a radioiodinated analog of A-85380 for in vivo studies of central nicotinic acetylcholine receptors.," *Life Science*, vol. 62, pp. 351-357, 1998.

[6] Y. Wang, W. E. Klunk, G. F. Huang, M. L. Debnath, D. P. Holt, and C. A. Mathis, "Synthesis and evaluation of 2-(3'-iodo-4'-aminophenyl)-6-hydroxybenzothiazole for in vivo quantitation of amyloid deposits in Alzheimer's disease," *Journal Of Molecular Neuroscience*, vol. 19, pp. 11-16, 2002.

[7] L. T. Chang, "A method for attenuation correction in radionuclide computed tomography," *IEEE Transactions on Nuclear Science*, vol. 25, pp. 638, 1978.

[8] Y. Censor, D. E. Gustafson, A. Lent, and H. Tuy, "A new approach to the emission computerized tomography problem: simultaneous calculation of attenuation and activity coefficients," *IEEE Transactions on Nuclear Science*, vol. 26, pp. 2275-2279, 1979.

[9] D. L. Bailey, B. F. Hutton, and P. J. Walker, "Improved SPECT using simultaneous emission and transmission tomography," *Journal of Nuclear Medicine*, vol. 28, pp. 844-851, 1987.

[10] S. C. Blankespoor, X. Wu, K. Kalki, J. K. Brown, H. R. Tang, C. E. Cann, and B. H. Hasegawa, "Attenuation correction of SPECT using x-ray CT on an emission-transmission CT system: Myocardial perfusion assessment," *IEEE Transactions on Nuclear Science*, vol. 43, pp. 2263-2274, 1996.

[11] B. M. W. Tsui, G. T. Gullberg, E. R. Edgerton, J. G. Ballard, J. R. Perry, W. H. McCartney, and J. Berg, "Correction of nonuniform attenuation in cardiac SPECT imaging," *Journal of Nuclear Medicine*, vol. 30, pp. 497-507, 1989.

[12] H. Zaidi and B. H. Hasegawa, "Attenuation correction strategies in emission tomography," in *Quantitative Analysis in Nuclear Medicine Imaging*, H. Zaidi, Ed. New York: Springer Science+Business, Inc, 2006, pp. 167-204.

[13] H. Firooznia, C. Golimbu, M. Rafii, M. Schwartz, and E. Alterman, "Quantitative computed tomography assessment of spinal trabecular bone. Age-related regression in normal men and women`," *Journal of Computed Tomography*, vol. 8, pp. 91-97, 1984.

[14] C. E. Cann, "Quantitative CT for determination of bone mineral density: a review," *Radiology*, vol. 166, pp. 509-522, 1988.

[15] H. R. Tang, "A Combined X-ray CT-Scintillation camera System for Measuring Radionuclide Uptake in Tumors," Ph.D. dissertation, University of California San Francisco and University of California Berkeley, San Francisco, CA, 1998.

[16] I. A. Elbakri and J. A. Fessler, "Statistical image reconstruction for polyenergetic x-ray computed tomography," *IEEE Transactions on Medical Imaging*, vol. 21, pp. 89-99, 2002.

[17] P. M. Joseph and C. Ruth, "A method for simultaneous correction of spectrum hardening artifacts in CT images containing both bone and iodine," *Medical Physics*, vol. 24, pp. 1629-1634, 1997.

[18] J. M. Meagher, C. D. Mote Jr., and H. B. Skinner, "CT image correction for beam hardening using simulated projection data," *IEEE Transactions on Nuclear Science*, vol. 37, pp. 1520-1524, 1990.

[19] M. A. King, B. C. Penney, and S. J. Glick, "An image-dependent Metz filter for nuclear medicine images," *Journal of Nuclear Medicine*, vol. 29, pp. 1980-1989, 1988.

[20] W. S. Xia, R. M. Lewitt, and P. R. Edholm, "Fourier correction for spatially variant collimator blurring in SPECT," *IEEE Transactions on Medical Imaging*, vol. 14, pp. 100-115, 1995.

[21] B. M. W. Tsui, H.-B. Hu, D. R. Gilland, and G. T. Gullberg, "Implementation of simultaneous attenuation and detector response correction in SPECT," *IEEE Transactions on Nuclear Science*, vol. 35, pp. 778-783, 1988.

[22] D. Strul, G. Santin, D. Lazaro, V. Breton, and C. Morel, "GATE (Geant4 Application for Tomographic Emission): a PET/SPECT general-purpose simulation platform," *Nuclear Physics B (Proc. Suppl.)*, vol. 125, pp. 75-79, 2003.

[23] G. Santin, D. Strul, D. Lazaro, L. Simon, M. Krieguer, M. Vieira Martins, V. Breton, and C. Morel, "GATE: A Geant4-based simulation platform for PET and SPECT integrating movement and time management," *IEEE Transactions on Nuclear Science*, pp. 1516-1521, 2003.

[24] D. P. McElroy, L. R. MacDonald, F. J. Beekman, Y. Wang, B. E. Patt, J. S. Iwanczyk, B. M. W. Tsui, and E. J. Hoffman, "Performance evaluation of A-SPECT: a high resolution desktop pinhole SPECT system for imaging small animals," *IEEE Transactions on Nuclear Science*, vol. 49, pp. 2139-2147, 2002.

[25] Y. Qi, "Optimized collimator designs for small animal SPECT imaging with a compact gamma camera," presented at IEEE Engineering in Medicine and Biology, Shanghai, China, 2005.

[26] F. van der Have and F. J. Beekman, "Penetration and scatter in channel micro-pinholes for SPECT: a Monte Carlo investigation," *2004 IEEE Nuclear Science Symposium Conference Record*, vol. 4, pp. 2575-2578, 2004.

[27] E. C. Frey and B. M. W. Tsui, "Collimator-detector response compensation in SPECT," in *Quantitative analysis in nuclear medicine imaging*, H. Zaidi, Ed. New York, NY: Springer Science+Business Media, Inc., 2006, pp. 141-166.

[28] H. Zaidi and K. F. Koral, "Scatter modelling and compensation in emission tomograhpy," *European Journal of Nuclear Medicine*, vol. 31, pp. 761-782, 2004.

[29] P. Msaki, B. Axelsson, C. M. Dahl, and S. A. Larsson, "Generalized scatter correction method in SPECT using point scatter distribution functions," *Journal of Nuclear Medicine*, vol. 28, pp. 1861-1869, 1985.

[30] Y. Dewaraja, J. Li, and K. Koral, "Quantitative ^{131}I SPECT with triple energy window Compton scatter correction," *IEEE Transactions on Nuclear Science*, vol. 45, pp. 3109-3114, 1998.

[31] E. C. Frey and B. M. W. Tsui, "A New Method for Modeling the Spatially-Variant, Object-Dependent Scatter Response Function in SPECT," presented at IEEE Nuclear Science Symposium, Anaheim, CA, 1986.

[32] E. C. Frey and B. M. W. Tsui, "A practical method for incorporating scatter in a projector-backprojector for accurate scatter compensation in SPECT," *IEEE Transactions on Nuclear Science*, vol. 40, pp. 1107-1116, 1993.

[33] G. L. Zeng, C. Bai, and G. T. Gullberg, "A projector/backprojector with slice-to-slice blurring for efficient three-dimensional scatter modeling," *IEEE Transactions on Medical Imaging*, vol. 18, pp. 722-732, 1999.

[34] Y. S. Gur, T. H. Farncombe, P. H. Pretorius, H. C. Gifford, M. V. Narayanan, D. Gagnon, and M. A. King, "Comparison of scatter compensation strategies for myocardial perfusion imaging using Tc-99m labeleld sestamibi," *IEEE Transactions on Nuclear Science*, vol. 49, pp. 2309-2304, 2002.

[35] A. Welch, G. T. Gullberg, P. E. Christian, F. L. Datz, and H. T. Morgan, "A transmission-map-based scatter correction technique for SPECT in inhomogeneous media," *Medical Physics*, vol. 22, pp. 1627-1635, 1995.

[36] D. J. Kadrmas, E. C. Frey, S. S. Karimi, and B. M. W. Tsui, "Fast implementations of reconstruction-based scatter compensation in fully 3D SPECT image reconstruction," *Physics in Medicine and Biology*, vol. 43, pp. 857-873, 1998.

[37] G. L. Zeng and G. T. Gullberg, "Unmatched projector/backprojector pairs in an iterative reconstruction algorithm," *IEEE Transactions on Medical Imaging*, vol. 19, 2000.

Chapter 5: Error Sources in Quantitative SPECT Imaging

5.1. Introduction

In current clinical practice, nuclear medicine images are generally interpreted in a qualitative manner in which the results are visually inspected to determine the presence or absence of a pathological condition. However, the consistency, sensitivity, and arguably the clinical utility of the interpretation of these data would be increased if they were analyzed and recorded quantitatively, and in fact, various approaches have been developed to analyze nuclear medicine data in a quantitative manner. For example, the glucose metabolism rate can be quantified using compartmental analysis of a dynamic sequence of PET images acquired with ^{18}F-fluorodeoxyglucose [1]. In another example, the regional uptake of radiopharmaceuticals such as ^{99m}Tc-sestamibi or ^{201}Tl-thallous chloride often are compared against results from a database of scans from normal volunteers to quantify the severity of perfusion defects in the myocardium of patients with coronary artery disease. These examples illustrate two of the many different ways that quantitative analysis is applied to nuclear medicine images.

The term "radionuclide quantification" also has a number of different meanings in the medical imaging literature. Several definitions include: 1) "semi-quantification", the comparison of relative measurements between normal and diseased regions, 2) "physiologic quantification", the measurement of a physiologically meaningful parameter, and 3) "absolute physical quantification", the accurate measurement of radioactivity concentration with corrections for perturbations such as photon attenuation [2]. Within the scope of this thesis, radionuclide quantification is used to mean absolute physical quantification, or the measurement of the absolute concentration of radiotracer within a volume of interest.

5.1.1. Sources of error

Ideally, when analyzing radionuclide images, a physician or scientist would like to define a "region of interest" on a planar radionuclide image (or a "volume of interest" on slices from a tomographic radionuclide scan", and then sum the voxel values within those regions or volumes of interest to measure the radionuclide uptake in the corresponding region of tissue in the patient. Typically, these numbers would be reported in terms of the radionuclide concentration in units of MBq/ml or MBq/cc of tissue. However, when this is performed experimentally in phantoms or large animals approximating the size of humans, the noninvasive measurement obtained from the images typically is incorrect (typically too low) by an order of magnitude. Therefore, although the concept of "radionuclide quantification" seems straightforward, it remains an elusive goal that in practice is difficult to perform experimentally. The challenges and difficulties in radionuclide quantification arise from several potential sources of error which can lead to erroneous measurements. These sources of error include physical perturbations such as photon attenuation, photon scatter, and the partial volume effect. Photon attenuation arises when overlying tissues absorb photon emitted from a target tissue, leading to a decrease in the number of observed counts, which subsequently can cause a decrease in the apparent (*i.e.*, measured) concentration of radioactivity and image artifacts. Similarly, photons from the target tissue can scatter in the surrounding tissue, and photons from radioactivity in background regions can scatter in regions of the image that coincide with the region or volumes of interest. As a result, photon scatter can decrease the image contrast, and introduce false counts into regions of interest when the reconstructed image is analyzed quantitatively. Partial volume errors arise from the limited spatial resolution of the imaging system, which causes blurring of the

radioactivity from the target region into the background region, and similarly blurring of the radioactivity from the surrounding background into the target. As a result, when the image is analyzed quantitatively, a region of interest carefully defined over the anatomical boundary of the target region generally will measure a mix of the radioactivity concentrations from the target and background regions. This leads to quantitative errors, especially when the size of the target region is close to or smaller than the spatial resolution of the imaging system. This chapter will describe these physical perturbations that lead to errors in radionuclide quantification, estimate the magnitude of these errors in the context of small animal imaging, and evaluate the effect of improved reconstruction algorithms on mitigating the effect of these perturbations on the quantitative accuracy of SPECT images.

5.1.1.1. Photon attenuation and scatter

As discussed in Chapter 4, photon attenuation and scatter radiation result from the interaction of photons with matter, where the magnitude of the interaction is a function of photon path length through the body, photon energy, and tissue composition (Fig. 5.1). The absorption of photons within the patient (human or animal) being imaged decreases the total number of photons detected, resulting in an apparent decrease in radioactivity within a given target region. In radionuclide imaging, these errors can be compensated using attenuation correction techniques. One such technique is to use anatomical information from an x-ray CT image of the object to create a model of the photon attenuation that can be incorporated in an iterative reconstruction algorithm as described in Chapter 4. In human imaging, it is commonly accepted that attenuation correction is necessary for quantitatively accurate, artifact free data [3], and a number of strategies have been devised for attenuation correction. In comparison, in small animal imaging,

the magnitude of errors from photon attenuation, and consequently the need for attenuation correction has not been clearly established. Likewise, the quantitative effects of photon scatter in small animal SPECT are not fully understood, nor have scatter correction algorithms been developed and tested for small animal SPECT.

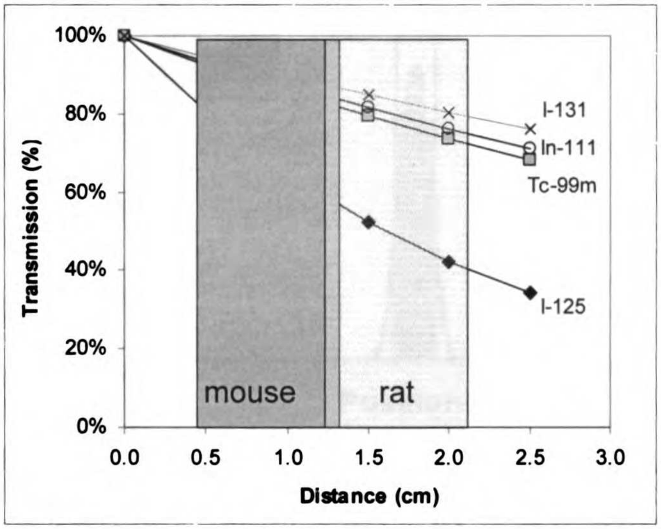

Fig. 5.1: Narrow beam photon transmission through water for four isotopes used in small animal SPECT imaging. The results in this graph were analytically calculated, and show that iodine-125 (27.5 keV photon) should be much more prone to the effects of photon attenuation in small animal imaging than higher energy isotopes such as technetium-99m (140 keV), indium-111 (171 keV and 245 keV), and iodine-131 (365 keV). The shaded areas show the approximate length scales encountered in imaging mice and rats.

5.1.1.2. Partial volume effect

One of the inherent limitations of radionuclide imaging is poor spatial resolution. Small animal SPECT and PET systems typically achieve spatial resolutions in the range of 1-2 mm, in comparison to microCT which can achieve spatial resolution in the range of 50-100 μm or better. As a result, when SPECT or PET is used to measure the amount of tissue radioactivity, partial volume errors can create quantitative errors in the resulting data. The limited spatial resolution of a SPECT imaging system can lead to blurring of the radioactivity distribution, which increases its apparent size, leading to an underestimation of the concentration of the radioactivity present (Fig. 5.2), an effect

known as "spill-out". Conversely, "spill-in" can result from the presence of radioactivity in neighboring structures, and leads to the apparent increase of radioactivity in a volume of interest (Fig. 5.3).

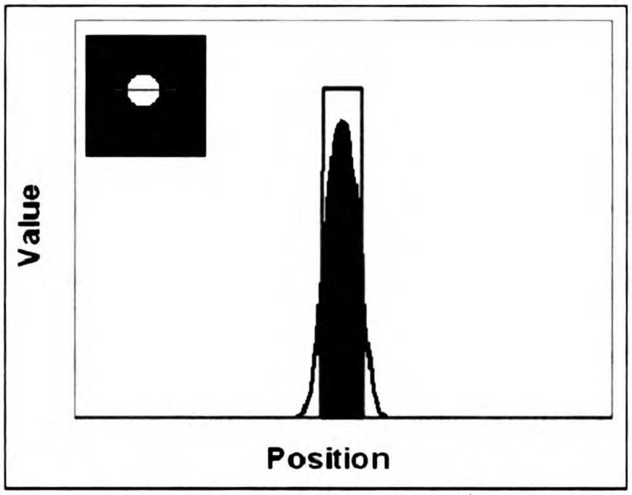

Fig. 5.2: This figure illustrates the effect of partial volume errors on quantitative measurements. A line profile through the region of interest (inset) is shown as the rectangular line. However, due to the finite spatial resolution of imaging systems, the measured line profile is blurred, and the radioactivity appears to be spread out over a larger region. A measurement within the region of interest shows an apparent decrease in radioactivity.

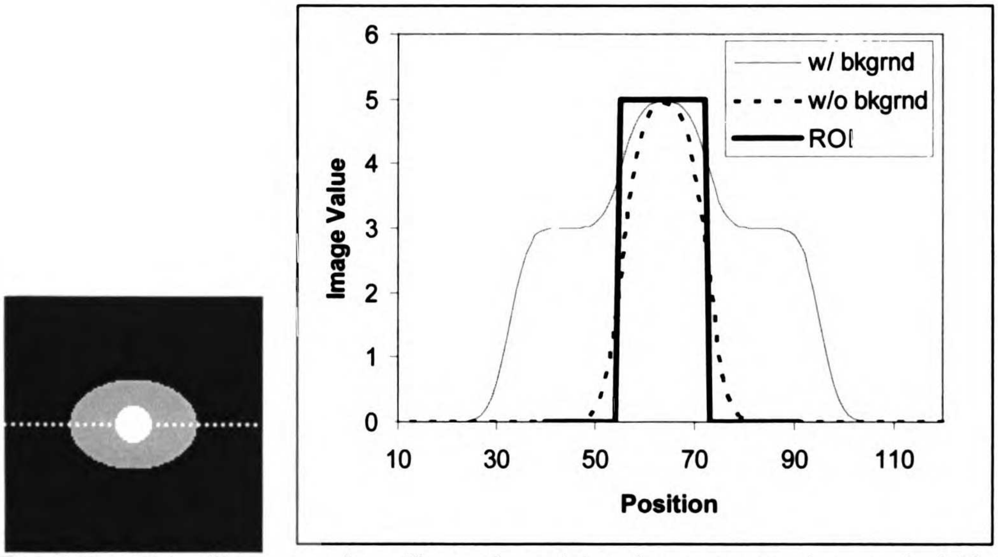

Fig. 5.3: This illustrates the effect of partial volume errors due to "spill-in" of background radioactivity into a region of interest. The left image shows an unblurred target in an elliptical source of background radioactivity. The line profiles show the radioactivity in the target region (after blurring with a Gaussian) with and without background radioactivity. The result shows that the apparent amount of radioactivity in the target region is increased when background radioactivity is present.

5.2. Monte Carlo simulations

Monte Carlo methods are powerful tools for simulating a variety of physical processes and are often used to model and evaluate radionuclide imaging. These simulations are particularly useful for studying quantitative measurements in SPECT because it becomes possible to simulate the imaging of a well defined radionuclide source, while modeling complex physical phenomena such as photon scatter. In the work described below, the simulations were performed using the GATE ("Geant4 Application for Tomographic Emission") Monte Carlo simulation package [4, 5] based on Geant4, a general purpose simulation package used for a variety of applications. ("Geant", in turn, is an acronym for "Geometry ANd Tracking".) The simulation geometry was modeled on the X-SPECT scanner in our laboratory using the simplified simulation geometry described in Chapter 4, Section 3.2.2. The simulated energy resolution and energy windows were based on the expected performance of the X-SPECT system and are shown in Table 5.1 below.

Table 5.1: Simulated energy resolution and energy windows used in Monte Carlo simulations of X-SPECT system

	I-125	Tc-99m
Simulated source energy	27.5 keV	140 keV
Energy resolution (%FWHM)	26%	12%
Energy window	10-50 keV	126-161 keV

5.2.1. Methods and materials

5.2.1.1. Simulations to study photon attenuation and scatter

Monte Carlo simulations using the GATE package were performed to estimate the effect of photon attenuation on quantitative accuracy by simulating the imaging of a radioactive source in the center of an attenuating medium. The amount of attenuation

UCSF LIBRARY

was varied, and the simulation repeated. The resulting projection data were reconstructed, and the apparent change in radioactivity was measured as a function of the amount of attenuation, and compared against the known amount of radioactivity in the radionuclide source.

A spherical source with a radius of 2 mm was defined at the center of a cylinder of water to simulate the imaging of a tumor in the torso of a small animal. The axis of the cylinder was aligned with the axis of rotation, and the height was kept constant at 3 cm. The radius of the cylinder was varied to assess the effect of varying the cylinder size, and thus the amount of photon attenuation, on the reconstructed image, and the energy of the emitted photons was also varied in order to simulate the imaging of technetium-99m and iodine-125. For each case, a set of 64 projections were generated over 360° rotation around the object, with 1.5×10^6 emission photons simulated per projection. Furthermore, the simulation output was used to create two sets of data from each simulation, consisting of one set of projection data with all photons detected within the energy window, and another set of projection data with only unscattered photons detected within the energy window, which constituted a "scatter-free" data set. The simulated projection data were reconstructed, and the voxel values in the volume of interest corresponding to the source were calculated.

5.2.1.2. Simulations to study partial volume effect

The effect of partial volume errors was studied by simulating the imaging of a series of spherical sources of differing size, reconstructing the data, and measuring the change in apparent radioactivity as a function of the size of the source by calculating the mean voxel values in a volume of interest corresponding to the spherical source. The simulation did not have any photon attenuation in the source (*i.e.*, the sources were in air)

or background activity, which allowed us to evaluate the partial volume effect independently of other factors that may affect the quantitative accuracy. The simulations were performed for both 1 mm and 2 mm pinhole apertures, so that the effect of changing the pinhole aperture could be assessed. Each source had 2000 Bq/mm^3 of radioactivity, and emitted 140 keV photons. The sources were located at the center of rotation, at a distance of 4 cm from the pinhole, and a total of 64 projections were generated for each source with a rotation angle of 360°. The photon emission angle was limited to a solid angle of 0.5π around pinhole in order to decrease computation time.

5.2.1.3. Effect of background radioactivity

Additional simulations were performed to assess the effect of background radioactivity on radionuclide quantification. This was done by generating simulated projection data using a cylindrical source and the imaging geometry described in the previous paragraph. The simulated source had a radius of 1 cm, and a height of 3 cm, in order to approximate a uniform radioactivity distribution within the dimensions of a mouse torso. The sources were simulated to have 222 Bq/mm^3 for one set of data, and the simulations were repeated with radioactivity set to 278 Bq/mm^3. The projection data for the cylinder were combined with the projection data for the spheres, in order to create a single set of projection data of a cylinder containing a sphere at the center. The various projection sets were added together in order to create sets of projection data with different values for the target to background ratio (10:1 and 5:1), target size (radius of 1 mm to 5 mm), and pinhole aperture size (1 mm and 2 mm pinhole diameter). The projection data were reconstructed, and the voxel values in the target volume of interest were compared with the results obtained without background radioactivity by plotting the voxel values as a function of background activity and target size.

5.2.1.4. Image reconstruction and data analysis

The projection data generated by the Monte Carlo simulations were reconstructed using with different levels of physical modeling incorporated in the projector-backprojector pair in an ordered subsets-expectation maximization (OS-EM) reconstruction algorithm as described in Chapter 4. For simulations studying partial volume effect, the projection data were reconstructed using the OS-EM algorithm both with and without the collimator response model described in the previous chapter. When the data were reconstructed using the OS-EM algorithm without compensation for finite collimator response, 5 iterations (8 subsets) were used. In comparison, when compensation for collimator response was included in the algorithm (OSEM+CR), the data were reconstructed using 20 iterations (8 subsets). All data were reconstructed in a matrix size of $(64)^3$, with a voxel size of 0.77 mm. In addition, for simulations studying photon attenuation and scatter, the data were reconstructed using OS-EM with attenuation correction (OSEM+AC). The attenuation maps used in reconstructing these data were generated using the known simulation geometry of the object, and the photon attenuation coefficient for water at the energy of the source photon (Table 5.2). In addition, projection data for iodine-125 were reconstructed using OS-EM with corrections for scatter, attenuation, and collimator response using the algorithm described in Chapter 4, Section 5, which models photon scatter in the forward projector by considering each voxel in the image as both a potential source of photons and a potential site for photon scatter using anatomical information from the attenuation map and the estimated source distribution.

The reconstructed data were displayed using AMIDE, an image display and analysis software [6]. A volume of interest (VOI) corresponding to the size and shape of the

source was defined, and the total and average voxel values within the VOI were calculated. The results were normalized to the average voxel value in the reconstructed image of a 250 μL source simulated without photon attenuation.

Table 5.2: Photon energy used for Monte Carlo simulations to study photon attenuation

Isotope	Photon Energy (keV)	Photon attenuation coefficient μ (cm^{-1}) for water
Iodine-125	27.5*	0.43
Technetium-99m	140 keV	0.15

* Iodine-125 emits x-rays primarily in the range of 27-31 keV [7]. We have modeled it as a monoenergetic source at 27.5 keV.

5.2.2. Results

5.2.2.1. Effect of photon attenuation and scatter

The scatter-to-primary ratio (the number of scattered photons divided by the number of unscattered photons detected) for a small spherical source at the center of a cylinder of water is plotted as a function of the cylinder radius in Fig. 5.4. As expected, increasing the size of the cylinder increased the scatter-to-primary ratio for both iodine-125 and technetium-99m. The results show that the scatter-to-primary ratio could reach approximately 35% when imaging iodine-125 in a rat sized object. In comparison, the scatter-to-primary ratio in human myocardial perfusion imaging with technetium-99m has been estimated to be approximately 25-45%, depending on the distribution of the radionuclide and the energy windows selected [8].

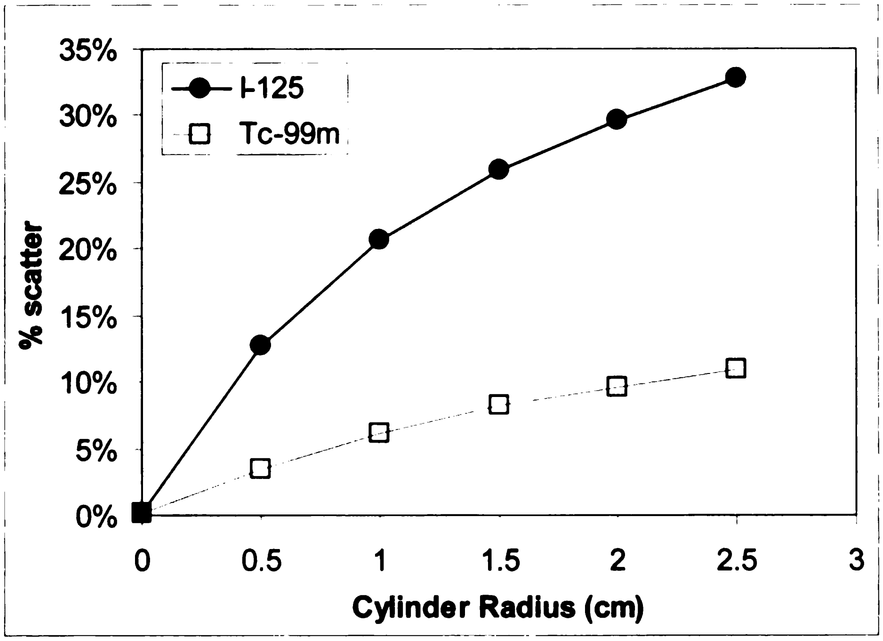

Fig. 5.4: Plot of the scatter-to-primary ratio (number of scattered photons detected in energy window divided by the number of primary photons in the energy window) from a simulated source at the center of a cylinder of water. Increasing the size of the cylinder increases the scatter-to-primary ratio.

The normalized VOI values for iodine-125 are plotted as a function of the cylinder radius in Fig. 5.5. As expected, photon attenuation decreases the measured radioactivity in the source. In a rat sized object (~2 cm radius), the apparent radioactivity of the source is decreased by approximately 50% in comparison to the same source imaged without photon attenuation. The results show that attenuation correction can compensate for this effect, but with up to 20% overcompensation, which we hypothesize is due to scatter. Reconstructing the image using primary photons reduces the overcompensation (Fig. 5.6), which supports the hypothesis that part of the overcompensation shown in Fig. 5.5 was due to scatter.

The same data were also reconstructed using an OS-EM algorithm which includes models for both the photon attenuation and the collimator response. Interestingly, by comparing the data reconstructed without collimator response (Fig. 5.6) with the results

reconstructed with the collimator response correction (Fig. 5.7), we observed that adding the collimator response model to the reconstruction algorithm also reduced the difference in the voxel values between the data with and without scatter, demonstrating that including the collimator response decreases the effect of scatter and thereby improved quantitative accuracy (Table 5.3). We also found that adding scatter correction (*i.e.*, data points denoted by "♦" *vs.* "○" in Fig. 5.7) to the reconstruction algorithm (in addition to collimator response and attenuation correction) did not have a significant effect on quantitative accuracy.

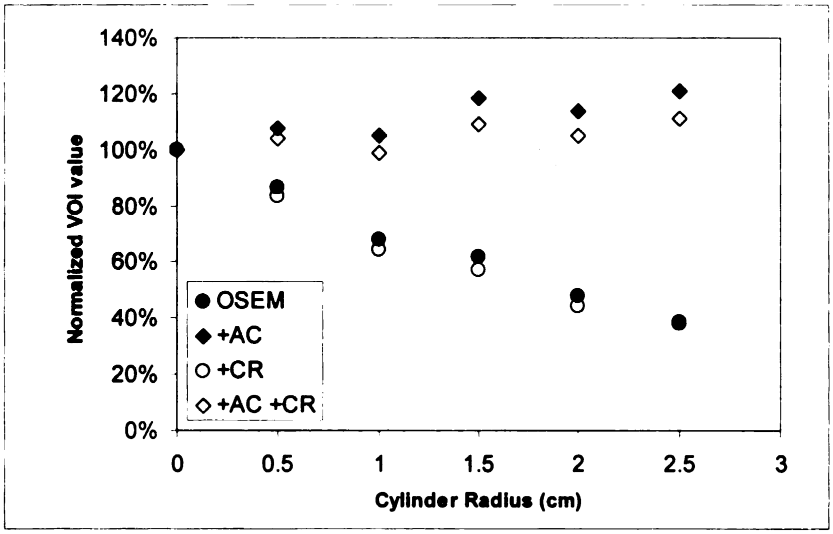

Fig. 5.5: Plot of the mean VOI value as a function of the amount of water around the source for iodine-125. Data are reconstructed with and without attenuation correction (AC), and with and without collimator response (CR).

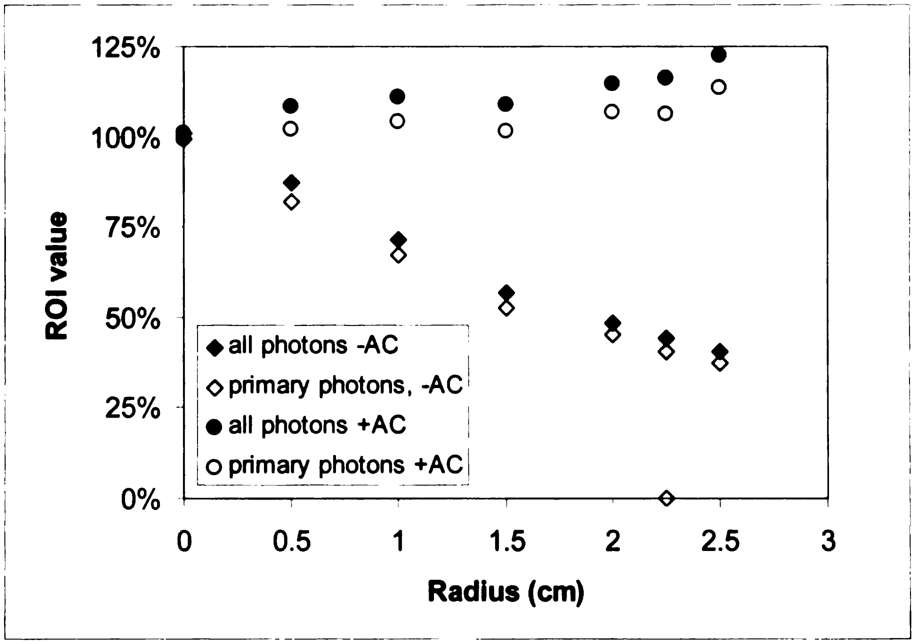

Fig. 5.6: Plot of VOI values as a function of the amount of water around the source for iodine-125. Data were reconstructed with all photons, and again using only unscattered photons. The results show that photon attenuation leads to a decrease in the measured radioactivity of the source, which is compensated by using attenuation correction (AC). There is some overcompensation due to scatter. The effect of the scatter can be seen by reconstructing the data using only unscattered (primary) photons.

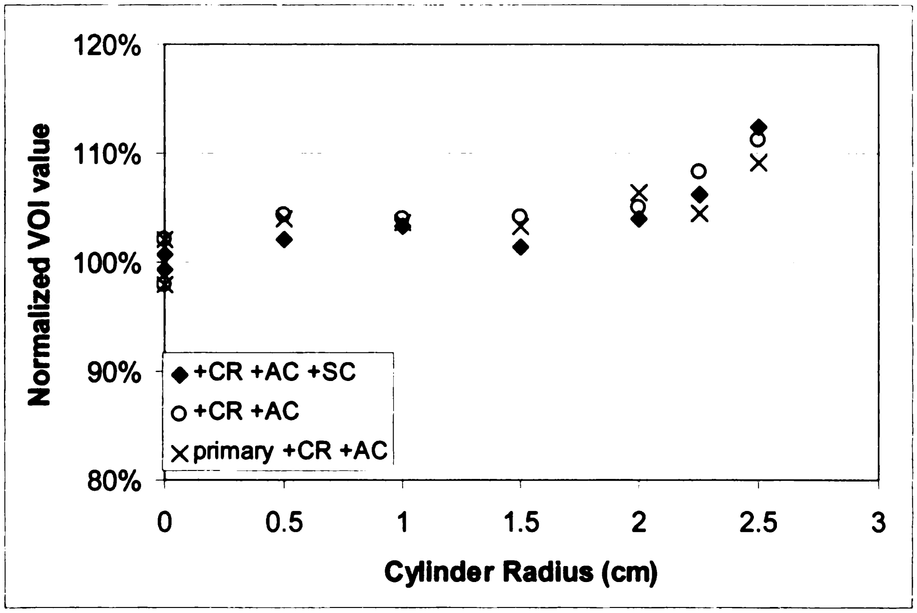

Fig. 5.7: Plot of VOI values as a function of the amount of water around the source for iodine-125. Data were reconstructed using variations of OSEM with collimator response (CR), attenuation correction (AC), and scatter correction (SC). Data with only unscattered (primary) photons were reconstructed using OS-EM with collimator response and attenuation correction.

Table 5.3: Change in a VOI voxel value resulting from scatter in a cylinder of water

Cylinder radius (cm)	Reconstructed with OS-EM with collimator response and attenuation correction	Reconstructed with OS-EM and attenuation correction (no collimator response)
0.0	0.0%	0.0%
0.5	0.3%	6.5%
1.0	0.2%	6.4%
1.5	0.8%	7.8%
2.0	0.5%	8.0%
2.5	3.7%	9.9%

The effects of photon attenuation on data acquired with technetium-99m are shown in Fig. 5.8 by plotting the normalized VOI value as a function of the radius of the cylinder of water surrounding the source. The results show that the effect of attenuation is to decrease the apparent radioactivity of the source, as the average voxel value in the VOI decreases as the size of the cylinder increases. This effect is smaller for technetium-99m (Fig. 5.8) than for iodine-125 (Fig. 5.6), but photon attenuation can still result in a 25% decrease in measured radioactivity in technetium-99m imaging with a rat sized object, which is approximately equal to the decrease in photons due to photon attenuation. The results also show that data reconstructed with attenuation correction do not underestimate the amount of radioactivity in the VOI when the source is surrounded by water.

The effects of photon scatter on data acquired with technetium-99m were assessed by reconstructing simulated projection data with and without scatter using OS-EM. The data were reconstructed both with and without attenuation correction (Fig. 5.9). The average voxel value in the VOI corresponding to the source was calculated, and plotted as a function of the radius of the cylinder of water surrounding the source. The results show that the images reconstructed with attenuation correction do not over-estimate the activity in the source. In general, the quantitative results obtained from the projection data with scatter ("all") did not differ from those obtained from scatter-free data ("primary") regardless of whether or not the data were reconstructed with ("+AC") or without ("-AC") attenuation correction.

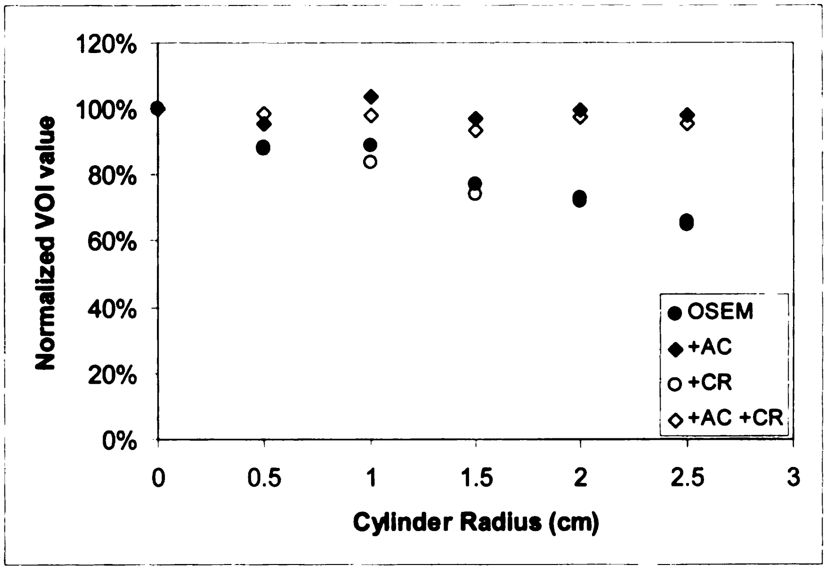

Fig. 5.8: Effect of photon attenuation on technetium-99m images. VOI values are plotted as a function of the radius of the cylinder of water around the source.

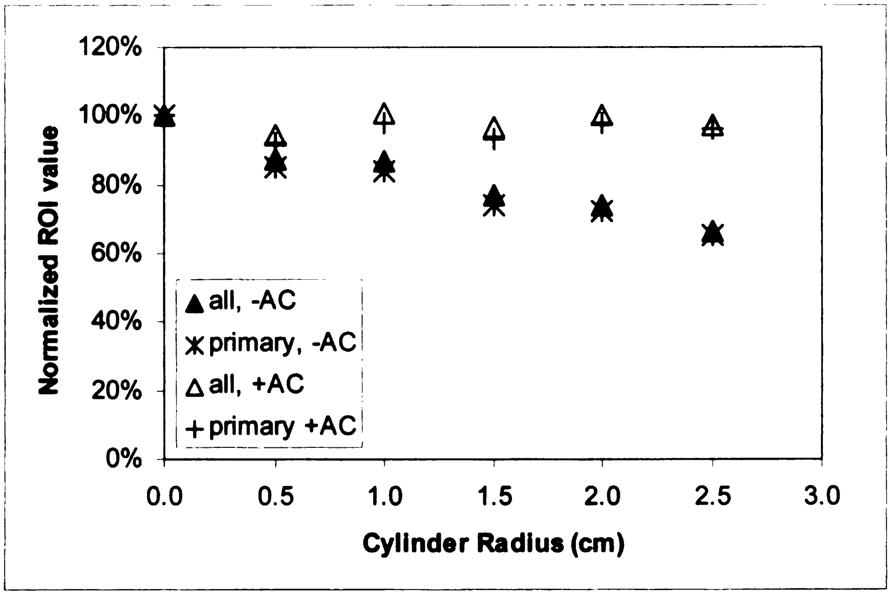

Fig. 5.9: Plot of the average voxel value (normalized to the case with no attenuation) in a VOI corresponding to a spherical source of technetium-99m in a cylinder of water. The projection data were separated into two data sets, one with all detected photons and the other with only unscattered (primary) photons. Data were reconstructed using OS-EM with and without attenuation correction.

UCSF LIBRARY

5.2.2.2. Partial volume effect

The partial volume effect in radionuclide imaging is caused by the limited spatial resolution of SPECT and PET imaging. In small animal SPECT with pinhole collimators, the spatial resolution of the imaging system is dominated by the collimator design, specifically the diameter of the pinhole aperture. Therefore, in the Monte Carlo simulations, we simulated data acquired with both the 1 mm and 2 mm pinhole apertures. For each pinhole aperture size, the average value in the VOI (normalized to the result with a source with a volume of 250 mm^3) was plotted as a function of the source radius. These results are shown in Fig. 5.10. As expected, the smaller sources have a lower measured radioactivity than larger sources, due to "spill-out" of radioactivity. In addition, the effect of source size on measured radioactivity is more pronounced with the larger pinhole, due to the poorer spatial resolution achieved with the larger aperture. However, when data are reconstructed using OSEM with CR, the difference between the larger and smaller pinhole is essentially negligible.

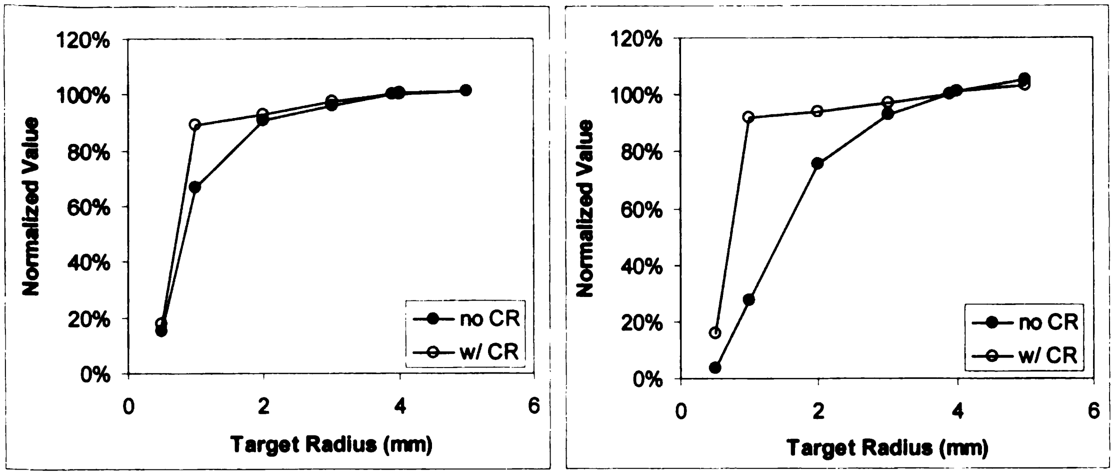

Fig. 5.10: Average VOI value for data reconstructed from simulated data for a 1 mm pinhole (left), and 2 mm pinhole (right). Data are normalized to the result for a 250 μL sphere, and demonstrate the effect of partial volume errors on the measured concentration.

5.2.2.3. Effect of background radioactivity

The measured radioactivity value as a function of source size in the presence of background radioactivity is shown in Fig. 5.11 and Fig. 5.12. These results show that the presence of background radioactivity will influence the measured radioactivity in the volume of interest, particularly for smaller volumes. In general, the presence of background radioactivity tends to cause an increase in the measured radioactivity in the volume of interest, due to "spill-in" caused by the finite spatial resolution. However, with the 2 mm pinhole and collimator response, the presence of background radioactivity causes the measured radioactivity in the volume of interest to be underestimated, particularly in the smaller target volumes. This effect suggests that the reconstruction algorithm behaves in a nonlinear manner because the expected result is that spill-in from the background region will increase the measured activity in the target volume. In addition, the presence of background radioactivity slows the convergence of the reconstruction algorithm (*i.e.*, more iterations are needed in order to reach convergence), especially for smaller volume of interest (Fig. 5.13). This effect would explain part of the decrease in measured values in data with background radioactivity because all the data (both with and without background radioactivity) were reconstructed using 20 iterations.

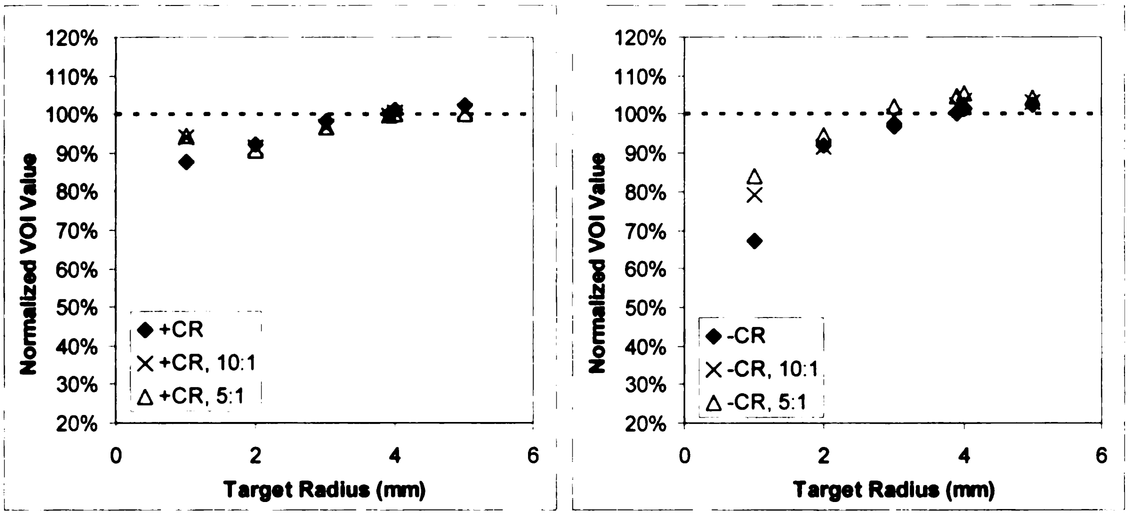

Fig. 5.11: Effect of background radioactivity on voxel values in the volume of interest. The normalized VOI values are plotted as a function of target size for simulated data generated with a 1 mm pinhole. Background radioactivity was added, with target to background ratios of 10:1 and 5:1. Data were reconstructed using 20 iterations of OS-EM with collimator response (left) and 5 iterations of OS-EM without collimator response (right).

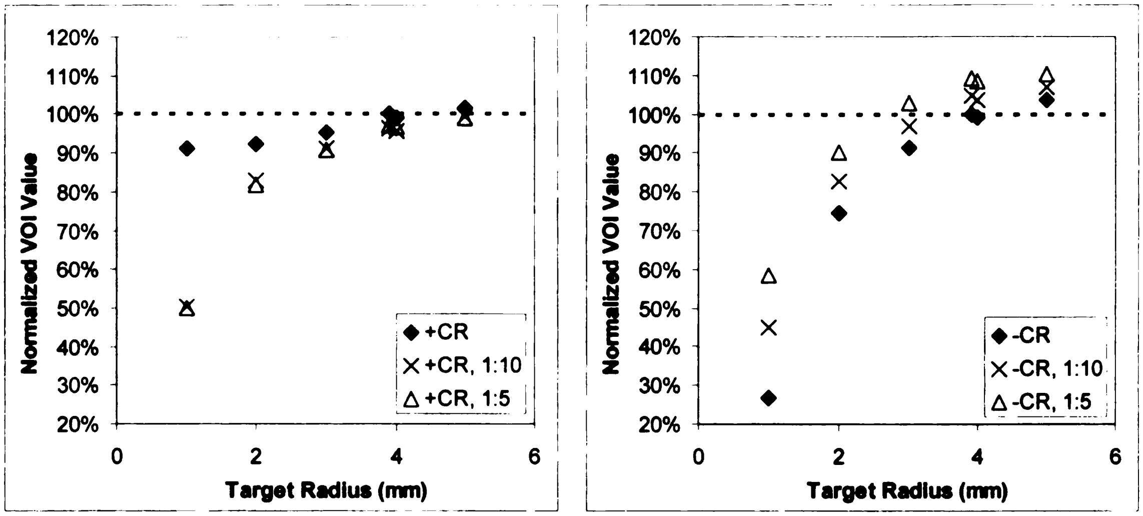

Fig. 5.12: Effect of background radioactivity on voxel values in the volume of interest. The normalized VOI values are plotted as a function of target size for simulated data generated with a 2 mm pinhole. Background radioactivity was added, with target to background ratios of 10:1 and 5:1. Data were reconstructed using OSEM with and without collimator response (+CR and –CR).

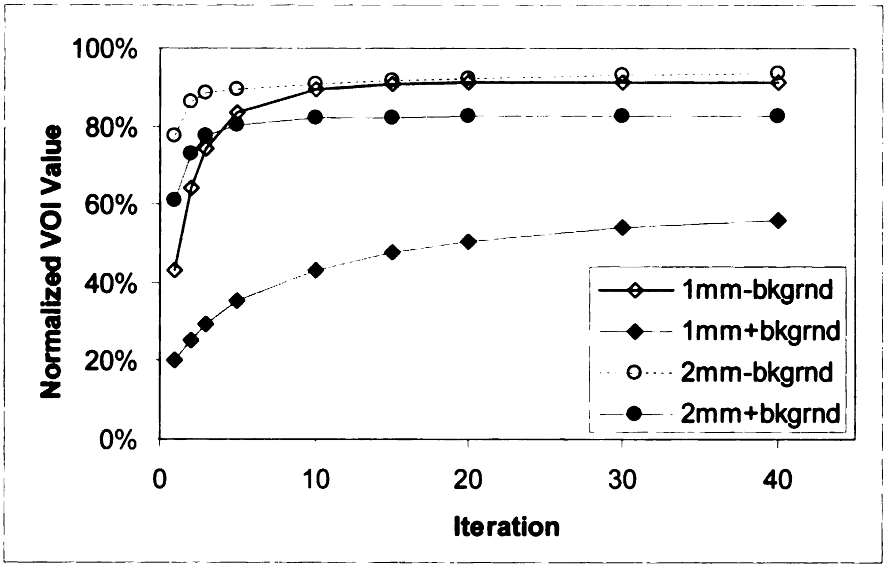

Fig. 5.13: The effect of background radioactivity on the convergence of the reconstruction algorithm is shown in this plot. The mean VOI values are shown as a function of iteration number for target spheres with radius of 1 mm and 2 mm with and without background radioactivity, reconstructed using OSEM with collimator response.

5.2.3. Discussion

5.2.3.1. Effect of scatter

In our simulation, we found that photon scatter did not have much effect on the quantitative accuracy of the image. However, this result probably should not be generalized to all cases because the distributions of both the source and the scattering medium have a strong effect on the scatter. For example, if the volume of interest contained materials with high density and was within a region with large amount of background radioactivity, the effect of scatter might be more apparent. In order to attempt to further study the effect of scatter and scatter correction on quantitative accuracy, we performed an additional Monte Carlo simulation which simulated the imaging of a sphere (radius 2 mm) containing iodine-125 and located within a cylinder with a radius of 1.5 cm. This source was located at the axis of rotation, in the center plane of the image space. A second spherical source of 27.5 keV photons was added (3 mm radius), also on the axis of rotation, but located 1 cm away. The activities of the

sources were 100,000 and 150,000 Bq, respectively. This simulations geometry represents the imaging of a tumor, with uptake of radioactivity in a nearby organ. A total of 64 projections (30 seconds each) were simulated.

After simulation, the projection data were reconstructed, and the effect of scatter on the measured activity in the volumes of interest was determined by reconstructing the projection data both with and without scatter photons using the OS-EM algorithm with collimator response and attenuation correction. We compared the measured radioactivity in the VOI's reconstructed with and without scatter and found that the effect of scatter on the quantitative accuracy was to increase the average voxel value by approximately 5% for the larger volume of interest and by 0.4% for the smaller VOI. This result demonstrates that 1) the effect of scatter on quantitative accuracy when imaging with iodine-125 is fairly small and 2) is dependent on the geometry (*i.e.*, size and locations of the volumes of interest, amount and spatial distribution of radioactivity not in the volume of interest). Reconstruction of the data with scatter correction helped reduce the measured activity in the regions outside of the source, but did not have a large effect on the quantitative measurement of radioactivity within the sources.

5.2.3.2. Effect of background and nonlinearity

When imaging with radionuclide tracers in live subjects, the tracer almost never behaves perfectly, that is, there will be tracer uptake in both the target (*e.g.*, the tumor) and other tissues. As we showed earlier, this background uptake has an effect on the quantitative accuracy of SPECT images. This effect of background radioactivity can be confusing, because the presence of background radioactivity can actually lead to a decrease in the apparent radioactivity in the target volume of interest, instead of increasing the apparent radioactivity due to "spill-in". We hypothesized that this effect

can be attributed to nonlinear behavior of the iterative image reconstruction process. (In contrast, filtered backprojection algorithms such as the Feldkamp algorithms can be demonstrated to be linear in a mathematical sense). We studied this nonlinearity by taking projection data of the background region (which we will denote as B) and projection data of the target region (denoted as T) generated with the 2 mm pinhole (as described in Section 2.1.3) and reconstructing the two sets of projection data separately using OS-EM (with and without collimator response). The resulting tomograms (of the background and target regions, Rec(B) and Rec(T), respectively) were then added together (Rec(T) + Rec(B)), and the summed image compared with the image obtained by reconstructing the combined projection of the target and background regions. If the process was linear, then the difference would be 0, because for a linear reconstruction process:

$$\mathrm{Rec}(T + B) = \mathrm{Rec}(T) + \mathrm{Rec}(B) \qquad (5.1)$$

where Rec is the reconstruction process, T is the projection of the target region, and B is the projection of the background region. The difference in the voxel values in the target region of the resulting images is plotted as a function of target size in Fig. 5.14. When the data were reconstructed with collimator response, the tomogram reconstructed from the combined projection data had a reduced value in the VOI relative to the VOI value in the sum of the tomograms reconstructed from projections of the target and background separately (*i.e.*, $\mathrm{Rec}(T+B)<\mathrm{Rec}(T)+\mathrm{Rec}(B)$). This nonlinear behavior of the OS-EM algorithm for SPECT reconstruction was also observed by Du, *et al.* [9]. This nonlinearity is most noticeable for smaller volumes imaged with large pinholes and reconstructed with collimator response modeling, and is least noticeable with larger

volumes reconstructed without collimator response, which is consistent with the results described in Section 2.2.3 of this chapter.

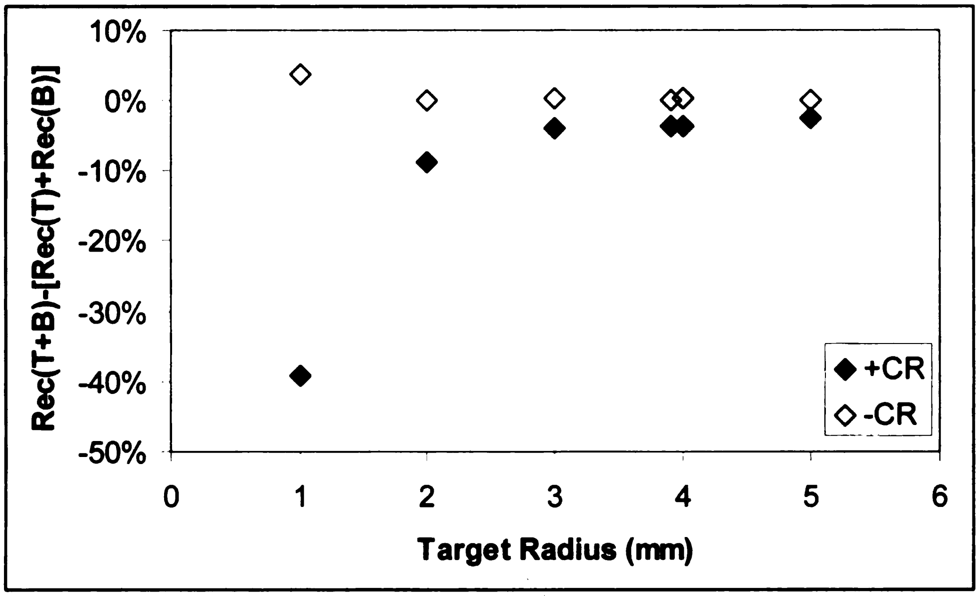

Fig. 5.14: Voxel values in the volume of interest of reconstructed data demonstrate the nonlinearity of the image reconstruction process. Data were generated by reconstructing the projection data (generated using a simulated 2 mm pinhole) from the target and background regions separately, and then summing the results [Rec(T)+R(B)], and by reconstructing the projection data from target and background regions simultaneously [Rec(T+B)]. Reconstruction algorithms with and without collimator response (CR) were used.

5.2.3.3. Detector pixel size

The magnitude of partial errors is strongly affected by the spatial resolution of the imaging system, which in pinhole SPECT is determined by the imaging geometry, the pinhole aperture design, and the spatial resolution of the gamma camera. During the course of this thesis work, a second X-SPECT system was added to the laboratory. As described in Chapter 2, Section 6, this second instrument has a gamma camera with finer pixel pitch (1.5 mm *vs*. 2.2 mm). Therefore, the effect of detector pixel size was studied by performing a set of Monte Carlo simulations where the detector pixel size was reduced to 1.5 mm. The simulations were otherwise identical to the previously described simulations, and the resulting projection data were also reconstructed and analyzed in the

same manner. The results indicated that there is only a minimal reduction in the partial volume effect with the smaller detector pixels (Fig. 5.15), consistent with the fact that the spatial resolution of the system is dominated by the effect of the pinhole aperture size.

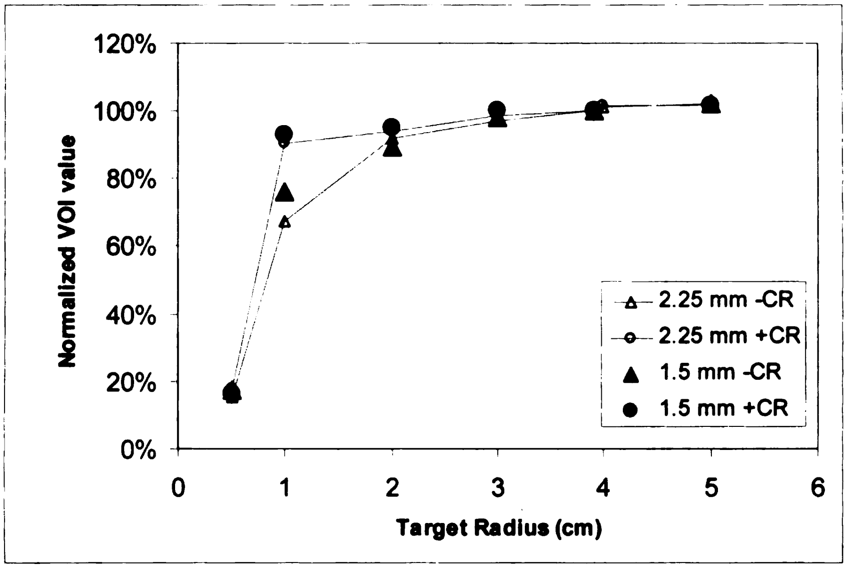

Fig. 5.15: Plot of the VOI values as a function of the target radius for technetium-99m imaged with a 1 mm pinhole. The values were normalized to the results obtained with a 250 μL sphere (*r*=3.91 mm). This plot demonstrates that improving the detector resolution from 2.25 mm to 1.5 mm results in a small reduction in the partial volume effect.

5.3. Experimental measurements

Experimental measurements were performed using the X-SPECT scanner in order to assess the effect of photon attenuation and partial volume effects on quantitative accuracy. Almost all the measurements were performed using technetium-99m rather than iodine-125 because the latter has a long half-life and can form I_2, which is volatile, making this isotope very difficult to handle and decontaminate when spills occur. On the other hand, technetium-99m has a half-life of 6 hours, and disappears within a 3-4 days and thereby represents a lower hazard than iodine-125. In addition, technetium-99m is readily available, inexpensive, and commonly used in radionuclide imaging, making it a very convenient radionuclide for experimental measurements.

5.3.1. Methods and materials

5.3.1.1. Phantoms

Phantom measurements were performed using the X-SPECT scanner in order to test experimentally the ability of SPECT imaging to quantify radioactivity in a rodent-sized object containing a distribution of radioactivity with known geometry and concentration. In addition, the geometry was designed to approximate the size and geometry of biologically relevant targets, such as a tumor in a mouse. For these reasons, a set of hollow microsphere phantoms (Data Spectrum Corporation, Chapel Hill, NC) were used (Fig. 5.16), along with a fillable cylindrical phantom that also served as a mount for the microspheres. These spheres have nominal dimensions listed in Table 5.4, and are referred to as spheres 1 through 4 in the text, with sphere 1 being the largest. The microspheres were filled with aqueous ^{99m}Tc-$NaTcO_4$, and the radioactivity of the filled spheres was measured using a dose calibrator (Biodex Medical Systems) before each experiment.

Table 5.4: Dimensions of microspheres

Sphere Volume (μL)	Outside Diameter (mm)	Inside Diameter (mm)
250	9.86	7.86
125	8.23	6.23
62.5	6.95	4.95
31.3	5.95	3.95

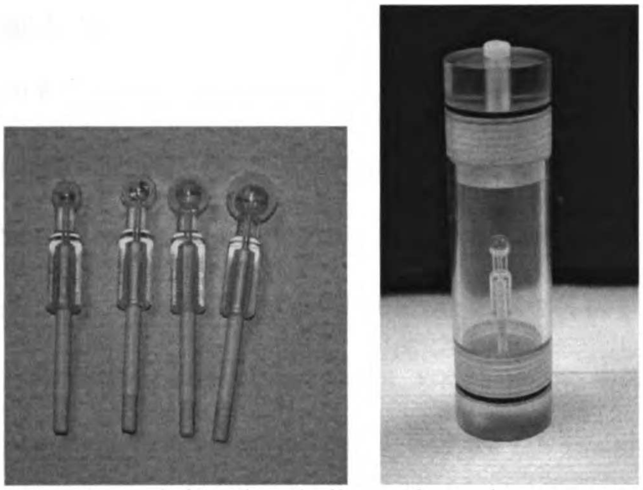

Fig. 5.16: (left) Micro hollow sphere phantoms purchased from Data Spectrum. From left to right, the nominal volumes are 31.3, 62.5, 125, and 250 μL. The dimensions of the spheres are listed in Table 5.4. (right) Micro-sphere phantom mounted inside a water filled cylinder to assess the effect of attenuation.

5.3.1.2. Study of photon attenuation

In order to experimentally assess the effect of photon attenuation on the measured concentration of radioactivity, the largest microsphere was filled with ^{99m}Tc-$NaTcO_4$, and imaged in the phantom both with and without water in the surrounding cylinder. SPECT data were acquired at 64 projections over 360° using the 1 mm pinhole. After SPECT acquisition, CT data were acquired using the parameters in Table 5.5.

The SPECT data were reconstructed using OS-EM both with and without attenuation correction to assess the effect of photon attenuation on the image values in the reconstructed image. The CT data were first reconstructed using the software supplied by the manufacturer of the scanner, and attenuation maps were created from the reconstructed images as described in Chapter 4. The SPECT data were then reconstructed using 5 iterations (8 subsets) of the OS-EM reconstruction algorithm with and without attenuation correction. Following reconstruction, AMIDE software was used to create volumes of interest with size and shape corresponding to the nominal dimensions of the microsphere. The VOI's were then visually placed in the SPECT

image to match the location of the radioactivity in the microsphere as closely as possible, and the total and mean VOI values were determined. The mean voxel value in the VOI was then plotted as a function of the known concentration of radioactivity in the microsphere for data acquired with and without water in the surrounding cylinder. A linear least-squares fit was performed for each case, and the difference in the slopes of the regression lines (*i.e.,* mean voxel value measured from the image vs. known radionuclide concentration multiplied by the imaging time) demonstrated the effect of photon attenuation.

Table 5.5: X-ray CT acquisition parameters for microsphere experiments

Parameter	**Value**
Source to detector distance	298 mm
Detector to center of rotation distance	73 mm
x-ray tube voltage	50 kVp
x-ray tube current	0.6 mA
Number of projections	256

5.3.1.3. Study of partial volume effect

The partial volume effect introduces a size dependent change on the measured concentration of radioactivity in a given volume of interest. We chose to measure the magnitude of that effect in small animal imaging using the X-SPECT system by acquiring SPECT scans of micro-sphere phantoms of different sizes. All data were acquired using a known quantity of ^{99m}Tc-NaTcO$_4$ as measured with a dose calibrator, and the imaging parameters in Table 5.6. Acquisition of SPECT data was followed by CT acquisition at 256 projection angles using the parameters in Table 5.5.

Table 5.6: SPECT imaging parameters for microsphere experiments

Parameter	**Value**
Radius of rotation (cm)	4.0
Time / projection	20 – 40 s
Number of projections	64
Angle range	360 °
Energy window	Tc-99m, -10% to +15%
Collimator	1 mm and 2 mm pinholes

After imaging, the SPECT data were reconstructed using the OS-EM algorithm described in Chapter 4 both with and without collimator response to assess the differences of these reconstruction techniques on quantitative measurements in the reconstructed images. The quantitative measurements from the SPECT image were performed using the known size and shape of the VOI and structural or "anatomic" data from the correlated CT scan to define a volume of interest over the sphere containing the radioactivity. An additional VOI was created to measure the total radioactivity present in the "stalk" of the microsphere (Fig. 5.17). This was used to correct for radioactivity present in the stalk of the microsphere using the following equation which uses the imaging data to estimate the percentage of the total radioactivity that is in the stalk:

$$A_{corr} = A_{total} \cdot \left(1 - \frac{\sum\limits_{stalk} x_i}{\sum\limits_{all\_voxels} x_i}\right) \tag{5.2}$$

where A_{corr} is the corrected radioactivity, A_{total} is the total measured radioactivity introduced into the phantom, and the summations represent the sum of the voxel values in the stalk VOI and the whole reconstructed image, respectively.

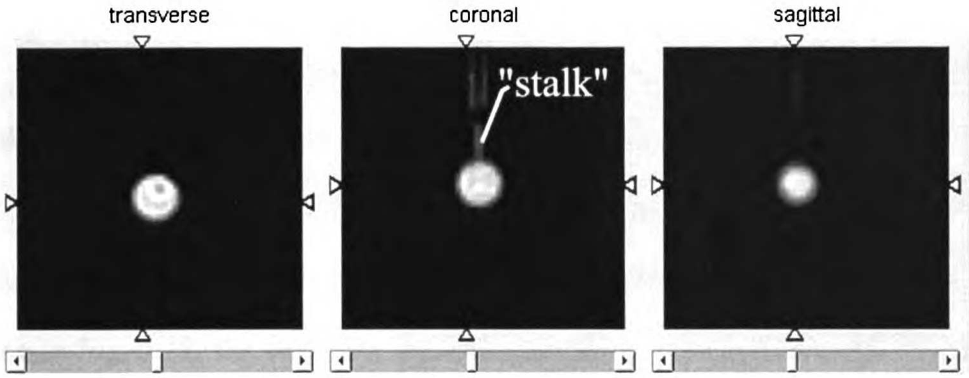

Fig. 5.17: The radioactivity in "stalk" of the microhollow sphere phantom causes an overestimation of the radioactivity in the target region, particularly when using the smaller microspheres.

5.3.2. Results

5.3.2.1. Calibration

The voxel values in the volume of interest in the reconstructed image were plotted as a function of the product of the radioactivity concentration and total imaging time. The results show that, as expected, the voxel values are proportional to radioactivity concentration (MBq-s/L) multiplied by imaging time (Fig. 5.18).

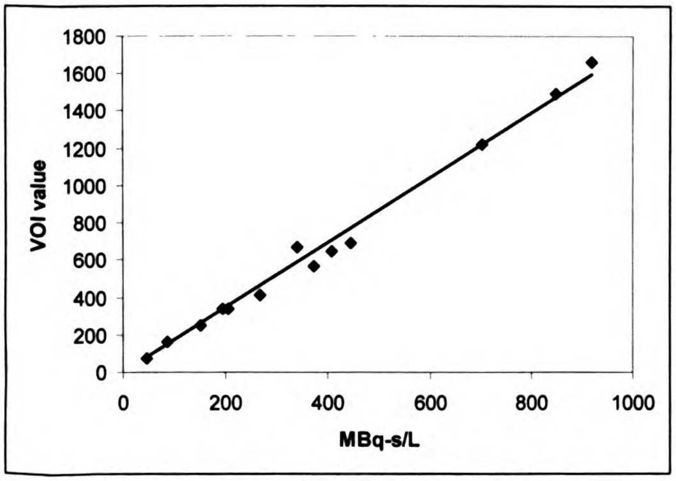

Fig. 5.18: Plot of the voxel values in a VOI corresponding to a 250 μL microsphere filled with techetium-99m imaged with a 1 mm pinhole as a function of the product of radioactivity concentration and imaging time. The data were fit to a line with the intercept forced to zero ($r^2>0.98$).

5.3.2.2. Photon attenuation

The average voxel value in the VOI was plotted as a function of the product of the radioactivity concentration and total imaging time (Fig. 5.19) for the sphere in air (without attenuation) and for the sphere in water (with attenuation). A linear least squares fit with the intercept forced to 0 was performed on each data set. As can be seen in Fig. 5.19, the slope for the data with the sphere in water is 17% lower than the slope for the data with the sphere in air. The difference in slope reflects the effect of photon attenuation on quantitative SPECT measurements. When the data are reconstructed with attenuation correction, the two data sets fall on the same line (Fig. 5.20), demonstrating that attenuation correction removes the quantitative error caused by photon attenuation.

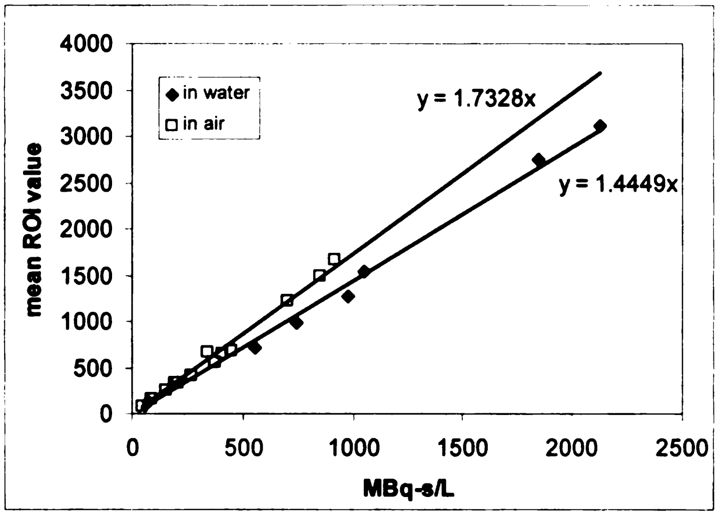

Fig. 5.19: Plot of the average voxel value in the VOI for a technetium-99m filled microsphere. The data were acquired with the sphere either in air or in a water filled acrylic cylinder. Data were reconstructed without attenuation correction, and the difference in the slope reflects the effect of photon attenuation due to the water in the cylinder on the measurement of radioactivity in the sphere.

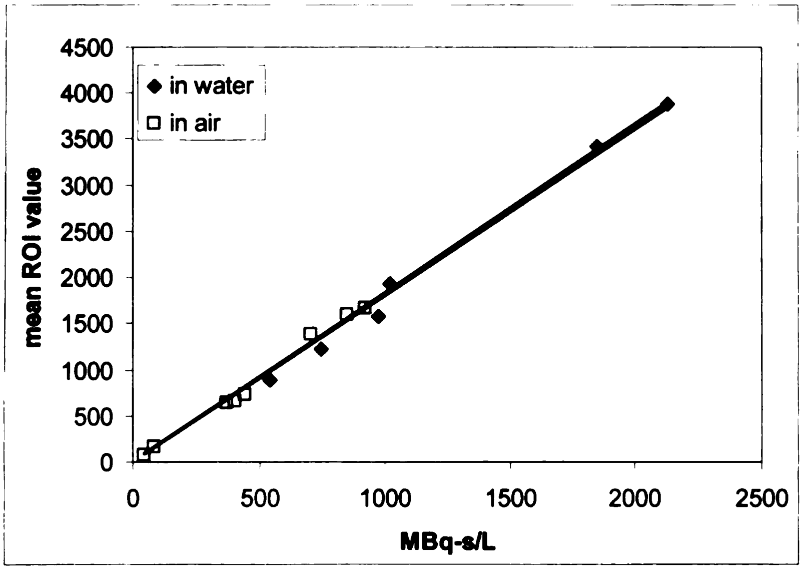

Fig. 5.20: Plot of the average voxel value in the VOI for a technetium-99m filled microsphere. Data were reconstructed with attenuation correction. The data acquired with and without water around the sphere fall on a single line, demonstrating that attenuation correction improves the quantitative accuracy of the result.

5.3.2.3. Partial volume effect

The average voxel value in the VOI was plotted as a function of the product of the radioactivity concentration and total imaging time for data obtained using each of the different sized spheres and reconstructed with OS-EM (Fig. 5.21). A linear least squares fit was performed on each data set, with the intercept forced to 0. This slope can be regarded as a calibration curve for the data, where the inverse of the slope gives the value of the scaling factor needed to convert the image voxel values into absolute concentration of radioactivity multiplied by the imaging time (or radioactive decays per volume) in units of MBq-s/L. The differences in the slopes for spheres of different sizes (Table 5.7) reflect the effect of the sphere size on the measured radioactivity due to partial volume errors. That is, the slopes are lower for the smaller spheres (*i.e.*, Sphere 4 vs. Sphere 1), reflecting that the image values are lower for a given amount of radioactivity are decreased due to partial volume errors when imaging smaller spheres. These data were also reconstructed using OSEM with collimator response (Fig. 5.21), and the same analysis was repeated. Data acquired with the 2 mm pinhole aperture were reconstructed with OS-EM with correction for collimator response ("OS-EM+CR") and without correction for collimator response ("OS-EM"), and analyzed in the same manner (Fig. 5.22). The results of the linear fitting are shown in Table 5.6.

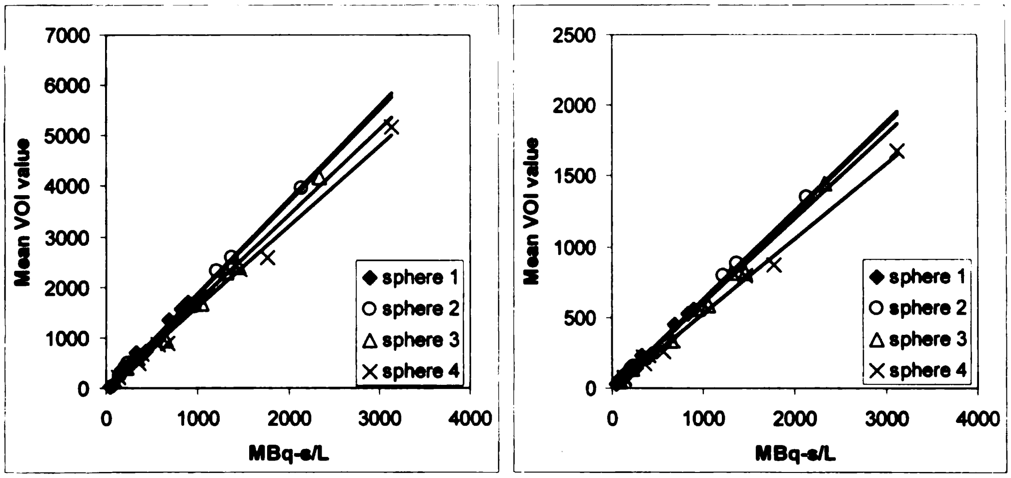

Fig. 5.21: Plot of mean VOI value as a function of radioactivity concentration multiplied by the imaging time. Data were acquired using technetium-99m and a 1 mm pinhole, and reconstructed using OS-EM without collimator response (left), and OS-EM with collimator response (right). The difference in slopes for different size spheres result from the partial volume effect.

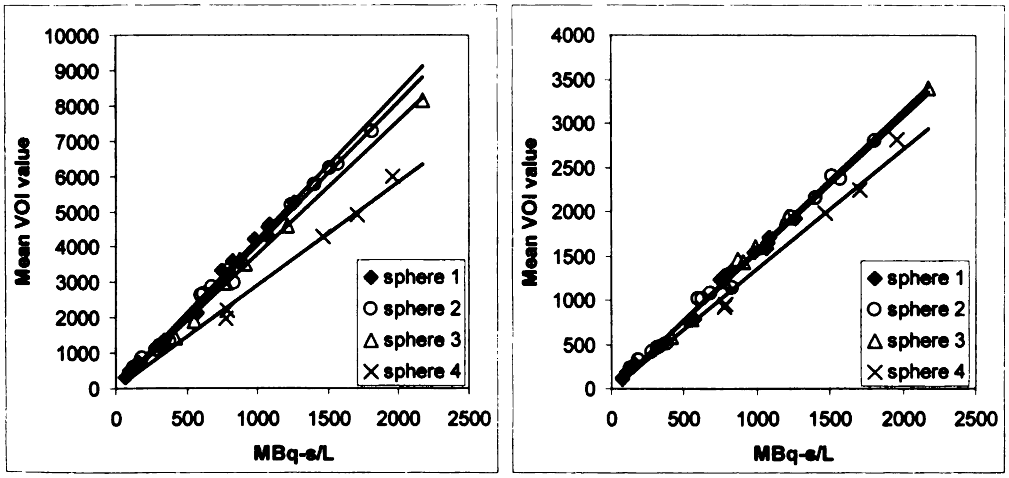

Fig. 5.22: Plot of mean VOI value as a function of radioactivity concentration multiplied by the imaging time. Data were acquired using techetium-99m and a 2 mm pinhole, and reconstructed using OS-EM without collimator response (left), and OS-EM with collimator response (right). The difference in slopes for different size spheres result from the partial volume effect.

Table 5.7: Linear fitting results for VOI values as a function of (activity×time)

Reconstruction algorithm	Sphere Size (mL)	Slope $(\text{MBq-s/mL})^{-1}$	r^2
OS-EM	0.25	1.87±0.04	>0.99
OS-EM	0.125	1.84±0.03	>0.99
OS-EM	0.062	1.72±0.04	>0.99
OS-EM	0.031	1.60±0.03	>0.99
OS-EM+CR	0.25	0.62±0.01	>0.99
OS-EM+CR	0.125	0.63±0.01	>0.99
OS-EM+CR	0.062	0.60±0.01	>0.99
OS-EM+CR	0.031	0.53±0.01	>0.99

Data acquired using 1 mm pinhole.
VOI values [arbitary units] = slope×(activity×imaging time [MBq-s/mL]).

Table 5.8: Linear fitting results for VOI values as a function of (activity×time)

Reconstruction algorithm	Sphere Size (mL)	Slope $(\text{MBq-s/mL})^{-1}$	r^2
OS-EM	0.25	4.12±0.06	>0.99
OS-EM	0.125	4.03±0.07	>0.99
OS-EM	0.062	3.77±0.04	>0.99
OS-EM	0.031	2.93±0.06	>0.99
OS-EM+CR	0.25	1.54±0.02	>0.99
OS-EM+CR	0.125	1.55±0.02	>0.99
OS-EM+CR	0.062	1.58±0.02	>0.99
OS-EM+CR	0.031	1.36±0.04	>0.99

Data acquired using 2 mm pinhole.
VOI values [arbitary units] = slope×(activity×imaging time [MBq-s/mL]).

5.3.3. Discussion

5.3.3.1. Photon attenuation

The experimental data in Fig. 5.19 show the change in measured radionuclide value in a small (2 mm diameter) source when placed in a water-containing cylindrical container, and simulates, for example, the measurement of radionuclide uptake in a small tumor within the torso of a mouse or other small animal. As expected, the radioactivity measured from the image is lower than the actual source radioactivity due to photon attenuation introduced by the water-equivalent material surrounding the source. The results show that photon attenuation due to 1.5 cm of water surrounding a technetium-99m target reduces the apparent radioactivity by almost 20% compared to the data acquired without the surrounding material, which is similar to the result predicted by the Monte Carlo simulation. The results also demonstrate that using CT data for iterative reconstruction based attenuation correction is an effective method for compensating for the effect of photon attenuation on quantitative accuracy.

5.3.3.2. Partial volume effect

When imaging a small target (*e.g.*, a small tumor within a mouse), the limited spatial resolution of the imaging system will blur the image, leading to a reduction in the measured radioactivity in the volume of interest. This was experimentally confirmed by imaging microspheres of various sizes filled with technetium-99m using the X-SPECT system, and the results from Section 5.3.2.2 demonstrate that the partial volume effect will lower the apparent radioactivity present in smaller volumes of interest. The slopes obtained by performing a linear fit to each set experimental data (Table 5.7 and Table 5.8) were normalized to the slope fit to the corresponding data (*i.e.*, using the same pinhole and reconstruction algorithm) obtained with the 250 μL sphere, and the results are plotted in Fig. 5.23 as a function of the sphere radius. As discussed earlier, the smaller spheres tend to have a lower slope due to the reduced image intensity caused by the partial volume effect. Thus, the change in slope reflects the loss in measured radioactivity. For comparison, the results from Section 2.2.2 obtained using data generated with Monte Carlo simulations are also shown in Fig. 5.23. The comparison shows that the decrease in the voxel values in the smallest sphere is slightly larger in the measured data than in the simulation data when the data are reconstructed with collimator response. The following paragraphs discuss some possible causes for this deviation.

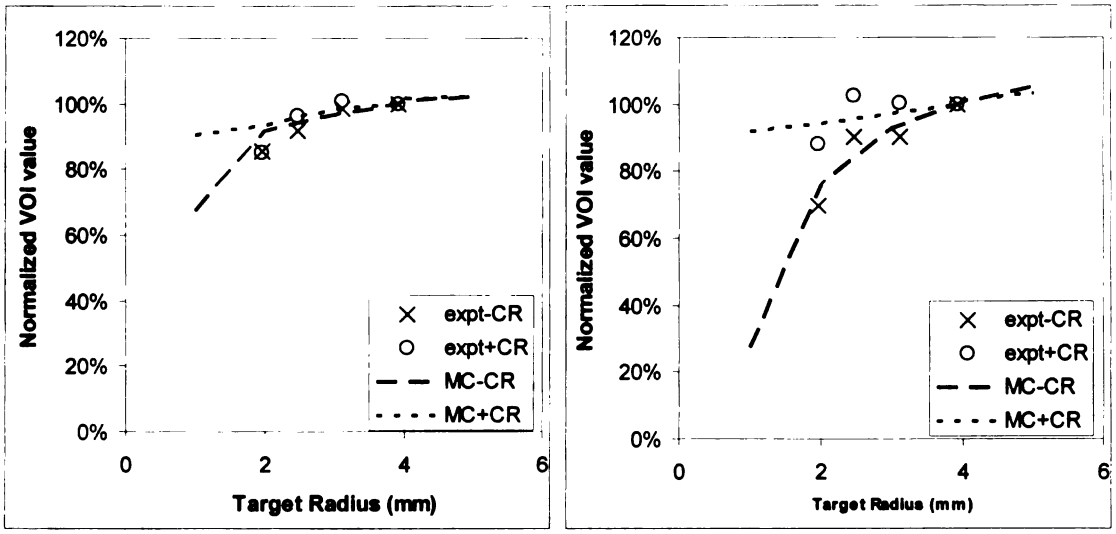

Fig. 5.23: Plot of the average voxel value in a spherical VOI as a function of the radius of the VOI. Data are normalized to the value for a 250 μL VOI. The data are for a technetium-99m source imaged with the (left) 1 mm pinhole aperture, and (right) 2 mm pinhole aperture. For comparison, the results obtained from data generated by Monte Carlo simulation are plotted in the figure (dashed lines) as well.

One possible explanation for the difference between the experimental and simulation is the effect of uncertainties in the imaging geometry on the reconstruction process. The geometry used to generate simulated data is precisely known, but there is slightly uncertainty in the geometry of the experimental measurements. Therefore, we studied the effect of errors in the imaging geometry on the quantitative measurement of radioactivity, by intentionally introducing errors into the geometrical parameters used to reconstruct the data generated by the Monte Carlo simulation. Specifically, we varied the mechanical shift, which describes the alignment of the detector with the axis of rotation. Errors in this parameter have a strong effect on the spatial resolution of the reconstructed images, and hence the partial volume effect.

The projection data were generated using GATE to simulate the imaging of a spherical source with a 2 mm pinhole with no mechanical shift. The projection data were then reconstructed using 20 iterations of OS-EM with collimator response and 5 iterations of OS-EM without collimator response while assuming mechanical shift values of 0.2 mm and 0.5 mm. The mean VOI values in the reconstructed images were measured using AMIDE. The resulting VOI values were normalized to the mean VOI value in the reconstructed image of a 250 μL sphere, and plotted as a function of the source radius (Fig. 5.24). The results demonstrate that changing the value of the mechanical shift has little effect on data reconstructed without collimator response because the blurring introduced by the geometric error is smaller than the spatial resolution of the pinhole aperture (2 mm aperture). However, with collimator response, the extra mechanical shift has the effect of increasing partial volume errors with smaller sized targets.

Other possible causes for the increased partial volume error in experimental data include count rate effects (discussed below), VOI volume, VOI placement, and errors filling the phantom, *e.g.* the radioactivity in the stalk. Most of these effects are magnified with the smaller spheres, and could be partially responsible for the difference between the measured and predicted results. For example, the volume of interest was defined as a sphere with a volume equal to the nominal volume of the microsphere and was placed on the image based on the reconstructed CT and SPECT images to encompass the activity as shown on the image. If the VOI excluded any area with radioactivity, then the result would underestimate the total radioactivity in the sphere. Although the VOI's were placed as carefully as possible, discrepancies between the volume of interest and the radioactivity distribution are possible. The smaller spheres would be particularly sensitive to this sort of error. For example, an error in the position of the VOI by 0.3 mm (approximately half a voxel in the SPECT image) will lead to the exclusion of 12% of a 31 μL sphere, but would only result in the exclusion of 6% of a

250 μL sphere from the volume of interest. The exclusion of part of the sphere from the VOI would cause a decrease in the measured radioactivity in the volume of interest.

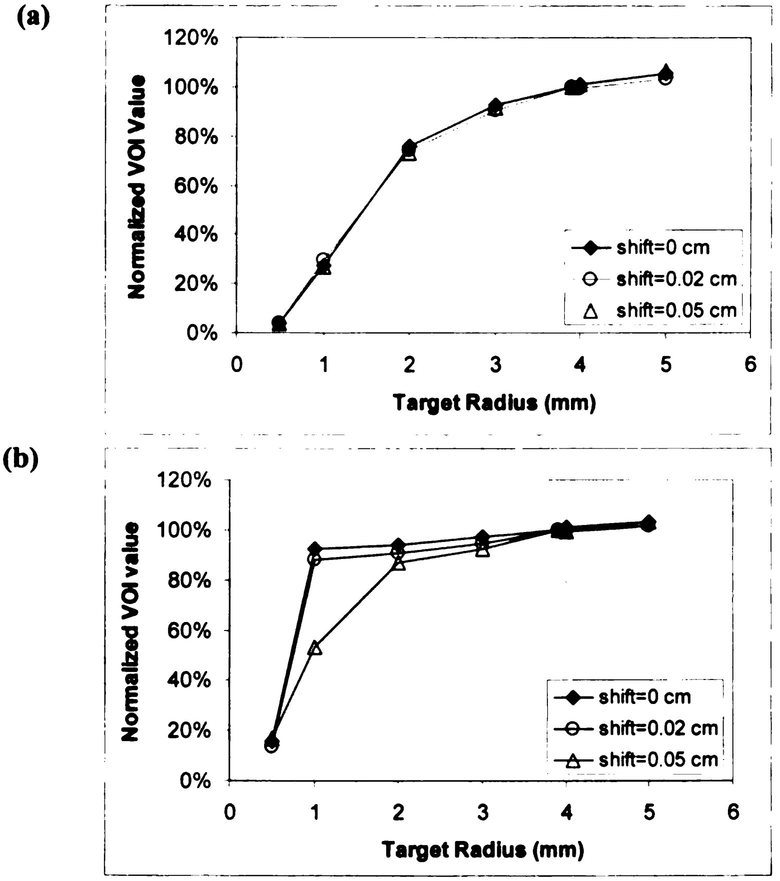

Fig. 5.24: Plot of the average voxel value in the VOI of simulated data reconstructed with various values for mechanical shift (target value=0). The VOI values are normalized to the value of the 250 μL sphere. Data were reconstructed using OS-EM (a) and OS-EM with collimator response (b).

5.3.3.3. Count rate effect

Another discrepancy between the measured data and the expected results can be seen in the graph on the right side of Fig. 5.23, where the apparent radioactivity in the largest sphere is actually slightly lower than the apparent radioactivity in the second and third largest spheres, although we expect the smaller spheres to have slightly lower apparent radioactivity due to the partial volume effect. An investigation found that this deviation could be attributed to the count rate effect.

The count rate effect is due to limitations in the rate at which gamma camera electronics can process signals, that is, the proportion of photons recorded by the detector decreases with increased event rate. This causes a loss of "counts" when imaging objects containing large amounts of radioactivity, and therefore causes the amount of radioactivity in the sphere to be underestimated when imaging high levels of radioactivity at high event rates. In order to determine if the X-SPECT gamma camera has a significant count rate limitation, projection data were acquired using a 250 μL microsphere containing technetium-99m. The gamma camera was fitted with a 2 mm pinhole aperture, and the phantom placed approximately 4 cm from the pinhole. Data were acquired over a period of approximately 2 days in order to allow the technetium-99m in the phantom to decay, thus decreasing the amount of radioactivity in the phantom by 2^8 or 256-fold. The count rate (counts measured divided by imaging time) was plotted as a function of the radioactivity in the phantom (Fig. 5.25). The results show that the relationship between the measured count rate and the known radioactivity content is not linear. At high levels of radioactivity, the count rate deviates from a line fitted to the data acquired with low levels of radioactivity. Thus, it is clear that high count rates cause a loss of counts, leading to a decrease in the measured radioactivity. This effect is most evident with larger spheres imaged using the 2 mm pinhole aperture. The microsphere data acquired with the 2 mm pinhole in Fig. 5.23 were adjusted to compensate for the effect of count rate, and compared again with Monte Carlo results in Fig. 5.26. These results that have been corrected for the count rate effect show a closer agreement to the results obtained with Monte Carlo simulation.

The count rate limitation was significant when the radioactivity in the phantom was over approximately 200 MBq (5.4 mCi). This is a relatively high amount of radioactivity, and is higher than the amounts (i.e., < 37 MBq) that we normally use in small animal imaging, although higher amounts have been used in animal experiments in the past [10]. This level (>200 MBq) of radioactivity was used for phantom studies involving larger microspheres, but the smaller microspheres usually had lower levels of radioactivity due to their smaller volume. In addition, this data were acquired with the 2 mm pinhole aperture with a 4 mm radius of rotation. If the data were acquired using a smaller (*i.e.*, 1 mm) pinhole or a larger of radius of rotation, the reduced detection efficiency would allow higher levels of radioactivity to be imaged without significant losses due to count rate limitations.

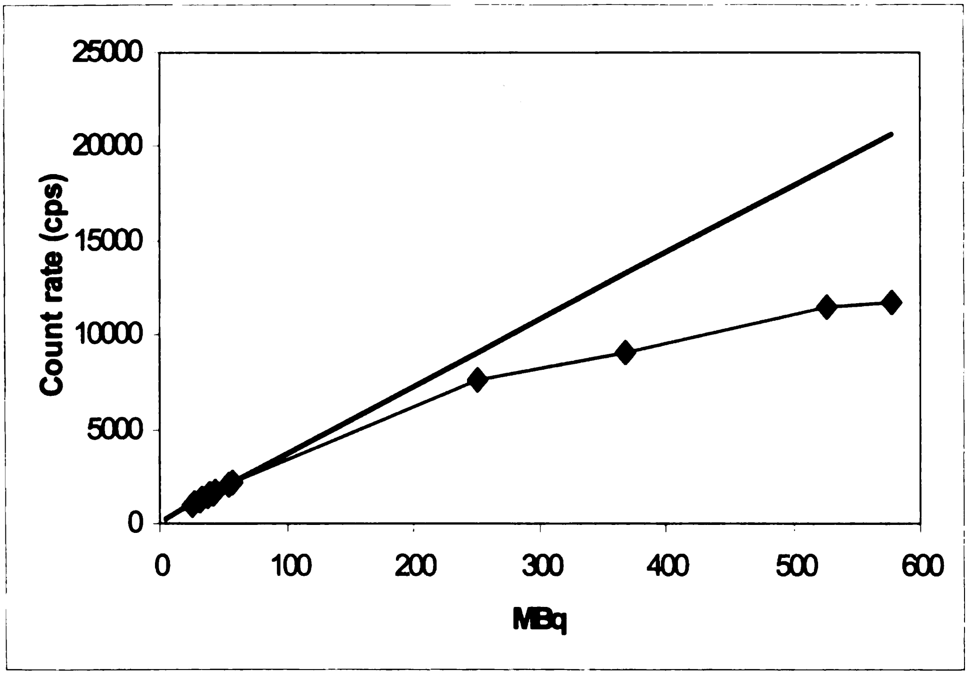

Fig. 5.25: Plot of the measured count rate as a function of the radioactivity in the phantom. The data were acquired with a 2 mm pinhole at a nominal radius of rotation of 4 cm. The line is extrapolated from data acquired with less than 60 MBq in the phantom. The deviation of measured count rates from this line at high radioactivity is most likely due to a count rate limitation in the gamma camera.

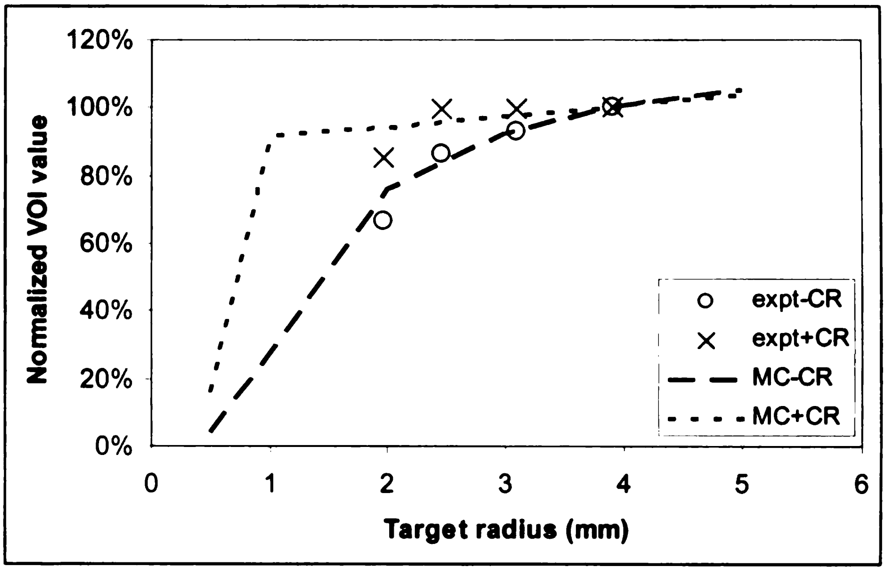

Fig. 5.26 Plot of the average voxel value in a spherical VOI as a function of the radius of the VOI. Data are normalized to the value for a 250 μL VOI. The data are for a technetium-99m source imaged with a 2 mm pinhole aperture, .and have been adjusted for the effect of count rate.

5.3.3.4. Partial volume correction methods

Partial volume errors can lead to a significant underestimation of the radioactivity in smaller volumes of interest, as shown in the previous section. The magnitude of these errors is dependent on the characteristics of the imaging system (specifically the spatial resolution) and the size and shape of the volume of interest. Because x-ray CT is an anatomical imaging modality, it can provide information about the size and shape of structures, which can then be used to improve the quantitative accuracy of the SPECT data. We will describe one such method called template projection-reconstruction.

Template projection-reconstruction is described by Tang [11], and uses the *a priori* anatomical information to compensate for partial volume errors. In this method, volumes of interest are defined on the CT images of the target and neighboring structures. These "templates" are given unit concentrations of radioactivity, and projection data for each template are calculated using a realistic model of the imaging system. The projection data are then reconstructed with the same reconstruction algorithms used to reconstruct the radionuclide (*i.e.*, SPECT) data. The reconstructed templates can then be used in one of several ways. One application is to divide the reconstructed SPECT image by the reconstructed template of the target on a voxel by voxel basis prior to calculating the average activity concentration in the target volume. This will effectively apply a size and shape dependent correction to the target volume of interest. Tang also describes methods to use this technique to correct for the effect of "spill-in" from neighboring structures. However, his analysis assumed that the reconstruction process is linear, which is not strictly true for OS-EM (or ML-EM) algorithms, particularly when data acquired using a larger pinhole aperture are reconstructed using an algorithm that models the collimator response. This problem may be avoided by using an iterative algorithm that does not model the collimator response, and thus behaves in a more linear manner, or by using an analytical algorithm that behaves linearly such as filtered backprojection.

Because iterative reconstruction are not necessarily linear, Du *et al.*, describe a method that is similar to the template projection-reconstruction method that the authors call the pGTM (perturbation based Geometric Transfer Matrix) method to correct partial volume errors in brain imaging [9]. The pGTM method treats the measured activity in a volume of interest as the linear combination of true activities:

$$\vec{a} = W \cdot \vec{A} \qquad (5.3)$$

where $\vec{a}$ is a vector describing the measured activity in the volumes of interest, matrix W is called the geometric transfer matrix, and vector $\vec{A}$ contains the true activities. If the values of matrix W can be determined, then the true activity values can be calculated from the measured values. In the GTM (Geometric Transfer Matrix) method, the values in *W* are essentially calculated using the method of template projection-reconstruction. In the pGTM method, the authors account for the nonlinearity of the reconstruction process by calculating the elements of *W* by taking the reconstructed SPECT image, perturbing the voxel values in each VOI in turn, creating projections, and then reconstructing the data. The effect of the perturbation on the reconstructed image can then be used to determine the value of the elements in matrix *W*, or in other words, determining the effect of the presence of radioactivity in a given VOI on the measured activity in the other VOI's.

Both the template projection-reconstruction and pGTM methods utilize *a priori* anatomical information to compensate for the effects of partial volume errors on the quantitative accuracy of SPECT images. Because of the ready availability of coregistered CT data when imaging with a SPECT-CT system, these techniques can potentially improve the quantitative accuracy of data acquired with small animal SPECT-CT systems. However, these methods are labor intensive, as volumes of interest need to be defined manually on the x-ray CT images, and computationally expensive, as multiple "projections" and reconstructions need to be performed.

5.4. Conclusion

In this chapter, we have used Monte Carlo simulations to demonstrate the effect of various physical perturbations on the quantitative accuracy of small animal SPECT data. Specifically, we examined the effect of partial volume errors, photon attenuation, and photon scatter. We then studied the use of improved reconstruction algorithms to compensate for these effects.

The results from simulated data predicted that partial volume errors will affect the quantitative accuracy of microSPECT measurements. These errors will reduce the measured radioactivity of small sources of radioactivity, and become more pronounced when the volume of interest becomes smaller, or when the spatial resolution is poorer. The results predict that including the collimator response in the reconstruction algorithm can reduce the partial volume errors when using the 2 mm pinhole aperture, but that the collimator response correction does not give significant improvements when using the 1 mm pinhole aperture.

The simulations also predicted that photon attenuation has a significant effect on the quantitative accuracy of iodine-125 images, and may have a measurable effect on technetium-99m, although the effects are significantly smaller than those found in human imaging [12]. The deleterious effects of photon attenuation on quantitative accuracy can be compensated for by using an iterative reconstruction algorithm with CT based attenuation correction.

We found that photon scatter only has relatively minor effects on the quantitative accuracy and image quality of SPECT images acquired in small animals. Photon scatter was found to be significant only with for data recorded with relatively wide energy windows, typically low energy photons such as those emitted by iodine-125. Scatter radiation can cause approximately 10% overestimation of radioactivity in data reconstructed with attenuation correction. In the geometries studied, reconstruction based scatter correction algorithm resulted in a slight qualitative improvement in the resulting images, but did not significantly improve the quantitative accuracy of the results.

The results obtained with Monte Carlo simulation were verified using experimental measurements with microsphere phantoms. In these measurements, we found that count rate limitations of the camera will decrease the apparent radioactivity in certain circumstances.

References

[1] W. A. Weber, M. Schwaiger, and N. Avril, "Quantitative assessment of tumor metabolism using FDG-PET imaging," *Nuclear Medicine and Biology*, vol. 27, pp. 683-687, 2000.

[2] K. Van Laere and H. Zaidi, "Quantitative analysis in functional brain imaging," in *Quantitative Analysis in Nuclear Medicine Imaging*, H. Zaidi, Ed. New York: Springer Science+Business Media, Inc, 2006, pp. 435-459.

[3] H. Zaidi and B. H. Hasegawa, "Attenuation correction strategies in emission tomography," in *Quantitative Analysis in Nuclear Medicine Imaging*, H. Zaidi, Ed. New York: Springer Science+Business, Inc, 2006, pp. 167-204.

[4] D. Strul, G. Santin, D. Lazaro, V. Breton, and C. Morel, "GATE (Geant4 Application for Tomographic Emission): a PET/SPECT general-purpose simulation platform," *Nuclear Physics B (Proc. Suppl.)*, vol. 125, pp. 75-79, 2003.

[5] G. Santin, D. Strul, D. Lazaro, L. Simon, M. Krieguer, M. Vieira Martins, V. Breton, and C. Morel, "GATE: A Geant4-based simulation platform for PET and SPECT integrating movement and time management," *IEEE Transactions on Nuclear Science*, pp. 1516-1521, 2003.

[6] A. M. Loening and S. S. Gambhir, "AMIDE: A free software tool for multimodality medical image analysis," *Molecular Imaging*, vol. 2, pp. 131-137, 2003.

[7] H. H. Ertl, L. E. Feinendegen, and H. J. Heiniger, "Iodine-125, a tracer in cell biology: physical properties and biological aspects," *Physics in Medicine and Biology*, vol. 15, pp. 447-456, 1970.

[8] Y. S. Gur, T. H. Farncombe, P. H. Pretorius, H. C. Gifford, M. V. Narayanan, D. Gagnon, and M. A. King, "Comparison of scatter compensation strategies for myocardial perfusion imaging using Tc-99m labeleld sestamibi," *IEEE Transactions on Nuclear Science*, vol. 49, pp. 2309-2304, 2002.

[9] Y. Du, B. M. W. Tsui, and E. C. Frey, "Partial volume effect compensation for quantitative brain SPECT imaging," *IEEE Transactions on Medical Imaging*, vol. 24, pp. 969-976, 2005.

[10] M. C. Wu, "Development and Application of a High-Resolution Nuclear Medicine Imaging System," Ph.D. dissertation, University of California San Francisco and University of California Berkeley, Berkeley, CA, USA, 2001.

[11] H. R. Tang, "A Combined X-ray CT-Scintillation camera System for Measuring Radionuclide Uptake in Tumors," Ph.D. dissertation, University of California at Berkeley and University of California at San Francisco, Berkeley, CA, USA,1998.

[12] G. El Fakhri, I. Buvat, H. Benali, A. Todd-Pokropek, and R. Di Paola, "Relative Impact of Scatter, Collimator Response, Attenuation, and Finite Spatial Resolution Corrections in Cardiac SPECT," *Journal of Nuclear Medicine*, vol. 41, pp. 1400-1408, 2000.

Chapter 6: Application of Quantitative Imaging

6.1. Background

Although current methods rely on visual interpretation of image results, quantitative imaging with SPECT and PET has the potential to yield *in vivo* functional and physiological measurements that could be compared objectively against themselves and against expected normal values. Quantitative radionuclide imaging also would allow accurate radiation dosimetry of radionuclide labeled cancer-targeted agents for the purposes of treatment planning or monitoring therapeutic response. Interest in radionuclide quantification has expanded with the recent advent of small animal radionuclide imaging, which has multiple applications in biological research that would benefit from improved quantitative accuracy. The techniques and methods described in the previous chapters such as geometric calibration and attenuation correction certainly improve the quantitative accuracy of the reconstructed image data. In this chapter, we apply these methods to a phantom study to help assess the quantitative accuracy of radionuclide measurements performed using SPECT-CT. We then describe an experiment where we evaluate radionuclide quantification in a study of a new radiotracer using a mouse model of prostate cancer.

6.1.1. SPECT imaging in prostate cancer

SPECT imaging plays an important role in the staging and diagnosis of prostate cancer, which is a common cancer in American males, with approximately 200,000 new cases diagnosed annually [1]. A wide variety of treatments are available, ranging from external beam radiation therapy to surgery. As with most cancers, the optimal choice of treatment is dependent on the extent of the disease. For example, surgery to remove the prostate (*i.e.*, prostatectomy) is a viable option only if the disease has not spread beyond the prostate gland. One method to determine the presence of metastatic disease is SPECT-CT imaging with ^{111}In-ProstaScint® (capromab pendetide, Ctyogen Corp.) [2].

^{111}In-Prostascint is based on the monoclonal antibody to the prostate specific membrane antigen (PSMA). Therefore, Prostascint will preferentially bind to cells expressing high levels of PSMA. Although PSMA is present in normal prostate tissues, it is over-expressed in prostate cancer cells, making ^{111}In-Prostascint a useful agent for imaging metastatic prostate cancer.

In addition to acting as a target for imaging agents, PSMA is a potential target for radioimmunotherapy for the treatment of metastatic prostate cancer. Radioimmunotherapy is the treatment of cancer using radiolabeled antibodies to deliver radiation (using beta-emitters) to cancer cells, combining the effects of radiation and monoclonal antibody therapy in a single treatment. Therefore, an experimental agent has been developed using the anti-PSMA monoclonal antibody (7E11) labeled with lutetium-177 [3].

Lutetium-177 is a radioactive isotope that can be used for delivering therapeutic doses of radiation. This isotope decays to hafnium-177 via beta decay, with a half-life of 6.7 days. The β^- emission in the decay of lutetium-177 makes it a useful isotope for radioimmunotherapy, because the β^- particles have a short range and thus deposit energy close to the decay site.

In addition to delivering a therapeutic dose of radiation, lutetium-177 also emits photons that can be imaged using a gamma camera. In the radioactive decay process, lutetium-177 emits photons ranging in energy from 71 keV to 321 keV, with the dominant emissions at 113 and 208 keV, well within the energy range useful for SPECT imaging. The photon energy of 208 keV qualifies lutetium-177 as a medium energy imaging isotope, along with isotopes such as indium-111. The higher photon energy has implications for image quality, such as increased septal penetration and depth of interaction effects, decreased scatter and photon attenuation, improved energy resolution, and decreased detection efficiency. The detection of photons of two different energies will affect attenuation correction and collimator response correction, as the 113 keV and 208 keV photons will be attenuated differently in the tissue and collimator material.

6.1.2. Animal model

The lutetium-177 labeled immunoconjugate is being characterized at our laboratory in animals to study the distribution of the agent as a function of time. The animal model being used for this study is a mouse model for metastatic prostate cancer. This cancer model uses nude mice injected with cells from the LNCaP cell line, which was derived from a lymph node metastasis of human prostate carcinoma [4]. The result is a mouse that develops a tumor with the characteristics of metastatic prostate cancer. In addition, we will use this data to test the ability of SPECT-CT to quantitatively measure the tumor uptake of this lutetium-177 labeled antibody *in vivo*.

6.2. Monte Carlo simulations

Because of the unique imaging characteristics of lutetium-177 (*i.e.*, dual energy photon emissions), Monte Carlo simulations were first performed to estimate the effect of perturbations such as photon attenuation and partial volume errors on the quantitative accuracy. These simulation studies were based on the methods and results described in the earlier chapters for imaging with iodine-125 and technetium-99m, and formed a base on which subsequent phantom and animal studies could be discussed and interpreted.

6.2.1. Methods

6.2.1.1. Simulations to study partial volume errors

The first set of Monte Carlo simulations was performed to assess the effect of partial volume errors on quantitative accuracy when imaging lutetium-177 pinhole aperture, by simulating the imaging of spheres of different sizes and determining the change in image values as a function of the target size. The simulations were performed using the GATE ("Geant4 Application for Tomographic Emission") Monte Carlo simulation package [5, 6] using the simplified geometry based on the X-SPECT system described in Chapter 5. In the simulation, the detector had a pixel size of 1.5 cm×1.5 cm (based on the new X-SPECT scanner described in Chapter 2, section 6), and was equipped with a 2 mm pinhole collimator. The simulation parameters (*e.g.*, pinhole size, number of projections, radius of rotation) were chosen to approximate those used in the animal study, and are listed in Table 6.1. The simulation was performed several times, to simulate the imaging of spherical sources of different size located at the center of the imaging system. The sources emitted photons at 208 keV and 113 keV, in a ratio of 1.72:1, to reflect the relative abundance of the photons emitted by lutetium-177. The radius of the sources was varied from 0.5 mm to 5.0 mm, and the amount of simulated radioactivity per volume was kept constant (2000 Bq/mm^3 for the 208 keV photon, 1163 Bq/mm^3 for the 113 keV photon). A total of 64 projections each simulating 30 seconds of imaging time were generated for each size source. The photon emission angles were restricted to be within a solid angle of 0.5π radians of the pinhole aperture to increase the efficiency of the simulation. The projection data were reconstructed, and the mean voxel value was determined in the volume of interest corresponding to the source. Because the different sized sources had the same concentration of radioactivity, differences in apparent radioactivity as a function of source size can be attributed to the partial volume effect.

Table 6.1: Parameters for Monte Carlo simulations

Parameter	**Value**
Collimator focal length	9.0 cm
Radius of rotation	4.0 cm
Detector pixels	81×81
Detector pixel size	1.5 mm × 1.5 mm
Energy resolution	10.5% FWHM
Energy window	208 keV ±10% 113 keV ±10%
Photon energy	113 keV, 208 keV

6.2.1.2. Simulations to study photon attenuation and scatter

The effect of photon attenuation was also studied using Monte Carlo simulations. A spherical source of lutetium-177 was placed in the center of a cylinder of water, and simulated projections were generated using various values for the radius of the cylinder from 0 to 2 cm. The source was simulated to have emissions at 208 keV and 113 keV, and had a radius of 2 mm. The other imaging parameters were as described in Table 6.1. The projection data were reconstructed, and the measured amount of radioactivity in the source was plotted as a function of the radius of the cylinder to provide an estimate of the effect of photon attenuation on the measurement of radioactivity. Data were also reconstructed with attenuation correction to verify that attenuation correction improves the quantitative accuracy of the SPECT measurement.

The output data were also used to estimate the scatter-to-primary ratio as a function of the cylinder size. Furthermore, the simulation output was used to create two sets of data from each simulation, consisting of one set of projection data with all photons detected within the energy window, and another set of projection data with only unscattered photons detected within the energy window, which constituted a "scatter-free" data set.

6.2.1.3. Simulation to study the effect of the radius of rotation

An additional set of simulations were performed to study the quantitative effect of varying the radius of rotation. In this simulation, the source was a 2 mm spherical source imaged with a radius of rotation was set to 5.0 cm, and the other parameters held constant. The data were reconstructed, and the mean voxel value in the volume of interest (VOI) was determined to verify that the radius of rotation did not affect the measured amount of radioactivity.

6.2.1.4. Image reconstruction

When an OS-EM or ML-EM algorithm is used to reconstruct data, the results can be noisy as the algorithms approach convergence. Theoretically, the noise is not an obstacle to quantitative accuracy, as we are usually interested in the mean voxel value in a volume of interest, and are using anatomical information from CT data to define the volume of interest. In addition, the ML-EM and OS-EM algorithms are known to conserve counts, so noise will not affect the average voxel value in the image. However, practical considerations (*e.g.*, uncertainty about the VOI boundary) make it desirable to limit the noise to prevent the inclusion or exclusion of a few voxels from having undue influence on the mean value of a given VOI.

One method to reduce noise is to apply a low pass or smoothing filter to the reconstructed image. An alternative method to suppress the noise is to impose a constraint on the image estimate in the reconstruction algorithm using a MAP (*maximum-*

a-posteriori) reconstruction algorithm. Implementing a MAP reconstruction algorithm requires a modification to the objective function, which in ML-EM is the likelihood of measuring the observed data given a particular radionuclide distribution. We chose to implement a MAP algorithm by modifying the OS-EM algorithm by adding a constraint to the image estimate similar to the one described by Nuyts, *et. al* [7]:

$$M(\lambda) = -\beta \sum_{j} \sum_{k \in N_j} \frac{(\lambda_j - \lambda_k)^2}{(\lambda_j + \lambda_k) + \gamma |\lambda_j - \lambda_k|} \tag{6.1}$$

where $M(\lambda)$ is the natural logarithm of the penalty added to the likelihood function that is being minimized in the OS-EM algorithm, λ is the amount of radioactivity in a voxel, and the summation over k is over the N neighbors of voxel j. This constraint penalizes image estimates that have local deviations in voxel values in order to suppress noise, while allowing the preservation of edges. Details of this implementation are described in Appendix 3.

In this study, the MAP algorithm was considered as an alternative to OS-EM for reconstructing the animal data to reduce the noise in the reconstructed images. The simulated projection data were reconstructed using the 20 iterations of the OS-EM reconstruction algorithm with collimator response described in Chapter 4. In addition, data were reconstructed using a MAP reconstruction algorithm that was created by modifying the OS-EM algorithm.

6.2.1.5. Dual energy attenuation correction

As described above, lutetium-177 emits photons at two different energies, 113 keV and 208 keV, and the image is reconstructed using photons of both energies. Naturally, the two photons will be attenuated differently. If the projection data for the two different photons are recorded separately, it is possible to model the effect of attenuation on the two photons independently in the reconstruction algorithm. However, the X-SPECT scanner records the results for both photons in a single image, so that it is not possible to distinguish the two photons in the projection data.

One way to model the attenuation of an isotope emitting two photons of different energies is to calculate a single effective attenuation coefficient for the two photons. The effective attenuation coefficient is the value μ_{eff} such that:

$$\frac{N}{N_0} = \exp(-\mu_{eff} x) \tag{6.2}$$

where N_0 is the total number of incident photons, x is the path length of the photon through the attenuating material, and N is the number of photons that are transmitted through the material. For a dual energy photon source, the total number of incident photons is equal to the sum of the number of incident photons at Energy 1 (N_{01}) and the number of incident photons at Energy 2 (N_{02}). It is then possible to write the following expression:

$$\frac{N}{N_0} = \frac{N_1 + N_2}{N_{01} + N_{02}} = \exp(-\mu_{eff} x) \tag{6.3}$$

where N_1 is the number of transmitted photons with Energy 1 and N_2 is the number of transmitted photons with Energy 2. The attenuation process for the two energies are independent, so that the number of transmitted photons is equal to the sum of the number of photons transmitted at Energy 1 ($N_1 = \exp(-\mu_1 x)$)and at Energy 2 ($N_2 = \exp(-\mu_2 x)$), where μ_1 and μ_2 are the linear attenuation coefficients of the material at Energy 1 and Energy 2, respectively. After substituting $N_1 = \exp(-\mu_1 x)$ and $N_2 = \exp(-\mu_2 x)$, it is possible to solve for μ_{eff}, which gives the following results [2]:

$$\mu_{eff} = \frac{\ln[1+\alpha] - \ln[\exp(-\mu_1 x) + \alpha \exp(-\mu_2 x)]}{x} \tag{6.4}$$

where μ_1 and μ_2 are the linear attenuation coefficients for the photons at Energy 1 and Energy 2, x is the path length, and α is defined as the number of photons at Energy 2 divided by the number of photons at Energy 1 (N_{02}/N_{01}). This effective attenuation coefficient is a function of path length through the attenuating material (x), but is effectively constant over the distances encountered in small animal imaging (Fig. 6.1).

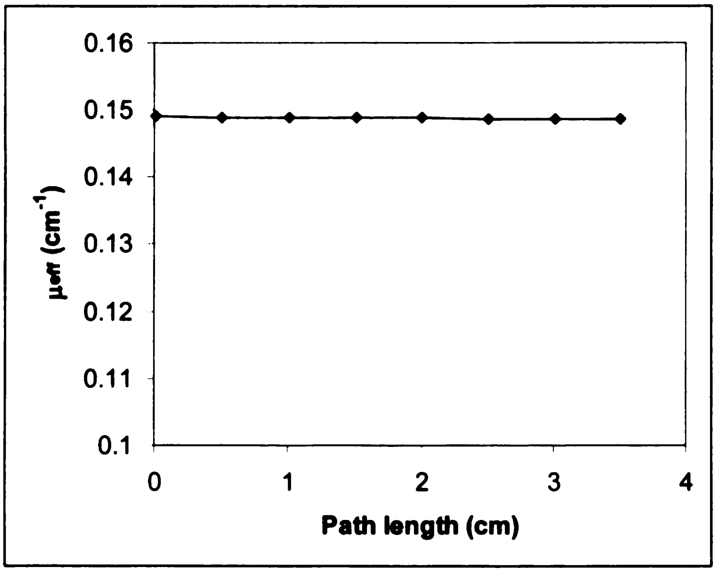

Fig. 6.1: Plot of the effective attenuation coefficient (μ_{eff}) as a function of path length for lutetium-177 in water as calculated by Eq. 6.4.

Although this equation was analytically derived and thus comprises an exact solution for μ_{eff}, it does not account for the relative detection efficiency for the photons of different energy. In the case of imaging lutetium-177 with the X-SPECT scanner, the energy of the 208 keV photon combined with the relatively thin (6 mm) scintillator crystal results in reduced detection of the 208 keV photon. Thus, the gamma camera is expected to have higher intrinsic sensitivity to the 113 keV photon, and the effective attenuation coefficient needs to be adjusted because α does not account for this difference in detection efficiency. Monte Carlo simulations suggest that the numbers of photons detected in the two energy windows (113 keV ± 10%, 208 keV ± 10%) are approximately equal, so the effective attenuation coefficient was calculated with the value of α set to 1 instead of the nominal value of 0.58, which changes the effective attenuation coefficient of water from 0.146 cm^{-1} to 0.149 cm^{-1}.

The simulated projection data were reconstructed using 20 iterations (8 subsets) of the MAP reconstruction algorithm using attenuation maps based on effective attenuation coefficient of water and the geometry of the simulated phantom. The voxel values in a spherical volume of interest corresponding to the source were extracted, and these results were compared to the data reconstructed without attenuation correction to estimate the effect of attenuation correction on quantitative accuracy.

6.2.2. Results

6.2.2.1. Partial volume error

The images reconstructed from simulated data were used to assess the quantitative effect of partial volume errors. The mean VOI values for simulated spheres reconstructed with various algorithms are plotted in Fig. 6.2 as a function of the sphere radius. Because the different sized sources had the same concentration of radioactivity, differences in apparent radioactivity as a function of source size can be attributed to the partial volume effect. For larger spheres, the MAP and the OS-EM with collimator response (OSEM+CR) algorithms give very similar results. Using the MAP algorithm causes a very small decrease in the measured radioactivity (*i.e.*, increase in the partial volume error) for smaller spheres due to the smoothing constraint in the reconstruction algorithm, but otherwise does not affect the quantitative accuracy of the result. Data reconstructed with the MAP algorithm have a reduction in the variability of voxel values within the

VOI by approximately 30% compared to the results obtained using OSEM+CR algorithm, demonstrating that using MAP reconstruction yields a "smoothed" image.

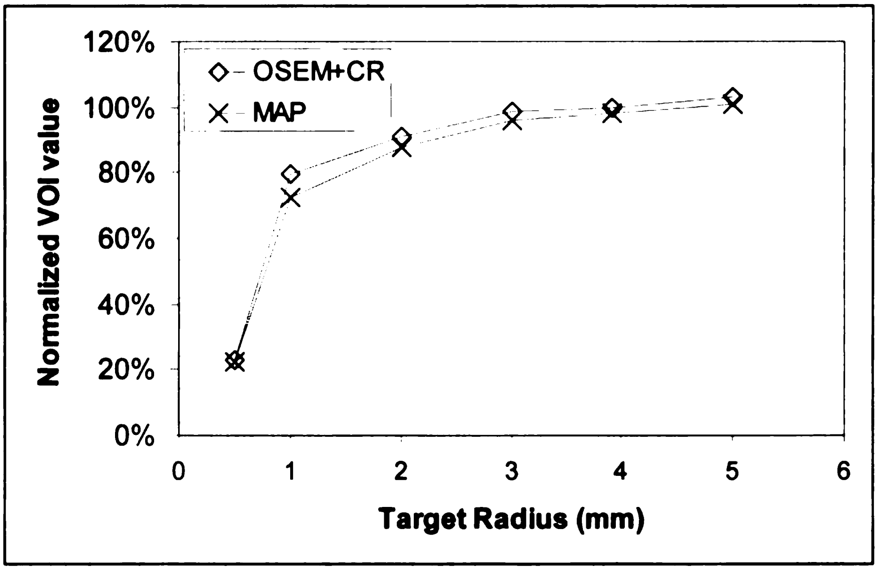

Fig. 6.2: Plot of the average voxel value in the volume of interest corresponding to the simulated source. Data were reconstructed using OS-EM with collimator response (OSEM+CR), and MAP (with collimator response). The values were normalized to the result obtained from a simulated sphere with a volume of 250 μL (radius = 3.9 cm) reconstructed using OSEM+CR. These results demonstrate the effect of partial volume errors on the quantitative accuracy, and also show that using MAP reconstruction does not have an effect on quantitative accuracy, except to slightly increase partial volume errors.

6.2.2.2. Effect of photon attenuation and scatter

The effect of photon attenuation and attenuation correction on voxel values in the VOI of interest is shown in Fig. 6.4 by plotting the apparent radioactivity in the source as a function of the radius of the surrounding cylinder of water. The results indicate that photon attenuation will reduce the apparent radioactivity from a source in the center of a cylinder of water by up to 20% in a rat sized object. Attenuation correction will compensate for this reduction, but there appears to be some overcompensation. Projection data containing only unscattered photons was reconstructed using attenuation correction, which virtually eliminated the overcompensation (Fig. 6.4), allowing us to conclude that the measured increase in radioactivity was due to photon scatter.

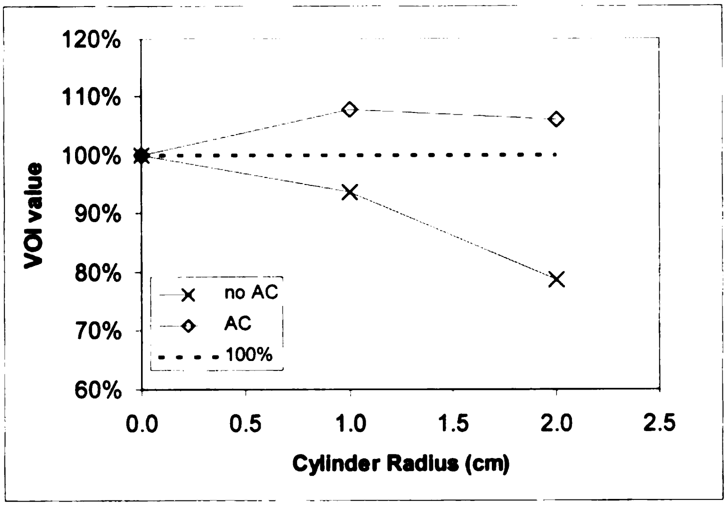

Fig. 6.3: Voxel values in a volume of interest corresponding to a simulated lutetium-177 source at the center of a cylinder of water. Data were reconstructed with the MAP reconstruction algorithm, with and without attenuation correction (AC).

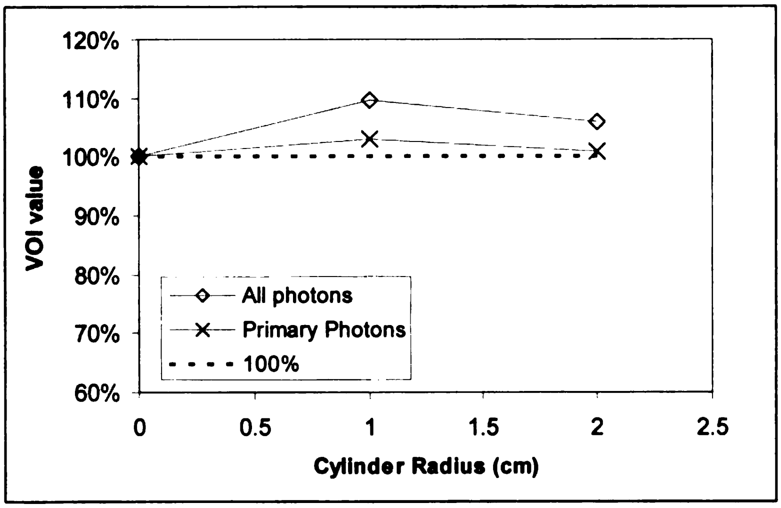

Fig. 6.4: Voxel values in a volume of interest at the center of a cylinder of water. Data were reconstructed with the MAP reconstruction algorithm with attenuation correction, first using all photons detected within the energy window, and then using only unscattered photons detected. Over-estimation of voxel values is reduced by removing scatter photons from the projection data.

The scatter-to-primary ratio (calculated as the ratio of the number of scattered photons detected to the number of primary photons detected) is plotted as a function of the cylinder radius in Fig. 6.5. For a rat sized object, the scatter-to-primary ratio could be as high as 15%. This result shows that the scatter-to-primary ratio with lutetium-177 is higher than the scatter-to-primary ratio with technetium-99m, although the result is still significantly less than that obtained with iodine-125.

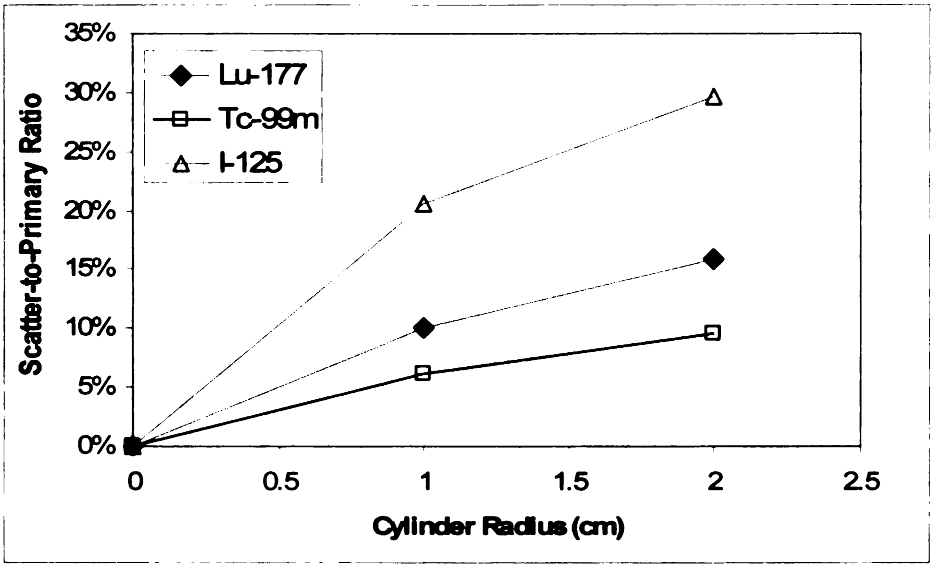

Fig. 6.5: Scatter-to-primary ratio for a source in the center of a cylinder of water. The results were generated using Monte Carlo simulations, and include modeling for detector energy resolution and energy windows based on the specifications of the X-SPECT scanner. The simulation for lutetium-177 included the emissions at 208 keV and 113 keV, with energy windows of ±10% around each peak.

6.2.2.3. Effect of radius of rotation

The effect of increasing the radius of rotation is shown in Fig. 6.6 by comparing the mean VOI data as a function of source size for data with radius of rotation of 4.0 cm and radius of rotation of 5.0 cm. The results show that partial volume errors become more pronounced with a larger radius of rotation, probably due to the loss in spatial resolution resulting from the increased radius of rotation. However, because the reconstruction algorithm correctly models the effect of radius of rotation on detection efficiency, the quantitative accuracy for the larger spheres is not significantly affected.

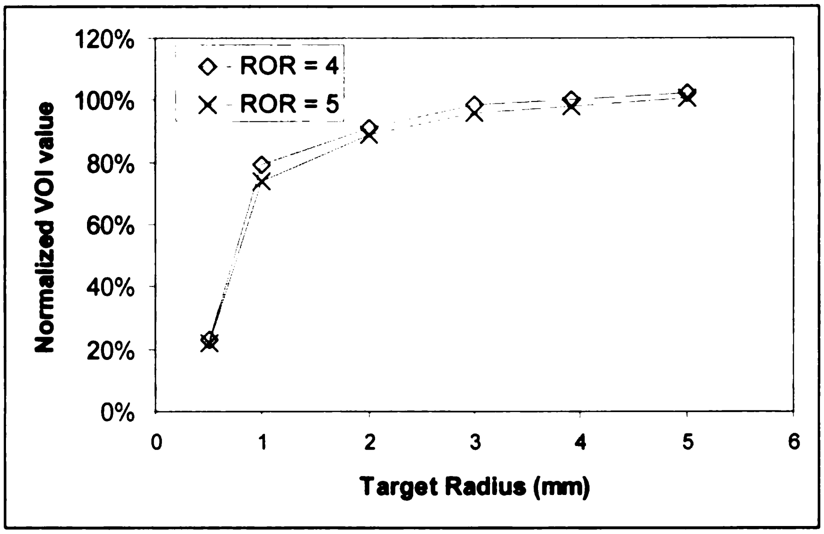

Fig. 6.6: Plot of the normalized voxel value in the volume of interest corresponding to a simulated source. The data were simulated with radius of rotation values of 4.0 cm and 5.0 cm, and the results normalized to the value obtained with a 250 μL sphere imaged at 4.0 cm. This graph demonstrates that 1) partial volume errors increase slightly with increased radius of rotation, and 2) quantitative values are not significantly affected by the radius of rotation.

6.2.3. Discussion

The simulation results for lutetium-177 predict that partial volume errors will be greater with lutetium-177 than with technetium-99m (Chapter 5). This was observed for data reconstructed both with and without collimator response, and can be attributed to the influence of the higher photon energy of lutetium-177 (208 keV). The higher energy of the 208 keV photon leads to greater septal penetration through the collimator, depth of interaction ("parallax") effects in the detector, and Compton scatter in the detector crystal. Although the septal penetration and depth of interaction effects are modeled in the reconstruction algorithm, the model are limited by the computation time required, and as a result, these effects combine to degrade spatial resolution and increased partial volume errors.

The amount of detected photon scatter for lutetium-177 is also higher than expected. The amount of scatter is greater than in technetium-99m, which is surprising considering that the primary emission of lutetium-177 is at 208 keV. However, the scatter-to-primary ratio is increased because of the relatively high sensitivity of the system to photons in the energy window centered at 113 keV, which due to their energy, are more likely to interact with matter. In addition, the 208 keV photons can be scattered and then detected in the energy window at 113 keV. The simulation results show that approximately half of the detected scatter photons are higher energy photons that were scattered and subsequently detected within the lower energy window.

6.3. Calibration measurements

Because of the studies described in the chapter will use lutetium-177 and the newer X-SPECT scanner described in chapter 2, several calibration studies needed to be performed prior to imaging. These include the geometric, CT attenuation, and image coregistration calibrations described in Chapters 2 through 4 for iodine-125 and technetium-99m. In addition, calibration scans will be performed to determine the scaling factor needed to rescale reconstructed SPECT images so that the image voxel values will be calibrated in units of MBq/mL.

6.3.1. Methods

6.3.1.1. Data acquisition

Data were acquired using the newer X-SPECT described in Chapter 2, Section 6. Because of the photon energy of the 208 keV photon emitted by lutetium-177, the medium energy pinhole collimator was used with a 2 mm pinhole aperture in all experimental measurements to maximize detection efficiency. Other data acquisition and reconstruction parameters are summarized in Table 6.2.

CT data were acquired at 512 projections in continuous acquisition mode. The projection data were binned with a 2×2 kernel to yield a projection image size of

1184×1120. Data were reconstructed with the manufacturer supplied reconstruction software (using the Feldkamp algorithm) into a $(512)^3$ matrix format. CT data acquisition and reconstruction parameters are summarized in Table 6.3.

Table 6.2: SPECT data acquisition and reconstruction parameters

Parameter	Value
Collimator focal length	9 cm
Collimator type	Medium energy 2 mm pinhole
Mechanical shift	0.88 mm
Number of projections	64 over 360°
Time / projection	15-30 s
Radius of rotation	4-4.5 cm
Subsets	8
Reconstructed image matrix size	$(72)^3$
Image voxel size	$(0.7 \text{ mm})^3$

Table 6.3: CT data acquisition and reconstruction parameters

Parameter	Value
Projection angles	512
X-ray tube voltage	75 kVp
X-ray tube current	0.32 mA
Projection data binning	2×2
Reconstructed voxel size	170 μm
Reconstruction matrix size	$(512)^3$

6.3.1.2. Attenuation calibration

As before, attenuation correction was performed by converting x-ray CT images of the object into "attenuation maps" representing the calibrated linear attenuation coefficient at each point in the object. It was necessary to calibrate the x-ray CT images generated using the newer X-SPECT scanner because the new scanner uses a different x-ray tube than the older system used for the results presented in the Chapter 4 of this dissertation. This calibration was performed using phantoms and methods described previously (Chapter 4), using both the solid and liquid calibration phantoms. The liquid phantom was filled using air, ethanol (as a stimulant for fat), and aqueous K_2HPO_4 (as a stimulant for bone) in concentrations of 50 mg/mL, 100 mg/mL, and 200 mg/mL. CT data were acquired at 75 kVp, and reconstructed using the manufacturer supplied software as described above. The reconstructed data were rebinned into a $(256)^3$ matrix format, and the voxel values were extracted from VOIs in the reconstructed image corresponding to the different calibration materials.

A calibration curve was constructed by plotting the effective photon attenuation coefficient values (Eq. 6.4) of the different calibration materials as a function of their CT image value. The effective linear attenuation coefficients for the different materials were calculated using Eq. 7.3 assuming $\alpha = 1$. Data obtained from the solid calibration materials and from K_2HPO_4 solutions were combined to estimate the slope for the data with voxel values greater than 0 Hounsfield units (HU). Data from water, ethanol, and air were used to estimate the slope for voxels less than 0 HU.

6.3.1.3. Geometric calibration and coregistration

Geometric calibration studies and coregistration imaging studies were performed using the methods described in Chapters 2 and 3. The SPECT data were acquired at 64 projections using the 2 mm medium energy pinhole aperture and technetium-99m. The data were analyzed using the limited fitting method described in Chapter 3 Section 1.2 to determine the focal length, radius of rotation, and mechanical shift values. Data were acquired using the calibration phantom containing three technetium-99m point sources described earlier, and a total of six calibration scans were performed over approximately 5 months to determine the imaging geometry parameters for reconstruction.

For coregistration studies, the SPECT data were acquired using the technetium-99m point sources as described in Chapter 2. The projection data were reconstructed using 20 iterations of the OS-EM algorithm with collimator response (but without attenuation correction) into a $(72)^3$ matrix format with an isotropic voxel size of 0.7 mm. The SPECT geometry parameters for reconstruction were set using the final result of the geometric calibration studies. CT data were acquired at 512 projection angles, and reconstructed using the parameters given in Table 6.3, and rebinned to $(256)^3$. The experiment was repeated 5 times over approximately 4 months. The accuracy of the coregistration was tested by applying the coregistration transform to a set of reconstructed data and measuring the mean positioning error between the SPECT and CT images.

6.3.1.4. SPECT calibration

The SPECT system was calibrated so that the SPECT images could be represented in absolute units of Bq/mm^3, rather than in relative units. The calibration was performed by imaging a phantom filled with a known amount of radioactivity. The data were reconstructed, and the voxel values in the reconstructed images were correlated with the concentration of radioactivity. The experiment was performed using a hollow sphere phantom ("microsphere") (Data Spectrum Corp.) with a volume of 2 mL filled with aqueous ^{177}Lu-LuCl$_3$ (Perkin-Elmer, Inc.). The radioactivity in the sphere was measured using a dose calibrator (CRC-15R, Capintec, Inc.), and then SPECT data were acquired with the X-SPECT scanner at 64 projection angles over 360°. The radius of rotation was varied between 4-5 cm, and projection time varied from 15-30 s. A CT scan was performed following SPECT acquisition. The acquisition was repeated multiple times over a period of several days. The SPECT data were reconstructed, using 20 iterations (8 subsets) of the MAP reconstruction with collimator response and attenuation correction. A volume of interest corresponding to the nominal dimensions of the sphere was drawn, and the voxel values in the VOI were measured. The voxel values were plotted as a function of the radioactivity in the sphere, and the resulting curve was used to weight the reconstructed images so that the voxel values in the output image corresponded to Bq/mm^3. This procedure was repeated using the same MAP reconstruction algorithm without attenuation correction. The data were also reconstructed using 5 iterations (8 subsets) of the OS-EM algorithm (without collimator response) with and without attenuation correction.

6.3.2. Results

6.3.2.1. Attenuation calibration

The photon attenuation coefficient is plotted as a function of CT image intensity in Fig. 6.7. The relationship between photon attenuation coefficient and CT image value was described by the following equation:

$$\begin{aligned} \mu(cm^{-1}) &= 1.60\cdot 10^{-4} \times HU + 0.149, HU < 0 \\ \mu(cm^{-1}) &= 3.98\cdot 10^{-5} \times HU + 0.149, HU > 0 \end{aligned} \qquad (6.5)$$

where *HU* is the CT image voxel value in Hounsfield units.

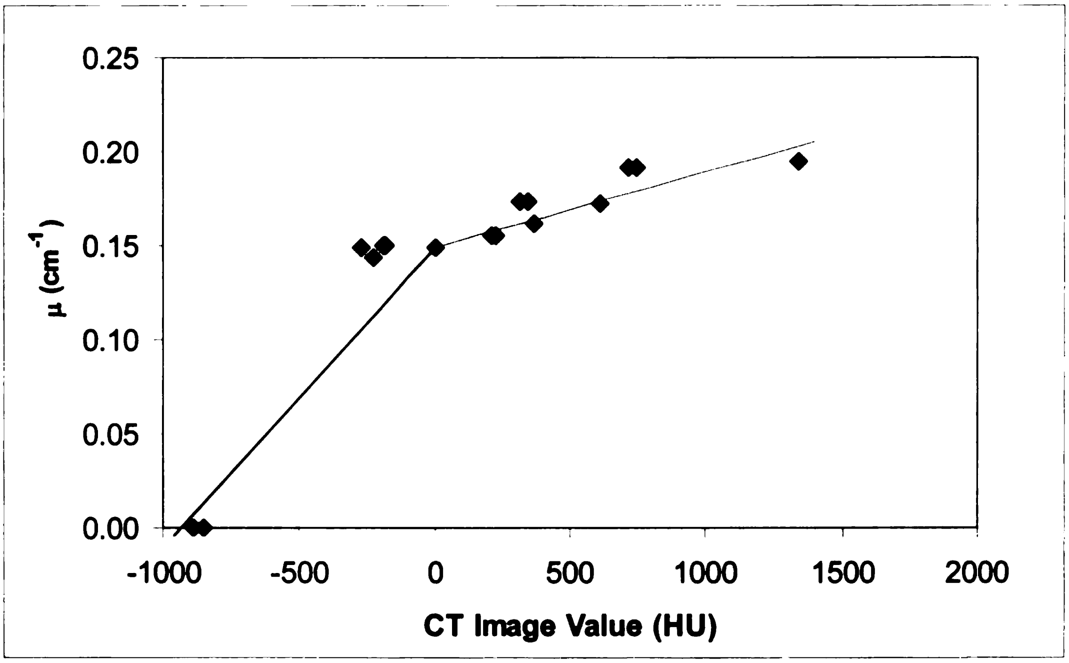

Fig. 6.7: Calibration result for converting CT image values into photon attenuation coefficients for Lutetium-177. The data were fit with a bilinear curve, with the intercept forced to 0.146 cm^{-1}, the effective attenuation coefficient for water calculated using the photon energies for Lu-177.

6.3.2.2. Geometric calibration and coregistration results

The results of the geometric calibration showed that the actual magnification (focal length divided by the radius of rotation) was consistently greater than the nominal magnification (Fig. 6.8). This is consistent with the results described in Chapter 3, obtained with the older X-SPECT scanner, indicating that the deviation is a systematic error.

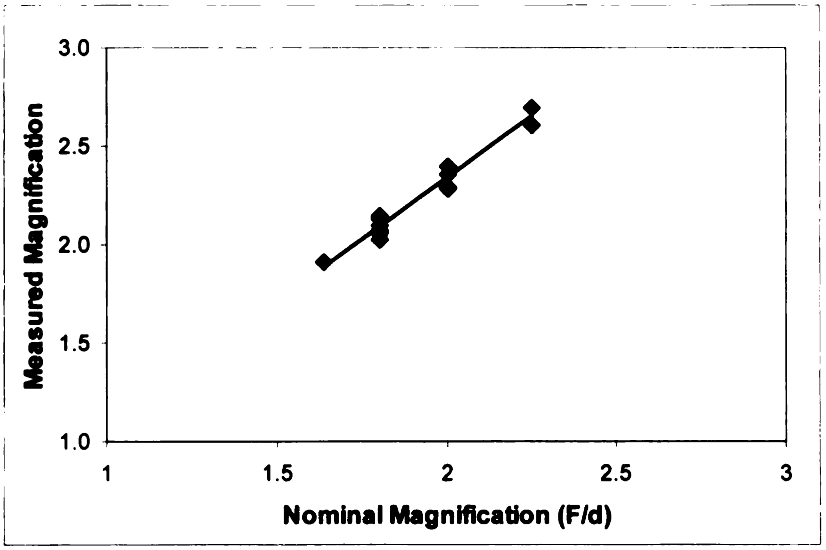

Fig. 6.8: The measured magnification (focal length divided by the radius of rotation) plotted as a function of the nominal magnification. A linear least-squares fit found that the magnification and nominal magnification were related by the equation $y = 1.24x - 0.15$.

The mechanical shift values were measured over the course of several months. The result from the first measurement was not consistent with the remaining results, and was excluded, giving a final value of 0.87±0.06 mm for the mechanical shift. The effective focal length was estimated to be 96±2 mm. The effective radius of rotation was calculated by first calculating the true magnification from the nominal magnification using the relationship in Fig. 6.8, and then using the relationship between focal length (*F*), magnification (*Mag*), and radius of rotation (ROR):

$$Mag = \frac{F}{ROR} \tag{6.6}$$

in order to determine the radius of rotation.

The mean (± standard deviation) values of the coregistration transform parameters are tabulated in Table 6.4. The coregistration tests showed that the calibration was fairly stable, although there was a slight variation observed in the y-shift, which reflected in the high standard deviation associated with the y-shift value. The mean position error between the CT and SPECT images was 0.8 mm, which was primarily due to errors in the y direction.

Table 6.4: Coregistration parameters for newer X-SPECT scanner

Parameter	Value
Magnification	0.582±0.008*
Rotation (deg)	1.4±1.4
Shift in x-direction (mm)	0.1±0.2
Shift in y-direction (mm)	-0.4±0.6
Shift in z-direction (mm)	-1.8±0.1

*Parameter for a SPECT field of view of 5.04 cm

6.3.2.3. SPECT calibration

Reconstructed SPECT and CT images of the microsphere are shown in Fig. 6.9. The image demonstrates that the sphere boundaries are clearly seen in the CT scan, and that the SPECT and CT images are well aligned. It can also be seen that some radioactivity was present in the stalk of the sphere, and data were corrected for this radioactivity, as described in Chapter 5.

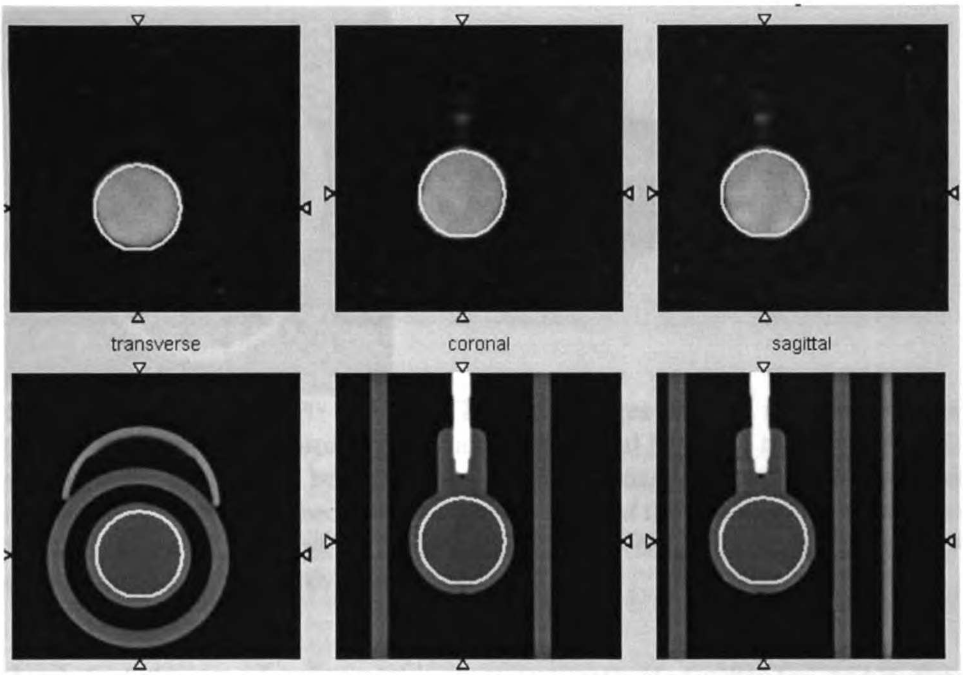

Fig. 6.9: Reconstructed SPECT and CT images of a 2 mL microsphere filled with lutetium-177. The SPECT image is shown in the top row, with the corresponding CT images in the bottom row. Transverse, coronal, and sagittal slices are shown from left to right, with lines shown to define the region of interest in each image.

Initial results also indicated that the lutetium-177 tended to concentrate on the inner acrylic surfaces of the microsphere after several days. This was demonstrated by acquiring the SPECT image of the microsphere after removing approximately half of the ^{177}Lu-LuCl$_3$ solution in the sphere. Although mostly empty, the walls of the sphere were still visible in the SPECT images (Fig. 6.10), showing that the radionuclide was attached to the plastic surface. The sphere was cleaned, and the calibration measurements were repeated with approximately 1 mg/mL of the chelating agent sodium EDTA (ethylenediaminetetraacete) added to the ^{177}Lu-LuCl$_3$ solution. This resulted in a uniform distribution of the radionuclide in the solution shown in Fig. 6.9.

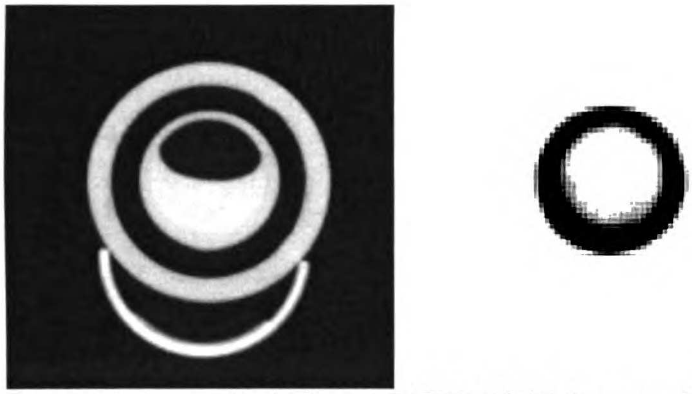

Fig. 6.10: x-ray CT (left) and SPECT (right) images of the 2 mL microsphere used for SPECT calibration. Approximately half of the liquid has been removed from the sphere, yet the walls continue to be visible in the SPECT image, indicating that the radionuclide (lutetium-177) has adsorbed onto the acrylic walls of the phantom. The color map of the SPECT image is inverted, *i.e.*, the darker shades of grade indicates areas with high concentrations of radioactivity.

A plot of the voxel values in images reconstructed with the MAP algorithm (with corrections for photon attenuation and collimator response) as a function of the radioactivity in the microsphere is shown in Fig. 6.11. This result shows that the algorithm behaves linearly as expected, and was used to calibrate the reconstruction algorithm so that the voxel values in the reconstructed SPECT image could be calibrated in units of MBq/mm^3. Additionally, the results also show that the calibration is independent of projection time and radius of rotation, as these two parameters are modeled in the reconstruction algorithm. Similar calibration curves were generated for the MAP algorithm without attenuation correction, MAP with attenuation correction, and MAP without corrections for either photon attenuation or collimator response.

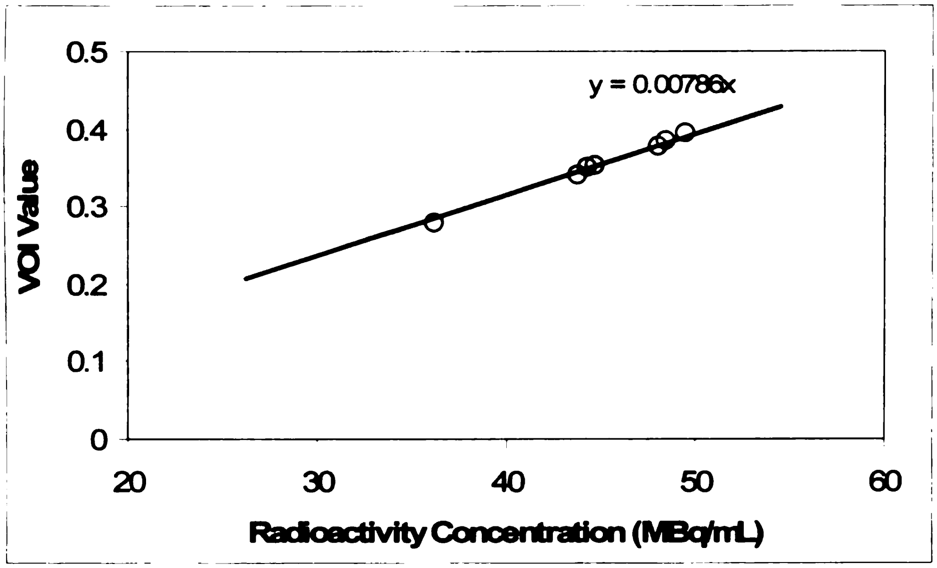

Fig. 6.11: Calibration plot showing the voxel values as a function of the radioactivity concentration in the phantom (MBq/mL). The linear fit has an intercept forced to 0, a slope of 0.0079, and r^2 > 0.99. The data were reconstructed using the MAP reconstruction algorithm, modeling both the collimator response and photon attenuation.

6.4. Phantom study

A phantom study was performed to evaluate the quantitative accuracy of the SPECT imaging prior to analysis of the animal data. A small microsphere was filled with lutetium-177, and imaged under conditions similar to those used in the animal study. The data were reconstructed using various algorithms, and the results were compared to the known results measured using a dose calibrator.

6.4.1. Methods

A 250 μL microsphere was filled with ^{177}Lu-LuCl$_3$, sodium EDTA, food coloring, and water, and placed inside a water filled acrylic cylinder (diameter = 3.2 cm). The phantom was then imaged using SPECT and x-ray CT with the X-SPECT scanner. The SPECT data were acquired using 64 projection angles over 360° with the 2 mm medium energy pinhole. The CT data were reconstructed, and used to generate an attenuation map. The SPECT data were then reconstructed using various versions of the MAP algorithm described in the last section, using the previously generated calibration curves to scale the output.

The reconstructed CT image was transformed to coregister it with the reconstructed SPECT data. The data were displayed using the software program Amira (Mercury Computer Systems, Inc.), and a volume of interest was manually drawn on the CT image. This VOI was then used to calculate the average value in the sphere in the SPECT image, which was compared to the result given by the dose calibrator. In cases where there was insufficient CT contrast to visualize the sphere, the VOI was defined as a 250 μL sphere on the SPECT image.

6.4.2. Results

The microsphere volume was visible in the CT images when food coloring was added to the contents of the sphere. The volume of interest drawn on the CT images had an average volume of 251±15 μL (n=3), which agrees very well with the nominal volume of 250 μL. The radioactivity concentration measured by SPECT was plotted as a function of the "true radioactivity", as determined by the dose calibrator (Fig. 6.12). A linear least squares fit was performed for each data set with the intercept forced to 0, and the results of the fitting are shown in Table 6.5. The slope is indication of the accuracy of the result; perfect accuracy would result in a slope of 1. The data yielded slopes less than 1 for all the algorithms, indicating consistent underestimation of the radioactivity. The results show that reconstructing the data with corrections for collimator response and attenuation correction yielded the best result. The relative root mean square (RMS) error, *E*, was calculated for the results, using the following equation:

$$E = \frac{\sqrt{\frac{\sum_{i=1}^{N}(y_i - x_i)^2}{N}}}{\bar{x}} \quad (6.7)$$

where E is the error, y_i is the measured value (*i.e.*, measured using SPECT), x_i is the expected value, N is the total number of samples, and $\bar{x}$ is the mean value of x. The results are shown in Table 6.5.

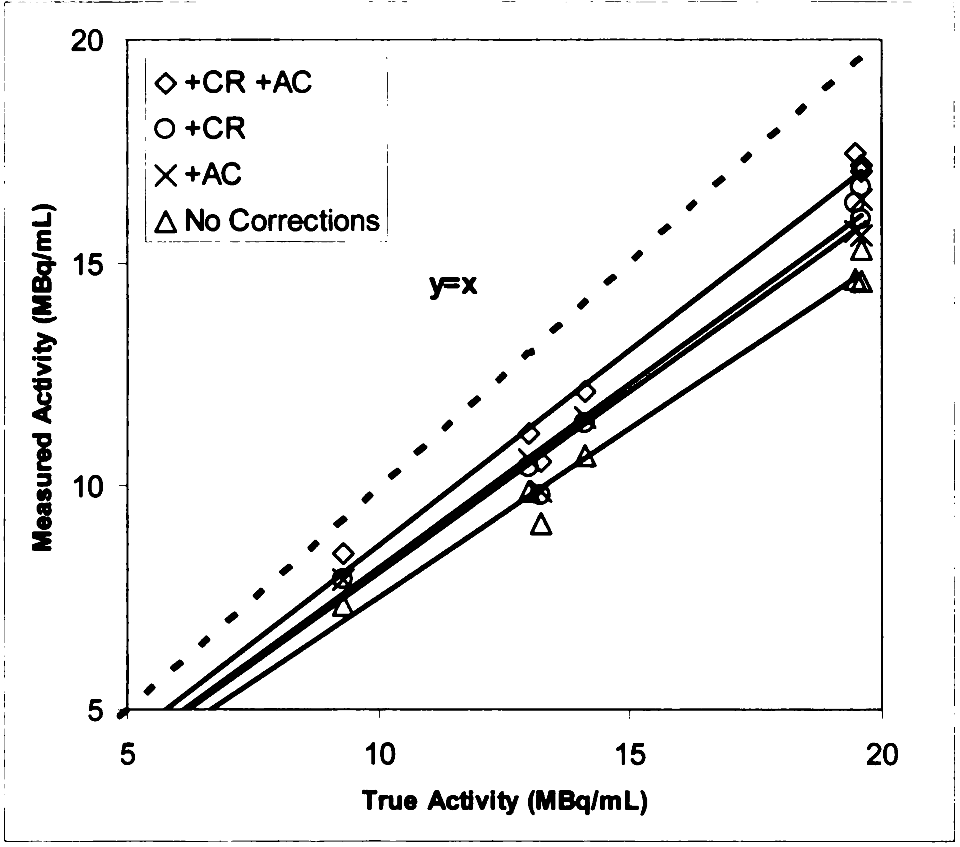

Fig. 6.12: The radioactivity concentration in a 250 μL sphere as measured by SPECT is plotted as a function of the "true radioactivity" measured with a dose calibrator. Data were reconstructed using MAP with collimator response and attenuation correction (+CR, +AC), MAP with collimator response (+CR), MAP with attenuation correction (+AC), and MAP without any corrections.

Table 6.5: Correlation between measured and true radioactivity concentration

Algorithm	Slope	RMS Error
MAP (no corrections)	0.75±0.01	25%
MAP with atten. corr.	0.81±0.01	19%
MAP with coll. resp.	0.82±0.01	18%
MAP with CR and AC	0.87±0.01	13%

6.4.3. Discussion

The results indicate that adding attenuation correction has a significant effect on the accuracy of the radioactivity measurement, as does adding collimator response. However, the best quantitative accuracy was obtained by reconstructing the data with a reconstruction algorithm that models both photon attenuation and depth dependent collimator response.

The results suggest that the measurement of the absolute radioactivity concentration can be made within 15% of the true value when all the corrections are included. Partial volume errors likely account for part of the underestimation of radioactivity in the phantom. The reconstructed images were scaled using data acquired with a 2 mL microsphere, whereas the volume of the sphere used in phantom measurements was only 250 μL. Extrapolating the simulation results indicate that the partial volume error would be less than 10%, but there are several reasons for the spatial resolution to be poorer, and consequently the partial volume effects to be greater, in the experimental data compared to the simulation data. One reason is the use of machinable tungsten in the pinhole aperture. This tungsten alloy has better machining properties than pure tungsten, but is less dense than the pure material modeled in the simulation. The reduced density results in a decrease in the linear attenuation coefficient, and there is increased septal penetration as a result. Although this is modeled in the reconstruction algorithm, the accuracy of the model is limited by the increased computational demands, and thus does not fully model the septal penetration because the number of rays that can be generated is limited. Therefore, in the reconstruction algorithm the maximum width of the point spread function is limited, whereas the true point spread function has a very wide tail (with low amplitude). In addition, the simulation does not model nonidealities in the detector, such as spatial nonlinearity, which are present in the experimental data and absent from the simulation results. This results in a loss of spatial resolution in the experimental data, leading to an increase in the partial volume error.

6.5. Animal studies

Studies were performed using a mouse model of prostate cancer to study the behavior of a lutetium-177 labeled antibody to prostate specific membrane antigen. The techniques and methods developed in this thesis (*e.g.*, geometric calibration, improved reconstruction algorithms) were applied to the data obtained in this study to both to improve and test the quantitative accuracy of these techniques.

6.5.1. Methods

Animal studies were performed using a xenograft mouse model of the "lymph node cancer of the prostate" (LNCaP) cell line that was developed from a heavily pretreated patient with hormone refractory prostate carcinoma. In this study, the LNCaP xenograft mouse model was being used to characterize the pharmacokinetics and biodistribution of a lutetium-177 labeled antibody for the prostate specific membrane antigen that is being investigated for radioimmunotherapy of prostate cancer. As explained earlier, lutetium-177 also emits gamma rays having energies of 113 and 208 keV that can be imaged with

SPECT to study the biodistribution of the lutetium labeled agent *in vivo*. In this specific study, the LNCaP xenograft mouse was administered with the Lu-177 labeled PSMA antibody, then imaged with SPECT and CT using the X-SPECT scanner. The resulting image data then were used to calculate the tumor uptake of the agent using the methods developed and tested in this thesis project. The animal was sacrificed, and the amount of radioactivity in the tumor was measured using a dose calibrator, and used as a gold standard for comparison with the values obtained with *in vivo* imaging using the small animal SPECT-CT system.

6.5.1.1. Imaging agent

The mouse model for prostate cancer was prepared by Dr. Mei-hsiu Pan and Dr. Dong-wei Gao by implanting LNCaP cells in the flank of SCID (severe combined immune deficiency) mice. The xenograft tumors were allowed to grow for 8-10 weeks to a mass of approximately 1 gram (*i.e.*, approximately 1 cm in diameter) before the radiolabeled agent was administered. The lutetium-177 labeled imaging agent was also prepared by Dr. Pan. The antibody and chelating agents were supplied by Cytogen Corporation, and the lutetium-177 purchased from Perkin-Elmer, Inc.

6.5.1.2. Data acquisition

The animal studies, including acquisition of the imaging data, were performed by Drs. Gao and Pan. The animals were injected with 6-70 MBq of the lutetium-177 labeled imaging agent. At various time intervals from 2 hours to 7 days after injection, SPECT projection data were acquired at 64 projections over 360° using the medium energy pinhole collimator with a 2 mm aperture. The radius of rotation was between 3 and 5 cm, and the data were acquired for 15 – 60 seconds per projection. Coregistered CT data were acquired, as well as SPECT data using the parallel hole collimator. The 512 CT projections were acquired over 360° in continuous acquisition mode, with the x-ray tube set to 75 kVp and 0.32 mA. A total of 27 animals were imaged, 8 of which were control animals with sham tumors. The control animals were imaged, but were not included in the results of this thesis, because the analysis and results presented are focused on measurement of the radioactivity uptake in the tumor.

6.5.1.3. Animal handling

Animals were handled in accordance in accordance with UCSF and government regulations regarding laboratory animals, and all animal protocols were reviewed by the Institutional Animal Care and Use Committee (IACUC)_ and supervised by the UCSF Laboratory Animal Resource Center (LARC). Mice were anesthetized during imaging using inhaled isofluorane. After imaging, the animals were euthanized without recovering from anesthesia, and a blood sample was collected first through cardiac puncture. Organs including the heart, lungs, brain, and liver were removed, and the tumor was resected as well. The mass of each sample was determined, and the radioactivity in each sample measured using a calibrated gamma scintillation counter (Wizard 1480, Perkin Elmar, Wellesley, MA)

6.5.1.4. Image reconstruction

The CT projection data were reconstructed using the manufacturer supplied reconstruction software as described above. The reconstructed CT data were rebinned to a matrix size of $(256)^3$.

The SPECT data were first reconstructed using 10 iterations (8 subsets) of the MAP algorithm without attenuation correction, with the geometric parameters set using the results of the geometric calibration studies. The data were reconstructed to a matrix size of $(72)^3$ voxels, with a voxel size of 0.7 mm. These images were used to check the coregistration of the CT and SPECT images. The coregistration parameters were adjusted if needed, and then were used to create an attenuation map from the CT data using the method described in Chapter 4 section 2.1.3 and the calibration curve in Fig. 6.7. The SPECT data were then reconstructed using 20 iterations of the MAP algorithm with collimator response and attenuation correction.

6.5.1.5. Data processing

The geometric transform described in Chapter 2 section 4.1 was applied to the reconstructed CT image in order to coregister it with the reconstructed SPECT image. A volume of interest corresponding to the tumor was manually drawn on the CT data using information from both CT and SPECT data. This was then used to calculate the average voxel value in the SPECT image.

6.5.2. Results

The tumor volume measured using SPECT-CT was compared to the mass of the excised tumor, and the results are shown in Fig. 6.13. The results show a good correlation between the volume and mass. However, a linear fit between the tumor mass and volume shows a slope of 1.30±0.05 mL/g, which would indicate an average tumor density of 0.8 g/mL. This is lower than the expected density of soft tissue (~1.05 mg/mL), and indicates that the estimate of the tumor volume in the CT image is consistently too high by approximately 25%.

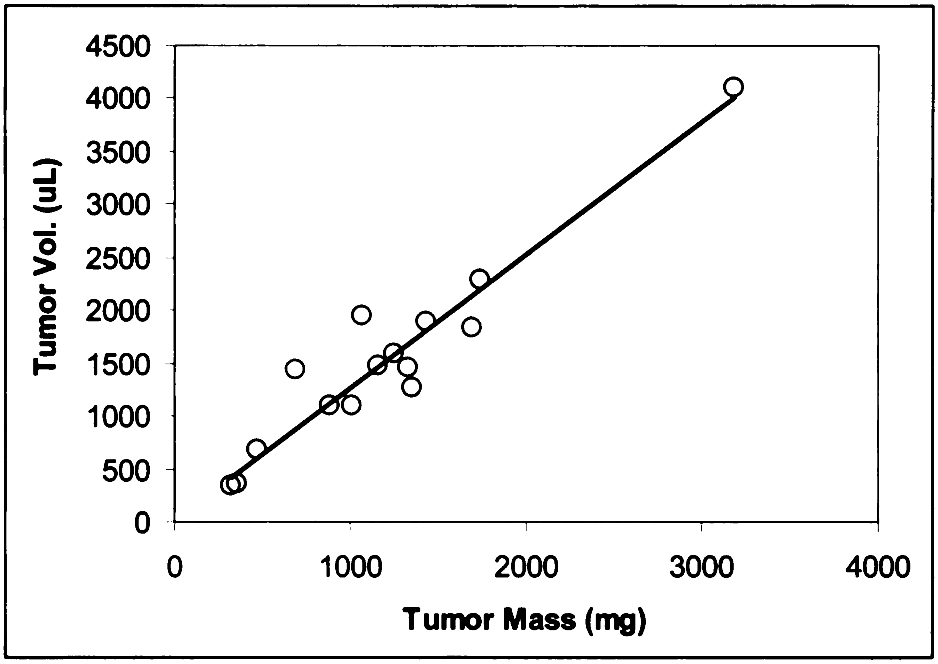

Fig. 6.13: Tumor volume measured on the SPECT-CT images is plotted as a function of the tumor mass. A linear regression was performed, with the result $y=1.23x+94$ ($r^2=0.88$). The intercept is not significantly different than 0 (intercept±standard error =94±145). With the slope forced to 0, the slope is 1.30.

The total radioactivity in the tumor in each animal was calculated from the SPECT data using the previously defined tumor volumes. This was plotted as a function of the tumor radioactivity measured using the dose calibrator, and a linear least-squares fit was performed with the intercept forced to 0 (Fig. 6.14). The resulting slope was 2.0±0.4, and the relative RMS error was 215%. This result indicates that the radioactivity values measured by imaging are approximately twice the value measured by excising the tissue, and that the correlation between the results obtained by the two methods is poor.

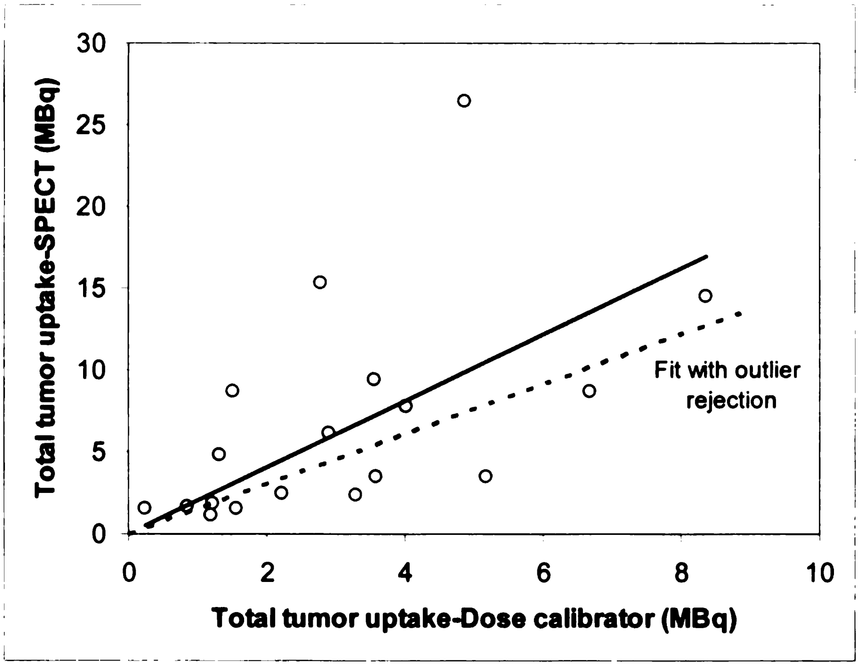

Fig. 6.14: Plot of radioactivity in the tumor determined by SPECT-CT imaging is plotted as a function of the tumor radioactivity measured using a dose calibrator. A linear regression was performed with the intercept forced to 0, and the resulting slope was determined to be 2.0±0.4. After outlier rejection, the slope was 1.5±0.2.

The plot shown in Fig. 6.14 has what appear to be two outliers. This was evaluated objectively by performing outlier rejection using the "externally studentized residual" values flir[8]. This method adjusts the residual (the difference between the measured value and the value estimated by the linear fit) by dividing it by the estimated standard deviation so that the resulting value has the same distribution as Student's t-distribution. The externally studentized residual for a particular data point uses the parameters of the linear fit (*e.g.*., the slope) and the standard deviation calculated in the absence of that particular data point. Based on the results, one of the points in the plot above is clearly an outlier (p<0.001) and another is marginally an outlier (p<0.10). If these two points are excluded from the plot, the slope of the least-squares linear fit becomes 1.5±0.2. The relative RMS error (calculated using Eq. 6.6) was 105% after outlier rejection.

6.5.3. Discussion

In this study, the total radioactivity in the tumor was measured *in vivo* using SPECT and also by euthanizing the animal, excising the tumor, and measuring the *ex vivo* radioactivity using a dose calibrator. We plotted the value obtained using SPECT as a function of the radioactivity measured using the dose calibrator and performed a linear least-square fit to the data with the intercept forced to 0. If the SPECT data matched the *ex vivo* data perfectly, the result would be a line with a slope equal to 1. However, after outlier rejection, the result was a line with slope of 1.5, suggesting that the SPECT results overestimate the total radioactivity in the tumor, and that there is a fair amount of variability in the measurement. This overestimation of the radioactivity present in the tumor is unexpected, as the primary sources of errors in quantitative SPECT imaging (partial volume errors and photon attenuation) lead to underestimation of the radioactivity. In contrast, the phantom measurements yielded better results, with only a slight underestimation of the total radioactivity in the phantom with much less variability. A number of factors combined to contribute to limit the accuracy and precision of the measurement.

As noted previously, the definition of the boundaries of the tumor volume used to calculate the total radioactivity in the tumor was performed manually, based on visual inspection of the combined CT and SPECT images. Although there was a good correlation (r^2=0.88) between the image derived tumor volume and the mass of the excised tumor, the tumor volume measured on the CT image was consistently larger than the expected volume based on the mass of the tumor and the density of soft tissue (~1.05 g/mL). Thus, the tumor volumes measured using CT are estimated to be approximately

20-25% larger than the excised tumors. This overestimation of the tumor volume could cause the radioactivity within the tumor to be overestimated by a similar proportion.

A second source of error could be introduced by the presence of radioactive blood in the *in vivo* measurements which likely would be absent in the *ex vivo* measurements, resulting in a higher measured amount of radioactivity in the *in vivo* measurements relative to the *ex vivo* measurements. The amount of radioactivity in the blood would be highest shortly after injection of the imaging agent, and will decrease as the antibody binds to the target or is metabolized. A plot of the relative error in the total radioactivity in the tumor as a function of the time delay prior to imaging is shown in Fig. 6.15. Although the results were not statistically significant, the results suggest that data acquired a short time after injection have greater errors.

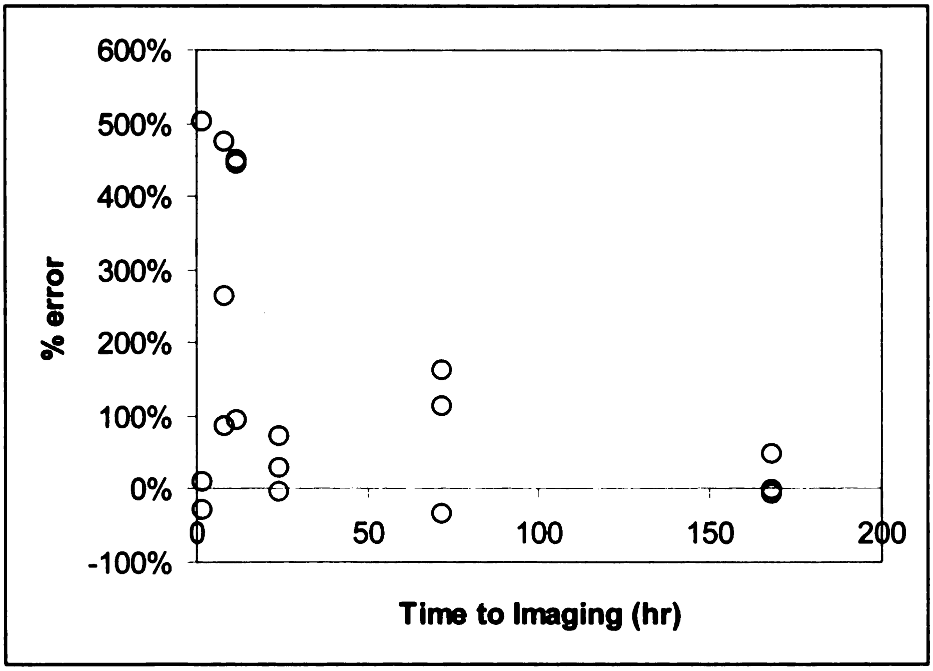

Fig. 6.15: Plot of the relative error in the measurement of total tumor radioactivity as a function of the time between the injection of the imaging agent and data acquisition. The results suggest that the errors are greatest at short time points (*i.e.*, t<12 hrs), when there is a large amount of background radioactivity present.

Another difference between the phantom study and the animal study is the presence of background radioactivity. In the phantom study, all of the radioactivity was within the volume of interest, whereas in the animal study the radioactivity was distributed throughout the animal. The amount of radioactivity uptake in the tumor is believed to be a function of time, where the agent binds to the tumor over time, while background radioactivity is excreted (Fig. 6.16). As we showed earlier in Fig. 6.15, the data suggest that image data acquired a short time after injection have do not correlate as well with the *ex vivo* measurements.

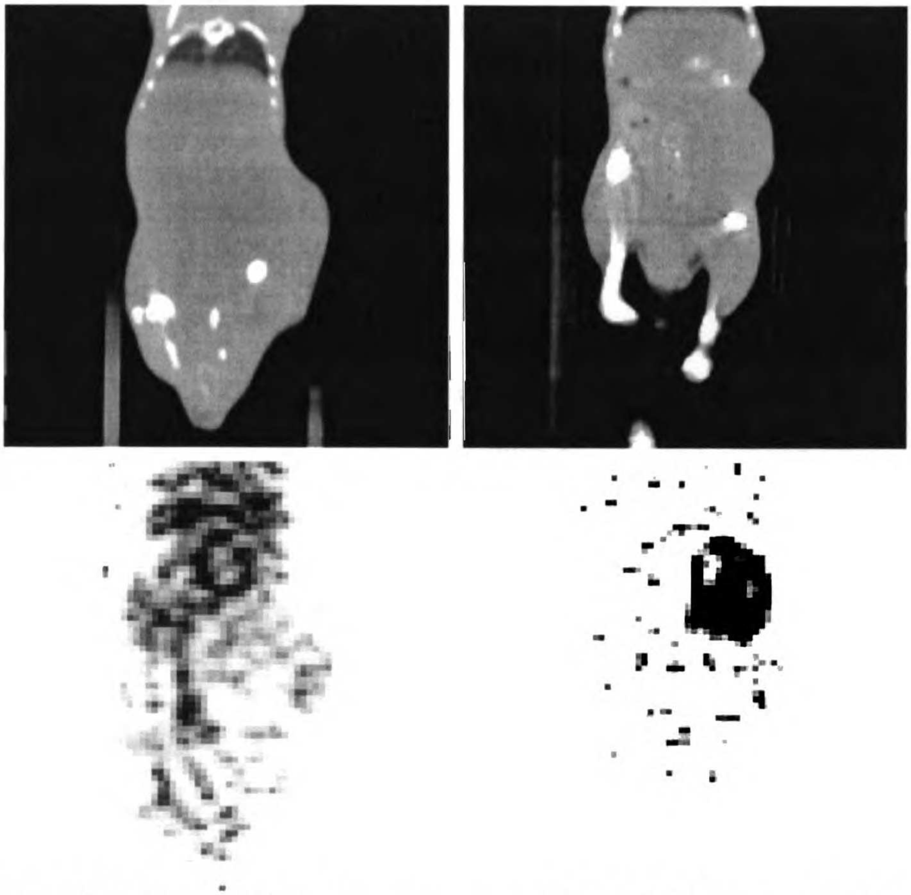

Fig. 6.16: Coronal slices from reconstructed SPECT-CT images of LNCaP mice, with the CT shown in the top row, and the SPECT data in the bottom row. The color scale of the SPECT images have been inverted such that the dark areas correspond to high concentrations of radioactivity. The mouse on the left was imaged 2 hours after injection, and the mouse on the right was imaged 7 days after injection, showing increased tumor binding of the imaging the tumor and decreased background activity.

UCSF LIBRARY

We also found that there was very little contrast between the tumor and normal tissue in the CT images, making it difficult to define the tumor boundary. In order to assess the effect of the impact of the placement of the volume of interest on the result, the volumes of interest in 2 representative mouse studies were manually drawn five times each. The results are compared in Table 6.6, and show that the standard deviation of the measured volume was approximately 5%. In addition, the standard deviation of the total radioactivity in the tumor was 4 to 7%. This contributes to the variability in the measurements, and the poor correlation between the imaging and *ex vivo* measurements. In the future, this problem may be partially alleviated by injecting CT contrast agent prior to imaging to improve soft tissue contrast. In addition to the difficulty in defining the tumor volume in the images, in certain cases there was also difficulty in defining the exact extent of the tumor when excising the tissue, which also certainly contributed to the error in the measurements.

Table 6.6: Variability in the definition of the volume of interest

	Mouse 8	**Mouse 10**
Tumor volume from CT	1546 mm^3	1176
% standard deviation	6.4%	5.0%
Total radioactivity in tumor	2.58 MBq	8.46 MBq
% standard deviation (	7.1%	3.9%

6.6. Conclusions

In this chapter, we have described an application of SPECT-CT imaging to the quantitative measurement of radioactivity *in vivo*. In addition to the phantom and animal studies, we also performed studies to characterize the SPECT imaging geometry, CT image intensities, and SPECT image intensities. The results of these calibration studies were used to reconstruct data from a phantom study, which showed that the data reconstructed using an iterative algorithm incorporating compensations for both photon attenuation and collimator response predicted the amount of radioactivity in the spherical phantom to within 13% of the true value, with a consistent bias towards underestimating the amount of radioactivity.

Based on the phantom results obtained in this chapter, radionuclide quantification in small animal SPECT-CT can be accurate to within 15% of the true value under optimal conditions where the volume of interest is well defined. In addition, the size of the volume of interest will affect the accuracy of the measurement in that partial volume errors will increase with smaller target volumes. For targets volumes 250 μL or greater, the partial volume errors will be minimal. Corrections for photon attenuation and collimator response also help to reduce errors in quantification.

The animal studies showed that the tumor volumes measured in the CT images correlated well with the mass of the excised tumor, but the tumor volume was consistently overestimated by approximately 25%. The SPECT data also overestimated the total radioactivity in the tumor compared to the results obtained using a dose calibrator, and the data had a lot of variability. We found that variability in the definition of the volume of interest in the image data to cause approximately 5% variability in the radioactivity measured. In summary, the inherent difficulties and variability associated with biological systems in this experiment outweighed the errors in the imaging physics such as partial volume errors.

References

[1] R. T. Greenlee, M. B. Hill-Harmon, T. Murray, and M. Thun, "Cancer Statistics, 2001," *CA: a Cancer Journal for Clinicians*, vol. 51, pp. 15-36, 2001.

[2] K. H. Wong, "Multi-modality imaging for improved staging of prostate cancer," in *Bioengineering*. San Francisco: University of California, San Francisco University of California, Berkeley, 2002, pp. 251.

[3] J. Tedesco, W. Goeckeler, M. Becker, K. Frank, G. Gulyas, and S. A. Young, "Development of optimal Lu-177 labeled monoclonal antibody (7E11) constructs for radioimmunotherapy of prostate cancer," *Journal of Clinical Oncology*, vol. 23, 2005.

[4] X. Wang, Z. An, J. Geller, and R. M. Hoffman, "High-malignancy orthotopic nude mouse model of human prostate cancer LNCaP," *The Prostate*, vol. 39, pp. 182-186, 1999.

[5] D. Strul, G. Santin, D. Lazaro, V. Breton, and C. Morel, "GATE (Geant4 Application for Tomographic Emission): a PET/SPECT general-purpose simulation platform," *Nuclear Physics B (Proc. Suppl.)*, vol. 125, pp. 75-79, 2003.

[6] G. Santin, D. Strul, D. Lazaro, L. Simon, M. Krieguer, M. Vieira Martins, V. Breton, and C. Morel, "GATE: A Geant4-based simulation platform for PET and SPECT integrating movement and time management," *IEEE Transactions on Nuclear Science*, pp. 1516-1521, 2003.

[7] J. Nuyts, D. Bequé, P. Dupont, and L. Mortelmans, "A concave prior penalizing relative differences for *Maximum-a-Posteriori* reconstruction in emission tomography," *IEEE Transactions on Nuclear Science*, vol. 49, pp. 56-60, 2002.

[8] F. A. Graybill, *Regression analysis: concepts and applications*. Belmont, CA: Duxbury Press, 1994.

UCSF LIBRARY

Chapter 7: Conclusion

The advancement of molecular imaging requires the development of quantitatively accurate imaging methods for many applications. SPECT-CT is a powerful modality for molecular imaging because of the versatility of tracers labeled with single photon emitting radionuclides and because of its ability to image both physiological function and anatomical structure. Conventionally, the coregistered SPECT and CT images are used to visualize physiological-anatomical correlations, and are interpreted qualitatively. The objective of this thesis was to characterize and improve the quantitative accuracy of small animal SPECT-CT.

The X-SPECT® scanner, a commercial small animal SPECT-CT imaging system used for the experiments in this thesis, was characterized through measurements of spatial resolution and detection efficiency. The spatial resolution for SPECT was between 1 mm to 2 mm full width at half maximum (FWHM), and the detection efficiency 2×10^{-5} to 1×10^{-4}. Both the spatial resolution and detection efficiency depend on the choice of pinhole aperture and radius of rotation. For x-ray CT imaging, the spatial resolution of the X-SPECT system was measured to be 260 μm FWHM. In general, we found that the measured system performance agreed well with the performance predicted by analytical models.

A method to determine the imaging geometry from projection data was implemented, tested using simulated data, and then applied to experimental measurements with the X-SPECT scanner. The nominal magnification was consistently less than the measured value, leading to errors in the dimensions of the reconstructed images. These errors were corrected by reconstructing the projection data using the measured magnification value.

A strength of iterative reconstruction algorithms is the ability to include realistic models of the imaging process to correct for non-idealities in the imaging process. We implemented ordered subsets-expectation maximization (OS-EM) iterative reconstruction algorithms incorporating corrections for photon attenuation, collimator response, and photon scatter to improve the quality of reconstructed SPECT images. The qualitative effects of these corrections on reconstructed data were demonstrated experimentally. For example, attenuation correction was shown to compensate for the "cupping" artifact caused by photon attenuation, and collimator response modeling was shown to improve the spatial resolution of reconstructed images.

The quantitative accuracy of SPECT images was studied using both Monte Carlo simulations and experimental methods. The effects of photon attenuation, scatter, and partial volume errors on quantitative measurement of radioactivity were studied. In addition, the effects of the improved reconstruction algorithms on quantitative accuracy were determined.

Photon attenuation is known to significantly affect the quantitative accuracy of human SPECT imaging, and its effects in small animal imaging were studied both experimentally and with Monte Carlo simulations. The effect of photon attenuation on the quantitative measurement of radioactivity was assessed by simulating the imaging of a spherical source at the center of a cylinder of water. Simulations, performed for iodine-125, technetium-99m, and lutetium-177, demonstrated that photon attenuation led to an underestimation of the amount of radioactivity by up to 50% when imaging iodine-125 in a rat sized object. Attenuation correction effectively compensated for this effect, but resulted in a slight overestimation (~10%) of the amount of radioactivity in cases where photon scatter was significant. Experimental studies confirmed that photon attenuation will measurably reduce the amount of technetium-99m measured in a volume of interest, and verified that reconstructing the data with attenuation correction compensates for this effect.

The Monte Carlo simulations indicated that the scatter-to-primary ratio is generally lower in small animal imaging than in human imaging, even in the case of iodine-125. Although the scatter-to-primary ratio can reach 30% when imaging larger animals with iodine-125, much of the scatter is due to Rayleigh scatter, resulting in smaller scattering angles than occur with Compton scatter, which is the predominant mechanism for scatter with higher energy isotopes. A model of photon scatter for iodine-125 was implemented in the forward projector of the reconstruction algorithm for scatter correction. This reconstruction based scatter correction algorithm was shown to compensate for the qualitative effects of scatter (*i.e.*, loss of image contrast), but was computationally intensive and the improvement in quantitative accuracy was minimal.

Partial volume errors were assessed by using technetium-99m and spherical sources of different sizes. With a 1 mm pinhole, the amount of radioactivity in targets with a radius of less than 2 mm is significantly underestimated. With a 2 mm pinhole, the measured radioactivity in targets with a radius of less than 4 mm will be significantly low. Compensation for collimator response in the reconstruction algorithm was shown to improve the quantitative accuracy of radioactivity measurement in smaller spheres, especially with the 2 mm pinhole. The simulation results were verified by the experimental measurements, although it was found that count rate limitations affected the measurement of high concentrations of radioactivity with the 2 mm pinhole, resulting in

UCSF LIBRARY

the underestimation of the amount of radioactivity when the count rate was high (*i.e.*, measuring high concentrations of activity).

The calibration methods and reconstruction algorithms were used to determine the biodistribution of a lutetium-177 labeled antibody targeting the prostate specific membrane antigen in a xenograft mouse model of metastatic prostate cancer. The mass of the excised tumor was compared with the volume measured using SPECT-CT, and a good correlation was found. However, the correlation showed that the tumor volume determined by imaging was approximately 25% greater than predicted by the tumor mass. It was also found that the total radioactivity in the tumor measured by imaging was 50% higher than the values measured with the dose calibrator, with a relative root mean square error of 105%. The difference was largest at early time points, when less than 12 hours had passed from injection to imaging. The difference between the *in vivo* and *ex vivo* measurements of radioactivity in the animal study were much larger than the errors obtained in a phantom study performed using a lutetium-177 filled microsphere, the results of which showed that the radioactivity in the sphere could be measured to an accuracy within 15%. This suggests that much of the variability in the results of the *in vivo* imaging was due to biological factors (*e.g.*, uncertainty in the tumor boundaries) and not in the imaging system itself.

In this dissertation, we have explored the use of small animal SPECT imaging as a quantitative molecular imaging modality. Based on the results of phantom and simulation studies, it was demonstrated that the quantitative and qualitative accuracy of small animal SPECT images can be improved using improved reconstruction algorithms incorporating compensation for photon attenuation and collimator response to minimize

UCSF LIBRARY

the effect of attenuation and partial volume errors.

Improved image reconstruction algorithms incorporating compensations for effects such as photon attenuation have improved the quantitative accuracy in clinical SPECT-CT systems, and further improvements in reconstruction algorithms will lead to improved quantitative accuracy. In addition, quantitative accuracy will benefit from the improved spatial resolution and detection efficiency enabled by improved collimator designs, particularly the multi-pinhole collimators that recently have become common [1-3].

The quantitative accuracy of SPECT-CT imaging is affected by a number of factors, such as the choice of isotope and the size of the volume of interest, which are determined by the specific application of the imaging study. For example, partial volume errors may be larger in myocardial perfusion studies due to the motion and thinness of the heart wall. For this reason, more experience with animal studies is needed to validate the correlation between imaging results and the measured biological parameters, ultimately leading to the goal of replacing traditional, invasive methods with imaging technologies. This in turn will improve the quality of the data collected from animal studies by allowing *in vivo* measurements of parameters in living animals and enabling longitudinal studies using a single animal. At the same time, this will reduce the time and the number of animals needed to obtain the data, thereby decreasing the cost and increasing the rate of biomedical research and drug development.

References

[1] F. J. Beekman, F. van der Have, B. Vastenhouw, A. J. A. van der Linden, P. P. van Rijk, J. P. H. Burbach, and M. P. Smidt, "U-SPECT-I: A novel system for submillimeter-resolution tomography with radiolabeled molecules in mice," *Journal of Nuclear Medicine*, vol. 46, pp. 1194-1200, 2005.

[2] N. U. Schramm, G. Ebel, U. Engeland, T. Schurrat, M. Behe, and T. M. Behr, "High-resolution SPECT using multipinhole collimation," *IEEE Trans Nuc Science*, vol. 50, pp. 315-320, 2003.

[3] T. Funk, P. Després, W. C. Barber, K. S. Shah, and B. H. Hasegawa, "A multipinhole small animal SPECT system with submillimeter spatial resolution," *Medical Physics*, vol. 33, pp. 1259-1268, 2006.

UCSF LIBRARY

Appendix 1: Geometric Calibration Programs

A1.1. Introduction

This appendix describes two computer programs which were written in order to characterize the pinhole imaging geometry using projection data measured using point sources. In addition to the values of the geometric parameters, the programs estimate the position of the point sources used to generate the projection data. The two versions of the programs are very similar, and differ only in the number of parameter values used to characterize the imaging geometry.

The geometric parameters are estimated by performing a least-squares fit of the measured projection data with the calculated projection data. The parameters varied in the fitting process consisted of the geometrical parameters describing the imaging process, and 6 parameters describing the position of the point sources. The first version of the program models the geometry using 3 parameters, and the second version models the geometry using 7 parameters. The source codes are in the files `geocal2.c` and `geocal3.c`, respectively.

This appendix gives an overview of the programs, and gives instructions for their use.

A1.2. Usage

The programs were written to be run from the command line. In the Windows environment, they are run from a DOS prompt. They can also compiled and used with Linux, Unix, or other operating systems. To run the program, simply type the program name (`geocal2` or `geocal3`), followed by the file names of the parameter file, input file containing centroid information, and output file. The parameter and input files will be described in more detail below.

UCSF LIBRARY

A1.2.1. Parameter file

The parameter file is a text file, where each line contains the name of a parameter (case sensitive), followed immediately by the equal sign ("=", with no spaces before or after), followed by the numeric value of the parameter. Table A1.1 lists and describes the parameters.

The majority of the parameters fall into two categories. The first set of parameters consists of initial estimates for the imaging geometry parameters, and the second set of parameters describes known values for the imaging geometry.

Table A1.1: Contents of the parameter for geometric calibration

Parameter	Description
Focal length	initial estimate for collimator focal length (mm)
Radius of rotation	initial estimate for radius of rotation (mm)
Mechanical offset	initial estimate for lateral shift (mm)
x0	initial estimate for point source location (mm)
y0	initial estimate for point source location (mm)
z0	initial estimate for point source location (mm)
rotate0	initial estimate for angle used to describe point source location (deg)
rotate1	initial estimate for angle used to describe point source location (deg)
rotate2	initial estimate for angle used to describe point source location (deg)
npix u	detector size, orthogonal to the rotation axis (# pixels)
npix v	detector size, parallel to the rotation axis (# pixels)
Range	rotational range (degrees)
Nangles	number of projection angles
Direction	Rotation direction (+1 or -1)
D01	distance between points 0 and 1 in the phantom (mm)
D02	distance between points 0 and 2 in the phantom (mm)
D12	distance between points 1 and 2 in the phantom (mm)
Ftol	fractional tolerance parameter for Powell's algorithm

We found that the algorithm is not particularly sensitive to the values of the initial estimates for the geometric parameters. However, the definition of D01, D02, and D12 must be correct in relation to the point numbers assigned to centroid data in the input file. In addition, the rotation direction must be correct (should be -1 for the X-SPECT). If the algorithm does not converge to a reasonable solution, it may be necessary to change these parameters. For example, the values of D01, D02, and D12 may be out of order.

A1.2.2. Input file

The input file is a text file, where each line represents the centroid position of one point source in a projection image. Each line consists of four numbers. The first number is the slice number (starting from 0), the second and third numbers are the pixel coordinates of the centroid of the projection of the point on the detector in the *u* and *v* directions (coordinates defined in Fig. 3.4), respectively, and the last number describes the point number (0, 1, or 2).

The centroid positions can be calculated manually, but a semi-automated method was also devised. The semi-automated method consists of several Matlab functions that calculate the centroid location within a rectangular region. The boundaries of the region in the first slice are defined manually. The functions then calculate the centroid, proceed to the next slice, update the boundaries based on the previous centroid location, and then calculate the next centroid location.

A1.2.3. Output

The results are output in a text file, as well as displayed on the screen. The data file contains a number of lines of output intended for use in debugging. However, in both versions of the program, the final estimates of the parameter file are output in a table,

UCSF LIBRARY

with the parameter number and corresponding parameter value on the same line. The parameter numbers and names are summarized in Table A1.2 for both version of the calibration program. The last 6 values output are the variables used to describe the location of the point sources.

Table A1.2: Output parameter numbers and names

Parameter Number	Parameter Name (geocal3)	Parameter Name (geocal2)
1	Focal length	Focal length
2	Radius of rotation	Radius of rotation
3	Mechanical shift	Mechanical shift
4	Electrical shift (u)	Shift x, source location
5	Electrical shift (v)	Shift y, source location
6	Detector twist	Shift z, source location
7	Detector tilt	Rotate 1, source location
8	Shift x, source location	Rotate 2, source location
9	Shift y, source location	Rotate 3, source location
10	Shift z, source location	-
11	Rotate 1, source location	-
12	Rotate 2, source location	-
13	Rotate 3, source location	-

A1.3. Implementation

As mentioned previously, the programs minimize the difference between the location of the measured point source in the projection image and the calculated location of the point source, which involves a process of several steps. First, the location of the point sources must be calculated. Second, the location of the projection of the point source onto the detector must be determined from the point source locations and the estimated imaging geometry. The value of the cost function must be calculated, and than the cost function must be minimized.

UCSF LIBRARY

A1.3.1. Calculation of estimated u and v

Calculation of the location of the estimated point source projection on the detector face is accomplished using the functions `EstU` and `EstV`, which return the *u* and *v* coordinates, respectively (see Figures 3.2-3.4). The input to the functions include an array containing the geometric parameter values, the *x*, *y*, and *z* coordinates of the point source, and the projection angle in degrees. The functions then rotate the *x*, *y*, *z* coordinates of the point source to account for the projection angle, tilt angle, and twist angle in turn. Then the *u* (or *v*) position is calculated using geometrical arguments. This method was described in the paper by Beque, *et al* [1].

Given estimated values for three rotation angles and three translations, and the measured distances between the three points, the point source locations are calculated using the following method. The points are assumed to form a triangle, with the first point at the origin. Because the distances between the points are known, the lengths of the three sides of the triangle are also known. The second point is assumed to lie on the x-axis, such that its position is defined by the coordinates (D_{01}, 0, 0). The position of the third point can be calculated, and must be at (x_2, $\pm\sqrt{{D_{02}}^2 - x_2^2}$, 0), where $x_2 = \frac{{D_{02}}^2 - {D_{12}}^2 + {D_{01}}^2}{2D_{01}}$. We select the positive value for the y coordinate, and then rotate the points on the triangle about the *z*-, *y*-, and *x*-axes, sequentially. The final step is to translate all three points in the *x*, *y*, and *z* directions.

A1.3.2. Calculation of cost function

The cost function is the objective of the minimization routine. It is basically the summed square error between the estimated *u* and *v* coordinates of the point source

UCSF LIBRARY

locations, and the measured u and v coordinates (Eq. 3.1). Calculating the cost function involves calling the function `Cost`, as well as several subroutines. The first step is to calculate the location of the point sources in the (x, y, z) coordinate space using the function `Pos`, given the values of the 6 parameters used to define the point source locations. The second step is to loop through the projection views, compare the measured u and v values with the estimated values, and add the square of the difference to the output. Finally, the values of the geometric parameters are compared to the limit values, and a penalty proportional to the square of the deviation is added if the parameter values are outside the limits.

A1.3.3. Minimization of cost function

The value of the cost function was minimized by changing the geometric parameters and the point source location parameters. The minimization was performed using an implementation of Powell's algorithm taken directly from Numerical Recipes in C [2].

References

[1] D. Beque, J. Nuyts, G. Bormans, P. Suetens, and P. Dupont, "Characterization of Pinhole SPECT Acquisition Geometry," *IEEE Transactions on Medical Imaging*, vol. 22, pp. 599-612, 2003.

[2] W. H. Press, B. P. Flannery, S. A. Teukolsky, and W. T. Vetterling, *Numerical Recipes in C*. Cambridge: Cambridge University Press, 1988.

UCSF LIBRARY

Appendix 2: Ray-driven Projector

A2.1. Overview

A projector (or forward projector) is an algorithm to estimate the measured projection data given information about the imaging system and the object being imaged. Projectors are an important part of iterative reconstruction algorithms, and are also useful for generating simulated projection data used for evaluating imaging systems. This appendix describes a ray-driven projector based on ray casting which was written in the C programming language as part of this thesis project.

Ray casting is a general technique used to model the path of light in optics. In this technique, rays are "cast" from a detector element towards the object. If the ray intersects a source of photons, then the detector elements "sees" these photons, and its output is adjusted accordingly.

We implemented various versions of the program. Several versions of the projector were implemented. The various versions differ in how they model the collimator, and also how many geometric parameters (e.g., detector twist and tilt) are modeled. In this appendix, we will describe a version of the projector (called projection4b) that models an ideal pinhole, in other words, a pinhole with an infinitesimally small opening. The other versions are used in a similar manner.

A2.2. Usage

All versions of the program take a text based parameter file and a binary input file describing the radionuclide distribution, and output simulated projection data for a pinhole collimator system. Some versions will also require another input file describing

UCSF LIBRARY

the photon attenuation characteristics. This section of the appendix will describe the program inputs, details of the implementation, and the output format.

A2.2.1. Program input

Most versions of the projector program require three inputs: a text parameter, a file describing the source distribution, and a file describing the photon attenuation of the object being imaged. The file names are specified when running the program. In other words, in order to run the program projection4b, the user will type:

```
projection4b parameter_file input_file output_file.
```

The name of the attenuation map file is omitted in this case, because this version of the program does not model photon attenuation. Each input file will be described in turn.

A2.2.1.1. Parameter file

The parameter file is the first input file, and is a text file containing the names of the various parameters and their values. The name of the parameter file is given as the first argument after the program name at the time of execution.

Each line in the parameter file consists of a parameter name, followed by the equal symbol (=), followed by the parameter value. The program is case sensitive, and the equal sign must follow the parameter name without a space. The parameter names, followed by a description of the parameters, are given in Table A2.1.

Table A2.1: Parameter names for projector

Parameter Name	Description (units)
PH2COR	Radius of rotation (cm)
DET2PH	Focal length (cm)
shift	Lateral shift (cm)
twist	Detector twist (degrees)
Eu	Electrical shift, u (cm)
Ev	Electrical shift, v (cm)
Tilt	Detector tilt (degrees)
nAngles	Number of projection angles
range	Angle range (degrees)
DET_WIDTH	Width of detector (cm)
DET_HEIGHT	Height of detector (cm)
direction	Rotation direction (-1 or +1)

A2.2.1.2. Input file

The input file consists of a representation of the source distribution in the binary "IM" format. The IM format is a binary format with a 48 byte tagged header that was developed, and is still used in the UCSF Physics Research laboratory. The data are arranged in a 3-dimensional image matrix of numbers in either floating point or unsigned short integer format. The name of the input file is the second command line argument when running the program.

A2.2.1.3. Attenuation map

The attenuation map is an image file in the binary "IM" format described above. The dimensions of the attenuation map need to be the same as the input file. The voxel values in the image are floating point numbers that represent the linear attenuation coefficient in units of inverse cm (cm^{-1}). If a model of attenuation is not desired, then an attenuation map containing only values of zero can be used.

A2.2.2. Output

The output is a file with the "IM" format described above, and consists of a matrix of floating point numbers. Each "slice" in the reconstructed image represents a single projection image.

A2.3. Projector implementation

A description of the implementation of the projector can be divided into two parts, where the first part describes the rays and the second part describes the projection itself.

A2.3.1. Calculation of rays

The projector was implemented using a ray casting algorithm. The key step to this implementation is the creation of the rays. Each ray has the form of a linked list, which are described by House [1]. Each element in the linked list represents a voxel through which the ray passes, and contains information about the voxel position, the length of the ray through the voxel, and the distance that the ray passes from the voxel center. Also, each element contains a pointer (memory address) to the next element on the list, except for the last element of the ray, which contains has the value NULL in place of a pointer.

The imaging geometry used for ray tracing assumes that the detector is positioned perpendicular to the x-axis, and that the rays travel from larger values of x to smaller values of x. Each time the ray passes through a voxel, an element is added to the linked list. In our implementation, the detector remains in the stationary frame, and the image is rotated and resampled. This allows a single set of rays to be used for all projection views.

Multiple rays can be generated for each pixel. The specific paths of the rays can be varied to model collimator behavior and also variations in the imaging geometry. For example, in the case of an ideal pinhole, multiple rays start on each detector pixel and pass through the same point. To model a realistic pinhole, the rays will diverge as they pass through the pinhole (Chapter 4). Geometric effects can be modeled by changing the starting or ending points of the ray. For example, detector twist can be modeled by changing the starting points of the rays.

A2.3.2. Projection

In order to calculate the projection, two steps need to be performed. The first step is rotating-resampling the image space, followed by "tracing" each ray through the image space. The first step is done by rotating the input data, then resampling the rotated data so that the rows of the image matrix are perpendicular to the detector face. This method is described by Tang [2].

The second step is to trace each ray through the image matrix, and add to the output value of each detector pixel. The algorithm starts at each detector pixel and steps through the elements of every ray associated with that pixel. Each ray element represents a position within a voxel in the image space. The value of the image at that particular position is calculated using tri-linear interpolation of the image matrix [3], and is added to the detector output after scaling by the photon attenuation. The effect of photon attenuation is modeled by calculating the cumulative sum of the product of the attenuation coefficient and ray length encountered by the ray, and weighting the contribution of a voxel accordingly [4]. The contribution of the voxel to the output is also scaled by the length of the ray through the voxel, and a ray weighting factor which can be used to account for other effects such as the angular dependence of the sensitivity.

A2.4. Conclusion

We have implemented a projector that creates simulated projection data for pinhole imaging geometry. The program uses a ray-driven projector, and is capable of including a model of the photon attenuation.

References

[1] R. House, *Beginning with C.* Boston, MA: PWS Publishing Company, 1994.

[2] H. R. Tang, "A Combined X-ray CT-Scintillation camera System for Measuring Radionuclide Uptake in Tumors," in *Joint Graduate Group in Bioengineering.* San Francisco: University of California at Berkeley and University of California at San Francisco, 1998.

[3] G. L. Zeng and G. T. Gullberg, "A Study of Reconstruction Artifacts in Cone Beam Tomography Using Filtered Backprojection and Iterative EM Algorithms," *IEEE Transactions on Nuclear Science*, vol. 37, pp. 759-767, 1990.

[4] G. T. Gullberg, R. H. Huesman, J. A. Malko, J. P. Norbert, and T. F. Budinger, "An attenuated projector-backprojector for iterative SPECT reconstruction," *Physics in Medicine and Biology*, vol. 30, pp. 799-816, 1985.

Appendix 3: Iterative Reconstruction Algorithm with Collimator Response and Attenuation Correction

A3.1. Overview

Many different versions of EM reconstruction algorithms were written during the course of this thesis work. This appendix is directed towards the later versions, specifically versions of the OS-EM algorithm which used ray-tracing to model the depth-dependent collimator response, *e.g.* the code contained in the file `map3g.c`. This appendix will first describe details about the implementation, and will end with instructions for using the code.

The reconstruction algorithm described here is an OS-EM reconstruction algorithm written to reconstruct SPECT data acquired using a single pinhole collimator. It also includes the option of applying a smoothing prior, in which case the algorithm would be considered a MAP (*maximum a priori*) reconstruction algorithm. This algorithm uses a ray-driven projector/backprojector, and models the depth-dependent collimator response, and photon attenuation. It can also be used without a model for photon attenuation.

A3.2. Implementation

The objective of ML-EM or OS-EM for emission tomography is to find the activity distribution, $\lambda(b)$, which maximizes the probability of observing the measured data, n'. The activity distribution is found iteratively using the following equation, first described by Shepp and Vardi [1]:

$$\lambda_{k+1}(b) = \frac{\lambda_k(b)}{\sum_{d=1}^{N_d} p(b,d)} \sum_{d=1}^{N_d} \left[\left(\frac{n'(d)}{\sum_{b'=1}^{N} \lambda_k(b') p(b',d)} \right) p(b,d) \right] \qquad \text{(A3.1)}$$

where $\lambda_k(b)$ is the estimated radionuclide concentration in voxel *b* at iteration *k*, $\lambda k+1(b)$ is the next estimate of the radionuclide concentration, $n'(d)$ is the value of measurement *d*, $p(b,d)$ is the probability of detecting an emission from voxel b in detector position *d*, and *N* and N_d are the number of voxels and detector positions, respectively. The different terms in the equation can also be interpreted conceptually in the following manner. The measured data, $n'(d)$, is compared with the expected projection data on a given the current estimate of the activity distribution, which are estimated using the "forward projector" ($\sum_{b'=1}^{N} \lambda_k(b')p(b',d)$). The ratio between the measured and expected projection data is calculated on a pixel-by-pixel basis, and then backprojected into the image matrix (summation over *d*). The result is then normalized by $\sum_{d=1}^{N_d} p(b,d)$, and then is multiplied with the current image estimate to obtain the new image estimate.

In the MAP algorithm, the objective is also to maximize the likelihood function. However, in the case of MAP, the likelihood function has been changed to include *a priori* assumptions or information about the activity distribution. Most commonly, this likelihood function is chosen to reduce noise and smooth the data. In particular, we have chosen to implement the MAP algorithm using the smoothing function described by Nuyts, *et al* [2]. This smoothing function is known as a prior.

A3.2.1. Calculation of ray weights

The behavior of the collimator is modeled by modifying the orientation and the weight of the rays. For each detector pixel, a fixed number of rays are defined. The orientation of each ray is defined by two points, a starting point in the plane of the detector, and an ending point in the plane of the pinhole aperture. Each ray has a predefined endpoint, representing one of the points in a square grid around the center of the pinhole aperture. The number of points in this grid is user selectable, and the spacing of the points is adjusted to ensure that the points cover the pinhole opening. For each ray, 25 different starting points are evaluated. The weighting factor for each combination of ray starting point and end point is calculated, and the actual starting point is calculated using a weighted average of the points evaluated. After the starting and end points have been determined, the ray path through the image matrix is determined, and the weight of the ray stored in memory for later use.

As mentioned above, a weighting factor is calculated for each combination of ray starting and ending points. This weighting factor is calculated to account for the influence of attenuation in the collimator on the ray. The attenuation factor is calculated by determining the location where the rays enter and exit the collimator. This was done by checking the ray location at various points along its path, and determining if each point lay within the collimator material or in air. This is done using user input values for the pinhole insert thickness, diameter, and keel length. The pinhole acceptance angle is assumed to be equal to 90 degrees. The attenuation factor can then be determined using $\frac{I}{I_0} = \exp(-\mu L)$, where I is the intensity, I_0 is the incident intensity, μ is the linear attenuation coefficient, and L is the distance traveled.

A3.2.2. Forward projection

Forward projection is performed in the manner described in Appendix #, with the added step of multiplying the contribution of each ray to the final result by the previously calculated ray weight.

A3.2.3. Modeling the depth of interaction effect

The depth of interaction effect is modeled by modifying the projection. The DOI effect is calculated by tracing a single ray from the center of the pinhole to the center of each pixel. The ray is then followed into the detector. At 50 intervals in the detector, the ray position is calculated, and part of the initial projection value is added to the pixel value in the output image. This is repeated until the algorithm reaches the back of the scintillator crystal. This process is a numerical model for the depth of interaction effect. The DOI effect is modeled only in the forward projection process.

A3.2.4. Backprojection

Backprojection is performed in an analogous to forward projection, except that the values are taken from the "detector", and added to the image matrix. In order to account for the effect of detector rotation, it is first necessary to rotate the attenuation map, perform the backprojection, and then rotate the results to the orientation of the image estimate.

A3.2.5. Image uniformity and normalization

The data taken from the X-SPECT may or may not have had a flat-field correction applied to compensate for the non-uniform sensitivity of the collimator. The collimator response model attempts to model this response. The ray tracing algorithm accounts for the change in sensitivity with angle for the collimator configuration. However, a $\cos^3\phi$ term is added when making the rays, where ϕ is the angle between the line normal to the detector and the line from the pinhole to the source. Part of this term ($\cos^2\phi$) accounts for the added distance between the pinhole and the detector face away from the center of the detector. This added distance means that each ray actually accounts for a smaller solid angle in space, and thus should have reduced sensitivity. The other cos ϕ term accounts for the fact that the rays away from center are not normal to the pinhole plane.

In order to model the sensitivity, a projection is generated at the beginning of the program using a numerical flat-field source to create a simulated uniformity correction matrix. If the experimental data are not flat-field corrected, then nothing is done. If the data are flat field corrected, then the program creates the normalization matrix using the inverse of the simulated uniformity correction matrix generated above.

The normalization matrix is the backprojection of a uniform matrix of value 1, which can be understood in the following manner. In the ML-EM equation, it can be seen that the ratio between the measured data and the estimated projection data is backprojected. If the measured data are equal to the estimated projection data, then the ratio is one, the desired result has been obtained, and $\lambda_{k+1}(b)$ should be equal to $\lambda_k(b)$. Thus, the normalization term should be equal to the backprojection of a matrix of unit value. This is done for each subset at the beginning of the program, and the results are stored in memory.

A3.2.6. Updating the image estimate

In a ML-EM or OS-EM algorithm, the image estimate can be updated by using Eq. A3.1. However, if the algorithm has been modified with the addition of a prior, then Eq. A3.1 can no longer be used. Nuyts *et al* show a different approach, where they re-write the ML-EM equation in the form:

$$\lambda_{k+1}(b) = \lambda_k(b) + \frac{\lambda_k(b)}{\sum_{i=1}^{N_d} p_{ij}} \frac{\partial L}{\partial \lambda_k(b)} \qquad \text{(A3.2)}$$

where L is the likelihood value. We can rewrite this equation by factoring for $\lambda_k(b)$:

$$\lambda_{k+1}(b) = \frac{\lambda_k(b)}{\sum_{i=1}^{N_d} p_{ij}} \left[1 + \frac{\partial L}{\partial \lambda_k(b)} \right] \tag{A3.3}$$

In this equation we can see that the term in the square brackets is equal to the term in the square brackets in the ML-EM equation. Thus, we have a way of calculating $\frac{\partial L}{\partial \lambda_k(b)}$ using the forward and backprojectors. Nuyts *et al* adapt the ML-EM algorithm to form a preconditioned gradient ascent algorithm:

$$\lambda_{k+1}(b) = \lambda_k(b) + \frac{\left(\frac{\partial L}{\partial \lambda_k(b)} + \frac{\partial M}{\partial \lambda_k(b)} \right)}{\left(\frac{\sum_{i=1}^{N_d} p_{ij}}{\lambda_k(b)} - \frac{\partial^2 M}{\partial \lambda_k{}^2(b)} \right)} \tag{A3.4}$$

where M is the logarithm of the prior. The derivatives for M for the prior that we used are derived by Nuyts *et al* in their paper, and thus we can calculate all the terms in Eq. A3.4.

A3.2.7. Smoothing prior

We used the smoothing prior developed by Nuyts *et al.* The logarithm of the prior is shown in Eq. A3.5 below.

$$M(\lambda) = -\beta \sum_j \sum_{k \in N_j} \frac{(\lambda_j - \lambda_k)^2}{(\lambda_j + \lambda_k) + \gamma |\lambda_j - \lambda_k|} \tag{A3.5}$$

where *Nj* is the set of neighboring voxels around voxel *j.* The term β controls the "strength" of the prior, and the term γ is used to tune the behavior of the prior. When β is equal to 0, then the prior does not contribute to the reconstruction algorithm, and the algorithm behaves like a regular ML-EM or OS-EM.

A3.3. Using the reconstruction algorithm

The reconstruction programs are executed from the command line (*i.e.*, a DOS prompt in windows or from the command prompt in Linux). Image input and output files are in "IM" format used at the UCSF Physics Research Lab. The command to execute the program is: `map3g par_file inp_file atten_file output_file`, where the four arguments after the command name are the file names of the parameter file, input file, attenuation map file, and output file. These will be described in more detail below.

A3.3.1. Parameter file

The parameter file is a text file, where each line contains the parameter name, followed by immediately by the equal sign, followed by the numeric value of the parameter. The parameter names are case sensitive, and are listed in Table A3.1, followed by their description.

Table A3.1: Input parameters for reconstruction algorithm

Parameter name	**Description**
PH2ROR	Pinhole to center of rotation distance (cm)
DET2PH	Collimator focal length (cm)
shift	lateral shift (cm)
flat	Is input flat field corrected? 0=no, 1=yes
Eu	Electrical shift (cm) perpendicular to z-axis
Ev	Electrical shift (cm) parallel to z-axis
pixels	Output dimension (pixels)
pixels-Z	Output dimension, z-direction (pixels)
FOV	field of view diameter, optional (cm)
FOV-z	field of view in z-direction, optional (cm)
range	rotation range of input data (degrees)
iterations	Number of iterations
DET_HEIGHT	Height of detector (cm)
DET_WIDTH	Width of detector (cm)
direction	Rotation of gantry. -1 or 1. X-SPECT = -1
save intermediate	save intermediate iterations? 0=no, 1 = yes
Proj time	Time per projection (same units as Half-life)
Half-life	Half life of radionuclide decay (same units as Proj time)
Energy	Photon energy (keV). If Energy is 27.5, 140, or 208, then hard wired values for pinhole properties are used
Pinhole	Pinhole size. If Pinhole=1 or 2, then predefined values for pinhole dimensions are used
autoROR	Automatically correct radius of rotation? 0=no, 1=yes
PH mu	Linear attenuation coefficient of pinhole material (cm^{-1})
PH keel	Keel length of pinhole (cm)
PH thickness	Thickness of pinhole insert (cm)
PH diameter	Diameter of pinhole opening (cm)
Crystal thickness	Thickness of scintillator (cm)
Cystal mu	Linear attenuation coefficient of scintillator (cm^{-1})
Start angle	starting angle of rotation (degrees). Set to 90 for X-SPECT
nray	Number of rays per pixel
nray2	Square root of nray
DOI	Model DOI in projector? 0=no, 1=yes
Weight	Scaling factor for output

A3.3.2. Input file

The input file consists of an IM file, which is a binary image file where each slice represents a single projection. The IM file can be generated from the Interfile output of the X-SPECT scanner using the `rawus2im` utility program to add the appropriate header to the binary data.

A3.3.3. Attenuation map file

The attenuation map file is also an IM file, and consists of a binary image file where the value of each voxel is equal to the linear attenuation coefficient in units of cm^{-1}. The dimensions of the attenuation map must match the dimensions of the output, and the attenuation map data should be aligned with the SPECT coordinate space.

A3.4. Summary

Multiple versions of the SPECT reconstruction algorithm have been developed. This appendix describes the use and implementation of `map3g`, which includes collimator response for the pinhole collimator, attenuation correction, depth of interaction, and an optional smoothing prior.

References

[1] L. A. Shepp and Y. Vardi, "Maximum Likelihood Reconstruction for Emission Tomography," *IEEE Transactions on Medical Imaging*, vol. M1-1, pp. 113-122, 1982.

[2] J. Nuyts, D. Bequé, P. Dupont, and L. Mortelmans, "A concave prior penalizing relative differences for *Maximum-a-Posteriori* reconstruction in emission tomography," *IEEE Transactions on Nuclear Science*, vol. 49, pp. 56-60, 2002.

UC San Francisco
LIBRARY

7732475
3 1378 00773 2475

LIBRARY
USE ONLY